THE STARTING TRANSIENT
OF SOLID-PROPELLANT ROCKET MOTORS
WITH HIGH INTERNAL GAS VELOCITIES

Aerospace and Mechanical Sciences Report
No. 1100

by

A. Peretz, L. H. Caveny
K. K. Kuo and M. Summerfield

April 1973

PRINCETON UNIVERSITY

DEPARTMENT OF
AEROSPACE AND MECHANICAL SCIENCES

THE STARTING TRANSIENT
OF SOLID-PROPELLANT ROCKET MOTORS
WITH HIGH INTERNAL GAS VELOCITIES
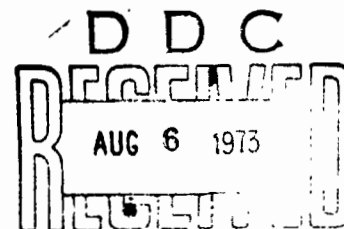
Aerospace and Mechanical Sciences Report
No. 1100

by

A. Peretz, L. H. Caveny,
K. K. Kuo and M. Summerfield

April 1973

D D C
RECEIVED
AUG 6 1973
C

Transmitted by:

Martin Summerfield
Principal Investigator

1. Distribution of this document is unlimited.

Guggenheim Laboratories
Department of Aerospace and Mechanical Sciences
PRINCETON UNIVERSITY
Princeton, New Jersey

ACKNOWLEDGEMENTS

Conditions of Reproduction

ABSTRACT

The starting transients of high-performance solid-propellant rocket motors having small port-to-throat area ratios are inaccurately predicted and unsatisfactorily analyzed by either the widely used lumped chamber-parameter models, or the quasi-steady one-dimensional flow models. In this study, a comprehensive analytical model has been developed to describe the transfer of mass, momentum and heat, and the fast ignition propagation along the port of monolithic rocket motors with high internal gas velocities during the three major phases of the starting transient: induction, flame spreading, and chamber filling. Both time and space development of the flow field in the motor are considered.

The gas dynamics in the chamber is governed by a set of three hyperbolic partial differential equations, that are coupled with the ignition and flame spreading events, and with the axial variation of mass addition. The flame spreading rate is calculated by local successive heating-to-ignition along the propellant grain surface. Local augmentation of the burning rate due to erosive burning is considered by using a modified Lenoir-Robillard's law. Entrance, boundary-layer, and surface roughness effects are accounted for in the empirical expressions for heat-transfer and friction coefficients.

The numerical solution of the governing equations utilizes an implicit finite-difference scheme combined with suitable initial conditions and proper physical and extraneous boundary conditions at both ends of the motor. The solution yields pressure, velocity and temperature distributions along the port for each calculation time step.

Experimental diagnostic studies were carried out with a laboratory-size rectangular window motor (50 cm grain length, 5 cm burning perimeter, and 1 cm hydraulic port diameter), using a controllable, head-end gaseous pyrogen igniter. Pressure measurements were taken at five stations along the port. Tests were conducted with unmetallized AP composite propellant at port-to-throat area ratios (A_p/A_t) of 2.0, 1.5, 1.2, and 1.06. Accordingly, the head-end pressures varied from 37 to 75 atm.

Calculated pressure transients $[p(t,x)]$ are in very good agreement with those measured in the experimental system, for all port-to-throat area ratios tested. Agreement within 10% has been obtained between calculated and experimentally measured ignition-delay and flame-spreading times, pressure peaks and times to achieve the pressure peaks for A_p/A_t = 2.0, 1.5 and 1.2. For A_p/A_t = 1.06, the agreement in times was within 15%, due to high gas velocities and low induction pressures. The highest pressurization rates

in all tests were measured at mid-motor. Rates as high as 7,000 atm/sec with $A_p/A_t = 2.0$ and as low as 3,000 atm/sec with $A_p/A_t = 1.06$ were measured.

Parametric studies have shown that the induction period and flame spreading duration are greatly affected by the igniter mass flow rate and gas temperature, the correlation for heat-transfer coefficient, A_p/A_t between 1.06 and 1.5, and uncertainty in the thermal conductivity and ignition temperature of the propel ant. The maximum chamber pressure and pressurization rate are affected by the igniter mass flow rate, burning surface-to-throat area ratio, burning rate law, A_p/A_t, and axial distance along the port.

The analysis enables starting thrust transient prediction and control by proper calculation of the stagnation pressure at the nozzle entrance.

An important area for future work is to extend this analysis to segmented motors.

The formulation of the analytical model allows an easy extension of the analysis to various types of solid propellants and operational motor configurations.

TABLE OF CONTENTS

Table of Contents - Continued   Page

NOMENCLATURE

A_b = burning surface area of propellant, cm^2

A_m = cross-sectional area of motor, cm^2

A_p = cross-sectional area of the port (port area), cm^2

A_t = motor nozzle throat area, cm^2

A_1, A_2, A_3 = points in Figs. 8 and 9

a = pre-exponential factor in the non-erosive burning rate law ($r_0 = ap^n$)

a_h = coefficient in the expression for convective heat-transfer coefficient [see Eq. (III-27)]

$a_1, a_2, a_3, a_4, a_5, a_6$ = coefficients in correlations and correction functions for the convective heat-transfer coefficient (see Section D, Chapter III)

B_ℓ, B_r = points at left boundary and right boundary, respectively (see Figs. 8 and 9)

b = burning perimeter, cm

c = speed of sound, cm/sec; when with subscript - specific heat, cal/g-°K

$c*$ = characteristic velocity, cm/sec

c_p = specific heat at constant pressure, cal/g-°K

d = duct diameter, cm

d_h = hydraulic diameter of the port, cm

d_p = diameter of a cylindrical port, cm

E = total stored energy per unit mass, $e + u^2/2gJ$, cal/g

E_a = activation energy of propellant surface reaction, cal/g-mole

e = internal energy of gas, cal/g

F = functional coefficient [see Eq. (IV-2)]

f = friction coefficient, $2g\tau_w/\rho u^2$

$f_{v\ell}$ = volumetric loading-density factor [see Eq. (I-3)]

G = mass velocity, $\rho u/A_p$, g/cm^4-sec

g = acceleration of gravity, conversion factor, g-cm/gf-sec^2*

h_c = local convective heat-transfer coefficient, cal/cm^2-sec-°K

h_{cp} = local convective heat-transfer coefficient over the propellant surface, cal/cm^2-sec-°K

h_{cw} = local convective heat-transfer coefficient over the non-propellant port wall, cal/cm^2-sec-°K

h_f = enthalpy of the propellant combustion gas at the adiabatic flame temperature, cal/g

h_p = port height (see Fig. 2), cm

I_{sp} = specific impulse of the solid propellant, gf-sec/g

I_{tot} = total impulse delivered by a rocket motor, kgf-sec

I_u, I_T, I_p = inhomogeneous terms in the governing equations [see Eq. (IV-2)]

J_c = mechanical equivalent of heat, gf-cm/cal

k = erosive burning coefficient, cm^3-°K/cal

k_0, k_1, k_2, k_3 = coefficients in Eq. (III-40)

L = effective length of motor combustion chamber, cm

L^* = characteristic length, cm

M = Mach number

m = mass velocity exponent in correlations for the convective heat-transfer coefficient (see Section A, Chapter II)

m_{ig} = igniter mass flow rate, g/sec

m_n = mass flow rate through the motor nozzle, g/sec

N = number of spacewise mesh points for the numerical calculation

Nu = Nusselt number

---

*gf denotes unit of gram force.

n = pressure exponent in the non-erosive burning rate law ($r_0 = ap^n$)

Pr = Prandtl number

P_w = wetted perimeter of the port, cm

p = static pressure, gf/cm^2

p_a = ambient pressure, gf/cm^2

p_{as} = stagnation pressure at the motor aft end (nozzle entrance), gf/cm^2

P_{ind} = pressure level during the induction interval, gf/cm^2

p_t = static pressure at the motor nozzle throat, gf/cm^2

P_1, P_2, P_3, P_4, P_5 = static pressure at stations 1 through 5, respectively (see Fig. 2), gf/cm^2

$P_{1,fs}$ = pressure at station 1 at time t_{fs}, gf/cm^2

q_ℓ = rate of heat transfer, cal/cm^2-sec

R = specific gas constant of the combustion gases, gf-cm/g-°K

Re = Reynolds number

R_u = universal gas constant, 1.98 cal/g-mole-°K

r = burning rate of the solid propellant, including the erosive burning contribution, cm/sec

r_0 = non-erosive burning rate of the solid propellant, ap^n, cm/sec

r_p = flame propagation (spreading) rate, cm/sec

T = temperature; without subscript - static gas temperature, °K

T_{af} = average film gas temperature, $(T + T_{ps})/2$, °K

T_f = adiabatic flame temperature of the solid propellant, °K

T_{ig} = effective mean temperature of the igniter gas, °K

T_{pi} = initial propellant temperature, °K

T_{ps} = propellant surface temperature, °K

$T_{ps,ig}$ = propellant surface temperature, at which propellant ignition occurs, °K

T_s = duct surface temperature (in general), °K

T_{ws} = non-propellant wall surface temperature, °K

St = Stanton number

s = exponent of the length-to-diameter ratio in correlations for the heat-transfer coefficient (see Section D, Chapter III)

t = time, sec

t_{ig} = ignition delay time (time from onset of igniter to the instant of first ignition of propellant), sec

t_{dp} = pressure delay time (time from onset of igniter to the instant of attaining 10% of the maximum pressure at the motor fore-end), sec

t_{fs} = time from onset of igniter to the instant of flame spreading completion, sec

t_{pm} = time from onset of igniter to attainment of maximum fore-end pressure, sec

t_{prm} = time from onset of igniter to attainment of maximum pressurization rate at motor fore-end, sec

u = gas velocity, cm/sec

V = volume, cm^3

W = molecular weight of the combustion gases, g/g-mole

x = axial distance from igniter nozzle end, cm

x_E = position at the motor aft end (entrance to motor nozzle), cm

x_{im} = position at the impingement of the igniter jet

x_p, x_0 = position at the entrance to the propellant section (propellant slab leading edge), cm

x_r = axial distance from the point of igniter jet impingement, $x - x_{im}$, cm

y = perpendicular distance from the propellant surface into the solid (see Fig. 7), cm

Greek letters

α = thermal diffusivity, cm^2/sec

β = erosive burning exponent [see Eq. (III-35)]

Γ = a function of γ, $\{\gamma[2/(\gamma+1)]^{(\gamma+1)/(\gamma-1)}\}^{1/2}$

γ = ratio of specific heats

Δ = difference

Δt = mesh size on t-axis

Δx = mesh size on x-axis

δ = penetration distance (see Section G, Chapter III), cm

δ_{ph} = characteristic thickness of preheated layer, cm

ϵ = a small number in Eq. (III-71), °K

ϵ_s = equivalent sand roughness, cm

η_i = internal performance of a solid-propellant motor [see Eq. (I-1)], $kgf\text{-}sec/cm^2$

θ = weighting parameter for the implicit numerical scheme

λ = thermal conductivity, cal/cm-sec-°K

μ = viscosity of the combustion gases, g/cm-sec (poise)

ρ = density (without subscript - gas density), g/cm^3

τ_c = relaxation time for the condensed phase, sec

τ_{ph} = time for burning through preheated layer, sec

τ_p = characteristic time for pressure variation, sec

$\tau_{p,m}$ = characteristic pressurization time, corresponding to maximum pressurization rate [see Eq. (C-3)], sec

$\tau_{p,t}$ = total time of pressurization, sec

τ_s = characteristic time for surface reactions, sec

τ_w = shear stress on the port wall, gf/cm^2

τ_{xx} = normal shear stress, g/cm^2

Superscripts

j = index for mesh time increments, $t^j = j\Delta t$

* = reference quantity for non-dimensionalization (see Appendix A)

- = weight-averaged quantity

^ = non-dimensionalized quantity

Subscripts

$A2, \overline{A}2$ = values at points A_2 and $\overline{A}_2$, respectively [see Figs. 8 and 9 and Eq. (IV-15)]

af = evaluated at the average film gas temperature (T_{af})

d = based on diameter

E = motor chamber aft end (entrance to motor nozzle)

es = entrance section

i = initial value

max = maximum value

n = index for mesh points in the axial direction, $x_n = n\Delta x$

pd = calculated by the latest predictor calculation [see Eq. IV-8)]

pr = solid propellant (condensed phase)

x0 = values at position x_0

I = along right-running characteristics

II = along left-running characteristics

III = along particle-path line

xiv

LIST OF TABLES

LIST OF FIGURES

CHAPTER I

INTRODUCTION

A. Motivation and Purpose of the Study

Prediction and control of the pressure-time and thrust-time programs of high-performance solid propellant rocket motors during the early phases of operation often depend on proper understanding of the complex interactions between elements such as, the igniter gas flow, heat transfer to the propellant, flame spreading, developing flow field, and erosive burning. The ability to predict and control the motor starting transient enables the following typical design and analysis objectives to be considered and approached:

(1) Keeping the overall transient time within specified limits;

(2) Reducing motor-to-motor variations (which is important, for instance, in the start of clustered motors);

(3) Extrapolation of sea-level motor ignition data to high altitude ignition conditions;

(4) Extrapolation of tests at normal temperatures ($\simeq 20°C$) to a wide temperature range (e.g., $-40°C$ to $+60°C$);

(5) Prediction and reduction of the overpressure, that sometimes accompanies ignition;

(6) Avoiding misfires and hangfires;

(7) Predicting the effects of long term storage on ignition requirements, once the effect of the influence of aging on ignition energy is known, and

(8) Predicting how a design modification will alter performance (e.g., propellant substitution, changes in throat area and motor dimensions, and propellant surface treatment).

Quantitative prediction and knowledge of the maximum pressure and pressurization rate during the ignition transient are very important to the rocket-motor designer. They allow and justify the use of a small margin of safety for the engine parts, thus obtaining high motor mass ratios. The pressure peak, frequently encountered during the starting transient of high-performance rocket engines, affects the structural design of the hardware, the grain integrity, and the use of acceleration-sensitive parts in the propelled

system. For particular designs, the rate of pressure rise may detrimentally affect the steadiness and stability of burning, the viscoelastic response of the grain and inhibitors, and the dynamic response of the hardware parts.

The broad task of ignition research is to provide a sound basis for defining and achieving the design and development goals with a minimum of expensive testing. This study is directed at developing analytical and experimental techniques that can be applied to achieve the above-mentioned goals and objectives.

Many studies have dealt with a particular fundamental process taking place during the start of solid propellant motors or have focused on practical correlations to facilitate igniter design. Also, previous models which were directed at the analysis of the overall starting transient can be categorized into two major groups: (1) lumped chamber-parameter, or p(t) models,[1-6] and (2) quasi-steady one-dimensional flow, or p(x) models.[7-12] The models of the first group assume uniform pressure and temperature distributions in the combustion chamber port. In the models of the second type, quasi-steady pressure, temperature, and velocity distributions along the port are supposed at each instant of time during the transient. The flame spreading is treated in studies of both groups in various ways: an experimentally determined function of time;[1,7-9] partially or fully instantaneous;[2,13] a linear function of the burning rate;[4] proceeding in a constant average rate;[6] calculated from an experimental pressure-time plot;[3] or calculated as a function of the axially varying heat flux to the propellant surface due to changing gas temperature[14] or boundary layer development.[5,15] The flame spreading analyses of Most and Summerfield[5] and Brown et al[14] are the most advanced studies among the lumped chamber-parameter models. A review of previous studies is presented in Chapter II.

Many modern, high-performance solid propellant rocket motors have high volumetric loading densities and small port-to-throat area ratios, frequently combined with large length-to-diameter ratios. Such motors, referred to in this study as HVT (High Velocity Transient) motors, are characterized by high internal gas velocities, significant axial pressure and temperature gradients, pressure overshoots, and relatively short transient times. The starting transients of the HVT motors are inaccurately predicted and unsatisfactorily analyzed by either one of the above-mentioned classes of approaches. Figure 1 shows schematically a typical starting transient of HVT motors compared with that of motors having a high port-to-throat area ratio.

This study investigates the starting transient of HVT motors, both analytically and experimentally. Pressure,

temperature, and velocity variations with time and axial position in the motor [p(t,x) model] are considered. Interactions between processes, such as the developing flow field, igniter gas flow, convective heat transfer to the solid propellant, flame spreading, and erosive burning are taken into account. A practical igniter-motor combination, utilizing a head-end pyrogen igniter is analyzed and discussed.

The primary objectives of the research described in this work, directed at achieving the previously stated tasks, were:

(1) To develop an analytical model for calculation and prediction of the starting transient of HVT motors;

(2) To design and build a laboratory-size, experimental HVT motor for diagnostic studies at low port-to-throat area ratios;

(3) To solve the analytical model for the physical situation of the experimental motor;

(4) To provide necessary empirical data and to verify experimentally the theoretical calculations, and

(5) To determine the effect of different igniter, propellant, and motor parameters on the starting transient.

As can be seen from the above list of objectives, in addition to the many practical aspects of this work, attention is directed at the fundamental processes that are of broad scientific interest, e.g., unsteady one-dimensional compressible fluid flows and combustion wave development.

B. The Internal Performance of Solid Propellant Motors With an Internal-Burning Grain

Other consequences of this work are contributions to optimization trends in solid propellant rocketry, which are becoming more important as more reliable, as well as inexpensive, motors are needed for space applications (such as shuttle boosters and impulsive thrusters) and for sophisticated missiles.

The internal performance of a solid propellant motor with an internal-burning grain, η_i, may be defined as follows:

$$\eta_i \equiv \frac{\text{Total Impulse Delivered by Motor}}{\text{Cross-Sectional Area of Motor}} = \frac{I_{tot}}{A_m} \quad (I-1)$$

The total impulse, I_{tot}, is given by

$$I_{tot} \approx \rho_{pr} V_{pr} I_{sp} \tag{I-2}$$

where: V_{pr} is the total available volume of propellant in the motor, and

I_{sp} is the specific impulse of the propellant.

A Volumetric Loading-Density factor, $f_{v\ell}$, is defined as

$$f_{v\ell} \equiv \frac{\text{Volume of Propellant to be Burned}}{\text{Total Available Volume of Combustion Chamber}} \equiv \frac{V_{pr}}{A_m L} \tag{I-3}$$

Substituting Eqs. (I-2) and (I-3) into Eq. (I-1) yields

$$\eta_i = \rho_{pr} I_{sp} f_{v\ell} L \tag{I-4}$$

The first two factors in Eq. (I-4) are the so-called density specific impulse, $\rho_{pr} I_{sp}$, which describes the delivered impulse per unit propellant volume, and is a measure of the quality of propellant and chemical-to-kinetic energy conversion process.

The last two factors in Eq. (I-4), $f_{v\ell} L$, describe the amount of propellant loaded per unit cross-sectional area of the motor and are a measure of the quantity of propellant used, for a given motor diameter.

This study is concerned mainly with highly-loaded motors, i.e., motors having high $f_{v\ell} L$-factors. High internal performance and efficient motor design require knowledge of the effect of the $f_{v\ell} L$-factor on the various ballistic parameters. The relation between propellant-charge configuration and various aspects of the ballistic parameters has been the subject of many investigations.[16-19]

A concise description of this study was presented elsewhere.[20]

CHAPTER II

REVIEW OF PREVIOUS STUDIES ON THE STARTING TRANSIENT

A large number of fundamental and applied researches have been conducted over the past twenty years to define and study the processes taking place during the ignition of solid propellant motors and to develop methods for prediction and control of the starting transient. Previous empirical tailoring, experience accumulation and rules-of-thumb are being replaced by analytical modeling, systematic tests, and prediction programs. A comprehensive and orderly literature review was presented by Most and Summerfield,[5,15] who summarized many previous studies according to approach, aspects of theoretical model, and experimental features. Detailed data on the performance characteristics of typical igniter systems along with design criteria, as well as data on propellant response and prediction techniques were compiled and published by Falkner and Miller.[21] In the present investigation an attempt is made to categorize generally the studies on the starting transient, especially those directed at the treatment of the entire transient, and review briefly representative works.

The studies on the ignition transient of solid propellant motors may be classified into the following four major categories:

(1) Studies of fundamental processes, such as ignition mechanisms of various propellants, chemical reactions taking place during the ignition, heat transfer to the condensed phase, flame propagation over the exposed surface, gas dynamics of the chamber pressurization, unsteady (dynamic) burning, and erosive burning of the propellant.

(2) Studies of ignition systems, aimed at their optimization by investigating the combustion properties of igniter ingredients, gas composition, and performance characteristics, and by formulation of desired compositions.

(3) Studies of the transient of a particular rocket motor, when a given grain design, specified motor size, and/or special firing conditions (e.g., extreme temperatures, vacuum, or body force fields) require precise transient prediction and control.

(4) Studies of the entire ignition transient, directed at the calculation of the pressure-time and thrust-time histories, considering interactions between the previously described transient processes and simultaneous phenomena.

Some studies belong to two or more categories. Another classification of studies may be made according to the laboratory-type of energy stimulus, which determines the mode of energy transfer to the propellant: shock tube, arc image furnace, radiation furnace with hot stagnant gas, laser apparatus, pyrotechnic or pyrogen-type igniter, operating in a real rocket motor, etc. This study belongs to Category (4).

A. Studies of Fundamental Processes

Most previous studies of the starting transient belong to the first, above-mentioned category. Comprehensive critical reviews of contemporary ignition theories are given in Refs. 22, 23, and 24. Analytical and experimental studies of the mechanisms of solid propellant ignition have resulted in three major ignition models, that are classified as solid phase, gas phase, and heterogeneous ignition theories. These theories differ mainly in the postulated place of the dominant, exothermic, runaway reactions, physical state of reactants, and sequence of processes. Accordingly, different ignition criteria may be presumed. The solid phase ignition theory, analytically established by Frazer and Hicks,[25,26] and further developed at the University of Utah,[27-29] and at NWC (formerly NOTS)[30,31] assumes, that condensed phase exothermic reactions dominate the runaway process, and neglects any participation of gas phase species. The gas phase ignition theory, developed mainly at Princeton University,[32-34] assumes that fuel vapors created from decomposition-gasification of the solid fuel diffuse into the hot, oxidizing, environmental gas and react exothermally near the propellant surface. The heterogeneous ignition theory, developed mainly at UTC[35,36] and recently advanced by Bradley and Williams,[37,38] and by Waldman and Summerfield[39,40] proposes, that the hot oxidizer gas formed from the decomposition of the ammonium perchlorate oxidizer reacts exothermally with the fuel in the condensed phase to provide the controlling reaction. The chemical reactions, involved in the ignition and combustion processes, have been treated in a global manner,[26,30,32] or in a general scheme, according to the model,[41] or by extensive investigation of a certain process, such as the decomposition of the ammonium perchlorate oxidizer,[42-44] and other propellant ingredients. Experimental studies try to determine gas species composition and concentrations by spectrometry and mass spectroscopy.

The process of heat transfer to the solid propellant, in all its major modes, has received considerable attention, due to its vital importance to the ignition transient. The rate of propellant heat-up is a complex function of simultaneous heat-transfer processes, such as convection, radiation, hypergolic heating, condensation, hot-particle impingement, and chemical recombination. Moreover, the unsteady turbulent flow with chemical reaction over the rough, decomposing pro-

pellant surface, in a complicated-geometry duct, makes an appropriate analytical study a formidable task. Instead, current analyses use simplified, semi-empirical heat-transfer correlations, based on experimental results. In the following paragraphs, numerous published studies are described briefly. Some heat transfer phenomena and correlations are discussed further in Chapter III.

An extensive research program, studying various aspects of ignition in practical situations has been conducted at the United Technology Center since 1962. Pyrogen igniters, both head-end and aft-end, have been fired into instrumented solid propellant motors,[45] and into a cylindrical copper duct, equipped with an exhaust orifice.[46] Heat-flux and flame-propagation measurements were made in a series of experiments, which resulted in empirical heat-transfer correlations for both the induction and flame spreading periods.[45,47] These correlations are based on expressions for fully-developed turbulent flow, modified for duct-entrance and jet-impingement effects. Analytical models for ignition and flame propagation, taking into account contributions of exothermic heterogeneous chemical reactions and assuming propellant surface autoignition temperature also were established.[14,45] The theory considers axial variation of the heat flux due to the drop in gas temperature along the port and increasing convective fluxes during flame spreading. Agreement between theoretically predicted and experimentally measured ignition delay times and flame propagation rates were reported. Extensive data on the effect of heat-flux, pressure levels, and solid-phase composition on the ignition response of various propellants also have been published by UTC.[48,49]

Carlson, Seader, and Wrubel of Rocketdyne carried out a thorough study of the heat transfer from pyrogen igniters to propellant grains of various configurations. First, they used a simulated igniter-motor combination, in which a hot nitrogen gas was forced through an instrumented duct.[50-52] The duct consisted of thin copper liners (installed in stainless steel test sections), and had a nozzle at the aft end. Various head-end and aft-end igniter-nozzle configurations were tested. Later, practical pyrogen igniters were fired into the instrumented duct and into real propellant charges.[53] Measured heat-transfer coefficients were compared with the classical turbulent pipe flow correlation and plotted versus nondimensional distance. The results are of particular interest to this study, since port-to-throat area ratios of 1.1, 2.0, and 3.0 were used. Unfortunately, no analytical correlations have been deduced by the investigators. However, their research revealed many of the parameters affecting the heat transfer to propellant grains, such as, entrance effects, igniter jet structure, port configuration and port-to-throat area ratio.

Lovine and Fong,[54] at Aerojet-General Corp. have also measured heat fluxes by firing subscale, pyrotechnic igniters into an instrumented test chamber. They correlated their heat-transfer data for the inlet region of the chamber by the expression for turbulent flow over a flat plate. However, a space-averaged heat-loss term is used in their gas-dynamics equations. Later, Micheli and Linfor[55] developed separate expressions for the heat-transfer coefficient for the three distinct regions of the port in a real rocket motor, namely, the impingement, downstream-of-impingement, and u stream-of-impingement zones, including a radiation contribution.

The ignition of solid propellants by radiative, convective, and chemical heating was the subject of many studies at Arthur D. Little, Inc.[56-59] Convective heating was studied by two methods: (1) in a hot-gas tunnel, by passing combustion gases through a rectangular test section, in which a propellant sample was held; and (2) in a cylindrical instrumented duct, into which practical pyrotechnic and pyrogen igniters were fired. Heat-flux measurements were interpreted in terms of developing turbulent flow correlations, assuming steady-state flow of the igniter gas. A simple two-layer film model, which accounts for the combined effect of all non-radiative heat-transfer modes, was introduced. Effects of gas velocity and port configuration were qualitatively studied by Bastress and Niessen.[59] They observed a marked increase in ignition times as the flow velocity is increased from Mach number 0.29 to 0.46. For long propellant samples first ignition was observed downstream from the sample leading edge. From the accumulated data Bastress and Niessen concluded that ignition behavior is sensitive to the local concentration of species evolved from upstream portions of the sample.

Intensive studies on radiative and convective ignition of solid propellants have been carried out at Princeton University. McAlevy[32] and Kashiwagi et al[60] studied the ignition of specimens of a solid fuel or propellant exposed to a hot, high-pressure stagnant oxidizing gas in a shock-tube. Their findings support the gas-phase ignition theory, and can be used as input to an applied ignition theory suitable for analyzing practical motors ignited by hot non-oxidizing high-velocity gases. The heat flux in an experimental rocket motor using a hot-wire, or gaseous pyrogen igniter was measured by Parker and Most.[3,15,61,62] A correlation of the type $Nu_x = a_1 Re_x^{0.8}$ was deduced from two measurement positions, large scatter of data, and several ad-hoc assumptions, such as, average constant driving temperature difference and a leading edge parameter based on a difficult-to-define duct leading edge. Both investigators report, however, good agreement between measured and predicted (with the above-mentioned correlation) flame spreading rates.

Extensive and systematic studies of AP-propellant ignition processes, by radiative heating in a radiation furnace, and convective heating in a shock-tube test section, have been conducted at the University of Utah. Baer, et al[27,28] measured convective heat fluxes and ignition times of propellant samples, mounted in the wall of a test section at the end of a shock tube. They found that ignition time depends primarily on propellant composition and heat flux, when air or nitrogen was used as the test gas. In this case, the dependence of ignition time on heat flux was correlated according to the solid-phase thermal ignition theory. When the propellant was heated by oxygen, a significant reduction in ignition delay, attributed to exothermic reaction between the oxygen and the fuel, was observed. Keller, Baer, and Ryan[63,64] in a systematic experimental study, investigated the effect of gas velocity on ignition, discovered previously by McCune[29] and Kling et al.[65] High-pressure (14 to 25 atm), high-temperature (1000-2600°K) gas behind the reflected shock wave in a shock-tube end was passed through a constant-area rectangular test section. The propellant samples were mounted flush with one of the test-section walls, and the test-gas velocity was controlled by critical-flow orifices at the downstream end of the section. Test-section Mach number was varied over the range of 0.07 to approximately 1.0. In general, the effect of higher gas velocities was to decrease the time to ignition for the same heat flux. This effect was found to decrease at very high velocities. Keller, Baer, and Ryan discovered an interesting effect of the propellant-surface condition, i.e., for the same heat flux at the surface, reduced ignition times were observed, when propellant surface was rougher, and gas velocity was lower. For propellants with a smooth surface, the effect of gas velocity on ignition was much diminished. For propellants with a rough surface, the effect of gas velocity was substantial only for gas velocities under Mach 0.5. It was postulated, that the improved ignitability of propellants with rough surfaces is produced by supplementary secondary ignition reactions among propellant decomposition products, that are generated at the surface by increased heating of surface irregularities. If the velocity of the heating gas is increased, the decomposition products are swept into the heating gas before reacting. It is unfortunate, that pressure effects were not considered in their study and no experiments were carried out at high velocities and heat fluxes, and low pressures, pertinent to HVT motors. In later studies by Richardson, Ryan, and Baer,[66,67] the surface roughness effect was not observed at lower heat fluxes (2 to 30 cal/cm^2-sec) and lower test-gas temperatures and pressures (760 to 1300°C, 2.9 to 7.7 atm, Mach Number from 0.05 to 0.3). Also, the observation of Bastress and Niessen[59] that the first evidence of ignition occurred at some distance from the leading edge was not confirmed, under these test conditions. The effect of test-gas temperature was also studied. Convective heat fluxes

were measured in many studies at the University of Utah[27,63, 66-68] and the heat-transfer coefficient was correlated in the form $h_c = \text{const} \times T^{0.3}G^m$. The power m of the mass velocity G was reported to have values ranging from 0.68 to 1.06, indicating, that in some experiments transition flow may have existed over the propellant sample. The values of the constant and the power m were found to depend upon the nature of hot gas used in the tests. It should be noted, that unsteadiness of the convective heat transfer during tests under constant flow conditions (7.7 atm pressure, Mach Number of 0.08, gas temperatures of 760 and 1000°C) was reported by Baer and Ryan.[67] This unsteadiness, which was not observed with different measuring techniques and at higher gas temperatures, was attributed to nonuniform flow in the test section. In another study of the effect of propellant surface roughness[69] propellant samples with surface imperfections as large as 30 microns were subjected to convective heating in a shock tube and the heating was stopped before ignition. These same samples were then immediately subjected to ignition tests. The results did not show agreement with the hypothesis that surface roughness causes early ignition, but no definite conclusion has been drawn.

An investigation of the effect of environmental gases and pressure on the ignition of a solid rocket propellant and ingredients was conducted by Hightower.[70] The propellant samples were ignited in an arc-image furnace by radiant energy fluxes over the range of 6.5 to 120 cal/cm^2-sec. Environmental gases used were air, oxygen, nitrogen, methane, and helium. The tests were carried out at pressures of 15, 45 and 100 psia. At the higher energy fluxes the ignition time was found to be dependent on the environmental pressure with ignition times increasing when decreasing pressure. The shortest ignition times were obtained with pure oxygen as the environmental gas. Hightower concluded that, under the experimental conditions of his investigation, exothermic gas phase reactions occurring in a zone immediately adjacent to the propellant surface play a role of major importance in the ignition of AP composite propellants by high intensity thermal radiation.

The rate of flame spreading over the exposed propellant surface is a necessary element for any analysis of the starting transient. Flame spreading is a complicated process, coupling igniter behavior, port geometry, propellant response, unsteady combustion, and chamber gas dynamics. It has been studied both experimentally and analytically, coupled, or uncoupled with other processes.

A comprehensive theoretical model of flame propagation along a smooth port was developed at UTC.[14,45] This model takes into account all major possible modes of heat transfer to the propellant (i.e., conduction, convection, radiation,

and heterogeneous exothermic reactions), and considers temporal and axial variations of the gas temperature and heat transfer. During the flame spreading the convective heat-transfer coefficient is enhanced by an experimentally-determined function of the igniter and burning propellant mass flow rates, $h_c = h_{c,ig}[(\dot{m}_{ig} + \rho_{prr}A_b)/\dot{m}_{ig}]^{0.5}$, where $h_{c,ig}$ is the heat-transfer coefficient for igniter operation alone, correlated for developing[45] or developed[14] turbulent flow. The flame spreading process is determined by calculating the time to reach a critical surface temperature for ignition for positions along the longitudinal axis. Besides use of empirical factors to account for the enhancement of the heat-transfer coefficient, this model does not consider coupling to the transient gas dynamics of the chamber. Instead, neither temporal nor spatial variation of the chamber temperature were considered, and only temporal change of pressure was assumed. Fair to good agreement between calculated and measured (by the trip-wire technique) flame spreading rates was reported.[45] In another study at UTC,[71] under the unrealistic assumptions of no axial variation of the heat-transfer coefficient and propellant surface temperature, a scaling law of the form $r_p \sim q_\ell^2 d_p/St$ (where r_p is the flame spreading rate, q_ℓ is the heat flux to the propellant, St is Stanton Number, and d_p is the diameter of a cylindrical port) was derived.

DeSoto and Friedman[2,72] developed in 1964 a model for flame spreading, which assumes an isothermal one-dimensional gas flow in the chamber, spatially uniform pressure and mass generation due to the grain burning only. The initial conditions in their analysis include instantaneous ignition of part of the grain, uniform pressure and temperature in the gas phase, a uniformly distributed temperature in the unignited portion of the propellant surface, and an axially varying velocity distribution. Pressure varies with time only; velocity varies with time and axial distance. The analysis was used also for calculation of the chamber-filling period. No comparisons with experiments were reported. In view of the many unrealistic assumptions, the practical application of this analysis is doubtful.

Paul, Lovine, and Fong,[13] of Aerojet-General Corp., presented an analysis in 1964, in which the area subjected to direct igniter jet impingement is assumed to be ignited instantaneously. The heat transfer downstream of the impingement zone is taken as being independent of axial distance, the gas temperature is assumed to be constant with respect to time and space, and only the temporal variations of the uniform chamber pressure and heat flux are considered. Adopting the critical-temperature ignition criterion, this analysis predicts the time to instantaneous flame spreading downstream. However, in practice, instantaneous flame spreading is generally not observed. The flame spreading in the stagnant

region upstream of the igniter jet impingement zone is cal-
culated by a simplified analysis, assuming temporal and
axial variation of the convective heat transfer and consider-
ing radiation from a cloud and heat conduction, as well.

Considerable research on the flame spreading and chamber
filling processes has been conducted at Princeton University.
A model, established by Parker, Summerfield, et al,[3,61,73-75]
is based on the so-called dynamic temperature, well-stirred
analysis. This analysis assumes uniform chamber pressure
and temperature, both changing with time. The first method
of using the analysis uses a given experimental pressure
variation and an assumed initial temperature. A system of
two ordinary differential equations for the time variation
of pressure and temperature is solved numerically to yield
the flame-spreading rate. In a second method of using the
analysis, initial conditions of burning area, chamber tem-
perature and propellant surface temperature are assumed.
In addition, an experimentally determined heat-transfer cor-
relation and a critical temperature for ignition are used.
The method solves the pressure and temperature variation
equations and the heat equation for the solid phase to yield
the chamber pressure history and flame spreading rate. Con-
ditions of gasless igniter are assumed in Parker's analysis.
The aforementioned assumptions of initial conditions make
the use of this analysis for prediction of the flame spread-
ing and pressure transient rather inconvenient. Parker's
analysis was modified by Most, Summerfield, et al.[5,15,76-78]
Most's analysis includes the igniter operation until an early
stage of the flame spreading (rather unrealistic assumption),
and calculates the flame spreading rate by solving the solid
phase heat-up equation, coupled to the gas-dynamics equations.
The heat flux is both time- and distance-dependent. However,
the driving temperature difference is assumed to be constant
in both time and distance. The ignition criterion used in
Most's study was also that of a critical surface ignition
temperature.

The flame spreading over the surface of double base
propellants and propellant ingredients in a quiescent atmos-
phere was studied by McAlevy, et al.[79,80] It was found ex-
perimentally that flame-spreading velocity varies directly
with pressure (between 0.1 and 1 atm), oxygen fraction of
environmental atmosphere, and surface roughness. The flame
spreading was presented as a continuous gas-phase ignition
process and the analytical model derived was verified exper-
imentally for smooth surfaces. For rough-surfaced samples,
photographic evidence of random ignition sites, ahead of the
flame front, was obtained.

Mitchell and Ryan[81-83] conducted flame spreading experi-
ments with a rarefaction-tube apparatus, under conditions of
constant pressure and velocity using a relatively cool gas

flowing over the propellant-sample surface. The T-shaped propellant sample was positioned near the nozzle-end of the tube and flame spreading was observed by means of high-speed photography. In their analysis, the effects of pressure and velocity, both enhancing the flame spreading rate, are isolated. The effect of pressure was found to be greater than the effect of velocity for a given fractional change.

In other studies, as mentioned in the Introduction, the flame spreading rate is based on very unrealistic assumptions, such as having an average constant value,[6] or being a linear function of the burning rate.[4] In some investigations, flame spreading rates are scaled from experimental data for similar systems.[1]

Recent studies on the response of solid propellant burning to pressure changes have shown that during rapid pressure excursions (pressurization or depressurization) the instantaneous burning rate differs from the steady-state values, corresponding to the instantaneous values of pressure. During the pressurization process in the starting transient, dynamic burning rates higher than the steady-state may be encountered due to unsteady thermal profile in the solid phase. Early investigations of the effect of pressure transients on the burning rate resulted in Von Elbe's model and formula for the dynamic burning rate.[84,85] This model and formula were subsequently modified and used by Paul, Lovine and Fong[86] at Aerojet and others. Detailed models of the combustion wave for calculation of the dynamic burning rate response were developed by Merkle, Turk, and Summerfield,[87] by Krier, T'ien, Sirignano, and Summerfield (KTSS model),[88] by Denison and Daum,[89] by McClure, Hart, and Bird,[90] etc. A critical classification and review of the various analyses was presented by Culick.[91] Recently, an approach, established by Zeldovich and extended by Novozhilov,[92-94] was successfully applied at Princeton University by Summerfield, Caveny, Battista, et al[95-97] for calculating extinction boundaries, and transient internal ballistics. In this latter method, experimental steady-state burning rate data $[r(p,T_{pi})]$ over a wide range of initial (ambient) temperatures is needed[95,97] instead of a detailed flame structure. It has been shown[86,96,97] that the dynamic burning causes pressure overshoots during ignition.

Another aspect of dynamic burning is the burning of preheated propellant layers during the flame spreading and chamber filling periods.[61,76] This is especially pronounced after long induction (heat-up-to-ignition) periods and may cause greatly increased instantaneous burning rates and subsequent pressure overshoots.

Erosive burning is a phenomenon frequently encountered in HVT motors. This process of burning rate increase, due to

the flow of combustion gases over the propellant surface, is most pronounced during the chamber filling period. Like the flame-spreading rate, quantitative knowledge of the erosive burning is necessary for the prediction and control of the starting transient. Therefore, numerous studies have been conducted on the subject, and many empirical and semiempirical correlations were developed in attempts to accurately account for erosive burning. Unfortunately, a totally-successful and general model of erosive burning has yet to be developed. An extensive research program on erosive burning was carried out at Purdue University by Zucrow, Osborn and Murphy.[98-101] A comprehensive review of previous investigations and laboratory methods was prepared by Murphy,[101] and by Williams, Barrere, and Huang.[102] The general conclusions drawn from the experimental studies are: (1) slow-burning propellants are more prone to erosive burning than fast-burning propellants;[99,103,104] (2) there is a threshold velocity (or mass velocity) for erosion, which may be pressure-dependent and is more pronounced for the faster burning propellants;[104-107] (3) grain configuration affects the erosive burning;[102,107,108] (4) at relatively high pressures (100 atm) the type of propellant binder and the binder-to-oxidizer ratio have little effect on the erosive burning, but at medium and low pressures (50 and 20 atm) the effect of binder type is large;[105,109] and (5) addition of aluminum has only a slight effect on the erosive burning sensitivity of propellants based on polyurethane and UTREZ binders.[108,110,111]

Among the analytical approaches,[101,112-115] that of Lenoir and Robillard[112] is the most widely accepted and experimentally confirmed.[12,105-107,111,116] The theory of Lenoir and Robillard postulates that the erosive-burning increment of the burning rate is proportional to the coefficient of convective heat transfer from the core of flowing combustion gas to the propellant burning surface. The latter is attenuated by the blowing from the burning surface according to an exponential law, derived from the data of Mickley, et al[117] and Rubesin, et al,[118] and thus the total burning rate law takes the form $r = ap^n + kh_c \exp(-\beta r \rho_{pr}/u\rho)$, where k is the proportionality coefficient evaluated analytically and β is an experimentally determined constant. Lenoir and Robillard used the Chilton-Colburn correlation for the heat-transfer coefficient, valid for turbulent flow over a flat plate. Lawrence, et al[111] used successfully Lenoir-Robillard's law with a turbulent pipe-flow heat-transfer correlation for grain length to port diameter ratios of up to 50.

B. Studies of Ignition Systems

Many studies on the igniter hardware and characterization of igniter materials for the initiation and energy release systems have been conducted in the industrial and governmental laboratories. Ignition systems fall into one of the three general types: pyrotechnic, pyrogen, and hypergolic. Each type has its own features and way of development. All three categories of systems, as well as multiple-ignition systems for use with restartable or pulse solid-propellant motors, are the subject of past and present extensive activity. A comprehensive review of the work, done by the major agencies, engaged in research and development of ignition systems prior to 1956, was reported in a concise form by Korpi.[119] Up to 1956, a great deal of practical work on development and performance of pyrotechnic systems, and formulation of igniter materials, such as metal-oxidizer compositions, was done in Aerojet,[120] Thiokol, Alleghany Ballistics Laboratory (ABL), Picatinny Arsenal, Ballistic Research Laboratory (BRL), Jet Propulsion Laboratory (JPL), Naval Ordnance Laboratory (NOL), Naval Ordnance Test Station (NOTS), University of Michigan, University of Utah, etc. In the past fifteen years much development work has been conducted by the Bermite Powder Co. (BPC).

A monograph on solid-propellant rocket igniters recently published by NASA,[121] presents accumulated experience and knowledge in an organized concise form for effective use in design. A highly recommended igniter-design handbook[122] which compiles experience gained and practical information, was prepared by Bermite Powder Co. (BPC).

Many studies have tried to determine the minimum igniter energy, required for propellant ignition, which, in turn, determines the igniter system characteristics. In the Bureau of Mines, ignition energy values from 2 to 15 cal/cm^2 for double base propellants were found.[119,123] Studies at BPC and NOL have resulted in empirical relationships between motor configuration parameters, propellant ignitability, type of igniter material used and energy required for satisfactory ignition.[5,121] As pointed out by several investigators (e.g., Refs. 5, 23-27, 63, 64, 66-69), the ignition limit is established by the rate of ignition energy supplied, rather than by the total energy only. Other studies on igniter sizing are based on attaining a given necessary-for-ignition pressure in the motor port.[124]

Studies of the energy transfer supplied by the igniter gases by convection and radiation (the latter i very pronounced for usual pyrotechnic compositions) were conducted by firing the igniters, both pyrotechnic and pyrogen-type of different charge weight, into instrumented ducts that simulate solid-propellant motors.[125,126]

A brief listing of igniter material considerations and applications, as developed at BPC, was recently presented by Robertson.[127] Hypergolic ignition systems, applying a hypergolic reagent (usually liquid chlorine trifluoride) to the propellant surface were developed mainly at UTC.[128,129]

C. Studies on the Transient of Particular Motors

The effects of motor and igniter configuration, igniter placement, and initial conditions on many processes taking place during the ignition transient, make special studies of particular cases inevitable. For instance, a specific grain design may cause the flow pattern of the igniter and propellant combustion gases to produce transients differing significantly from those obtained using a grain with a cylindrical port of the same cross-sectional area. Study[130] in which pyrogen igniters were fired into instrumented star-shaped port has shown that the heat flux at the star inner diameter is about 3 times higher than that at the outer diameter. Many transient prediction and design programs were developed for specific grain design and motor configuration. This is why every correlation model and analysis has to be checked for its domain of applicability, before being applied to a given situation (see p. 18 in Ref. 5).

The development of the Algol III solid-propellant motor[116] for example, was influenced by the configuration dependence of the erosive burning, which affects the starting transient. Inhibiting part of the exposed propellant surface, in this case, has brought the starting transient into an acceptable range. Conditions of spin and altitude have affected the performance and the transient of many rocket motors.[131-134] For the same igniter mass flow rate, motor spin shortens the transient and increases considerably the pressure level. The existence of a nozzle plug or diaphragm changes the entire pattern of flow in the chamber and heat transfer to the propellant, affecting largely the pressure-time curve.[2] High longitudinal motor acceleration may affect considerably the transient motor internal ballistics by reducing the pressure drop along the port as well as the fore-end pressure.[10] These are just a few examples to show the effects of particular conditions, which make the general application of an even comprehensive analysis a difficult problem.

D. Studies on the Entire Ignition Transient

As mentioned in the Introduction, previous studies on the entire starting transient may be divided into two major classes: (1) the lumped chamber-parameter models, known also as the homogeneous models, and (2) the quasi-steady, one-dimensional flow models. The major difference between the two groups lies in the assumptions under which the analytical model of the chamber gas dynamics is formulated.

The analysis of Adams[1,135] presented in 1966 is typical of the early studies of the first aforementioned group. The gas temperature in the chamber is assumed to be uniform space-wise and constant timewise (the so-called "isothermal analysis"). The pressure transient is calculated from the mass conservation equation for the motor chamber, assuming uniform pressure, and taking into account the igniter mass inflow rate. Flame-spreading rates are presumed to be a prescribed function of time (usually a linear function) and ignition times are also provided. Erosive burning effect is accounted for in the analysis by taking it as a function of an average value of the Mach number along the port axis. Burning rate correction for pressurization rate is included. Experimental values of c^* are used to account for heat transfer to the propellant. Reasonable agreement between calculated and experimental pressure-time histories is reported and it is claimed that ignition peaks are caused primarily by erosive burning. All assumptions in this analysis are inadequate for HVT motors. Mainly, the assumptions of uniform pressure and constant chamber temperature and the concept of an average Mach number are unsatisfactory.

Another isothermal analysis was presented by DeSoto and Friedman[2,72] in 1964. In their analysis, however, the flame spreading rate is calculated by consideration of spatial, as well as, temporal variation of the gas velocity and heat transfer to the propellant, and the use of the critical sur-face-temperature concept as ignition criterion. Thus a con-tradiction between the isothermal assumption, and the varying heat transfer is created. No igniter mass flow rate is con-sidered and no comparison between calculated and experimental pressure transients is reported.

Sharn, et al[136] (1964) carried out an experimental and analytical study of the ignition transient by firing a pyro-gen igniter into a small motor. The ignition time is calcu-lated using experimental data and the concept of critical surface temperature for ignition. An isothermal analysis, combined with an instantaneous flame spreading is used for the calculation of the pressure transient. A single compar-ison with an experimental pressure-time history shows good agreement during the first portion of the transient and a poor agreement during the later part.

An isothermal analysis of the starting transient was developed by Brown, et al[14,45] at UTC. The analysis uses time-dependent burning surface area which is determined from a flame-spreading model. The latter considers axial varia-tion of the gas temperature and heat flux to the propellant.

A further development of the lumped chamber-parameter models was the use of uniform but timewise changing chamber gas temperature (the so-called "dynamic temperature analysis").

This is performed by combining the mass and energy conservation equations for the gas in the combustion chamber. The "dynamic temperature analysis" was developed largely at UTC[5] starting with the analysis of Baker[137] in 1962. However, no attempt to couple the more-complicated chamber gas dynamics to a calculation of the flame spreading rate was reported. Instead, experimentally obtained time to first ignition and flame spreading rates or a specified burning surface area as a function of time were used.[137] The analysis of Baker considers the regimes of both choked and unchoked motor nozzle. It can also be used to calculate flame spreading rates for a given chamber pressure transient. Baker emphasized the error introduced by assuming constant stagnation temperature in the motor. He used his analysis to predict the starting pressure transient of a slotted-grain motor and reports good comparison with measured transients.

Bradley[4] published in 1964 a dynamic temperature analysis which assumes a homogeneous, adiabatic system. This was the first analysis to predict the effect of various igniter and motor parameters, e.g., burning rate pressure exponents of the igniter and propellant, igniter flame temperature, igniter-to-propellant mass flow ratio and the initial pressure and temperature in the motor. A general igniter form function was used to show the effect of varying igniter mass flow rate on the transient. Assuming a linear relationship between the flame spreading rate and the burning rate, Bradley showed the importance of flame spreading in the pressurization process. In particular, he pointed out the large effect of the fraction of propellant surface initially ignited.

Lovine and Fong[54] used a dynamic temperature analysis for the chamber filling period only, combined with expressions for unsteady burning rate and unsteady nozzle flow. The induction interval was treated by evaluating average values of igniter-induced heat flux and port pressurization and by using experimental pressure-heat flux-ignition time data. The flame-spreading interval was not treated in Ref. 54. In an earlier section it is mentioned that in another report[13] Paul, Lovine and Fong consider an instantaneous flame spreading.

The pressure transient analysis established at Princeton by Parker and Summerfield[3,61,73] and later modified by Most, Summerfield, et al[5,15,76,78] can be considered as the more comprehensive of homogeneous models. Parker's analysis, considering only the flame spreading and chamber filling intervals is described earlier in this Chapter. Since Most's work was the precursor of this study it deserves more description and attention. Most's analysis calculates the entire ignition transient. The three major assumptions on which his model is based are: (1) uniform pressure in the chamber ($\nabla p = 0$); (2) uniform gas temperature in the port ($\nabla T = 0$), and (3)

kinetic energy of the combustion gases is negligible, compared with their thermal energy $(u^2 << c_pT)$. All three assumptions are inappropriate for HVT motors (having low port-to-throat area ratio). Assumption (2) was found to be unrealistic by many investigators, including Most, even for motor with large A_p/A_t due to the high heat-transfer rate in the port, caused by large temperature difference. Most accounts approximately for this by using a lower constant igniter gas temperature, determined experimentally. In Most's analysis the two nonlinear ordinary differential equations for the chamber pressure and temperature are coupled to the flame spreading process through the instantaneous burning area. The latter is calculated from the solid phase heat-up equation, using an experimentally determined heat-transfer coefficient, and the critical ignition temperature, as the ignition criterion. The theoretical model was tested experimentally over a wide range of parameters. Good agreement between the calculated and measured pressure transients is reported.

Most[15] reported that Falkner and Kilgroe of CETEC Corp.[138] had used his model with reasonable success, utilizing heat-transfer correlations of the form developed by Kilgroe.[47]

Motors with high volumetric loading density and low port-to-throat area ratio have been analyzed by the one-dimensional quasi-steady models.[11,12] In these models, a series of control volume increments is assumed along the port axis, and one-dimensional (steady-state flow) conservation equations are written for the increment (the so-called "incremental analysis"). Variations of the port area, burning surface and burning rate along the port are taken into account.

The usual calculation technique[7-9,139] in the quasi-steady models starts with an approximation of the fore-end pressure from the steady-state formula for equilibrium pressure. Then, the steady-state continuity and momentum equations are iterated for each increment using the perfect gas law and the steady-state energy equation to yield the flow parameters at the exit plane of the increment. Nozzle entrance stagnation pressure predicted by this method is compared with that necessary for passing the calculated total mass flow rate through a given nozzle-throat area. The iteration procedure repeats until the two stagnation-pressure values converge. This calculation is repeated for each time step in the transient. All calculations are organized in computer programs, the descriptions of which are given in the aforementioned references. No coupled calculation of the flame spreading rate has been given by any of the reported analyses. The flame spreading is required as a prescribed input to the computer calculations. The induction interval is not treated. The computer program in Ref. 8 can calculate

ignition-delay times if the spatial and temporal distribution of the heat flux created by the igniter is specified. No detailed comparison of calculated and experimental pressure transient histories is reported. By their character, the quasi-steady models attribute pressure peaks during ignition only to erosive burning and mass acceleration losses along the port; for they contain no provision to account for the dynamic effects which may be prominent in HVT motors.

In Ref. 10 an attempt is made to account for unsteady gas dynamics in the port. The analysis was aimed at the prediction of the starting transient of the HIBEX motor, characterized by high axial acceleration forces and use of fast burning propellant. Unsteady mass and momentum conservation equations with spacewise variation of pressure, temperature and velocity, combined with the perfect gas law, are derived in the incremental analysis. However, in the solution by finite-difference methods, the timewise derivatives of temperature and velocity are neglected and use is made of the quasi-steady energy conservation equation. Good agreement between calculated overall fore-end pressure-time plot and three experimentally measured pressure histories is presented, but there is no detailed comparison of the starting transient part of the plots.

CHAPTER III

ANALYSIS OF THE STARTING TRANSIENT OF HVT MOTORS

A. Description of the Physical Model

The analytical model is established for the general
class of HVT motors and is solved for the physical situation
corresponding to the experimental rocket motor designed and
built (as part of the study) to provide detail.d information
on the ignition events and to test the validity of the ana-
lytical model.

The physical situation, analyzed and solved by the model,
considers a rectangular window motor, which consists of an
entrance section, a propellant section and an aft section, as
described in Fig. 2. Two opposing propellant slabs (2.54 cm
wide, 0.635 or 0.318 cm thick, and 49.5 cm long), cast into
trays, are positioned in the propellant section. The initial
cross-sectional dimensions of the rectangular port (2.54 cm
wide and 0.635 cm high), as shown in Fig. 3, are uniform
along the entire motor. The ignition stimulus is provided
by a fore-end, gaseous, pyrogen-type igniter, which discharges
the ignition gases into the entrance section through a cen-
trally located axial sonic nozzle. A rectangular replaceable
nozzle, having a short convergent part and a well-defined
throat, is attached to the motor aft-end. A detailed descrip-
tion of the experimental facility is given in Chapter V.

The first phase of the starting transient is the induc-
tion interval (ignition lag), which ends with the appearance
of the first flame on the propellant surface. The delay
associated with the processes in the igniter depends upon the
particular ignition system and is therefore excluded from the
general analysis. The beginning of the transient is deter-
mined to be the onset of igniter discharge, defined as the
start of pressure rise in the igniter chamber. A flow pattern
with pressure, temperature, and velocity distributions devel-
ops in the motor port at the igniter onset. Subsonic flow of
the igniter gas with wall friction and heat transfer to the
propellant and non-propellant port walls at low pressure (usu-
ally between 1 and 3 atm for the low port-to-throat area
ratios under investigation) is established in the chamber.
Therefore, the motor nozzle may be either choked or unchoked.
The heat flux to the propellant surface creates an unsteady
temperature profile in the solid phase with constantly in-
creasing surface temperature.

The second phase of the transient is the flame spreading
period which starts at first ignition and ends when the entire
initially exposed propellant surface is ignited. The ignition
criterion adopted in this study is that a point on the propel-
lant surface ignites when it attains some critical ignition

(or autoignition) temperature,[3,77] denoted here by $T_{ps,ig}$, at which rapid runaway reactions leading to ignition take place. This ignition criterion is frequently used and leads to results which are often indistinguishable from those obtained using other criteria. Many studies[23,47,48] have shown that (under most conditions of motor ignition and for many propellants) $T_{ps,ig}$ to a good approximation is an invariant quantity. It should be noted, however, that for certain propellants it may be pressure-dependent. Thus the process of flame spreading along the propellant surface is described by the model of successive ignitions.[2,3,15] Once started, the flame spreading is accelerated by the increased heat flux, due to the rapidly increasing mass flow originating from the already ignited propellant surface. The transition from unchoked to choked flow in the port is considered in the analysis. Rapid chamber pressurization usually begins with the initiation of fast flame spreading.

The third and last phase of the starting transient is the chamber filling period, which follows the completion of flame spreading. Severe erosive burning may take place during this period and thereafter, due to the high gas velocities in the chamber. Thus, the maximum pressure, attained in the chamber, may be much higher than the desired equilibrium pressure. Significant pressure and temperature drops, as well as velocity increases, are established along the port. Following the pressure peak, a quasi-steady situation develops and the head-end pressure decreases toward an equilibrium value, primarily due to diminishing erosive burning, as the port area increases.

B. Basic Assumptions

The following basic assumptions are used in the analytical model:

(1) All chemical reactions occur on the propellant surface in a combustion zone, which is so thin that it can be considered as a plane. The combustion products enter the main stream in the port with zero momentum.

(2) The gases flowing in the port obey the perfect gas law.

(3) Rate processes at the propellant surface are quasi-steady in the sense that their characteristic times are short, compared with the characteristic time of the pressure transient.

(4) The propellant combustion products and the pyrogen igniter gas have the same values of c_p, W and γ.

(5) The flow in the chamber port is one-dimensional, with the fluid pressure, temperature, and velocity varying both with time and axial distance.

Assumption (1) is based upon many theoretical and experimental studies on the combustion mechanisms of composite propellants,[41,95,140] and is widely used by the investigators.[3,95,141] A careful examination of this assumption is necessary, however, when this analysis is applied to double base and highly-metallized solid propellants.

Assumption (2) is well acceptable for the usual range of high gas temperatures and moderate pressures in solid propellant rocket motors.

Assumption (3) is justified for the following reasons. From Ref. 95 the characteristic time for surface reactions is $\tau_s \approx R_u T_{ps} \alpha_{pr} / E_a r^2$. For typical values of composite propellant properties[95] and burning rate varying from 0.3 to 0.6 cm/sec at 20 atm, τ_s varies from 0.0005 to 0.002 sec, which is much lower than the smallest pressurization time observed in this study.

Assumption (4) may not be needed, if the pyrogen igniter burns a solid propellant charge of the same composition as the propellant in the main motor. It has been proved by the solution of the analytical model that the effects of slightly different c_p, W and γ on the gas parameter distribution in the chamber are negligible during the induction interval, when they are most pronounced. The difference in temperature between the igniter gas and the propellant combustion gases is accounted for in the analysis, assuming instantaneous mixing with no chemical reactions.

Assumption (5) is a good approximation to the real situation in view of the highly turbulent flows encountered in HVT motors. Consideration of two-dimensional or three-dimensional phenomena, in addition to the variation with time, which exist to some extent in practical motor configurations, would make the solution of the problem very difficult to achieve with the existing mathematical tools. Willoughby[142] has modified a computer program, recently published by Patankar and Spalding[143] for a two-dimensional model of flow based on a turbulent compressible boundary-layer theory, to calculate quasi-steady pressure drop along the solid propellant motor. He found a remarkable agreement between the pressure distribution calculated by Patankar's program and that calculated by a simple one-dimensional model.

Multi-dimensionality affects mainly particular processes such as the heat transfer to the surface, skin friction and erosive burning. Changes of flow properties across the bound-

ary layer are considered in the expressions for heat transfer and friction coefficient used in this analysis. The assumption of one-dimensional flow is consistent with the data reduction methods used to obtain these correlations.

C. Description of the Analytical Model

A control volume element is established in the motor port, as shown in Fig. 4. The mathematical formulation of the approach to the above described problem consists of the following:

(a) Mass, momentum, and energy conservation equations in unsteady, quasi-one-dimensional form for the gas phase;

(b) Equation of state for the gas flowing in the motor;

(c) Proper initial conditions at the start of the transient (onset of igniter flow);

(d) Two boundary conditions at the fore-end of the propellant section, obtained from a pair of ordinary differential equations, which describe the rate of change of pressure and temperature in the entrance section;

(e) A third boundary condition, which describes the gas velocity at the entrance to the motor nozzle, for either choked, or unchoked flow;

(f) Semi-empirical correlations for the convective heat-transfer and friction coefficients for the highly turbulent flow in the port;

(g) Burning rate law for the solid propellant, including the effects of initial temperature, pressure, and velocity (erosive burning), and

(h) A solid-phase heatup equation for determination of the propellant surface temperature during the induction interval, coupled to an ignition criterion for the solid propellant.

1. Conservation Equations for the Gas Phase

The mass conservation equation for the control volume in Fig. 4, written for a unit volume, is

$$\frac{\partial \rho}{\partial t} \quad + \quad \frac{\partial(\rho u)}{\partial x} \quad + \quad \frac{\rho u}{A_p}\frac{\partial A_p}{\partial x}$$

RATE OF MASS   SPATIAL INCREASE   INCREASE OF MASS FLOW RATE
ACCUMULATION   OF MASS FLOW RATE   DUE TO INCREASE OF PORT AREA

$$= \frac{rb}{A_p}(\rho_{pr} - \rho) \qquad\qquad (III-1)$$

RATE OF MASS ADDITION DUE TO
BURNING MINUS RATE OF MASS ACCU-
MULATION IN THE FREE VOLUME CREATED
BY THE PROPELLANT SURFACE REGRESSION

The momentum conservation equation, written for a unit control volume, is

$$\frac{\partial(\rho u)}{\partial t} \quad + \quad \frac{\partial(\rho u^2)}{\partial x} \quad + \quad \frac{\rho u^2}{A_p}\frac{\partial A_p}{\partial x}$$

RATE OF MOMENTUM   SPATIAL INCREASE   INCREASE OF MOMENTUM
ACCUMULATION   OF MOMENTUM FLUX   FLUX DUE TO INCREASE
                                   OF PORT AREA

$$+ \quad \frac{rb}{A_p}\rho u$$

RATE OF MOMENTUM ACCUMULATION
IN THE FREE VOLUME CREATED BY
THE PROPELLANT SURFACE REGRESSION

$$= -g\frac{\partial p}{\partial x} \quad - g\left(\frac{\partial \tau_{xx}}{\partial x} + \frac{\tau_{xx}}{A_p}\frac{\partial A_p}{\partial x}\right) \quad - g\frac{\tau_w P_w}{A_p} \qquad (III-2)$$

PRESSURE   VISCOUS FORCE DUE   FRICTION FORCE
GRADIENT   TO NORMAL STRESS   ACTING ON FLUID
FORCE   BY THE DUCT WALLS

The energy conservation equation, written in terms of the stored total (internal and kinetic) energy per unit mass, E, for a control volume of unit length, is

$$\frac{\partial(\rho A_p E)}{\partial t} \qquad + \qquad \frac{\partial(\rho A_p u E)}{\partial x}$$

RATE OF ACCUMULATION OF STORED TOTAL ENERGY	+	SPATIAL INCREASE OF STORED TOTAL ENERGY FLUX

$$= \frac{\partial}{\partial x}\left(\lambda A_p \frac{\partial T}{\partial x}\right) \qquad - \frac{1}{J_c}\frac{\partial(A_p pu)}{\partial x} \qquad - \frac{1}{J_c}\frac{\partial}{\partial x}\left(\tau_{xx} A_p u\right)$$

	NET RATE OF ENERGY INPUT BY HEAT CON-DUCTION	+	RATE OF WORK DONE ON THE FLUID BY PRES-SURE FORCES	+	RATE OF WORK DONE ON THE FLUID BY VISCOUS FORCES
=

$$- q_\ell P_w \qquad\qquad + \qquad\qquad \rho_{pr} r b h_f \qquad\qquad\qquad (III-3)$$

-	RATE OF HEAT TRANSFER TO THE PORT WALLS	+	RATE OF ENTHALPY ADDI-TION BY BURNING OF THE SOLID PROPELLANT

The unit-conversion factors g and J_c are used in the conservation equations and throughout the analysis in order to carry out the entire study in a consistent, metric system of units, as denoted in the Nomenclature.

The gravitational force is the only body force that exists in the physical model analyzed in the study. However, the gravitational body force is negligibly small as compared to the surface forces for the physical situation considered, and therefore is not included in the mathematical model. Body forces such as centrifugal, axial acceleration, and electromagnetic forces which are important in certain applications can be included in the model, when necessary.

The above conservation equations, Eqs. (III-1) to (III-3), constitute a set of inhomogeneous, nonlinear partial differential equations. They are general in nature and can be applied to a broad range of practical rocket motors.

2. Simplification of the Conservation Equations

For a practical solution of the conservation equations a few simplifications are necessary. Each equation was nondimensionalized with respect to reference quantities specific for the general problem, and an order-of-magnitude analysis was performed to find the significance of each term. This procedure is described in Appendix A. As a result of the order-of-magnitude analysis the effects of the following terms were neglected:

(1) Rate of mass accumulation in the free volume, created by the propellant surface regression [as compared to the rate of mass addition due to burning, last term in Eq. (III-1)]. For the extreme operational conditions of $p = 100$ atm, $W = 40$ g/g-mole and $T = 1500°K$, there is $\rho = 0.02 \, \rho_{pr}$ (if $\rho_{pr} = 1.6$ g/cm^3). For the usual case of $p = 40$ atm, $W = 22$ g/g-mole and $T = 2500°K$, $\rho = 0.0026 \, \rho_{pr}$;

(2) Forces between gas molecules, due to the viscous stress in the axial direction, created by the axial velocity gradient [2nd term on the right-hand side of Eq. (III-2)];

(3) Axial heat conduction between gas molecules [1st term on the right-hand side of Eq. (III-3)]; and

(4) Rate of work done by the internal viscous forces and viscous dissipation [3rd term on the right-hand side of Eq. (III-3)].

The order-of-magnitude analysis shows that the friction force term in Eq. (III-2) cannot be neglected in laboratory-size HVT motors, even though it is small. Indeed, the parametric study conducted to investigate the effects of different parameters has confirmed this conclusion, as described in Chapter VI. Another reason for retaining the friction-force term is the tendency to have an analysis, which is able to check the effect of pre-firing propellant-surface roughening. This roughening has been explored as a means of shortening ignition delay times. However, it does not lead to reproducable results and is not widely used.

Many practical rocket motors are designed with initial port area which varies with distance from the fore-end. It should be pointed out that the analysis considers this initially prescribed function $A_{p,i}(x)$, as well as the variation of port area after ignition $A_p(x,t)$, caused by the uneven axial distribution of burning rate along the motor port. It should be also mentioned that the analytical model corresponds closely to motors with pyrogen igniters, but can be readily modified for application to motors using pyrotechnic igniters.

After deleting the above-mentioned terms of secondary importance, the conservation equations are rewritten in the following.

The mass conservation equation is

$$\frac{\partial \rho}{\partial t} + \frac{\partial (\rho u)}{\partial x} + \frac{\rho u}{A_p} \frac{\partial A_p}{\partial x} = \frac{rb}{A_p} \rho_{pr} \qquad \text{(III-4)}$$

Following the substitution of the mass conservation equation, Eq. (III-1), into Eq. (III-2), and the use of a conventional definition for the friction coefficient ($f = 2g\tau_w/\rho u^2$), the momentum conservation equation becomes

$$\rho \frac{\partial u}{\partial t} + \rho u \frac{\partial u}{\partial x} + g \frac{\partial p}{\partial x} = - \frac{rb}{A_p} \rho_{pr} u - \frac{fP_w}{2A_p} \rho u^2 \qquad \text{(III-5)}$$

After the substitution of the mass and momentum conservation equations [Eqs. (III-1) and (III-2)] into Eq. (III-3) (performed before the nondimensionalization and order-of-magnitude analysis) and some algebraic manipulations, the energy conservation equation, in terms of the static gas temperature, becomes

$$\rho c_p \left(\frac{\partial T}{\partial t} + u \frac{\partial T}{\partial x} \right) - \frac{1}{J_c} \left(\frac{\partial p}{\partial t} + u \frac{\partial p}{\partial x} \right)$$

$$= \rho_{pr} c_p \frac{rb}{A_p} \left(T_f - T + \frac{u^2}{2gJ_c c_p} \right) - \frac{q_\ell P_w}{A_p} + \frac{fP_w}{2gJ_c A_p} \rho u^3$$

$$\text{(III-6)}$$

For simplicity, the specific heat at constant pressure, c_p, the mean molecular weight, W, and the ratio of specific heats, γ, are assumed to be constant throughout the entire starting transient. Also, species diffusion effects due to concentration gradients caused by mixing of the propellant combustion gases and the igniter gas, and by axial variation of the flowing gas parameters, are neglected. The pressure-dependence of the propellant adiabatic flame temperature is neglected too.

3. The Governing Equations and Their Initial Conditions

After substitution of the perfect gas law, $p = \rho RT$, into Eq. (III-5), the momentum equation reduces to the first governing equation:

$$\frac{\partial u}{\partial t} + u\frac{\partial u}{\partial x} + gR\frac{T}{p}\frac{\partial p}{\partial x} = -\frac{\rho_{pr}Rrb}{A_p}\frac{Tu}{p} - \frac{fP_w}{2A_p}u^2 \qquad \text{(III-7)}$$

Two other governing equations are obtained by substitution of the perfect gas law into the mass and energy conservation equations [Eqs. (III-4) and (III-6)], combining the two, and some algebraic manipulations:

$$\frac{\partial T}{\partial t} + u\frac{\partial T}{\partial x} + (\gamma-1)T\frac{\partial u}{\partial x} = -\frac{(\gamma-1)uT}{A_p}\frac{\partial A_p}{\partial x}$$

$$+ \gamma\rho_{pr}R\frac{rb}{A_p}\frac{T}{p}\left[T_f - \frac{T}{\gamma} + \frac{u^2}{2gJ_cc_p}\right] - (\gamma-1)\frac{P_w}{A_p}\frac{T}{p}\left[J_cq_\ell - \frac{fpu^3}{2gRT}\right]$$

$$\text{(III-8)}$$

$$\frac{\partial p}{\partial t} + u\frac{\partial p}{\partial x} + \gamma p\frac{\partial u}{\partial x} = -\frac{\gamma pu}{A_p}\frac{\partial A_p}{\partial x} + (\gamma-1)\frac{\rho_{pr}rb}{A_p}\left[J_cc_pT_f + \frac{u^2}{2g}\right]$$

$$- \frac{(\gamma-1)P_w}{A_p}\left[J_cq_\ell - \frac{fpu^3}{2gRT}\right] \qquad \text{(III-9)}$$

The three governing equations [Eqs. (III-7), (III-8), and (III-9)] are first order, inhomogeneous, coupled, and nonlinear partial differential equations. The independent variables are time t, and distance along the port x, and the unknowns are the gas velocity u, temperature T, and pressure p. This set of governing equations contains all essential gas-dynamic features of the physical model, as applied to propellants with no or low aluminum content. However, rocket motors that use highly aluminized propellants that do not produce large Al_2O_3/Al agglomerates (i.e., the aluminum burns very close to propellant surface) are also closely approximated by this set of equations. When the aluminum particles are sufficiently small, the two phase flow effects are not important and effective values of γ, c_p, and W enable the aluminum/combustion gas mixture to be considered as if it were gas only.

The three necessary initial conditions, which describe a state of uniform distribution in the propellant and aft sections of the motor, are:

$$\left.\begin{array}{l} u(0,x) = u_i \\[6pt] T(0,x) = T_i \\[6pt] p(0,x) = p_i \end{array}\right\} \qquad \text{(III-10)}$$

where u_i, T_i, and p_i are the initial gas velocity, temperature, and pressure, respectively, in the motor. To facilitate the start of the numerical solution, it is assumed that p_i is slightly higher than the ambient pressure (by 0.0001 atm), with resulting small velocity u_i in the port.

Examination of the radiative heat transfer from the cloud of igniter gases or propellant combustion gases in the chamber to the port walls[144,145] shows that for the case and conditions considered in this study with unaluminized propellant, heat transfer by radiation is less than 5% of the convective heat transfer. This is in agreement with the measurements and findings of many investigators.[47,56,120]

The following expression for the rate of heat transfer to the propellant and nonpropellant walls, q_ℓ, pertinent to the physical and experimental configuration (see Fig. 3) is used in the analysis:

$$q_\ell = \left[2h_{cw}h_p\left(T-T_{ws}\right) + h_{cp}b\left(T-T_{ps}\right)\right]/P_w \qquad \text{(III-11)}$$

where h_{cp}, and h_{cw} are the local convective heat-transfer coefficients over the propellant and nonpropellant port walls, respectively.

In particular cases such as the presence of solid particles in the igniter gases and the use of metallized propellants, the radiative heat transfer may become substantial and should be considered.[146]

4. The Physical Boundary Conditions

The physical boundary conditions are specified in accordance with the flow conditions at both ends of the motor.

A comprehensive study of the structure (boundary and internal shock-pattern) of axisymmetric free jets exhausting into still air and into supersonic streams was conducted by Love and co-workers.[147] A research group in Rocketdyne investigated experimentally the gas-dynamics and heat-transfer characteristics of simulated head-end igniters in configurations generally identical with that in this study.[50,52,53] Figure 5, taken from Ref. 53, shows the jet structure of a head-end sonic igniter, exhausting into a duct with a nozzle at its other end, for two possible cases: (1) expansion into a duct with relatively small diameter (see Fig. 5a), and (2) expansion into a duct with relatively large diameter (see Fig. 5b). The sizes of igniter nozzle and motor port used in this study imply the existence of the case, described in Fig. 5a, in vertical direction, whereas the case, described in Fig. 5b

is valid in the horizontal direction (see Fig. 3). Therefore, the three-dimensional flow pattern in the entrance section of the experimental motor during the igniter operation is quite complex.

In the analytical model of this study it is assumed that fast stirring takes place in the entrance section, and therefore the gas properties are uniform therein. The mass and energy conservation equations for a control volume, taken to be the entire volume of the entrance section, provide two boundary conditions at the fore-end of the propellant section as described in the following paragraphs.

The mass conservation equation for the gas in the entrance section is:

$$V_{es} \frac{d\rho_{es}(t)}{dt} = m_{ig}(t) - A_{p,es}\rho_{es}(t,x_p)u_{es}(t,x_p) \quad \text{(III-12)}$$

where $m_{ig}(t)$ is the igniter mass flow rate into the entrance section. The second term on the right-hand side represents the mass flow rate out of the section.

The energy conservation equation for the entrance section is

$$V_{es} \frac{d}{dt}\left\{\rho_{es}(t)\left[\frac{c_p}{\gamma}T_{es}(t) + \frac{u_{es}(t)^2}{2gJ_c}\right]\right\}$$

$$= m_{ig}(t)c_pT_{ig} - \rho_{es}(t,x_p)u_{es}(t,x_p)A_{p,es}\left[c_pT_{es}(t) + \frac{u_{es}(t,x_p)^2}{2gJ_c}\right]$$

$$\text{(III-13)}$$

Order-of-magnitude evaluation, confirmed by the results of the numerical solution, shows that the rate of change of the kinetic energy in the entrance section is negligible in comparison with the rate of change of the thermal energy. Hence, the second term in the parenthesis on the left-hand side of Eq. (III-13) can be ignored in this analysis.

After substitution of the equation of state into Eq. (III-13), and rearrangement, the following equation is obtained:

$$\frac{dp_{es}(t)}{dt} = \frac{1}{V_{es}}\left[\gamma RT_{ig}m_{ig}(t) - \gamma A_{p,es}p_{es}(t)u_{es}(t)\right.$$

$$\left. - \frac{(\gamma-1)A_{p,es}p_{es}(t)u_{es}(t)^3}{2gRT_{es}(t)}\right] \quad \text{(III-14)}$$

Substituting the equation of state and Eq. (III-14) into Eq. (III-12) one gets the following equation after some algebraic manipulations:

$$\frac{dT_{es}(t)}{dt} = \frac{1}{V_{es}}\left\{\frac{RT_{es}(t)m_{ig}(t)}{p_{es}(t)}\left[\gamma T_{ig} - T_{es}(t)\right]\right.$$

$$\left. - (\gamma-1)A_{p,es}u_{es}(t)\left[T_{es}(t) + \frac{u_{es}(t)^2}{2gR}\right]\right\}$$

(III-15)

The igniter mass flow rate, m_{ig}, is a prescribed function of time, determined from the experimental study, as described in Chapter V. High heat-transfer and shock-pattern losses, taking place in the entrance section, are found[52,53] to lower the effective mean temperature of the igniter gas there, T_{ig}, which is assumed to be constant during the transient. This point is discussed in Section D of this Chapter.

Equations (III-14) and (III-15) form a pair of coupled ordinary differential equations, which describe the rate of change of the gas pressure and temperature in the entrance section. Their solution provides two boundary conditions for the governing equations, Eqs. (III-7) to (III-9). The two initial conditions for this pair of equations are

$$p_{es}(0) = p_{es,i} \quad \text{and} \quad T_{es}(0) = T_{es,i} \quad \text{(III-16)}$$

The physical boundary condition at the aft end of the motor chamber is derived assuming quasi-steady isentropic flow between the entrance to the motor nozzle, which coincides with the chamber end, and the nozzle throat (see Fig. 2). This assumption is justified by the very small length of the nozzle entrance. Using mass and energy conservation equations (as well as isentropic relations) between the two sections, the following equation is derived:

$$u_E(t)^2 = \frac{2g\gamma}{\gamma-1}RT_E(t)\frac{1 - \left[\frac{p_t(t)}{p_E(t)}\right]^{\frac{\gamma-1}{\gamma}}}{\left(\frac{A_p}{A_t}\right)^2\left[\frac{p_t(t)}{p_E(t)}\right]^{-\frac{2}{\gamma}} - 1}$$

(III-17)

When the motor nozzle (with no divergent section) is unchoked (which is the usual case during the induction interval for very low port-to-throat area ratio and low to moderate igniter mass flow rates), the pressure at the nozzle throat, p_t, equals the ambient pressure, p_a, and Eq. (III-17) becomes

$$u_E(t)^2 = \frac{2g\gamma}{\gamma-1}RT_E(t) \frac{1 - \left[\frac{p_a(t)}{p_E(t)}\right]^{\frac{\gamma-1}{\gamma}}}{\left(\frac{A_p}{A_t}\right)^2\left[\frac{p_a(t)}{p_E(t)}\right]^{-\frac{2}{\gamma}} - 1} \qquad \text{(III-18)}$$

It should be noted that Eq. (III-18) is given incorrectly by Shapiro on p. 966 of Ref. 148. This is probably a typographic error, since the plots accompanying the formula (p. 965 of Ref. 148) correspond to the correct equation, Eq. (III-18).

For the case of a choked motor nozzle, Eq. (III-17) becomes the following implicit relation:

$$u_E(t)^2 = \left[\frac{2}{\gamma+1}\right]^{\frac{\gamma+1}{\gamma-1}} \frac{\gamma g R T_E(t)}{\left(A_p/A_t\right)^2}\left[1 + \frac{\gamma-1}{2} \frac{u_E(t)^2}{\gamma g R T_E(t)}\right]^{\frac{\gamma+1}{\gamma-1}} \qquad \text{(III-19)}$$

The analysis considers both the unchoked and choked flow cases. The computing scheme in the numerical solution checks constantly the ratio of ambient pressure to stagnation gas pressure at the nozzle entrance for the choking condition and either Eq. (III-18) or Eq. (III-19) is used, accordingly. Usually the nozzle is choked at the early stages of the flame spreading phase. For instance, for m_{ig} = 15.0 g/sec at A_p/A_t = 1.2 the motor nozzle became choked when 10% of the exposed propellant surface had ignited.

It is noteworthy to mention, that if one considers a case in which a diaphragm is placed at the nozzle entrance, or a plug is inserted in the nozzle throat, the aft-end boundary condition for the period of time preceding the diaphragm burst, or the plug blowout, is simply

$$u_E(t) = 0 \qquad \text{(III-20)}$$

It should be also noted that a careful consideration of the physical situation after the motor nozzle throat is needed. Existence of a divergent part and an exhaust system should be taken into account when establishing the aft-end boundary condition.

In Appendix B the governing equations are presented in a form which shows the effect of mass addition, unsteadiness, heat transfer, etc. on the axial variation of pressure, temperature, and velocity. That presentation of the governing equations clarifies the contributions of this study as compared with the quasi-steady one-dimensional analyses.

D. Correlations for the Convective Heat-Transfer Coefficient

The flow in the port of HVT motors is highly turbulent (typical Reynolds numbers are given in Table 4). Dittus-Boelter's correlation for the convective heat-transfer coefficient for a fully-developed turbulent flow in a smooth pipe is widely accepted for use in solid-propellant rocket motors. This correlation has the following form:

$$Nu_d = 0.023\, Re_d^{0.8} Pr^{0.4} \qquad\qquad (III-21)$$

where subscript d denotes quantities based on duct diameter.

For turbulent flow in ducts with non-circular cross-section (and for $Pr > 0.6$ and $Re_d > 7{,}000$) the diameter successfully used in Eq. (III-21), as in expressions for the friction coefficient, is the equivalent hydraulic diameter d_h.[149,150] The applicability of the concept of the hydraulic diameter for turbulent flow has been verified experimentally up to a Mach number of 1.0.[150,151]

The flow in a solid-propellant rocket motor with an internal-burning grain differs from a fully-developed turbulent flow in a smooth duct. Therefore, if a proper application of Dittus-Boelter's correlation is to be made to a practical rocket motor, corrections for the following effects and phenomena must be considered:

(1) Entrance effects at the fore-part of the motor, resulting from the distance necessary for the development of the hydrodynamic and thermal boundary layers;

(2) Sharp variation of the fluid properties across the boundary layer;

(3) Highly transient flow conditions in the port;

(4) Propellant surface roughness which increases the heat transfer to the surface;

(5) Decomposition-gasification of the unburned propel-
lant surface, which attenuates the heat transfer
process;

(6) The general configuration of a solid rocket motor
with head-end ignition, in which a sonic jet is
discharged from an orifice of a relatively small
diameter into a duct that is constricted by an aft-
end nozzle [in contrast to the configuration for
which Eq. (III-21) applies directly];

(7) The configuration and stagnation properties of
the igniter jet, or jets, and the motor pressure
distribution.

(8) Impingement of incandescent particles, which may
exist in the flowing gas, on the unignited propel-
lant surface;

(9) Changes in flow conditions downstream of the igni-
tion front during the flame spreading, and

(10) Heat-releasing or heat-absorbing processes on the
unignited solid-propellant surface, such as gas-
phase condensation, and exothermic and/or endotherm-
ic reactions, which combine with the heat-transfer
from the hot gas flow.

Consideration of all these effects is a very complicated
task, especially because some of them are unclear quantita-
tively. Therefore, an experimental determination of the
heat-transfer correlation is necessary, even though it is
difficult to simulate all practical conditions for this pur-
pose.

A brief discussion of the above-mentioned phenomena af-
fecting the heat-transfer coefficient is pertinent here, be-
cause of its importance in calculating the starting transient
of HVT motors.

The entrance effects have been observed by many investi-
gators.[15,47,52,53,152-154] The developing flow at the en-
trance part of a duct, or a motor, has been correlated by
several methods: (a) assuming laminar or turbulent flow,
according to the flow conditions, over a flat plate[45,56,61,77]
(thus the coefficient in Eq. (III-21) is increased and the
effect of length appears through basing Reynolds and Nusselt
numbers on distance); (b) multiplying the Dittus-Boelter
expression by a power function of the length-to-diameter
ratio, such as $a_1(x/d)^s$, where a_1 takes values between 1
and 2, and the values of s range between -0.05 and -0.2;
[155-157] and (c) multiplying Eq. (III-21) by an exponential
function of the length-to-diameter ratio, usually of the

form $a_2[1 + a_3 \exp(-a_4 x_r/d)]$,[47,158] where a_2, a_3, and a_4 are constants. All three methods result in similar corrections, with pronounced entrance effects up to 6 to 20 duct diameters downstream. Maximum heat transfer for pyrogen igniters fired into instrumented ducts was found to occur in the igniter jet impingement zone and is up to 6 times that calculated by Eq. (III-21).

A consideration of the variation of fluid properties between the bulk of flow and the propellant surface is necessary in rocket motors because of the large temperature difference and considerable cross-sectional variation of transport properties. Several empirical methods of corrections to Eq. (III-21) have been proposed for this purpose: (a) multiplying Dittus-Boelter's correlation by a power function of the gas-to-surface temperature ratio of the type $a_5(T, T_s)^s$, or of the ratio of gas viscosity at the bulk temperature to gas viscosity at the surface temperature;[2,149,155,159,160] (b) evaluating the physical fluid properties in Eq. (III-21) at an average film temperature $T_{af} = (T + T_s)/2$ and using the bulk velocity, as correlated successfully by Humble, et al[154] for subsonic flow in long tubes and by Bartz[161] for highly turbulent flow in convergent-divergent nozzles, and as recommended by McAdams.[160]

The effect of flow unsteadiness on the convective heat transfer is, in general, not well known.[2,63] As described by DeSoto and Friedman,[2] at the onset of flow over a body, the boundary layer is not distinguishable and the entire flow pattern appears inviscid. As time progresses a boundary layer materializes. Thus the convective heat-transfer coefficients should be higher during the transient period than under steady-state conditions. Carlson and Seader[50,52] (using hot nitrogen at pressures from 570 to 620 psig and temperatures from 550 to 950°F) found a strong time dependence of the heat-transfer coefficient h_c. In some tests, h_c decreased by a factor of two at the end of 0.8 second at the location of the heat transfer maxima. In a later report, Wrubel and Carlson[53] attributed the transient effects observed by Carlson and Seader to undetected conduction losses and they considered time dependent effects to be negligible. Experiments[53] with high driving temperature potential (by firing pyrogen igniters into an instrumented duct) did not show transient heat-transfer behavior, except in areas with appreciable axial conduction losses. Knuth[162] showed from a theoretical analysis that for most applications forced-convection heat transfer rates to surfaces with time-dependent temperatures can be calculated to a good approximation using equations developed for the steady-state case. A comprehensive experimental work conducted at the University of Utah and reported in 1965[63,64] has confirmed the conclusions of

Knuth. In a later study, Baer and Ryan[67] observed unsteadiness effects (see Chapter II, Section A). Sparrow and Siegel[163] treated analytically the transient nature of the convective heat-transfer coefficient.

The effect of propellant surface roughness in increasing the convective heat transfer and thus decreasing ignition delay times and increasing flame-spreading rates has been widely observed. Unfortunately, well established quantitative data is missing. The increasing amount of experimental data indicates that the heat-transfer coefficient increases in a much slower rate with increasing surface roughness, than the friction coefficient.[150,159,164-166] Recent studies[167-170] have developed semiempirical correlations for heat transfer to rough surfaces in subsonic and supersonic turbulent flow and have concluded that the Reynolds analogy is invalid for rough surfaces. This invalidity increases with Reynolds number.[166,169]

The attenuation of convective heat-transfer coefficient and skin friction for turbulent flow over a surface with blowing has been the subject of many theoretical and experimental investigations.[117,118,171-179] However, until the physical law of the decomposition-gasification process taking place on the propellant surface is well established, applications to solid rocket motors can be done only in a speculatory manner.

The uniqueness of a solid-propellant rocket motor as compared to a pipe, as far as the convective heat transfer is concerned, was shown clearly by the studies of Carlson and Seader[50-52] and Wrubel and Carlson,[53] with the additional interpretation of Cohen, et al.[158] These studies have revealed the effects of igniter-nozzle configuration, motor-port to igniter-nozzle diameter ratio, and motor port-to-throat area ratio on the heat transfer distribution for relatively short motors. The importance of the igniter jet structure has also been shown. The secondary effects caused by the port-to-throat area ratio are primarily related to igniter jet expansion characteristics. It appears that these parameters have to be considered in HVT motors, since the above-mentioned studies were conducted with low port-to-throat area ratios (1.1, 2.0, and 3.0). This conclusion has been supported by the results of this investigation.

Most and Summerfield[5] studied the effect of molten aluminum particles liberated from the ignited portion of the grain during the flame spreading on the ignition of the remainder of the surface. No significant effect was observed. The particles that hit the unignited surface neither attached themselves to the surface, nor caused any spread of ignition as they traveled downstream. It was concluded that the quantity of hot aluminum particles in the flow was not sufficient

to augment significantly the flame spreading. However, radiation from densed clouds of incandescent particles should be considered.

The experimental study of Jensen and Cose[45] did not find any evidence that postulated vortex flow ahead of the advancing flame affects significantly the heat transfer downstream of the flame front. Most[15] also corcluded from his heat-flux measurements that the convective heat transfer during flame spreading is only very weakly dependent on the relative location of the flame and he related it to the original leading edge. However, when high burning rate propellants are used, with resulting large blowing parameter, this point should be considered carefully.

Propellant surface reactions have been considered in some heat-transfer studies[14,45] whereas very little has been published on gaseous condensation phenomena.[2]

After reviewing the large amount of literature on the convective heat transfer in real and simulated solid-propellant rocket motor, and in view of the highly turbulent flow in HVT motors in general, a correlation for the heat-transfer coefficient was deduced in this study. This deduction was made, keeping in mind the features of the experimental motor, for which the analytical model was first solved.

The expression for the local heat-transfer coefficient is based on the Dittus-Boelter correlation, Eq. (III-21), the dimensionless parameters, in which, are calculated using the local flow properties. This coupling to the chamber gas dynamics is necessary due to the large velocity, temperature, and pressure variations along the port, which are calculated by solving the governing equations, Eqs. (III-7 to III-9) (see Chapter VI). Corrections to Eq. (III-21) are introduced for the entrance effects, cross-sectional variation of gas temperature, and port-to-throat area ratio.

The corrections for the effects of length-to-diameter ratio and the variation of gas temperature from the core of flow to the surface are based on the studies of Humble, et al,[154] Cholette,[153] and Bartz.[161] The correction for port-to-throat area ratio is based on the interpretation of Cohen, et al[158] to the studies of Carlson, Seader, and Wrubel.[50-5?] The latter contain the best available experimental heat-transfer data concerning HVT motors with head-end pyrogen igniters.

Introducing the above-mentioned corrections to Eq. (III-21) the following correlation is obtained:

$$Nu_{d,af} = a_6 (x_r/d_h)^{-0.1} Re_{d,af}^{0.8} Pr_{af}^{0.4} (A_p/A_t)^{0.4} \qquad \text{(III-22)}$$

where: a_6 is a constant; x_r is the distance from the point of reattachment of the igniter jet, and the physical properties of the gas (except the velocity) in the Nusselt, Reynolds and Prandtl numbers are evaluated at the average film temperature T_{af}.

From Eq. (III-22) an expression for the local heat-transfer coefficient developed for this study is obtained in the following form:

$$h_c = a_6 (\rho_{af}u)^{0.8} \mu_{af}^{0.2} c_p Pr_{af}^{-0.6} \quad (x_r d_h)^{-0.1} (A_p/A_t)^{0.4}$$

(III-23)

The temperature dependence of the viscosity is determined from the recent calculations of Svehla[180] for the viscosity of air at high temperatures. It was shown by Bartz[181] that Svehla's values are very close to those in the previously published NBS data.[182]

Over the range from 1000 to 3500°K the calculated high-temperature viscosity values for air[180] were fit in this study by the formula

$$\mu = 0.87 \times 10^{-6} W^{0.5} T(°K)^{0.65} \quad \text{poise} \qquad \text{(III-24)}$$

Prandtl number is assumed to be constant and calculated from Svehla's equation[180]

$$Pr = \frac{\gamma}{1.77\gamma - 0.45} \qquad \text{(III-25)}$$

which gives approximately the same value of 0.71 for $\gamma = 1.22$ to 1.26 (usual propellant combustion gases).

Expressing the gas density ρ_{af} by the local pressure and average film temperature

$$\rho_{af} = p/RT_{af} \qquad \text{(III-26)}$$

and substituting Eqs. (III-24) and (III-26) into Eq. (III-23) the following expression is obtained:

$$h_c = a_h c_p Pr^{-0.6} W^{0.1} (pu/R)^{0.8} T_{af}^{-0.67} (x_r d_h)^{-0.1} (A_p/A_t)^{0.4}$$

(III-27)

where $a_h = (0.87 \times 10^{-6})^{0.2} a_6$.

As mentioned already, the best available pertinent experimental data on the convective heat transfer are those obtained by Carlson, Seader and Wrubel[50-53] at Rocketdyne. Examining carefully these data, Cohen, Derr and Price[158] proposed the following correlations for the convective heat transfer from an axial igniter with a sonic nozzle:
At the region of igniter-jet impingement (maximum heat transfer):

$$Nu_d = 0.0615 \ Re_d^{0.8} (A_p/A_t)^{0.4} \qquad \text{(III-28)}$$

Upstream of the impingement point:

$$Nu_d = 0.7 \ Re_d^{0.8} (A_p/A_t)^{0.4} (0.022 + 0.066 \ x/x_{im})$$

$$\text{(III-29)}$$

Downstream of the impingement point:

$$Nu_d = 0.7 \ Re_d^{0.8} (A_p/A_t)^{0.4} [0.031 + 0.057 \ \exp(-0.5 \ x_r/d)]$$

$$\text{(III-30)}$$

Unfortunately, the data in Refs. 50 through 53 extends only to $x/d = 10$ approximately. Eq. (III-30) gives almost a constant value for Nu_d after that point. The experimental motor in this study extends up to $x/d_h = 62$ with the propellant leading edge being at $x_p/d_h = 6.06$ (or $x_r/d_h = 5.06$ on the average). The constant a_6 in Eq. (III-23) was estimated so that over the propellant leading edge and up to $x/d_h = 10$ the heat-transfer coefficient calculated by Eq. (III-27) will be equal to that found in Refs. 50 through 53 and calculated by Eq. (III-30). A value of $a_6 = 2.56 \times 10^{-2}$ was determined. Therefore, the expression for the local heat-transfer coefficient [Eq. (III-23)] developed in this study becomes

$$h_c = 1.56 \times 10^{-3} c_p Pr^{-0.6} W^{0.1} (pu/R)^{0.8} T_{af}^{-0.67} (x_r d_h)^{-0.1} (A_p/A_t)^{0.4}$$

$$\text{(III-31)}$$

The position of igniter jet impingement, x_{im}, is found by the jet-boundary calculations presented by Love, et al.[147] For most of the experiments, the position was in the entrance section approximately at one port diameter downstream of the igniter nozzle exit, i.e., $x_{im} \approx d_h$.

Expression (III-31) was used throughout this study. It is based on experimental studies of others and it is recommended that experimental investigation will be conducted in the

test motor for verification (see Chapter VII). Good agreement between measured and calculated pressure-time-distance curves was obtained using Eq. (III-31). Since the computer program is flexible, there is no problem in using other expression, proved to be more precise, in the numerical solution of the analytical model.

Before local ignition, both the local heat-transfer coefficients to the propellant and nonpropellant walls of the port, h_{cp} and h_{cw} respectively, are calculated by expression (III-31), i.e., $h_{cp} = h_{cw} = h_c$. After local ignition $h_{cp} = 0$ and $h_{cw} = h_c$.

Equations (III-28 to III-30) are used to calculate the effective mean temperature of the igniter gas, T_{ig}. Calculation of the stagnation temperature in the igniter combustion chamber using pressure measurements during steady state igniter operation shows 5% losses due to incomplete combustion and heat transfer, as compared to the adiabatic flame temperature. The high heat transfer in the entrance section causes an additional drop of between 25 and 35%, according to the port-to-throat area ratio. It should be mentioned that Most,[15] using similar ignition system with convergent-divergent igniter nozzle and an entrance section a little shorter than the one in this study, measured igniter gas temperatures over the propellant leading edge, which are about one half of the igniter adiabatic flame temperature.

E. Correlation for the Friction Coefficient

The correlation for the friction coefficient, f, is deduced from Colebrook's expression for turbulent flow in pipes with roughness,[150,183,184] which is the basis of Moody diagram. Colebrook's formula is

$$\frac{1}{\sqrt{f}} = -0.8686 \ln\left(\frac{\varepsilon_s/d_h}{3.7} + \frac{2.51}{Re_d\sqrt{f}}\right) \qquad \text{(III-32)}$$

where ε_s/d_h is the relative equivalent sand roughness.

Observed effects of distance from the entrance[154,185] and cross-sectional variation of fluid properties are taken into account. Humble, et al[154] correlated successfully friction-coefficient measurements in smooth tubes with Prandtl's universal law of friction for smooth pipes evaluating density and viscosity at the average film temperature. They did not correct for observed entrance effects. Shapiro and Smith[185] observed entrance effects up to 20 to 30 tube diameters from the tube inlet. Therefore, Reynolds number in Eq. (III-32) is calculated with the local flow velocity, whereas density and viscosity are evaluated at the local

pressure and average film temperature. Entrance effect is considered by multiplying the friction coefficient by a power function of the distance-to-diameter ratio as for the heat-transfer coefficient, $a_1(x_r/d_h)^{0.1}$, and evaluating the coefficient so that this factor will become unity at twenty duct diameters.

After introducing the aforementioned corrections into Eq. (III-32), and some algebraic manipulations, the implicit correlation for the friction coefficient developed in this study is:

$$f = \frac{0.449(d_h/x_r)^{0.1}}{\left\{\ln\left[\dfrac{\varepsilon_s/d_h}{3.7} + \dfrac{1.27\ RW^{0.5}T_{af}^{1.65}(d_h/x_r)^{0.05}}{10^6\ pud_h f^{0.5}}\right]\right\}^2} \qquad \text{(III-33)}$$

Friction is considered over the entire surface during the induction interval and only downstream of the ignition front after first ignition. Zero wall friction is assumed at the burning surface due to the large friction attentuation caused by the blowing. Since the inert perimeter is small as compared to the burning perimeter, it is assumed in the model for simplicity that after ignition at a position the local friction coefficient is zero, i.e., the friction over the entire perimeter is neglected.

F. The Burning Rate Law

The solid propellant used in this study is a composite PBAA-AP propellant, composed of 20% PBAA-EPON 828 and 80% bimodal ammonium perchlorate. The properties of this propellant are listed in Table 1. The non-erosive burning rate law, of the Saint-Robert's type, as determined by strand-burner measurements is

$$r_0(cm/sec) = 0.927 \times 10^{-2}p(gf/cm^2)^{0.4} \qquad \text{(III-34)}$$

Figure 6 shows this burning rate law in the ..onventional log r_0 vs log p form. Pressure is given in gf/cm^2 for consistency of units in the entire analysis. It is recalled that

$$10^3 gf/cm^2 = 0.968\ atm = 0.981\ bars = 14.22\ psi$$

Large enhancement of the burning rate due to erosive burning, encountered in HVT motors, is taken into account by adopting the widely-used and accepted Lenoir-Robillard's semi-

empirical burning rate law[112]

$$r = ap^n + kh_c \exp(-\beta r \rho_{pr}/u\rho) \qquad \text{(III-35)}$$

where the non-erosive component is given by Eq. (III-34), the local zero-blowing heat-transfer coefficient, h_c, is calculated according to Eq. (III-31), and k and β are constants.

This is actually a modified form of Lenoir-Robillard's law, since the expression originally proposed for h_c is based on Chilton-Colburn's correlation for turbulent flow over a flat plate, whereas the expression used here [Eq. (III-31)] is a corrected Dittus-Boelter's correlation. The local burning rate as given by Eq. (III-35) is thus strongly coupled to the chamber gas dynamics and the propellant surface temperature.

The erosive-burning constant, k, is estimated from semi-theoretical considerations as proposed originally by Lenoir and Robillard.[112] The erosive-burning exponent, β, is evaluated from burned distance versus axial position measurements from propellant recovered from water-quench experiments conducted in this study. It was also adjusted to fit the experimental pressure-time curves for all values of A_p/A_t tested. The values of k and β used in this investigation are listed in Table 1.

The high pressurization rates encountered in HVT motors suggest the consideration of dynamic burning effects. These effects may be of two kinds: (1) due to burning of a pre-heated propellant layer on ignition, a phenomenon frequently oversized by undersized igniters, and (2) due to burning of a propellant layer, the temperature profile in which is not in phase with the rapidly varying pressure in the gas phase. Dynamic burning is not considered in this study. Its inclusion into the current model would further improve the analysis and the agreement with the experimental results. Dynamic burning is further discussed in the outline of suggestions for future work (see Chapter VII) and in Appendix C.

G. Determination of the Propellant Surface Temperature

To determine the amount of heat transferred to the solid propellant in the unignited region and the flame front location according to the ignition criterion, the propellant surface temperature must be evaluated as a function of time and distance along the port. The one-dimensional heat equation for the solid phase at a fixed axial location is

$$\frac{\partial T_{pr}(t,y)}{\partial t} = \alpha_{pr} \frac{\partial^2 T_{pr}(t,y)}{\partial y^2} \qquad \text{(III-36)}$$

where y is a coordinate normal to the surface with its positive direction into the solid (see Fig. 7). The propellant is assumed to be inert until the critical ignition temperature is reached.

The initial condition for Eq. (III-36) is

$$T_{pr}(0,y) = T_{pi} \qquad \text{(III-37)}$$

The boundary conditions for the heat equation are:

$$T_{pr}(t,\infty) = T_{pi} \qquad \text{(III-38)}$$

and

$$\frac{\partial T_{pr}}{\partial y}(t,0) = -\frac{h_c(t)}{\lambda_{pr}}[T(t) - T_{ps}(t)] \qquad \text{(III-39)}$$

The second boundary condition specifies that at the propellant surface the rate of heat transfer from the gas phase to the solid is equal to the rate of heat conduction into the solid, with the variables $h_c(t)$ and $T(t)$ depending on the local flow parameters. It follows that Eq. (III-39) is coupled to the gas phase conditions. This implies that the heat equation must be solved simultaneously with the governing equations for the gas phase to yield the time-dependent temperature profile within the solid at each given axial position in the motor. However, the main interest in this analysis is not a detailed knowledge of the temperature profile inside the propellant slab, but rather the propellant surface temperature, which determines the rate of heat transfer to the unburned propellant and the flame spreading rate.

A conventional way to treat the parabolic partial differential equation (III-36) is to reduce it to an ordinary differential equation by Laplace transformation and solve for the surface temperature.[186] However, since no explicit analytical expressions for $h_c(t)$ and $T(t)$ are available, the analytical solution can only be stated in the integral form. Solving for the propellant surface temperature along the port at each time step requires a lot of computations and computer storage spaces.

An approximate solution of the heat equation, which is quite accurate and saves much computation time may be obtained by using the so-called integral method.[187,188] Applying this method, a quantity $\delta(t)$ (called the penetration distance) is defined, so that for $y \geq \delta$ the solid is at equilibrium temperature and there is no heat transfer (see Fig. 7). It is assumed that a third-degree polynomial in y represents the transient temperature profile in the solid:

$$T_{pr} = k_0(t) + k_1(t)y + k_2(t)y^2 + k_3(t)y^3 \qquad \text{(III-40)}$$

where the coefficients k_0, k_1, k_2 and k_3 may be time-dependent. To determine them, four boundary conditions are necessary. These are:

(1) $\qquad T_{pr}(t,\delta) = T_{pi}$ $\qquad\qquad\qquad$ (III-41)

(2) $\qquad \dfrac{\partial T_{pr}}{\partial y}(t,\delta) = 0$ $\quad$ (no heat transfer at $y = \rho$)

$\qquad\qquad\qquad\qquad\qquad\qquad\qquad\qquad\qquad$ (III-42)

(3) $\qquad \dfrac{\partial^2 T_{pr}}{\partial y^2}(t,\delta) = 0$ $\quad$ (the smoothing condition)

$\qquad\qquad\qquad\qquad\qquad\qquad\qquad\qquad\qquad$ (III-43)

(4) $\qquad \dfrac{\partial T_{pr}}{\partial y}(t,0) = -\dfrac{h_c}{\lambda_{pr}}[T(t) - T_{ps}(t)]$ $\qquad$ (III-39)

Solving for the coefficients k_0 to k_3 and substituting into Eq. (III-40), the following expression for the temperature profile is obtained:

$$T_{pr} = T_{pi} + \frac{h_c(T-T_{ps})(\delta-y)^3}{3\lambda_{pr}\delta^2} \qquad \text{(III-44)}$$

$$= T_{pi} + (T_{ps}-T_{pi})\left(\frac{\delta-y}{\delta}\right)^3 \qquad \text{(III-45)}$$

Figure 7 shows the temperature profile in the solid expressed by Eq. (III-45).

The surface temperature is obtained by substituting $y = 0$ into Eq. (III-44)

$$T_{ps} = T_{pi} + \frac{h_c(T-T_{ps})\delta}{3\lambda_{pr}} \qquad \text{(III-46)}$$

Following the integral method, a heat balance integral is written for the penetration distance, $\delta(t)$:

$$\alpha_{pr} \int_{0}^{\delta(t)} \frac{\partial^2 T_{pr}}{\partial y^2} \, dy = \frac{d}{dt} \int_{0}^{\delta(t)} (T_{pr} - T_{pi}) \, dy \qquad \text{(III-47)}$$

Equation (III-47) is analogous to the momentum integral in boundary layer theory.[188] The left-hand side becomes, in view of conditions (III-39) and (III-42),

$$\alpha_{pr} \int_{0}^{\delta(t)} \frac{\partial^2 T_{pr}}{\partial y^2} \, dy = \alpha_{pr} \left[\frac{\partial T_{pr}}{\partial y}(t, \delta) - \frac{\partial T_{pr}}{\partial y}(t, 0) \right]$$

$$= \frac{\alpha_{pr} h_c}{\lambda_{pr}} (T - T_{ps}) \qquad \text{(III-48)}$$

The right-hand side of Eq. (III-47) becomes, using Eqs. (III-44) and (III-46),

$$\frac{d}{dt} \int_{0}^{\delta(t)} (T_{pr} - T_{pi}) \, dy = \frac{3}{4} \lambda_{pr} \frac{d}{dt} \left[\frac{(T_{ps} - T_{pi})^2}{h_c (T - T_{ps})} \right] \qquad \text{(III-49)}$$

The rates of change of the heat-transfer coefficient, h_c, and gas temperature, T, with respect to time, are neglected as compared with the rate of change of T_{ps}, which is completely justified for the entire induction interval, and the major part of the flame spreading period. Performing the differentiation in Eq. (III-49) and equating the result to Eq. (III-48) the following ordinary differential equation for the propellant surface temperature is obtained:

$$\frac{dT_{ps}}{dt} = \frac{4\alpha_{pr} h_c^2 (T - T_{ps})^3}{3\lambda_{pr}^2 (T_{ps} - T_{pi})(2T - T_{ps} - T_{pi})} \qquad \text{(III-50)}$$

To avoid the singularity at $t = 0$, the initial condition for Eq. (III-50) is taken as

$$T_{ps}(0) = T_{pi} + \epsilon \qquad \text{(III-51)}$$

where ϵ has a small value, e.g., 0.1°K.

It was shown by Goodman,[188] that for constant external heat flux the surface temperature increase of a semi-infinite slab calculated by the integral method using a cubic temperature profile is only 2% higher than that calculated from the exact solution of Eq. (III-36). As a check of Eq. (III-50), the heat transfer coefficient (h_c) was varied linearly with time in a manner that approximates the actual heating rates in the physical model. Solution of Eq. (III-50) by a fourth order Runge Kutta method was compared to an explicit finite-difference solution of the partial differential heat equation [Eq. (III-36)] for the same conditions of heating-gas temperature, propellant properties and variation of h_c. Maximum difference of 5% between the two solutions for heat-up times necessary to raise the surface temperature from 298 to 700°K was obtained.

Equation (III-40) is solved by a standard fourth-order Runge-Kutta method simultaneously with the governing equations for the chamber flow field to yield the propellant surface temperature at any calculated time and position. In this way flame spreading rates can be predicted, using the ignition criterion as described in Chapter III Section A.

The non-propellant walls of the port have a coating with thermal properties assumed to be equal to those of the propellant (see Chapter V, Section A). Therefore, before local ignition $T_{ws} = T_{ps}$. After ignition at a position, T_{ws} at that position is calculated continuously by Eq. (III-50).

The large number of coupled parameters involved in the analysis precludes a simple and useful nondimensionalization. Moreover, it is doubtful, if any use of normalized parameters can provide an easy and straight-forward interpretation of the results. Therefore, it was decided to carry on the numerical calculations in a dimensional form, using consistent, metric engineering system of units, thus allowing a direct comparison of predictions with experimental measurements.

CHAPTER IV

NUMERICAL SOLUTION

A. Implementation Scheme

Numerical mathematical techniques were developed for the simultaneous integration of the three governing equations, Eqs. (III-7), (III-8), and (III-9), the two equations for the entrance section, Eqs. (III-13), and (III-14), and the equation, which describes the rate of change of the propellant surface temperature, Eq. (III-50). The numerical steps were organized into a program for a large capacity digital computer.

It can be shown, that the set of governing equations is totally hyperbolic in nature.[189,190] Indeed, all three eigenvalues of its characteristic equation are distinct and real. The numerical techniques developed aimed at maximum accuracy, stable conditions, and computation efficiency. Recently obtained experience in solving hyperbolic partial differential equations[190] was utilized, and a generalized implicit scheme, based on central differences in spacewise derivatives,[191,192] was chosen to solve numerically the governing equations. Let the net of points in the t,x-plane be given by $t = j\Delta t$ and $x = n\Delta x$, where $j = 0,1,2. . .$, and $n = 0,1,2. . . $. The mesh size of the net is determined by Δt and Δx. Then the derivatives of pressure, for instance, are expressed in the following difference form:

$$\left.\frac{\partial p}{\partial t}\right|_n = \frac{p_n^{j+1} - p_n^j}{\Delta t}$$

$$\left.\frac{\partial p}{\partial x}\right|_n = \frac{\theta(p_{n+1}^{j+1} - p_{n-1}^{j+1}) + (1-\theta)(p_{n+1}^j - p_{n-1}^j)}{2\Delta x}$$

$$(IV-1)$$

where $p_n^j = p(j\Delta t, n\Delta x)$.

The weighting parameter θ is a real constant, lying in the interval $0 \leqq \theta \leqq 1$. For the implicit formulation no stability restriction exist if $0.5 \leqq \theta \leqq 1$.[191] Usually a value of $\theta = 0.6$ was used in the calculations.

B. Quasi-linearization and Predictor-Corrector Calculations of the Non-linear Terms in the Governing Equations

The governing equations may be written in the following matrix form

$$\frac{\partial}{\partial t} \begin{pmatrix} u \\ T \\ p \end{pmatrix} + \begin{pmatrix} F_{u,u} & F_{u,T} & F_{u,p} \\ F_{T,u} & F_{T,T} & F_{T,p} \\ F_{p,u} & F_{p,T} & F_{p,p} \end{pmatrix} \frac{\partial}{\partial x} \begin{pmatrix} u \\ T \\ p \end{pmatrix} = \begin{pmatrix} I_u \\ I_T \\ I_p \end{pmatrix} \qquad \text{(IV-2)}$$

where $F[u(t,x),T(t,x),p(t,x)]$ are the functional coefficients of the partial spacewise derivatives, and $I[u(t,x),T(t,x), p(t,x)]$ are the corresponding inhomogeneous terms in Eqs. (III-7), (III-8), and (III-9).

In order to obtain a system of linear algebraic difference equations, which can be solved simultaneously by matrix methods, the nonlinear coefficients $F(u,T,p)$ and inhomogeneous terms $I(u,T,p)$ are linearized in a way, described in the following paragraphs.

The inhomogeneous terms were first quasi-linearized, according to the scheme:[193]

$$I_n^{j+\theta} \approx I(u_n^j, T_n^j, u_n^j) + \theta(u_n^{j+1} - u_n^j) \frac{\partial I}{\partial u}\Big|_n^{j+\frac{\theta}{2}}$$

$$+ \theta(T_n^{j+1} - T_n^j) \frac{\partial I}{\partial T}\Big|_n^{j+\frac{\theta}{2}} + \theta(p_n^{j+1} - p_n^j) \frac{\partial I}{\partial p}\Big|_n^{j+\frac{\theta}{2}} \qquad \text{(IV-3)}$$

where the partial derivatives, which are actually algebraic terms, are evaluated with the flow properties at $(j + \theta/2, n)$, such as, for instance, $p_n^{j+\frac{\theta}{2}} = p_n^j + \frac{\theta}{2}(p_n^{j+1} - p_n^j)$.

A predictor-corrector technique was applied to the nonlinear coefficients $F(u,T,p)$, and the partial derivatives in Eq. (IV-3). According to this method, a predictor calculation is first made, in which previous-time flow properties are used to evaluate all the coefficients F and partial derivatives in the quasi-linearized inhomogeneous terms. Then, a corrector calculation is made, in which the coefficients F and the partial derivatives are evaluated with weight-averaged flow properties. The iterations may continue on until sufficient convergence is achieved.

After substitution of the aforementioned finite-difference representations into the governing equations, the velocity variation equation, Eq. (III-7), becomes

$$\frac{u_n^{j+1}-u_n^j}{\Delta t} + \bar{u}_n^j\left[\frac{\theta(u_{n+1}^{j+1}-u_{n-1}^{j+1}) + (1-\theta)(u_{n+1}^j-u_{n-1}^j)}{2\Delta x}\right]$$

$$+ gR\frac{\bar{T}_n^j}{\bar{p}_n^j}\left[\frac{\theta(p_{n+1}^{j+1}-p_{n-1}^{j+1}) + (1-\theta)(p_{n+1}^j-p_{n-1}^j)}{2\Delta x}\right] = I_u(u_n^j, T_n^j, p_n^j)$$

$$+ \theta(u_n^{j+1}-u_n^j)\frac{\partial I_u}{\partial u}\Big|_n^{j+\frac{\theta}{2}} + \theta(T_n^{j+1}-T_n^j)\frac{\partial I_u}{\partial T}\Big|_n^{j+\frac{\theta}{2}} + \theta(p_n^{j+1}-p_n^j)\frac{\partial I_u}{\partial p}\Big|_n^{j+\frac{\theta}{2}}$$

$$(IV-4)$$

The temperature variation equation, Eq. (III-8), becomes

$$\frac{T_n^{j+1}-T_n^j}{\Delta t} + \bar{u}_n^j\left[\frac{\theta(T_{n+1}^{j+1}-T_{n-1}^{j+1}) + (1-\theta)(T_{n+1}^j-T_{n-1}^j)}{2\Delta x}\right]$$

$$+ (\gamma-1)\bar{T}_n^j\left[\frac{\theta(u_{n+1}^{j+1}-u_{n-1}^{j+1}) + (1-\theta)(u_{n+1}^j-u_{n-1}^j)}{2\Delta x}\right] = I_T(u_n^j, T_n^j, p_n^j)$$

$$+ \theta(u_n^{j+1}-u_n^j)\frac{\partial I_T}{\partial u}\Big|_n^{j+\frac{\theta}{2}} + \theta(T_n^{j+1}-T_n^j)\frac{\partial I_T}{\partial u}\Big|_n^{j+\frac{\theta}{2}} + \theta(p_n^{j+1}-p_n^j)\frac{\partial I_T}{\partial p}\Big|_n^{j+\frac{\theta}{2}}$$

$$(IV-5)$$

and the pressure variation equations, Eq. (III-9), becomes

$$\frac{p_n^{j+1}-p_n^j}{\Delta t} + \bar{u}_n^j\left[\frac{\theta(p_{n+1}^{j+1}-p_{n-1}^{j+1}) + (1-\theta)(p_{n+1}^j-p_{n-1}^j)}{2\Delta x}\right]$$

$$+ \gamma\bar{p}_n^j\left[\frac{\theta(u_{n+1}^{j+1}-u_{n-1}^{j+1}) + (1-\theta)(u_{n+1}^j-u_{n-1}^j)}{2\Delta x}\right] = I_p(u_n^j,T_n^j,p_n^j)$$

$$+ \theta(u_n^{j+1}-u_n^j)\frac{\partial I_p}{\partial u}\Big|_n^{j+\frac{\theta}{2}} + \theta(T_n^{j+1}-T_n^j)\frac{\partial I_p}{\partial T}\Big|_n^{j+\frac{\theta}{2}} + \theta(p_n^{j+1}-p_n^j)\frac{\partial I_p}{\partial p}\Big|_n^{j+\frac{\theta}{2}}$$

$$\text{(IV-6)}$$

The barred parameters are weight-averaged quantities as follows:

$$\left.\begin{aligned}
\bar{u}_n^j &= \theta(u_n^{j+1})_{pd} + (1-\theta)u_n^j \\
\bar{T}_n^j &= \theta(T_n^{j+1})_{pd} + (1-\theta)T_n^j \\
\bar{p}_n^j &= \theta(p_n^{j+1})_{pd} + (1-\theta)p_n^j
\end{aligned}\right\} \qquad \text{(IV-7)}$$

whereas the flow parameters in the partial derivative form in Eqs. (IV-4), (IV-5), and (IV-6) are

$$\left.\begin{aligned}
u_n^{j+\frac{\theta}{2}} &= \frac{\theta}{2}(u_n^{j+1})_{pd} + (1-\frac{\theta}{2})u_n^j \\
T_n^{j+\frac{\theta}{2}} &= \frac{\theta}{2}(T_n^{j+1})_{pd} + (1-\frac{\theta}{2})T_n^j \\
p_n^{j+\frac{\theta}{2}} &= \frac{\theta}{2}(p_n^{j+1})_{pd} + (1-\frac{\theta}{2})p_n^j
\end{aligned}\right\} \qquad \text{(IV-8)}$$

The parameters $(\substack{j+1\\n})_{pd}$ are the quantities, calculated from the latest predictor iteration. In the first step predictor calculation they have the values of the previous time step.

As pointed out by Kuo, et al,[190,194] the predictor-corrector method, combined with the quasi-linearization scheme, is very helpful in stabilizing the numerical solution. However, the successful application of this combination to the present study does not generalize the approach for all similar problems.[190]

Negligibly small differences were found between final solutions obtained by single-step and multi-step predictor calculations. Therefore, to reduce computing time, a single-step predictor-corrector calculations are used in the actual computations. The final solution at every time step is obtained implicitly by a matrix method, discussed in a later section.

C. Extraneous Boundary Conditions

The use of central-difference formulation, as described in Eq. (IV-1), for all spacewise derivatives in the governing equations, requires six boundary conditions for the solution. In other words, the set of finite-difference equations corresponds to a hyperbolic system of 6th order.[190] Therefore, three boundary conditions, in addition to the physical ones defined by Eqs. (III-13), (III-14), and (III-17), or (III-18) are needed. These so-called extraneous boundary conditions for the hyperbolic system of governing equations studied are derived from the compatibility relations at the boundaries. The latter are obtained by solving the governing equations by the method of characteristics.[148]

The compatibility relations along the right-running and left-running Mach lines (defined by dx/dt = u ± c, respectively), in terms of p, u-characteristics, are

$$\left(\frac{dp}{dt}\right)_{I,II} = \mp \frac{\gamma p}{c}\left(\frac{du}{dt}\right)_{I,II} + \left(I_p \pm \frac{\gamma p}{c}I_u\right) \quad \text{(IV-9,IV-10)}$$

The relation along the particle-path line (defined by dx/dt = u), in terms of T,p-characteristics is

$$\left(\frac{dT}{dt}\right)_{III} = \frac{\gamma-1}{\gamma}\frac{T}{p}\left(\frac{dp}{dt}\right)_{III} + \left(I_T - \frac{\gamma-1}{\gamma}\frac{T}{p}I_F\right) \quad \text{(IV-11)}$$

In relations (IV-9), (IV-10), and (IV-11), I_u, I_T, and I_p are the inhomogeneous terms in the governing equations [see Eq. (IV-2)].

For a subsonic flow toward the nozzle in the motor which is the case during the entire transient in the physical model, described in Chapter III, the left-running characteristic line is considered at the left boundary, whereas the right-running

characteristic line together with the particle-path line are considered at the right boundary of the region of numerical computation. Taking into account the conditions at the right boundary, which is the aft-end of the motor (uniform perimeter, no area change, and no mass addition, see Fig. 2), the compatibility relation along the right-running characteristic, Eq. (IV-9), becomes

$$\left(\frac{dp}{dt}\right)_I = -\frac{\gamma p}{c}\left(\frac{du}{dt}\right)_I + \frac{P_w}{A_p}\left\{\frac{\gamma f p u^2}{2c}\left[(\gamma-1)\frac{u}{c}-1\right]\right.$$

$$\left. - (\gamma-1)J_c h_{cw}(T-T_{ws})\right\} \tag{IV-12}$$

The compatibility relation along the left-running characteristic, Eq. (IV-10), is

$$\left(\frac{dp}{dt}\right)_{II} = \frac{\gamma p}{c}\left(\frac{du}{dt}\right)_{II} + \gamma R\rho_{pr}\frac{rb}{A_p}\left(T_f + \frac{u}{c}T\right)$$

$$+ (\gamma-1)\rho_{pr}\frac{rb}{A_p}\frac{u^2}{2g} - \frac{\gamma pu}{A_p}\frac{\partial A_p}{\partial x}$$

$$- \frac{(\gamma-1)J_c}{A_p}\left[2h_p h_{cw}(T-T_{ws}) + bh_{cp}(T-T_{ps})\right]$$

$$+ \frac{\gamma P_w f}{2A_p}\frac{pu^2}{c^2}[(\gamma-1)u + c] \tag{IV-13}$$

The compatibility relation along the particle-path line, Eq. (IV-11), at the right boundary, becomes

$$\left(\frac{dT}{dt}\right)_{III} = \frac{\gamma-1}{\gamma}\frac{T}{p}\left(\frac{dp}{dt}\right)_{III} + \frac{\gamma-1}{\gamma}\frac{P_w}{A_p}\left[\frac{fu^3}{2gR} - \frac{J_c h_{cw}T}{p}(T-T_{ws})\right]$$

$$\tag{IV-14}$$

D. Treatment of the Boundary Conditions

The compatibility relation along the left-running characteristic line, Eq. (IV-13), and Eqs. (III-13) and (III-14) form a closed system of ordinary differential equations to determine the gas velocity, temperature, and pressure at the entrance to the propellant section. The system, formed by the other two compatibility relations, Eqs. (IV-12) and (IV-13), and Eq. (III-17), or (III-18) (unchoked, or choked flow, respectively), determines the flow parameters at the chamber aft-end. The equations in each system are expressed in a finite-difference form and quasi-linearized in an implicit form, using predictor-corrector iteration calculation in the same method which is utilized for the governing equations. As a result, a set of three linear inhomogeneous algebraic equations is obtained for every boundary. Each set of equations is solved by 3 x 3 matrix, using Kramer's rule, to yield the gas velocity, temperature, and pressure at the boundary for the next time step calculations. The characteristic line segments near the left and right boundary of the calculated domain are shown in Figs. 8 and 9, respectively. These figures also show the numerical calculation grid in an x,t-diagram.

In Fig. 8 the line sent out from A_2^j to the left-boundary point $B_\ell(x_0, t^{j+1})$ with a slope $(dx/dt)_{II} = u - c$ is the left-running characteristic. The process of determination of the boundary values is carried out in the following steps:

(1) With the calculation completed for the time step $j\Delta t$, all properties are determined at the point $\bar{A}_2^j$ by linear interpolation between the boundary (x_1, t^j). The position of $\bar{A}_2^j$ is taken from the previous-time-step calculations, as described below.

(2) The left-boundary system of equations [Eqs. (III-13), (III-14), and (IV-13)] is solved for u, T, and p at $B_\ell(x_0, t^{j+1})$. The flow parameters, present in the coefficient and inhomogeneous terms of these equations, are iterated with the solutions until sufficient convergence is reached.

(3) The corrected location of A_2^j at the current time is found from the slope of the left-running characteristic (solid line $A_2^j - B_\ell$ in Fig. 8), i.e.,

$$x_{A\,2}^j = x_0 - \frac{\Delta t}{2}\left[\left(u_{x\,0}^{j+1} + u_{\bar{A}\,2}^j\right) - \left(c_{x\,0}^{j+1} + c_{\bar{A}\,2}^j\right)\right]$$

(IV-15)

If $|x_{A2} - x_{\overline{A}2}|/x_{\overline{A}2} > 0.002$, steps (1), (2), and (3) are repeated with $(x_{\overline{A}2})_{i+1} = 0.8\, x_{A2} + 0.2\,(x_{\overline{A}2})_i$, where the subscript "i" denotes the number of the iteration step.

When the convergence condition for the point A_2^j is met (usually in two iterations), the distance x of this point becomes the distance for the first iteration in the next time step, i.e., $x_{\overline{A}2}^{j+1} = x_{A2}^j$ (dotted vertical line in Fig. 8).

In Fig. 9 the lines sent out from A_1^j and A_3^j to the right-boundary point $B_r(x_N, t^{j+1})$ are the right-running characteristic and particle path, respectively. The calculation of the right-boundary values by the simultaneous solution of the above-mentioned pertinent system of equations is similar to that of the left-boundary values.

The position of the points A_1, A_2, and A_3 changes very slowly with respect to time. The directions of exaggerated shifts shown in Figs. 8 and 9 are typical for the chamber-filling interval of the transient.

It should be noted that solutions, based on separate integrations along the characteristic lines,[190] have resulted in oscillations of the boundary values. The quasi-linearized simultaneous-solution method results in a smooth and stable solution. The method may be applied, however, with caution to other configurations which cause different boundary conditions, such as zero aft-end velocity during part of the transient due to use of a nozzle closure, and change of velocity direction at the fore-end due to short igniter operation.

E. Computation Efficiency and Convergence Tests

The numerical calculation solves Eqs. (IV-4), (IV-5), and (IV-6), which represent the governing equations in their implicit difference algorithm. For the N-1 spacewise interior points considered, 3(N-1) linear algebraic equations have to be solved simultaneously for every time step for 3(N-1) unknowns. The value of N-1 depends upon the given lengths of the propellant and aft sections, $x_E - x_p$, and the spatial mesh size, Δx, used in the calculation. The faster the pressurization process, the smaller the value of Δx that must be used, and therefore, the larger the number of interior calculation points. Also, the time step, or temporal mesh size, Δt, should be kept small enough, so that the variations in flow properties with respect to time can be studied, and the quasi-linearized nonlinear and inhomogeneous terms can be properly represented.

For efficient computation, the finite-difference equations, Eqs. (IV-4), (IV-5), and (IV-6), are arranged into so-called block-tridiagonal matrix form.[190,195] In this particular form, the 3(N-1) x 3(N-1) matrix of the coefficients of the unknowns has (3N-5) 3 x 3 square sub-matrices as single elements. An economical solution is obtained through block-factorization into two block-bidiagonal matrices.[190,195] For accurate computation, the computer option of double precision is used in the matrix calculation.

Variation of the mesh sizes, Δt and Δx, was carried out to test the convergence of the solution. This variation was conducted in connection with the so-called Courant-Friedrichs-Lewy stability condition for one-step space difference equations,[191] which is

$$(|u| + c)\Delta t/\Delta x \leq 1 \qquad\qquad (IV-16)$$

However, when an implicit difference scheme is used, the numerical solution becomes unconditionally stable.[191]

It has been found that within the region of tests with the experimental model, negligible changes in the solutions are obtained when Δt or Δx are reduced by a factor of five. Mesh sizes, for which the maximum value of $(|u| + c)\Delta t/\Delta x$ is slightly greater than one, are usually used.

Various tests were performed on the sensitivity of the solution to changes in initial conditions and small changes in important input parameters, such as the igniter mass flow rate, burning rate law, propellant ignition temperature, adiabatic flame temperature, and propellant density. In all these tests the solutions were bounded and smooth, and changed only slightly for small changes in these parameters. This demonstrates the existence of neighboring solutions and the convergence of the entire numerical solution.

Appendix D shows a flow chart for the solution of the governing equations, and Appendix E shows the overall computer program flow chart. Lists of the computer program subroutines and the input data cards are given in Appendix F. The Fortran IV computer program can be requested from L. H. Caveny at the Guggenheim Laboratories of Princeton University. Requests for the program should be accompanied by a 9 track magnetic tape. Compilation of the program on the IBM 360-91 requires an area of 350K for the IBM G level compiler and 500K for the IBM H level compiler.

CHAPTER V

EXPERIMENTAL INVESTIGATION OF THE STARTING TRANSIENT

A. The Experimental Motor

An extensive experimental program was carried out to provide the empirical data required as input to the theoretical model and to test the validity of the analysis. A laboratory-size solid-propellant window motor was designed and manufactured for the experimental investigation. The design of the motor was guided by the following primary requirements. It is necessary that:

(1) The experimental set-up be as close as possible to a practical rocket motor, both in configuration and range of operation;

(2) The motor has sufficient flexibility to permit wide-range diagnostic studies involving measurements of different types;

(3) The analytical model and the experimental model be compatible for tests of the theory without unnecessary complications, and

(4) The size of the motor be easily manageable and consistent with laboratory testing procedures.

Schematic longitudinal and cross sections of the experimental motor are shown in Figs. 2 and 3, respectively. Figure 10 shows an assembly drawing and Fig. 11 is an exploded view of the laboratory-size rectangular window motor. The propellant slabs were cast into brass trays. To insure good propellant-to-tray bonds, the inner surface of the tray was sand-blasted and coated with a thin layer of Duro-Plastic Epoxe glue (available from Woodhill Chemical Sales Corp.). The exposed propellant surface was cast and polymerized against the polished surface of a Teflon strip. Several types of trays with two propellant web thicknesses (0.635 and 0.318 cm) were used. Each tray had a constant web thickness. The two trays used at a test are so positioned in the propellant section, as to create an initial uniform port of 2.54 by 0.635 cm along the entire motor, from the end of the igniter nozzle to the entrance to the motor nozzle. The primary feature of the slab-grain geometry is that it permits direct photographic observations during ignition and flame spreading, and at the same time the chamber conditions realistically correspond to the conditions in a practical rocket motor. Furthermore, many diagnostic studies, such as pressure, temperature and heat-flux measurements can be conveniently conducted.

One side wall of the port is a two-part Plexiglas window. Tests with fast water quench revealed that no Plexiglas ablation occurs prior to the time of peak pressure up to 100 msec. The inner part of the window was replaced for each test. The window is sealed by an o-ring gasket and retained by a cover connected to the motor block by 26 high-strength bolts. For tests in which measurements other than photographic were made, the window was replaced by a stainless steel part having the same dimensions.

The side wall of the port channel opposite the window is used for the instrumentation ports. Five Dynisco PT76 high frequency pressure transducers can be installed along the port, 12.7 cm apart, starting from the propellant leading edge. A burst diaphragm is connected to each end of the motor for over-pressure protection. Three additional ports are available for thermocouple probes and heat-flux gauges. The total ten ports can be used in different combinations for techniques, such as depressurization, liquid quenching, side ignition, and purging.

The motor nozzle, made of copper, consists of a rectangular convergent section and a precisely defined rectangular throat. Four nozzles were manufactured for series of tests with port-to-throat area ratio of 1.06, 1.2, 1.5 and 2.0. There was no measurable erosion in all tests conducted. The nozzle block is bolted to the aft end of the motor with a connector, which leads the combustion gases from the nozzle to the exhaust vent system.

To reduce the heat loss to the chamber walls and, thus, to make the experimental motor more compatible with operational motors, the entrance and aft sections of the motor and the nonpropellant walls of the port (except the Plexiglas window, when used) were coated before each test with a thin polymeric layer consisting of a mixture of 50% PBAA/EPON binder and 50% TiO_2 powder. This layer ablated only slightly during the starting transient. In the analytical model it is assumed that this layer has the same thermal properties as the solid propellant. A special test (described in Section B, Chapter VI) was conducted to verify the validity of this assumption.

B. The Ignition System

The igniter source used in this study was a head-end pyrogen igniter, which burned gaseous methane and oxygen in a controllable manner. The system is capable of burning a wide variety of gaseous oxidizers and hydrocarbon fuels (or mixtures of gases) and thus operating with a wide range of igniter temperatures. The methane and oxygen were of research purity and supplied by the Matheson Gas Products Co.

The specially-designed igniter combustion chamber achieved 80% of the equilibrium operating pressure within 3 msec. The chamber consists of a small stainless steel tube (0.9 cm

in diameter and 7 cm long), placed in a copper block. The injector head comprises two carefully calibrated unlike impingement doublets. Fast ignition is achieved by four small 10 mm spark plugs (type Z-6, produced by Champion Spark Plug Co.), positioned along the igniter chamber. A small burst disk is also installed in the system for over-pressure protection. The pressure in the combustion chamber was measured by a Dynisco PT76 pressure transducer. The igniter gases were discharged into the entrance section of the motor through a convergent nozzle.

A controllable feed system supplies the gaseous reactants to the igniter combustion chamber. Each reactant, coming from the high-pressure cylinder, passes through a dome pressure regulator (Model 15H, 0-2000 psi, made by Grove Reg. Co.), which has remotely preset outlet pressure. At this pressure, the gas passes through a check valve (Type K-1359-8-S made by Kohler Co.) and an on-off pneumatically-operated valve (Model PV20F, made by Marotta Valve Corp.) before entering the injector. The two on-off valves on the feed lines are operated simultaneously by a single solenoid valve (Marotta, Model PV74). The total opening time of the on-off valves is 2 msec after the stem moves off the seat. The capacitance of the feed lines between the on-off valves and the injector was minimized to assure fast start-up and shut-off of the igniter. The feed pressures just upstream of the injector were measured by Dynisco PT76 pressure trans-ducers. A cold-flow adjustment of the feed pressures was performed before each run.

A purging subsystem is an integral part of the control-lable igniter. It consists of a nitrogen supply line, a solenoid valve (Marotta, model PV74) and two check valves (Kohler, type K-1359-2). The nitrogen purge enters the system just downstream of the on-off valves. The igniter chamber and rocket motor were flushed with nitrogen before and following each test.

Figure 12 depicts the assembled igniter combustion chamber, injector, two on-off valves, fuel-line pressure transducer, fuel-line purge check valve, and the sonic igni-ter nozzle. The entire assembled ignition system on the test bench is shown in Fig. 13.

For all runs the fuel and oxidizer feed pressures were selected to be higher than the maximum pressure in the motor. In this way back flow from the motor to the ignition system and erosion of the injector orifices were prevented. Com-binations of injector orifices and igniter nozzles were used to allow experiments with different igniter mass flow rates and equivalence ratios. The equilibrium pressure in the ig-niter combustion chamber during the induction period was usually between 20 and 30 atm. The injector orifices

were always choked during the induction interval and served as metering orifices. Real-gas effects, important at the high feeding pressures, were accounted for in the precise determination of the igniter mass flow rates.[196,197] The discharge coefficients of the various injection orifices were between 0.81 for the smallest fuel orifices and 0.92 for the largest oxidizer orifices. The c^* efficiency of the igniter chamber (defined as the ratio of c^* calculated from the measured mass flow rate and pressure in the combustion chamber and c^* calculated from adiabatic thermochemistry) was 95%.

As part of the efforts to simulate real rocket motors having pyrogen igniters, the ignition system operated during the entire starting transient with constant feed pressures. During the last part of the flame spreading period and thereafter, the igniter nozzle becomes unchoked, and the pressure in the igniter combustion chamber increases in accordance with the rising pressure in the motor. The quasi-steady igniter mass flow rate after the unchoking is somewhat less than the previous steady-state value, according to the particular combination of pressures. Since the effect of the igniter mass flow rate during the last stages of the transient is very small (as compared with that of mass addition from the burning propellant), it is assumed in the theoretical model that during this period the igniter operates with the same mass flow rate as before the unchoking.

Figure 14 shows a typical schematic variation with time of: (a) the quasi-steady igniter mass flow rate calculated from experimental pressure-time measurements, (b) the igniter mass flow rate used in the numerical calculations, and (c) the measured head-end motor pressure.

The sequence of events in the operation of the ignition system starts with establishing the desired feed pressures by adjusting remotely the two dome pressure regulators. An automatic electrical sequential cam system actuates the following operations. When the firing circuit is energized, the automatic sequencer first activates the spark plugs. Then the solenoid valve (which controls the feed valves) opens and the on-off feed valves unclose to start the flow of the reactants into the igniter combustion chamber. The igniter action is terminated when the sequencer signals the valves to close and afterwards power to the spark plugs is turned off. The duration of the igniter action can be altered simply by adjusting the timing of the shut-off cam. The easy variation of duration time, igniter-gas temperature and composition, and igniter mass flow rate are the main advantages of the gaseous ignition system.

The gaseous pyrogen igniter was usually operated slightly on the fuel-rich side (with an equivalence ratio ranging between 1.02 and 1.08). The stoichiometric mixture ratio of

the oxygen-methane system is 4:1. Thermochemical calculations[198] yield at 22 atm an adiabatic flame temperature of 3460°K and major product mole fractions of 43% H_2O, 15% CO and 13% CO_2.

For the same fuel-oxidizer combination, the adiabatic flame temperature of the gaseous igniter does not change significantly when changing the equivalence ratio between 1.0 and 1.4. Therefore, wide range of igniter gas temperatures may be obtained in experimental tests by using different fuel-oxidizer combinations.

Figures 15 and 16 show the experimental igniter-motor system mounted on the test bench in the Solid Propellant Test Cell.

C. Instrumentation and Data Reduction

Two types of physical measurements were conducted in the course of the experimental research program: pressure measurements and photographic observations. In each test, the fuel and oxidizer feed pressures (50 to 80 atm) and the pressure in the igniter combustion chamber were measured. In addition, up to five pressure measurements along the chamber port were made. The Dynisco pressure transducers used are of the bonded strain gauge type, Model PT76, suitable for dynamic pressure measurements. The natural frequency of these transducers as stated by the manufacturer is 25,000 cps. From the investigations of Thomas and Layton[199-201] it was deduced that the amplitude frequency response is flat up to 8,000 cps. The frequency range of the transient pressure phenomenon investigated in this study is 40 to 400 cps. The diaphragm of the transducers used for pressure measurements in the igniter chamber and in the motor was protected from the hot combustion gases by a 1/8 inch thick disk made of General Electric RTV-580, which was bonded to the diaphragm by RTV-108 adhesive. Shock-tube experiments showed that the natural frequency of the protected PT76 transducer is 24,000 cps. The installation of the transducers was performed according to the research experience accumulated in the AMS department of Princeton University[195-203] and elsewhere.[204-205] Figure 17 depicts the back side of the experimental motor showing the five pressure transducers installed along the motor.

The transducers in use were calibrated in position before each experimental test. The calibration was performed by pressurizing the assembled rocket motor with nitrogen gas and by regulating the nitrogen pressure. A master pressure gauge (Heise, Type H8755R, 0 to 2000 psi) was used for the calibration in steps of 100 psi. The master gauge was periodically checked and calibrated with an Amthor (Type 472, 0 to 2000 psi) dead-weight tester. Also periodically a calibration of

the pressure transducers after a test was performed with the transducers still in position. Figure 18 shows the Solid Propellant Test Cell Calibration and Firing Console and part of the Instrumentation Console.

The pressure transducers were driven with B&F Input Signal Conditioners. These units have a ripple level of less than 0.5 millivolts peak to peak and were used to supply 10 volts d.c. excitation signal. The pressure signals coming from the transducers were amplified by DANA (Models No. 3420 and 3520) d.c. amplifiers. Model 3520 has built-in filters with band pass widths ranging from wide band and 10 KC down to 0.01 KC. The amplified pressure signals were recorded on a Honeywell Visicorder (Model No. 1508) direct-recording oscillograph. The Visicorder used is capable of recording simultaneously on up to 12 active channels, using light-sensitive paper. The galvanometers used were Honeywell Series "M" sub-miniature, fluid damped, Type No. M1000 and M1650 with nominal undamped natural frequency of 1000 and 1650 cps, respectively. The visicorder was usually operated at its maximum speed, 120 inches of paper per second, with 10 millisecond timing marks. More details on the instrumentation used for the pressure measurements and recording can be found in the Instrumentation Manual[206] for the Solid-Propellant Test Cells in the Guggenheim Laboratories of Princeton University, and in Ref. 74.

The photographic observations were made by taking high-speed motion pictures with a 16 mm Wollensak Fastax camera (Model WF-16). Both black and white (using DuPont 931-A rapid reversal film) and color (using Kodak Ektachrome EF film) movies were taken. Operating speeds of 1200, 2000 and 4000 fps were used. The camera was synchronized with the experimental test so that the operating speed of the camera was attained before first ignition. Two neon timing lamps were used with the photography. The synchronization timing lamp was connected to a cam of the ignition sequence timer to generate a signal shortly after ignition, which was recorded simultaneously on the oscillograph and the film for synchronization. The second lamp was connected to a signal generator and produces timing marks every millisecond of real time on the film.

Data reduction of eight simultaneous records per test is a tremendous job if not performed in an automatic manner. In the later stages of the study analog-to-digital conversion (A - D) was used to reduce and process the data. The Datacom Data Acquisition System (Model 8015) used in this study is capable of acquiring analog data from up to 64 sources at a total sampling rate of 40,000 per sec. The analog channels are multiplexed, converted to 12-bit binary words by a Raytheon A-D Converter and recorded on a 9-track magnetic tape compatible with the IBM 360/91 computer. The data is recorded

in blocks which are stored in the system memory with a capacity of 2048 bytes. When a block is complete it is transferred automatically to the tape, while the next block is being filled. The Datacom system was used simultaneously with the Visicorder oscillograph during both calibration and test recording. Proper wiring and grounding was made to the Datacom system to make it compatible with the Visicorder. The data recorded on the tape was demultiplexed, converted back to pressure readings, and analyzed using an IBM 360/91 computer by means of a program specially written for this purpose. Typical use of the Datacom system in this study included recording of the five motor-pressure measurements at total sampling rate of 10,000 readings per second (or 2,000 readings per channel per sec) and block length of 1800 bytes with the pressurization part of the transient included in one block. A mean deviation of less than 1% was obtained between pressure vs time plots from manual reduction of Visicorder records and those processed by using the Datacom system. The mean deviation is defined here as the ratio between the area enclosed by the two $p - t$ plots obtained from the two systems and the area enclosed by the Visicorder plot and the time axis.

Figure 19 shows the Solid Propellant Test Cell Instrumentation Console and the Datacom Data Acquisition System with the related wiring before a test.

D. Experimental Test Series

The major parameters varied in the experimental study were the port-to-throat area ratio and the igniter mass flow rate. According to the four port-to-throat area ratios used, 2.0, 1.5, 1.2 and 1.06, four series of runs were conducted, designated C, D, E and F, respectively. In each series 5 to 6 tests were carried out with different igniter mass flow rates, ranging from 8.5 to 21.5 g/sec. In all these runs the gaseous igniter was operated at close to stoichiometric fuel-oxidizer mixture ratio, yielding a theoretical adiabatic flame temperature of 3460°K at 21 atm as described in Section B of this Chapter. The same composite propellant, the properties of which are listed in Table 1, was used in all experimental tests. The purpose of these run series was to test the entire experimental set-up, investigate the effects of port-to-throat area ratio and igniter mass flow rate on the various characteristic transient parameters of interest and check the validity of the analytical model. Several early experiments were conducted at the start of the experimental program to check reproducibility of test results. For the same igniter mass flow rate very good reproducibility of pressurization rates and maximum pressure was obtained. In all test motor runs $p(t,x)$ measurements were taken, and in some runs photographic observations were made. In addition to the aforementioned four series of runs several particularly diagnostic experimental tests were carried out as described in the following paragraphs.

An experimental test was conducted at $A_p/A_t = 1.2$ with the igniter operating at an equivalence ratio of 1.35, which yields a theoretical adiabatic flame temperature of 3360°K, to confirm experimentally the findings of the theoretical calculations about the effect of igniter gas temperature.

An experimental firing was carried out with shorter propellant slabs (33.0 cm long) in the upstream part of the propellant section. The PBAA/TiO$_2$ mixture was applied in a thin layer over the downstream tray surface to check: (1) the validity of the assumption that PBAA/TiO$_2$ layer has approximately the same thermal properties as the propellant, and (2) the effect of propellant grain length for the same configuration on the transient.

Liquid quench experiments were conducted to find the erosive burning exponent of the propellant and to check the validity of the analytical model in the post-transient period by measurements of distance burned. A quench system based on the study of Strand and Gerber[207] was designed, built, and successfully operated. Water was injected simultaneously through five ports along the motor. Check valves just upstream of the injector heads prevented entry of the combustion gases into the system. The water jets bounced off the opposite wall in small droplets and thus propellant surface cutting was avoided. Small amounts of water (as little as 5 gms) injected in 10 msec caused a complete extinguishment in 3 msec. It was discovered in the quench experiments that the Plexiglas window does not ablate even when the test time is extended to the period of steady-state operation. This means that no corrections are necessary in the analytical model for port area changes and for mass addition resulting from Plexiglas regression during the transient period.

Techniques for direct photographic measurements of burning rate during the transient and thereafter were attempted during the course of this study. The techniques were not developed fully since burning rate measurements were not considered a primary goal in the study. A promising technique tried with a partial success in the investigation will be mentioned. The propellant was cast simultaneously in the two opposing trays and then bonded to and polymerized with a Plexiglas window, which was connected by screws to the trays. The propellant grain-window assembly is depicted in Fig. 20.

CHAPTER VI

DISCUSSION OF RESULTS

Diagnostic experimental tests and corresponding numerical calculations were conducted with AP composite propellant at port-to-throat area ratios of 2.0, 1.5, 1.2 and 1.06 with igniter mass flow rates ranging from 8.5 to 20.5 g/sec. Table 1 lists the baseline values of propellant properties and motor parameters used in the calculations. These values correspond closely to the experimental conditions in all tests. A datum case was defined at $A_p/A_t = 1.2$ and $m_{ig} = 15.0$ g/sec using the baseline values of Table 1. It was so selected because port-to-throat area ratio of 1.2 and operating pressure of about 40 atm represent a realistic goal for high-performance motors that designers presently cannot analyze with confidence. The results of the experimental study are listed in Table 2. Table 3 summarizes the results of the theoretical parametric study about the datum case and calculations corresponding to experimental tests. A list of input values for the datum case calculations is presented in Table F1 (see end of Appendix F). Typical calculated Mach and Reynolds numbers during the transient for the different port-to-throat area ratios tested are given in Table 4.

A. Comparison Between the Theoretically Predicted and Experimentally Measured Pressure-Time-Space Traces

Typical starting transient $p(t,x)$ measurements, obtained during experimental tests at the five measurement stations (denoted in Fig. 2) at port-to-throat area ratios of 2.0, 1.5, 1.2, and 1.06 are shown in Figs. 21 through 24, respectively. By recalling Fig. 1, it is seen that HVT motors are operating in a pressurization regime which is totally different from that in the ignition studies of Most and Summerfield.[5] The plots show clearly the strong time and space-dependence of motor pressure during the transient and thus demonstrate the necessity of this analysis. Consider the starting pressure transient depicted in Fig. 23. Following a small pressure wave caused by the onset of igniter flow, an almost uniform pressure distribution at 1.2 atm was established in the motor cavity. At 36 msec after the igniter start, a flame was observed (on high speed photographs) at the leading edges of the propellant slabs and flame spreading begins, accompanied by increase of pressure. The pressure-rise at station 3 (middle of motor) starts later but increases at the fastest rate. Pressure peaks are achieved at 72 msec at the fore-end (station 1) and at 73.5 msec at the aft-end (station 5).

Axial variation of pressure increases as A_p/A_t decreases. In all tests, the pressure measured at station 2 was almost identical to that measured at station 1 (fore-end of motor) due to the igniter-motor configuration and the low Mach numbers at the fore-end part of the propellant section.

Comparisons between typical measured and calculated (by the analytical model) pressure-time curves at stations 1, 3, and 5 for port-to-throat area ratios of 1.5, 1.2, and 1.06 are shown in Figs. 25, 26, and 27, respectively. Also shown in these figures are the pressure-time traces calculated for no erosive burning and the calculated pressure-time point of flame spreading completion. In general, very good agreement between measured and calculated pressure-time plots is observed. The only input variable adjusted to achieve agreement was the erosive burning exponent β. However, in future β can be established a priori by erosive burning tests (such as burnt distance vs x measurements after extinguishment shortly after the transient). It is emphasized that no adjustments in parameters are made during the parametric studies. The solution of the analytical model predicts precisely the initial development of pressure distribution at the onset of igniter and the following nearly constant pressure distribution during the induction interval (not shown in Figs. 25 through 27). Agreement within 10% between measured and calculated time to first ignition (i.e., occurrence of first flame on propellant surface) and time to attain the maximum fore-end pressure is obtained for all comparisons at port-to-throat area ratio of 1.2, 1.5, and 2.0. No ignition time measurements were made at $A_p/A_t = 1.06$. The agreement between measured and calculated time to attain the maximum fore-end pressure for this case is within 15%.

An agreement within 10% (in most cases less than 5%) is obtained between calculated and measured pressure-peak values at all stations and for all port-to-throat area ratios investigated. The largest disagreement is observed at $A_p/A_t = 2.0$.

For $A_p/A_t = 1.2$, 1.5 and 2.0, during the flame spreading period the calculated pressure is usually slightly lower than the measured pressure, whereas during the chamber filling, the calculated pressure is slightly higher than the measured pressure. It should be mentioned that this type of deviation between the calculated and measured pressure transient is the same as the one obtained by Most and Summerfield[5,15] for motors with high port-to-throat area ratio using the dynamic-temperature homogeneous model. A possible explanation for this deviation may be, for instance, increased heat transfer to the propellant due to surface roughness at the early stages of flame spreading, and attenuated heat transfer to the unignited propellant surface at the later stages of flame spreading due to considerable blowing from the surface, when the ignition temperature is approached.

For $A_p/A_t = 1.06$, all calculated pressure-time plots precede the experimental ones. The maximum deviation in the time-axis direction for the range of igniter mass flow rates tested is 15%. For the same igniter mass flow rate, as the port-to-throat area decreases the velocity over the propellant

leading edge increases and the pressure decreases. The phenomenon of delayed ignition at high gas velocities was observed and discussed by McCune,[29] Kling, et al,[65] Keller, Baer, and Ryan,[63,64] and Bastress and Niessen.[59] The explanation of Keller, Baer, and Ryan is recalled here; as the gas velocity is increased, reactive species at or near the surface are being increasingly diluted and swept away by the fast-moving gas. This is consistent with the research of Kashiwagi and co-workers,[60] which shows that the gas-phase kinetic processes are important during ignition, and increased flow velocity shifts the ignition position downstream in the case of a gas-phase ignition model. At $A_p/A_t = 1.06$ and low to moderate igniter mass flow rates the pressure in the experimental motor (as in every HVT motor) is very close to the ambient The increase of ignition delay time when lowering the pressure (and approaching the atmospheric pressure) at moderate to high surface heat fluxes has been observed and studied by many investigators.[32,34,69,70,208,209] In this study, typical calculated convective heat flux at the propellant leading edge (average for the induction interval) for $A_p/A_t = 1.06$ and $m_{ig} = 17.2$ g/sec was 42 cal/cm^2-sec.

It should be noted that in many tests using photography start of pressurization in the motor chamber was measured before any ignition has been observed (typically a pressure-rise of 1 to 2 atm over the pre-ignition level). This may be a result of a pre-ignition decomposition-gasification of the solid-propellant. The reduced cooling of the igniter gas due to surface temperature increase, as calculated by the analytical model, does not cause a substantial change in chamber pressure.

The contribution of erosive burning to the increase of pressure is seen in Figs. 25 through 27. It may be defined as the ratio of maximum fore-end pressure calculated with erosive burning to the maximum fore-end pressure calculated without erosive burning. For the propellant used in this study (see Table 1) and the burning rate law given by Eq. (III-35), the aforementioned ratio is approximately the same for all values of A_p/A_t tested, and equals 1.5. This means that in terms of maximum pressure, the burning rate increase along the port due to erosive burning is fully compensated by the burning rate decrease due to the significant pressure drop. Indeed, the high value of the pressure exponent (n = 0.4) shows high pressure sensitivity, whereas the large value of the erosive burning exponent (β = 105) represents low sensitivity to erosive burning. With respect to motor design, this conclusion points out the feasibility of using propellants with relatively large values of n and β in high-performance rocket motors without facing unacceptably high fore-end pressures. In the range tested, the erosive burning contribution is only slightly affected by the igniter mass flow rate, due to its small magnitude as compared to the mass

added from the propellant burning. The ratio of steady-state igniter mass flow rate (m_{ig}) to maximum mass flow rate out of the nozzle varied between 3 and 6%, as listed in Table 3.

One of the principal advantages of the analytical model is the ability to calculate spatial, as well as temporal, variations of gas parameters. Measured and calculated spatial pressure distributions at four illustrative times (corresponding to different stages of the transient) of Run D-9 (A_p/A_t = 1.5) are compared in Fig. 28. Calculated spatial velocity and temperature distributions at the same times are plotted in Figs. 29 and 30, respectively. These plots correspond to the pressure-time traces in Figs. 22 and 25. The changes in velocity distribution during the transient are well depict.d in Fig. 29. During the induction interval there is a l-.je velocity decrease along the port due to gas cooling. Du.ing flame spreading there is velocity increase upstream of the ignition front (due to mass addition) and velocity decrease downstream of the front. After the completion of flame spreading the gas velocity increases considerably in the propellant section and changes only slightly in the aft section.

To show the effect of port-to-throat area ratio, the pressure, velocity, and temperature distributions at the different stages of the transient for a test with A_p/A_t = 1.06 are plotted in Figs. 31, 32, and 33, respectively. These plots correspond to the pressure-time traces in Figs. 24 and 27.

The significant changes in gas parameter distributions during the transient are well described in Figs. 28 through 33 and they emphasize the need for a distance and time [$p(t,x)$] analysis for proper prediction and control of the starting transient of HVT motors.

B. Ignition Delay Times, Flame Spreading, and Pressurization Rates

Most of the photographic observations were made at port-to-throat area ratio of 1.2. The event of first ignition was relatively easy to detect, whereas flame spreading photography was only partially successful as explained later in this section. First ignition, when detected, always appeared at the propellant leading edge. Figure 34 shows the measured and calculated effect of igniter mass flow rate on the ignition delay time t_{ig} (defined as the time from onset of igniter to the first appearance of flame on the propellant surface) for motor test series "E" (A_p/A_t = 1.2). From the thermal ignition theory, assuming an inert propellant being heated by a constant heat flux at the surface and a prescribed surface temperature for ignition, it is deduced that the square root of the ignition delay time is inversely proportional to

the surface heat flux. If a turbulent flow correlation for the convective heat-transfer coefficient is used [such as Dittus-Boelter correlation, Eq. (III-21)], it follows that $t_{ig} \sim m_{ig}^{-1.6}$. However, actually, the surface heat flux is not constant during the induction interval, because m_{ig} is not a step function of time (see Fig. 14), the heat-transfer coefficient is coupled to the varying gas dynamics in the motor chamber, and the rising surface temperature decreases the driving temperature difference. Figure 35 shows the variation with time of the calculated heat flux at the propellant surface at three different positions along the motor corresponding to pressure measuring stations 1, 3, and 5 (see Fig. 2) for a test with $A_p/A_t = 1.2$. The calculation is made in accordance with the experimental variation of igniter mass flow rate (see Fig. 14), such that steady-state value and 80% of it are obtained 12 msec and 2 msec after the onset of igniter, respectively. The shape of heat-flux variations shown in Fig. 35 are typical for the calculated distributions in this study. Figure 36 shows the calculated propellant surface temperature vs time at the same positions and for the heat flux variations as shown in Fig. 35.

The slope of the log t_{ig} vs log m_{ig} plot on Fig. 34 is -1.5. Similar plot of three measured ignition times (not shown here) for $A_p/A_t - 2.0$ (see Table 2) shows a slope of -1.42. For constant q and m_{ig}, it would mean that turbulent flow (although not fully developed) existed over the propellant leading edge. Calculated ignition delay times vs igniter mass flow rate for the four port-to-throat area ratios tested are shown in Fig. 37. The slope of the calculated lines varies between -1.25 and -1.35, which means that the aforementioned factors (accounted for in the analysis) affect the calculated ignition delay times. For the same igniter mass flow rate in the range investigated, calculated ignition delay times decrease slightly when increasing A_p/A_t between 1.06 and 1.5. No photographic measurements were made at $A_p/A_t = 1.06$.

High-speed photography of fast flame spreading is a difficult task. Flame propagation appears to be more like an increasing cross-sectional density of ignited points rather than a well-defined advancing flame front. Ignition spots appear at random downstream of the fully ignited surface. This may be caused by an increased heat transfer at local surface irregularities. The same phenomenon was observed by Mitchell and Ryan,[31,82] by Keller, Baer, and Ryan,[64] by McAlevy, et al,[80] and by Most and Summerfield.[5,15] Figure 38 shows calculated and measured locations of the flame front versus time for an experimental test with port-to-throat area ratio of 1.2. Typically, at the beginning of flame propagation experimentally measured rates are higher than the calculated and this difference reverses toward the end of the process. Flame propagation rates ranging from

920 cm/sec to 19,800 cm/sec at the start and the end of the process, respectively, were obtained for A_p/A_t = 2.0 and m_{ig} = 19.5 g/sec. Calculated initial flame spreading rates increase substantially with increasing igniter mass flow rate but do not show an effect of A_p/A_t, as seen in Fig. 39. The few experimental data are in agreement with the former observation but are insufficient to verify the latter. Calculated flame spreading times, however, show that for the same igniter mass flow rate (and chamber geometry), the average flame spreading rate decreases with A_p/A_t. The larger throat area results in lower pressures (and thus lower burning rates) and lower heat flux, because for the propellant and geometry used in this study, the effect of lower pressure overcomes the effect of higher velocities.

With respect to the total pressure rise, the calculated pressures at the instant of flame spreading completion vary from 25 to 30% of the maximum pressure for A_p/A_t = 2.0 to 50 to 55% for A_p/A_t = 1.06.

For all port-to-throat area ratios tested, the highest pressurization rates in the tests were measured at station 3 (middle of motor), as seen in Table 2. The maximum pressurization rates at the motor fore-end (station 1) were slightly lower. As far as the numerical calculations are concerned, the maximum calculated pressurization rates were usually obtained at a position between stations 2 and 3. Both measured and calculated maximum pressurization rates are obtained at the instant of flame spreading completion or immediately thereafter.

Measured and calculated maximum pressurization rates at station 1 vs igniter mass flow rate for the different A_p/A_t tested are plotted in Figs. 40 and 41, respectively. Fore-end maximum pressurization rates as low as 3,000 atm/sec for A_p/A_t = 1.06 and m_{ig} = 15.1 g/sec, and as high as 6,800 atm/sec for A_p/A_t = 2.0 and m_{ig} = 19.5 g/sec were measured. The calculated rates are greater than the measured ones on the average by a factor of 2. The maximum pressurization rate increases with both the igniter mass flow rate and the port-to-throat area ratio. The former effect is less pronounced experimentally than theoretically. The maximum pressurization rates decrease as the distance from the fore-end increases and this decrease is larger as A_p/A_t is smaller.

The test with shorter propellant trays (see Table 2) demonstrates the validity of the assumption that the PBAA/TiO_2 coating and Plexiglas window can be treated as having the same thermal properties as the propellant. It also shows the effect of burning-to-throat area ratio on pressurization rates and maximum pressures.

C. The Thrust Transient

Prediction and control of the thrust transient require knowledge of the transient stagnation pressure at the nozzle entrance, p_{as} , besides qualitative knowledge of the unsteady phenomena taking place in the nozzle. The calculated transient variation with time of the fore-end and aft-end (nozzle entrance) static pressures and the aft-end stagnation pressure for a test with $A_p/A_t = 1.2$ are shown in the upper part of Fig. 42. The lower part of the same figure shows the variation with time during the transient of the ratio of aft-end stagnation pressure (p_{as}) to fore-end static pressure (p_1). The stagnation pressure is calculated from the static pressure and velocity. During the induction interval p_{as} is higher than p_1 by 15 to 20% since the effect of gas cooling along the port is greater than the effect of friction. After first ignition, the ratio p_{as}/p_1 drops gradually to a minimum of 0.73 and increases afterward to the steady-state value of 0.844. After the completion of flame spreading the stagnation pressure decreases along the port due to the dominant effect of mass addition. Figure 42 illustrates the conclusion that calculation of the thrust transient of HVT motors by using measured or calculated fore-end static (or any "uniform") pressure is improper and misleading.[210]

Figure 43 shows the effect of A_p/A_t on calculated (in this study) ratios of maximum static and stagnation pressures at motor aft-end to maximum motor fore-end pressure. The obtained values correspond closely to the values calculated by using the steady-state approach of Price[210] and the baseline quantities listed in Table 1.

D. Parametric Studies

1. Effect of Igniter Mass Flow Rate

The igniter mass flow rate was the major variable in the experimental study. Its large effect on the ignition delay time and flame spreading rates, and small effect on the maximum pressurization rates is described in Section B of this Chapter. Experimental and calculated maximum fore-end (station 1) pressures vs igniter mass flow rate for the different port-to-throat area ratios tested are plotted in Fig. 44. A cross-plot of calculated maximum fore-end pressures vs A_p/A_t for two igniter mass flow rates is shown in Fig. 45. The maximum fore-end (and in other stations as seen from Tables 2 and 3) pressure increases slightly when increasing m_{ig}, as expected. The calculated rate of increase is higher at $A_p/A_t = 2.0$, than at the other port-to-throat area ratios. For a given igniter mass flow rate (and the constant configuration under consideration), the pressure level rises fast when increasing A_p/A_t (by decreasing the nozzle throat area), as illustrated in Fig. 45.

The aforementioned effects and trends apply to the range
of m_{ig} tested. They may change direction or be overcome by
other effects at extreme cases of marginal m_{ig} (causing a
hangfire) or very high m_{ig}. An experimental test at A_p/A_t
= 1.2 and m_{ig} = 8.5 g/sec shows higher maximum pressuriza-
tion rate and pressure peak than expected from the trend de-
duced from tests at higher m_{ig} (see Figs. 40 and 44). This
is an example of dynamic-burning effect caused by long pre-
heating of the propellant.

Calculated pressure delay time (time from igniter onset
to the instant at which 10% of the maximum pressure is attain-
ed at the fore-end, t_{dp}) and time to attain maximum fore-end
pressure are plotted vs A_p/A_t in Fig. 46 for two igniter mass
flow rates. Both times decrease appreciably when increasing
m_{ig} (see also Tables 2 and 3). For A_p/A_t = 1.2 increase of
m_{ig} from 11.5 to 19.5 (by 70%) decreases t_{dp} from 77.5 to
37.0 msec (by 52%).

2. Effect of Igniter Gas Temperature

The effective igniter gas temperature (T_{ig}) has a
strong effect on the ignition delay time and the initial flame
propagation rate (or the total flame spreading time) and thus
affects the starting transient in terms of time. Increase of
T_{ig} by 10% at the datum case (see Table 3) shortens the ig-
nition time by 24% and the flame spreading time by 14%, and
has no effect on maximum pressure or maximum pressurization
rate, because m_{ig} becomes a small fraction of the total
mass flow rate in the motor in the early stages of the flame
spreading process.

3. Effect of the Heat-Transfer Coefficient

The convective heat transfer correlation affects
strongly the induction period and flame spreading process.
An increase of the coefficient a_h in Eq. (III-31) from
1.56×10^{-3} to 1.704×10^{-3} (by 9.2%) at the Datum Case
shortens the ignition delay time by 13% and the flame spread-
ing time by 9%, and increases slightly the maximum pressur-
ization rates. If the effect of A_p/A_t on the heat-transfer
coefficient (see Section D, Chapter III) is not considered,
there is slight reduction in ignition delay and flame spread-
ing times when A_p/A_t is increased from 1.2 to 1.5, using the
same expression for the heat-transfer coefficient and the
same igniter gas temperature (see Table 3).

4. The Effect of Friction

The gas dynamic effect alone of friction is to re-
duce ignition delay and flame spreading times when the fric-
tion coefficient is increased, because increased friction
causes higher pressure distribution in the port, and thus

increased heat transfer to the propellant. For $A_p/A_t = 1.5$ and $m_{ig} = 11.5$ g/sec, use of 10 times smaller friction coefficient [by multiplying Eq. (III-33) by 0.1] prolongs the ignition delay and flame spreading times by about 5%. This proves that wall-friction terms have to be included in the analysis if precise prediction of the aforementioned times is needed. However, the effect of relative surface roughness is small and decreases further with increase of the port diameter. For example, for the datum case ($A_p/A_t = 1.2$, $m_{ig} = 15.0$ g/sec), an increase of the relative equivalent sand roughness (ε_s/d_h) from 10^{-3} to 10^{-2} shortens the ignition delay time by approximately 5% and the flame spreading time by approximately 2%.

5. The Effect of Uncertainty in Propellant Properties

Uncertainty in the propellant thermal properties affects the induction and flame spreading periods. Figure 47 shows the effect of uncertainty of 20% in the propellant thermal conductivity (and thermal diffusivity, accordingly) on the fore-end pressure transient for $A_p/A_t = 1.2$ and $m_{ig} = 15.0$ g/sec. The effect is also seen in Eq. (III-50). The ignition delay and flame spreading times are shorter by 20% and 16%, respectively, if λ_{pr} is smaller by 20%. The propellant ignition temperature ($T_{ps,ig}$) has, apparently, a similar effect.

The burning rate law affects, obviously, mostly the later part of flame spreading process and the entire chamber filling period. Therefore, for the same configuration, maximum pressurization rates and pressure levels are determined by the function $r(T_{pi}, p, \rho u)$. For example, changing the erosive burning exponent (β) from 105 to 115 for the datum case results in about 5% decrease in the maximum calculated fore-end pressure and pressurization rates.

For the configuration and range of investigation considered, the parametric study may be summarized as follows:

The ignition delay and flame spreading times decrease with:

(1) increasing the igniter mass flow rate, m_{ig};

(2) increasing the igniter gas temperature, T_{ig};

(3) increasing A_p/A_t (in part of the range);

(4) increasing the constant coefficient in the correlation for heat-transfer coefficient;

(5) increasing the relative propellant surface roughness;

(6) decreasing the thermal conductivity of the propel-
lant, λ_{pr}, and

(7) decreasing the ignition temperature of the propel-
lant, $T_{ps,ig}$.

The maximum chamber pressure and pressurization rate
increase with:

(1) increasing the igniter mass flow rate, m_{ig};

(2) increasing the burning surface-to-throat area
ratio, A_b/A_t;

(3) increasing the burning rate with respect to a
reference value at given T_{pi}, p, and ρu;

(4) increasing A_p/A_t, and

(5) decreasing the distance from the motor fore-end
part.

The dependence of the starting pressure vs time curve
shape upon various important parameters is shown schematically
in Fig. 48.

CHAPTER VII

SUGGESTIONS FOR FUTURE STUDIES

A. Extension of the Analysis

The next step in the investigation of the starting transient of HVT motors is extension of the model and analysis developed in this study to various classes of propellants and configurations. Certain applications (e.g., use of highly aluminized propellants) may require modification of the analysis and relaxation of some assumptions. However, the model is a detailed and fundamental one and any modifications, such as using different burning rate laws, inclusion of radiative heat transfer and consideration of various burning surface vs burnt distance functions can be easily introduced. Accompaniment of the analysis extension by experimental studies or results will verify the validity of the model and guide the necessary modifications. Increased versatility of the analysis will be very helpful to designers of high-performance rocket motors. In particular, the techniques should be extended to include the radial flow effects in segmented motors.

B. Study of Extreme Cases

The analysis of extreme cases, such as marginal igniter mass flow rate leading to hangfires or misfires, and oversized igniter resulting in high pressure peak, is very important to the proper design and performance of solid-propellant rocket motors. Study of the effect of marginal igniter on the transient may require consideration of exothermic pre-ignition reactions.[5] Analysis of vigorous ignition by oversized igniter, on the other hand, may require consideration of dynamic burning contribution.

The study of both cases as well as the broadening of the parametric study presented here are recommended as leading to further understanding and ability to control the starting transient of HVT motors.

C. Heat-Transfer Correlation

Due to the importance of the heat transfer correlation to proper transient analysis and prediction, it is recommended to conduct studies for determination of this correlation for HVT motors under different practical conditions. The experimental motor used in this study is an excellent tool for such investigations. Experimental heat-flux measurement and pertinent numerical computation techniques[61,68,211-213] are continuously developing. Detailed knowledge of the fluid dynamic flow characteristics is also important and may be obtained by optical recording methods.[50,53] Proper evaluation of the

effects and phenomena discussed in Section D, Chapter III is necessary for determination of the heat transfer to the propellant surface. The more is known about the heat transfer process, the better the prediction and control of the transient become.

D. Burning Rate Laws

The analysis developed in this study considers a burning rate which is a function of the initial propellant temperature (T_{pi}), pressure $[p(t,x)]$, heat transfer coefficient $[h_c(t,x)]$ and mass velocity $[\rho(t,x)u(t,x)]$, specific for the propellant investigated. One of the conclusions (see Chapter VIII) is that improvement of the analysis and prediction as applied to HVT motors may be obtained by consideration of unsteady (dynamic) burning, as discussed in Section F, Chapter III and in Appendix C. This calls for a broad theoretical as well as experimental study of the coupled effect of erosive and dynamic burning. Analytically, a burning rate law of the following general form is needed:

$$r(t,x) = r_0[T_{pi}, p(t,x)]F\left[\rho(t,x)u(t,x), \frac{\partial p}{\partial t}(t,x), T_{pr}(t,x,y)\right]$$

Experimentally, the microwave doppler shift technique developed by Shelton[214] and Strand, et al[215] is very promising. The direct photographic approach described in Section D, Chapter V may be considered too.

CHAPTER VIII

SUMMARY AND CONCLUSIONS

A successful analytical model was developed to describe and analyze the entire starting pressure transient of solid-propellant rocket motors with low port-to-throat area ratios, resulting in high internal gas velocities. The model was formulated in a general way, which enables an easy extension of application over a wide range of propellants and motor configurations. The flame spreading is coupled to the chamber gas dynamics through the solid phase heat equation and the ignition criterion. Velocity, pressure, and temperature variations can now be calculated as a function of time and axial distance.

A suitable numerical method was developed for an efficient solution of the complicated mathematical model. The pressure transients, calculated by the analytical model are in close agreement with the $p(t,x)$ measurements in an experimental motor, utilizing a head-end, pyrogen-type ignition system.

In comparison with previous studies, as reviewed by Most and Summerfield in Ref. 5 and in this work, the essential new elements in this study are:

(1)   ability to consider significant pressure, velocity and temperature spatial gradients, encountered in HVT (High Velocity Transient) motors and their variation with time during the starting transient;

(2)   calculation of the propellant surface heating-to-ignition coupled to both temporal and spatial changes of flow parameters in the chamber during the induction and flame spreading periods;

(3)   techniques to account for the strong contribution of erosive burning, coupled to the chamber gas dynamics;

(4)   account for axial variation of the port area during all three phases of the transient, and

(5)   ability for more precise transient thrust calculation and control.

For port-to-throat area ratios of 1.2, 1.5 and 2.0 an agreement within 10% between calculated and measured ignition delay times, flame spreading rates, pressure peaks, and times to attain the pressure peaks was obtained. For $A_p/A_t = 1.06$ deviations of up to 15% in time were caused by the high gas velocities and low induction pressures. Better agreement in
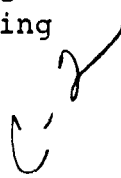
this case may be obtained by appropriate ignition criterion. Maximum pressurization rates as low as 3,000 atm/sec for port-to-throat area ratio (A_p/A_t) of 1.06 and igniter mass flow rate (m_{ig}) of 15 g/sec, and as high as 7,000 atm/sec for $A_p/A_t = 2.0$ and $m_{ig} = 19.5$ g/sec were measured. The highest pressurization rates in a test were obtained in the middle of the motor, with slight decrease upstream and large decrease downstream of mid-motor.

Par_metric studies have shown that ignition delay and flame spreading times decrease with increasing: (1) the igniter mass flow rate and temperature; (2) A_p/A_t between 1.06 and 1.5; (3) the leading constant in the correlation for heat-transfer coefficient, and (4) the relative propellant surface roughness. The aforementioned times decrease with decreasing the thermal conductivity and ignition temerature of the propellant. The maximum chamber pressure ɑnd pressurization rate increase with increasing: (1) the igniter mass flow rate; (2) the burning surface-to-throat area ratio; (3) the burning rate, (especially the sensitivity to erosive burning), and (4) A_p/A_t, and with decreasing the di;tance from the motor fore-end part.

When more precise calculation of the starting transient is required in particular investigations and applications, it can be obtained by using more comprehensive correlations for the convective heat-transfer coefficient and the burning rate, by taking into account effects, such as increased heat transfer to rough propellant surfaces, attenuation of heat transfer by the "blowing" at the propellant surface due to pre-ignition gasification, unsteady burning, resulting from preheating during the induction interval and high pressurization rates during the chamber pressure rise, and turbulent boundary layer structure. For very high gas velocities, an ignition criterion different from that of attaining a critical surface temperature for ignition is needed. Study of coupled erosive and dynamic burning may improve the applicability of the analysis presented.

The experimental system can be readily used to conduct various diagnostic tests, pertinent to modern rocket motors, e.g., heat-flux measurements, start-stop control, propagation of pressure perturbations, and fast liquid-quench extinguishment.

The results of this study are useful to designers of high-performance solid-propellant motors. In particular, by using the techniques developed in this work and the results obtained, the designer can prescribe the upper limit of volumetric loading density, that can be used, ɑnd predict more accurately the pressure-thrust-time motor performance during the starting transient.

REFERENCES

1. Adams, D. M., "Igniter Performance in Solid-Propellant Rocket Motors," Journal of Spacecraft and Rockets, Vol. 4, No. 8, Aug. 1967, pp. 1024-1029.

2. DeSoto, S. and Friedman, H. A., "Flame Spreading and Ignition Transients in Solid Grain Propellants," AIAA Journal, Vol. 3, No. 3, March 1965, pp. 405-412.

3. Parker, K. H., Most, W. J., and Summerfield, M., "The Ignition Transient in Solid-Propellant Rocket Motors," Astronautica Acta, Vol. 12, No. 4, July-Aug. 1966, pp. 245-257.

4. Bradley, H. H., Jr., "Theory of a Homogeneous Model of Rocket Motor Ignition Transients," AIAA Preprint No. 64-127, Jan. 1964.

5. Most, W. J. and Summerfield, M., "Starting Thrust Transients of Solid Rocket Engines," Aerospace and Mechanical Sciences Report No. 873, July 1969, AMS Department, Princeton University, Princeton, N.J.

6. Sforzini, R. H. and Fellows, H. L., Jr., "Prediction of Ignition Transients in Solid-Propellant Rocket Motors," Journal of Spacecraft and Rockets, Vol. 7, No. 5, May 1970, pp. 626-628.

7. Threewit, T. R., Rossini, R. A., and Uecker, R. L., "The Integrated Design Computer Program and the ACP-1103 Interior Ballistics Computer Program," Report No. STM-180, Dec. 1964, Aerojet-General Corp., Sacramento, Ca.

8. Barron, J. G., Jr., Cook, K. S., and Johnson, W. C., "Grain Design and Internal Ballistics Evaluation Program (IBM 7094 Fortran IV)," Program No. 64101, June 1967, Hercules Powder Co., Bacchus Works, Magna, Utah.

9. Vellacott, R. J. and Caveny, L. H., "A Computer Program for Solid Propellant Rocket Motor Design and Ballistic Analysis," ARS Preprint No. 2315-62, Jan. 1962.

10. Anon., "Solid Propellant Rocket Motor Internal Ballistics Computer Program (Program Manual)," Report No. RK-TR-67-7, Sept. 1967, The Boeing Co., Seattle, Wash.

11. Miller, W. H. and Barrington, D. K., "A Review of Contemporary Solid Rocket Motor Performance Prediction Techniques," Journal of Spacecraft and Rockets, Vol. 7, No. 3, March 1970, pp. 225-237.

12. Miller, W. H., "Solid Rocket Motor Performance Analysis and Prediction," NASA Monograph SP-8039, May 1971.

13. Paul, B. E., Lovine, R. L., and Fong, L. Y., "Propellant Surface Flame Propagation in Rocket Motors," AIAA Preprint No. 64-125, Jan. 1964.

14. Brown, R. S., Wirrick, T. K., and Anderson, R., "Theory of Ignition and Ignition Propagation of Solid Propellants in a Flow Environment," AIAA Preprint No. 64-157, Jan.1964.

15. Most, W. J., "Ignition Transient Prediction and Control of Solid Propellant Rocket Motors," Ph.D. Thesis, June 1969, AMS Department, Princeton University, Princeton,N.J.

16. Price, E. W., "Correlation of Physical and Performance Characteristics of Solid Propellant Rockets," NAVORD Report 1982, Aug. 1952, USN, Bureau of Naval Ordnance.

17. Price, E. W., "Charge Geometry and Ballistic Parameters for Solid Propellant Rocket Motors," Jet Propulsion, Vol. 24, No. 1, Jan.-Feb. 1954, pp. 16-21.

18. Green, L., Jr., "Some Effects of Charge Configuration in Solid Propellant Combustion," Jet Propulsion, Vol. 28, No. 7, July 1958, pp. 483-485.

19. Murphy, J. M. and Wall, R. H., "Effects of Grain Configuration upon the Burning Rate of a Spinning Rocket Motor," Journal of Spacecraft and Rockets, Vol. 3, No. 2, Feb. 1966, pp. 263-264.

20. Peretz, A., Kuo, K. K., Caveny, L. H., and Summerfield, M., "The Starting Transient of Solid-Propellant Rocket Motors with High Internal Gas Velocities," AIAA Paper No. 72-1119, Nov.-Dec. 1972 (accepted for publication in the AIAA Journal).

21. Falkner, C. E. and Miller, C. L., "Analytical Igniter Design for Solid Propellant Rocket Motors," Rept. AFRPL-TR-70-69, May 1970, CETEC Corp. (subsidiary of Technology Inc.), Mountain View, Ca.

22. Summerfield, M., Shinnar, R., Hermance, C.E., and Wenograd, J., "A Critical Review of Recent Research on the Mechanism of Ignition of Solid Rocket Propellants," Aeronautical Research Laboratory Report No. 666, Aug. 1963, Princeton University, Princeton, N.J.

23. Price, E. W., Bradley, H. H., Jr., Dehority, G. L., and Ibiricu, M. M., "Theory of Ignition of Solid Propellants," AIAA Journal, Vol. 4, No. 7, July 1966, pp. 1153-1181.

24. Anderson, R., Brown, R. S., and Shannon, L. J., "Critical Comparison of Solid Propellant Ignition Theories," Report TM-34-63-U2, Aug. 1963, United Technology Center, Sunnyvale, Ca.

25. Frazer, J. H. and Hicks, B. L., "Thermal Theory of Ignition of Solid Propellants," The Journal of Physical and Colloid Chemistry, Vol. 54, No. 6, June 1950, pp. 872-876.

26. Hicks, B. L., "Theory of Ignition Considered as a Thermal Reaction," Journal of Chemical Physics, Vol. 22, No. 3, March 1954, pp. 414-429.

27. Baer, A. D., Ryan, N. W., and Salt, D. L., "Propellant Ignition by High Convective Heat Fluxes," ARS Progress in Astronautics and Rocketry; Vol. 1: Solid Propellant Rocket Research, edited by Summerfield, M., Academic Press Inc., New York, 1960, pp. 653-672.

28. Baer, A. D., "Ignition of Composite Rocket Propellants," Ph.D. Thesis, June 1959, Dept. of Chemical Engineering, University of Utah, Salt Lake City, Utah.

29. McCune, C. C., "Solid Propellant Ignition Studies in a Shock Tube," Ph.D. Thesis, Aug. 1961, Dept. of Chemical Engineering, University of Utah, Salt Lake City, Utah.

30. Price, E. W., Bradley, H. H., Jr., Hightower, J. D., and Fleming, R. O., Jr., "Ignition of Solid Propellants," AIAA Preprint No. 64-120, Jan. 1964.

31. Bradley, H. H., Jr., "Theory of Ignition of a Reactive Solid by Constant Energy Flux," Combustion Science and Technology, Vol. 2, No. 1, Aug. 1970, pp. 11-20.

32. McAlevy, R. F., III, Cowan, P. L., and Summerfield, M., "The Mechanism of Ignition of Composite Propellants by Hot Gases," ARS Progress in Astronautics and Rocketry; Vol. 1: Solid Propellant Rocket Research, edited by Summerfield, M., Academic Press Inc., New York, 1960, pp. 623-652.

33. Summerfield, M. and McAlevy, R. F., III, "The Shock Tube as a Tool for Solid Propellant Ignition Research," Jet Propulsion, July 1958, pp. 478-481.

34. Hermance, C. E., Shinnar, R., Wenograd, J., and Summerfield, M., "Solid Propellant Ignition Studies: Ignition of the Reaction Field Adjacent to the Surface of a Solid Propellant," Report No. 674, Dec. 1963, Department of Aeronautical Engineering, Princeton University, Princeton, N.J.

35. Anderson, R., Brown, R. S., and Shannon, L. J., "Ignition Theory of Solid Propellants," AIAA Paper No. 64-156, Jan. 1964.

36. Anderson, R., Brown, R. S., and Shannon, L. J., "Heterogeneous Reactions in Ignition and Combustion of Solid Propellants," AIAA Journal, Vol. 2, No. 1, Jan. 1964, pp. 179-180.

37. Williams, F. A., "Theory of Propellant Ignition by Heterogeneous Reaction," AIAA Journal, Vol. 4, No. 3, Aug. 1966, pp. 1354-1357.

38. Bradley, H. H., Jr. and Williams, F. A., "Theory of Radiant and Hypergolic Ignition of Solid Propellants," Combustion Science and Technology, Vol. 2, No. 1, Aug. 1970, pp. 41-52.

39. Waldman, C. H. and Summerfield, M., "Theory of Propellant Ignition by Heterogeneous Reaction," AIAA Journal, Vol. 7, No. 7, July 1969, pp. 1359-1361.

40. Waldman, C. H., "Theory of Heterogeneous Ignition," Combustion Science and Technology, Vol. 2, Nos. 2 and 3, Nov. 1970, pp. 81-93.

41. Steinz, J. A., Stang, P. L., and Summerfield, M., "The Burning Mechanism of Ammonium Perchlorate-Based Composite Solid Propellants," AIAA Paper No. 68-658, June 1968.

42. Bircumshaw, L. L., and Newman, B. H., "The Thermal Decomposition of Ammonium Perchlorate II. The Kinetics of the Decomposition, the Effect of Particle Size, and Discussion of Results," Proceedings of the Royal Society (London), Vol. 227A, 1955, pp. 228-241.

43. Jacobs, P. W. M., and Pearson, G. S., "Mechanism of the Decomposition of Ammonium Perchlorate," Combustion and Flame, Vol. 13, 1969, pp. 419-430.

44. Pellett, G. L., "Heterogeneous NH_4ClO_4 Decomposition Using Isothermal and Pulsed Laser Mass Spectrometry," AIAA Journal, Vol. 8, No. 9, Sept. 1970, pp. 1560-1566.

45. Jensen, G. E., and Cose, D. A., "Studies in Ignition and Flame Propagation of Solid Propellants," UTC 2117-FR (Final Report), June 1966, United Technology Center, Sunnyvale, Ca.

46. Mullis, B., and Channapragada, R. S., "Heat Transfer Studies of Solid Rocket Igniters," UTC 2096-FR (Final Report), Sept. 1965, United Technology Center, Sunnyvale, Ca.

47. Kilgroe, J. D., "Studies on Ignition and Flame Propagation on Solid Propellants," UTC 2229-FR (Final Report), Nov. 1967, United Technology Center, Sunnyvale, Ca.

48. Beyer, R. B., "Ignition of Solid-Propellant Motors Under Vacuum," AFRPL-TR-65-74(UTC 2079-FR), April 1965, United Technology Center, Sunnyvale, Ca.

49. Shannon, L. J., "Composite Solid Propellant Ignition Mechanisms," AFOSR 68-1114 (UTC 2138-FR), June 1968, United Technology Center, Sunnyvale, Ca.

50. Carlson, L. W., and Seader, J. D., "A Study of the Heat Transfer Characteristics of Hot Gas Ignition," Technical Report No. AFRPL-TR-65-158, June 1965, Air Force Rocket Propulsion Laboratory, Edwards, Ca.

51. Carlson, L. W., and Seader, J. D., "A Study of Heat Transfer Characteristics of Hot-Gas Ignition," ICRPG 2nd Combustion Conference, CPIA Publication No. 105, Vol. 1, May 1966, pp. 563-597.

52. Carlson, L. W., and Seader, J. D., "Heat-Transfer Characteristics of Hot-Gas Ignition," AIAA Journal, Vol. 5, No. 7, July 1967, pp. 1272-1279.

53. Wrubel, J. A., and Carlson, L. W., "Study of Heat Transfer Characteristics of Hot-Gas Igniters," Technical Report AFRPL-TR-67-267, July 1967, Rocketdyne, Canoga Park, Ca.

54. Lovine, R. L., and Fong, L. Y., "Wing VI Minuteman Ignition Study Final Report," Technical Memorandum 249 SRP, April 1964, Aerojet General Corp., Sacramento, Ca.

55. Micheli, P. L., and Linfor, J. J., "The Empirical and Analytical Modeling of the Role of the Propellant in Ignition," Western States Section of the Combustion Institute, Paper 68-34, Oct. 1968.

56. Allan, D. S., and Bastress, E. K., "Heat Transfer Processes during Ignition of Solid Propellant Rockets," AIAA Journal, Vol. 4, No. 1, Jan. 1967, pp. 95-100.

57. Bastress, E. K., and Niessen, W. R., "A Hot-Gas Tunnel for Convective Heating Experiments," Journal of Spacecraft and Rockets, Vol. 5, No. 2, Feb. 1968, pp. 211-213.

58. Atallah, S., Allan, D. S., Comstock, D. F., Jr., and Bakerjian, B. H., "The Ignition of Solid Propellants by Radiative, Convective, and Chemical Heating," AFOSR 69-3091TR (Final Scientific Report), Nov. 1969, Arthur D. Little, Inc., Cambridge, Mass.

59. Bastress, E. K. and Niessen, W. R., "Solid Propellant Ignition by Convective Heating," AFOSR 67-0932 (Final Report), Oct. 1966, Arthur D. Little, Inc., Cambridge, Mass.

60. Kashiwagi, T., McDonald, B. W., Isoda, H., and Summerfield, M., "Ignition of Solid Polymeric Fuels by Hot Oxidizing Gases," AMS Report No. 947, Oct. 1970, Princeton University, Princeton, N.J. Information in this report was summarized in the Thirteenth Symposium (International) on Combustion, 1971.

61. Parker, K. H., "The Ignition Transient in Solid Propellant Rocket Motors," Ph.D. Thesis, Jan. 1966, AMS Department, Princeton University, Princeton, N.J.

62. Parker, K. H., Most, W. J., and Summerfield, M., "The Ignition Transient in Solid Propellant Rocket Motors," AIAA Paper No. 66-666, June 1966.

63. Keller, J. A., "Studies on Ignition of Ammonium Perchlorate-Based Propellants by Convective Heating," Ph.D. Thesis, Aug. 1965, Dept. of Chemical Engineering, University of Utah, Salt Lake City, Utah.

64. Keller, J. A., Baer, A. D., and Ryan, N. W., "Ignition of Ammonium Perchlorate Composite Propellants by Convective Heating," AIAA Journal, Vol. 4, No. 8, Aug. 1966, pp. 1358-1365.

65. Kling, R., Maman, A., and Bruland, J., "La Cinetique de L'allumage des Poudres Composites sous L'influence de Flux de Chaleur Elévés," La Recherche Aérospatiale, No. 103, Nov.-Dec. 1964, pp. 3-10.

66. Richardson, C. P., Ryan, N. W., and Baer, A. D., "Ammonium Perchlorate-Based Propellant Ignition by Low Convective Heat Fluxes," AFOSR 68-1665 (Technical Report), Aug. 1968, Dept. of Chemical Engineering, University of Utah, Salt Lake City, Utah.

67. Baer, A. D. and Ryan, N. W., "Ignition and Combustion of Solid Propellants," AFOSR 69-0349 (Final Report), 1969, Dept. of Chemical Engineering, University of Utah, Salt Lake City, Utah.

68. Keller, J. A. and Ryan, N. W., "Measurement of Heat Flux from Initiators for Solid Propellants," ARS Journal, Vol. 31, No. 10, Oct. 1961, pp. 1375-1379.

69. Mantyla, R. G., Cheng, J. T., Bouck, L. S., Keller, J. A., Baer, A. D., and Ryan, N. W., "Ignition and Combustion of Solid Propellants," AFOSR 67-1901 (Technical Report), 1967, Dept. of Chemical Engineering, University of Utah, Salt Lake City, Utah.

70. Hightower, J. D., "An Investigation of the Effect of Environmental Gases and Pressure on the Ignition of Solid Rocket Propellants," NWC TP 4431, October 1967, Naval Weapons Center, China Lake, Calif.

71. Jensen, G. E., Brown, R. S., Cose, D. A., and Anderson, R., "Ignition and Ignition Propagation in Solid Propellant Motors," AIAA Paper No. 66-677, June 1966.

72. DeSoto, S. and Friedman, H. A., "Flame-Spreading and Ignition Transients in Solid Grain Propellants," AIAA Preprint No. 64-122, Jan. 1964.

73. Parker, K. H., Wenograd, J., and Summerfield, M., "The Ignition Transient in Solid Propellant Rocket Motors," AIAA Preprint No. 64-126, Jan. 1964.

74. Lukenas, L. A., Most, W. J., Stang, P. L., and Summerfield, M., "The Ignitio. Transient in Small Solid Propellant Rocket Motors of Practical Configurations," Aerospace and Mechanical Sciences Report No. 801, July 1967, Princeton University, Princeton, N.J.

75. DiLauro, G. F., Linden, L. H., Most, W. J., and Summerfield, M., "Theoretically Predicted Ignition Transients in Solid Propellant Rocket Motors," Aerospace and Mechanical Sciences Report No. 802, July 1967, Princeton University, Princeton, N.J.

76. Most, W. J., MacDonald, B. W., Stang, P. L., and Summerfield, M., "Thrust Transient Prediction and Control of Solid Rocket Engines," Paper No. 68-33, The Fall Meeting of the Western States Section of the Combustion Institute, Menlo Park, Ca., Oct. 1968.

77. Summerfield, M., Parker, K. H., and Most, W. J., "The Ignition Transient in Solid Propellant Rocket Motors," Aerospace and Mechanical Sciences Report No. 769, Feb. 1966, Princeton University, Princeton, N.J.

78. Most, W. J., MacDonald, B. W., Stang, P. L., and Summerfield, M., "Thrust Transient Prediction and Control of Solid Rocket Engines," Aerospace and Mechanical Sciences, Report No. 837, June 1968, Princeton University, Princeton, N.J.

79. McAlevy, R. F., III, Magee, R. S., and Wrubel, J. A., "Flame Spreading over the Surface of Double Base Propellants," AIAA Preprint No. 64-109, Jan. 1964.

80. McAlevy, R. F., III, Magee, R. S., Wrubel, J. A., and Horowitz, F. A., "Flame Spreading over the Surface of Igniting Solid Rocket Propellants and Propellant Ingredients," AIAA Journal, Vol. 5, No. 2, Feb. 1967, pp. 265-271.

81. Mitchell, R. C., "Flame Spread on Solid Propellant," Ph.D. Thesis, 1963, Dept. of Chemical Engineering, University of Utah, Salt Lake City, Utah.

82. Mitchell, R. C. and Ryan, N. W., "Flame Spread on Solid Propellant," AIAA Preprint No. 64-128, Jan. 1964.

83. Mitchell, R. C. and Ryan, N. W., "Flame Spread on Solid Propellant," Journal of Spacecraft and Rockets, Vol. 2, No. 4, July-Aug. 1965, pp. 610-612.

84. Von Elbe, G., "Theory of Solid Propellant Ignition and Response to Pressure Transients," CPIA Publication 13, Bulletin of the Interagency Solid Propulsion Meeting, (Seattle, Wash.), July 1963.

85. Von Elbe, G., "Solid Propellant Ignition and Response of Combustion to Pressure Transients," AIAA Paper No. 66-668, June 1966.

86. Paul, B. E., Lovine, R. L., and Fong, L. Y., "A Ballistic Explanation of the Ignition Pressure Peak," AIAA Preprint No. 64-121, Jan. 1964.

87. Merkle, C. L., Turk, S. L., and Summerfield, M., "Extinguishment of Solid Propellants by Depressurization: Effects of Propellant Parameters," AIAA Paper No. 69-176, Jan. 1969.

88. Krier, H., T'ien, J. S., Sirignano, W. A., and Summerfield, M., "Nonsteady Burning Phenomena of Solid Propellants: Theory and Experiments," AIAA Journal, Vol. 6, No. 2, Feb. 1968, pp. 178-185.

89. Denison, M. R. and Baum, E., "A Simplified Model of Unstable Burning in Solid Propellants," ARS Journal, Vol. 31, No. 8, Aug. 1961, pp. 1112-1122.

90. McClure, F. T., Hart, R. W., and Bird, J. F., "Solid Propellant Rocket Motors as Acoustic Oscillators," ARS Progress in Astronautics and Rocketry; Vol. 1: Solid Propellant Rocket Research, edited by Summerfield, M., Academic Press Inc., New York, 1960, pp. 295-358.

91. Culick, F. E. C., "A Review of Calculations for Unsteady Burning of a Solid Propellant," AIAA Journal, Vol. 6, No. 12, Dec. 1968, pp. 2241-2255.

92. Zeldovich, Ya. B., "On a Burning Rate Under Nonsteady Pressure," *Zhurnal Prikladnoi Mekhaniki i Technicheskoi Fiziki*, No. 3, Jan.-Feb. 1964, pp. 126-130.

93. Novozhilov, B. V., "Transient Process of the Burning Powders," *Zhurnal Prikladnoi Mekhaniki i Technicheskoi Fiziki*, No. 5, Sept.-Oct. 1962.

94. Novozhilov, B. V., "Non-Steady Burning of Powder Having Variable Surface Temperature," *Zhurnal Prikladnoi Mekhaniki i Technicheskoi Fiziki*, No. 1, Jan.-Feb. 1967, pp. 54-63.

95. Summerfield, M., Caveny, L. H., Battista, R. A., Kubota, N., Gostintsev, Ya. A., and Isoda, H., "Theory of Dynamic Extinguishment of Solid Propellants with Special Reference to Nonsteady Heat Feedback Law," *Journal of Spacecraft and Rockets*, Vol. 8, No. 3, March 1971, pp. 251-258.

96. Turk, S. L., Battistia, R. A., Kuo, K. K., Caveny, L. H., and Summerfield, M., "Dynamic Responses of Solid Rockets During Rapid Pressure Change," *Journal of Spacecraft and Rockets*, Vol. 10, No. 2, Feb. 1973, pp. 137-142.

97. Battista, R. A., Caveny, L. H., and Summerfield, M., "Non-Steady Combustion of Solid Propellants," Aerospace and Mechanical Sciences Report No. 1049, Oct. 1972, AMS Department, Princeton University, Princeton, N. J. (AD 753835).

98. Zucrow, M. J., Osborn, J. R., and Murphy, J. M., "The Erosive Burning of a Homogeneous Solid Propellant," *Chemical Engineering Progress Symposium Series*, Vol. 60, No. 52, 1964, pp. 23-29.

99. Zucrow, M. J., Osborn, J. R., and Murphy, J. M., "An Experimental Investigation of the Erosive Burning Characteristics of a Non-Homogeneous Solid Propellant," *AIAA Journal*, Vol. 3, No. 3, March 1965, pp. 523-525; also AIAA Preprint No. 64-107, Jan. 1964.

100. Osborn, J. R., Murphy, J. M., and Kershner, S. D., "Photographic Measurement of Burning Rates in Solid Propellant Rocket Motors," *The Review of Scientific Instruments*, Vol. 34, No. 3, March 1963, pp. 305-306.

101. Murphy, J. M., "An Experimental and Analytical Investigation of the Erosive Burning Characteristics of a Non-Homogeneous Solid Propellant," Ph.D. Thesis, Jan. 1964, Department of Mechanical Engineering, Purdue University, Lafayette, Ind.

102. Williams, F. A., Barrere, M., and Huang, N. C., Funda
     mental Aspects of Solid Propellant Rockets, Technivi-
     sion Services, Slough, England, 1969, pp. 401-462.

103. Wimpress, R. N., Internal Ballistics of Solid-Fuel
     Rockets, McCraw Hill, New York, 1950, pp. 22-24.

104. Green, L., Jr., "Erosive Burning of Some Composite
     Solid Propellants," Jet Propulsion, Vol. 24,   ,
     Jan.-Feb. 1954, pp. 9-15.

105. Marklund, T. and Lake, A., "Experimental Investiga-
     tion of Propellant Erosion," ARS Journal, Vol. 30,
     No. 2, Feb. 1960, pp. 173-178.

106. Kreidler, J. W., "Erosive Burning - New Experimental
     Techniques and Methods of Analysis," AIAA Preprint
     No. 64-155, Jan. 1964.

107. Peretz, A., "Experimental Investigation of the Erosive
     Burning of Solid-Fropellant Grains with Variable Port
     Area," AIAA Journal, Vol. 6, No. 5, May 1968, pp. 910-
     912.

108. Dickinson, L. A., Jackson, E., and Odgers, A. L.,
     "Erosive Burning of Polyurethane Propellants in
     Rocket Engines," Eighth Symposium (International) on
     Combustion, The Williams and Wilkins Co., Baltimore,
     Md., 1962, pp. 754-759.

109. Vandenkerckhove, J. and Jaumotte, A., "Remarks on the
     Burning Mechanism and Erosive Burning of Ammonium
     Perchlorate Propellants," Fighth Symposium (Interna-
     tional) on Combustion, The Williams and Wilkins Co.,
     Baltimore, Md., 1962, pp. 689-692.

110. Dickinson, L. A. and Jackson, F., "Combustion in Solid
     Propellant Rocket Engines," Fifth AGARD Combustion and
     Propulsion Colloquium, Pergamon Press, New York,
     1963, pp. 531-550.

111. Lawrence, W. J., Matthews, D. R., and Deverall, L. I.,
     "The Experimental and Theoretical Comparison of the
     Erosive Burning Characteristics of Composite Propel-
     lants," AIAA Paper No. 68-531.

112. Lenoir, J. M. and Robillard, G., "A Mathematical Model
     to Predict the Effects of Erosive Burning in Solid
     Propellant Rockets," Sixth Symposium (International)
     on Combustion, Reinhold, New York, 1957, pp. 663-667.

113. Vandenkerckhove, J. A., "Theoretical Investigation of
     Erosive Burning of Solid Propellants," ARDC, USAF TN
     No. 2 (Contract AF 61(052)-354), July 1961.

114. Tsuji, H., "An Aerothermochemical Analysis of Erosive Burning of Solid Propellant," Ninth Symposium (International) on Combustion, The Williams and Wilkins Co., Baltimore, 1963, pp. 384-393.

115. Miller, E., "Erosive Burning of Composite Solid Propellants," Combustion and Flame, Vol. X, Dec. 1966, pp. 330-336.

116. Felix, B. R. and McBride, N. M., "Development of the Algol III Solid Rocket Motor for Scout," ASE Paper No. 710765, presented at the NASEM Meeting, Los Angeles, Sept. 1971.

117. Mickley, H. S., Ross, R. C., Squyers, A. L., and Stewart, W. E., "Heat, Mass, and Momentum Transfer for Flow over a Flat Plate with Blowing or Suction," TN 3208, July 1954, NACA.

118. Rubesin, M. W., Pappas, C. C. and Okuno, A. F., "The Effect of Fluid Injection on the Compressible Turbulent Boundary Layer-Preliminary Tests on Transpiration Cooling of a Flat Plate at M = 2.7 With Air as the Injected Gas," RM A55I19, Dec. 1955, NACA.

119. Korpi, K. J., "Survey of Ignition Literature," Report No. 1097 (Special), July 1956, Aerojet-General Corp., Azusa, Ca.

120. Anon., "Ignition System for Composite Solid Propellant," Report No. L255-1, Nov. 1955, Aerojet-C   .al Corp., Azusa, Ca.

121. Barett, D. H., "Solid Rocket Motor Igniters   ASA Monograph SP-8051, March 1971.

122. Lowry, E. M., "Solid Propellant Igniter Design Handbook," NAVWEPS 8015, April 1961, Bermite Powder Co., Saugus, Ca.

123. Von Elbe, G. and Lewis, B., "Minimum Ignition Energy of Propellants: Discussion and Preliminary Data," Bulletin of First Symposium on Solid Propellant Ignition, Sept. 1953.

124. Scheier, W., "Pressure Transients for Boron-Potassium Nitrate Igniters in Inert, Vented Chambers," Report TR-32-33, Sept. 1960, JPL, Ca.

125. Isom, K. B., "Heat Transfer from Pyrotechnic Igniters," 2nd ICRPG Combustion Conference, CPIA Publication No. 105, Vol. I, May 1966, pp. 605-615.

126. Cohen, N. S., and Lovine, R. L., "Fulfillment of Solid Propellant Ignition Requirements by Pyrogen Igniters," 4th ICRPG Combustion Conference, CPIA Publication No. 162, Vol. I, Dec. 1967, pp. 449-457.

127. Robertson, W. E., "Igniter Material Considerations and Applications," AIAA Paper No. 72-1195, Nov.-Dec. 1972.

128. Priary, J. J., "Advanced Ignition System for Solid Propellant Rocket Motors," AIAA Journal, Vol. 31, No. 7, July 1961, pp. 1029-1031.

129. Brown, R. S., "Investigation of Fundamental Hypergolic Ignition Phenomena Under Dynamic Flow Environments," Report UTC-2024 FR, Feb. 1965, United Technology Center, Sunnyvale, Ca.

130. Peleg, I. and Manheimer-Timnat, Y., "A Study of Solid Propellant Rocket Motor Ignition," Israel Journal of Technology, Vol. 6, No. 1-2, Feb. 1968, pp. 32-45.

131. Lucy, M. H., "Spin Acceleration Effects on Some Full-Scale Rocket Motors," Journal of Spacecraft and Rockets, Vol. 5, No. 2, Feb. 1968, pp. 179-185.

132. Northam, G. B. and Lucy, M. H., "On the Effects of Acceleration upon Solid Rocket Performance," AIAA Paper No. 68-530, June 1968.

133. Bahor, L. R., "Performance of the Aerojet-General Corp. ALCOR-1B Solid Propellant Rocket Motor under the Combined Effects of Rotational Spin and Simulated Altitude," AEDC-TR-66-186, Oct. 1966, Arnold EDC, Tullahoma, Tenn.

134. Broddner, S., "Effects of High Spin on the Internal Ballistics of a Solid Propellant Motor," Astronautica Acta, Vol. 15, No. 4, May 1970, pp. 191-197.

135. Adams, D. M., "Igniter Performance in Solid Propellant Rocket Motors," AIAA Paper No. 66-680, June 1966.

136. Sharn, C. F., et al, "Solid-Propellant Rocket Ignition Research (Final Report)," NOLTR 64-107, Sept. 1964, NOL, Silver Spring, Md.

137. Baker, D. L., "Method for Predicting Chamber Pressure Transients During the Ignition of Solid Propellant Rocket Motors," UTC TM-14-62-UZ, March 1962, United Technology Center, Sunnyvale, Ca.

138. Falkner, C. E. and Kilgroe, J. D., "Ignition Models-Solid Propellant Rocket Motors," Western States Section of the Combustion Institute, Paper No. 68-35, Oct. 1968.

139. Anon., "Final Report Design Study of Solid Propellant Configurations," Control No. U-A-61-28A, July 1961, Thiokol Chemical Corp., Re stone Division, Alabama.

140. Huggett, C., Bartley, C. E., and Mills, M. M., "Solid Propellant Rockets," Princeton Aeronautical Paperbacks, No. 2, Princeton University Press, Princeton, N.J.

141. Beckstead, M. W., Derr, R. L., and Price, C. F., "A Model of Composite Solid-Propellant Combustion Based on Multiple Flames," AIAA Journal, Vol. 8, No 12, Dec. 1970, pp. 2200-2207.

142. Willoughby, D. A., "Application of Turbulent, Compressible Boundary Layer Concepts to the Interior Ballistics of Rocket Motors," Technical Report S-266, Sept. 1970, Redstone Research Laboratories, Rohm and Haas Co., Huntsville, Ala.

143. Patankar, S. V. and Spalding, D.B., Heat and Mass Transfer in Boundary Layers; A General Calculation Procedure, 2nd ed., International Textbook Co., London, 1970.

144. Hottel, H. C. and Sarofim, A. F., "Gas Emissivities and Absorptivities," Radiative Transfer, 1st ed., Mc-Graw-Hill, New York, 1967, pp. 199-235.

145. Caveny, L. H. and Summerfield, M., "A Feasibility Study of Command Control of Solid Propellant Burning Rate," Aerospace and Mechanical Sciences Report No. 893, Feb. 1970, AMS Department, Princeton University, Princeton, N.J.

146. Chao, G. T. Y., Leslie, J. C., and Mancus, H. V., "A Direct Measuring Radiation Calorimeter for Determining Propellant Gas Emissivity," Journal of Spacecraft and Rockets, Vol. 3, No. 6, June 1966, pp. 928-930.

147. Love, E. S., Grigsby, C. E., Lee, L. P., and Woodling, M. J., "Experimental and Theoretical Studies of Axisymmetric Free Jets," TR R-6, 1959, NASA.

148. Shapiro, A. H., The Dynamics and Thermodynamics of Compressible Fluid Flow, Vol. II, The Ronald Press Co., New York, 1954.

149. Kutateladze, S. S. and Borishanskii, A Concise Encyclopedia of Heat Transfer, 1st ed., Pergamon Press, Oxford, 1966, pp. 109-114.

150. Schlichting, H., "Turbulent Flow Through Pipes," Boundary Layer Theory, 6th ed., McGraw-Hill, New York, 1968.

151. Naumann, A., "Druckverlust in Rohren nichtkreisförmigen Querschnittes bei hohen Geschwindigkeiten," ZAMM, Vol. 36, special issue, 1956, p. 25.

152. Iverson, H. W., "Variation of the Point Unit Thermal Conductance on the Entrance to Tubes for a Fluid Flowing Turbulently," M.S. Thesis, University of California at Berkeley, 1943.

153. Cholette, A., "Heat Transfer Local and Average Coefficients for Air Flowing Inside Tubes," Chemical Engineering Progress, Vol. 44, No. 1, Jan. 1948, pp. 81-88.

154. Humble, L. V., Lowdermilk, W. H., and Desmon, L. G., "Measurements of Average Heat-Transfer and Friction Coefficients for Subsonic Flow of Air in Smooth Tubes at High Surface and Fluid Temperatures," NACA Rept. 1020, 1951.

155. Davey, T. B., "Entrance Region Heat Transfer Coefficients," Heat-Transfer-Houston, Chemical Engineering Progress Symposium Series, published by AICE, Vol. 59, No. 41, 1963, pp. 47-51.

156. Holman, J. P., Heat Transfer, 2nd ed., McGraw Hill, New York, 1968, pp. 157-186.

157. Schack, A., Industrial Heat Transfer, J. Wiley & Sons, New York, 1965, pp. 127-140.

158. Cohen, N. S., Derr, R. L., and Price, C. F., "Study of Ignition and Extinguishment in Multiple Stop-Restart Duty Cycles," 8th JANNAF Combustion Meeting, Vol. II (CPIA Publication 220), Nov. 1971.

159. Kreith, F., Principles of Heat Transfer, 1st ed., International Textbook Co., Scranton, Pa., 1958, pp. 331-361.

160. McAdams, W. H., Heat Transmission, 3rd ed., McGraw Hill, New York, 1954, pp. 205-241.

161. Bartz, D. R., "A Simple Equation for Rapid Estimation of Rocket Nozzle Convective Heat Transfer Coefficients," Jet Propulsion, Vol. 27, No. 1, Jan. 1957, pp. 49-51.

162. Knuth, E. L., "Forced-Convection Heat Transfers with Time-Dependent Surface Temperatures," AIAA Journal, Vol. 1, No. 5, May 1963, pp. 1227-1229.

163. Sparrow, E. M. and Siegel, R., "Unsteady Turbulent Heat Transfer in Tubes," Transactions of ASME, Journal of Heat Transfer, Aug. 1960, pp. 170-180.

164. Eckert, E. R. G. and Drake, R. M., Jr., Heat and Mass Transfer, 2nd ed., McGraw Hill, New York, 1959, pp. 213-214.

165. Cope, W. F., "The Friction and Heat Transmission Co-efficients of Rough Pipes," Proceedings of the Institution of Mechanical Engineers, Vol. 145, 1941, pp. 99-105.

166. Nunner, W., "Heat Transfer and Pressure Drop in Rough Tubes," VDI Forshungsheft, 455, Ser. B, Vol. 22, pp. 5-39; A.E.R.E. Lib/Transl. 786, 1958.

167. Dipprey, D. F. and Sabersky, R. H., "Heat and Momentum Transfer in Smooth and Rough Tubes at Various Prandtl Numbers," International Journal of Heat and Mass Transfer, Vol. 6, May 1963, pp. 329-353.

168. Owen, P. R. and Thomson, W. R., "Heat Transfer Across Rough Surfaces," Journal of Fluid Mechanics, Vol. 15, 1963, pp. 321-334.

169. Gowen, R. A. and Smith, J. W., "Turbulent Heat Transfer from Smooth and Rough Surfaces," International Journal of Heat and Mass Transfer, Vol. 11, Nov. 1968, pp. 1657-1673.

170. Nestler, D. E., "Compressible Turbulent Boundary-Layer Heat Transfer to Rough Surfaces," AIAA Journal, Vol. 9, No. 9, Sept. 1971, pp. 1799-1803.

171. Mickley, H. S. and Davis, R. S., "Momentum Transfer for Flow over a Flat Plate with Blowing," TN 4017, Nov. 1957, NACA.

172. Butensky, M. S., "The Transpired Turbulent Boundary Layer on a Flat Plate," Sc.D. Thesis, Chemical Engineering Dept., MIT, 1962.

173. Smith, K. A., "The Transpired Turbulent Boundary Layer," Sc.D. Thesis, Chemical Engineering Dept., MIT, Mass., 1962.

174. Mickley, H. S., Smith, K. A., and Fraser, M. D., "Velocity Defect Laws for Transpired Turbulent Boundary Layers," AIAA Journal, Vol. 3, No. 4, April 1965, pp. 787-788.

175. Thielbahr, W. H., Kays, W. M., and Moffat, R. J., "The Turbulent Boundary Layer: Experimental Heat Transfer with Blowing, Suction, and Favorable Pressure Gradient," Report No. HMT-5, Department of Mechanical Engineering, Stanford University, Stanford, Ca., April 1969.

176. Whitten, D. G., Moffat, R. J., and Kays, W. M., "Heat Transfer to a Turbulent Boundary Layer with Non-Uniform Blowing and Surface Temperature," Report No. HMT-8, Department of Mechanical Engineering, Stanford University, Stanford, Ca., Sept. 1969.

177. Kearney, D. W., Moffat, R. J., and Kays, W. M., "The Turbulent Boundary Layer: Experimental Heat Transfer with Strong Favorable Pressure Gradients and Blowing," Report No. HMT-12, Department of Mechanical Engineering, Stanford University, Stanford, Ca., April 1970.

178. Marxman, G. A. and Woolridge, C. E., "Research on the Combustion Mechanism of Hybrid Rockets," Advances in Tactical Rocket Propulsion, AGARG Conference Proceedings No. 1, Technivision Services, Maidenhead, England, Aug. 1968, pp. 423-477.

179. Lees, L., "Convective Heat Transfer with Mass Addition and Chemical Reactions," Combustion and Propulsion, Third AGARD Colloquium, Pergamon Press, New York, 1958, pp. 451-498.

180. Svehla, R. A., "Estimated Viscosities and Thermal Conductivities of Gases at High Temperatures," NASA TR R-132, 1962.

181. Bartz, D. R., "Survey of the Relationship Between Theory and Experiment for Convective Heat Transfer from Rocket Combustion Gases," Advances in Tactical Rocket Propulsion, AGARD Conference Proceedings No. 1, Technivision Services, Maidenhead, England, Aug. 1968, pp. 291-381.

182. Hilsenrath, J., et al, "Tables of Thermal Properties of Gases," U.S. Department of Commerce, NBS Circular 564, Nov. 1955.

183. Colebrook, C. F., "Turbulent Flow in Pipes with Particular Reference to the Transition Region between the Smooth and Rough Pipe Laws," Journal of the Institution of Civil Engineers, Vol. 11, 1938-39, pp. 133-156.

184. Streeter, V. L., Fluid Mechanics, 3rd ed., McGraw-Hill, New York, 1962, pp. 213-222.

185. Shapiro, A. H. and Smith, R. D., "Friction Coefficients in the Inlet Length of Smooth Round Tubes," NACA TN No. 1785, Nov. 1948.

186. Carslaw, H. S. and Jaeger, J. C., Conduction of Heat in Solids, 2nd ed., Oxford University Press, London, 1959.

187. Goodman, T. R., "The Heating of Slabs with Arbitrary Heat Inputs," Journal of the Aerospace Sciences, Vol. 26, March 1959, pp. 187-188.

188. Goodman, T. R., "Application of Integral Methods to Transient Nonlinear Heat Transfer," Advances in Heat Transfer, Vol. 1, 1964, Academic Press, New York, pp. 51-122.

189. Courant, R., and Hilbert, D., Methods of Mathematical Physics, Vol. 2, Interscience Publishers, Inc., New York, July 1966, pp. 407-550.

190. Kuo, K. K., "Theory of Flame Front Propagation in Porous Propellant Charges under Confinement," Ph.D. Thesis, Aug. 1971, AMS Department, Princeton University, Princeton, N.J.

191. Richtmyer, R. D. and Morton, K. W., Difference Methods for Initial-Value Problems, Interscience Publishers, New York, 1967.

192. Salvadori, M. G. and Baron, M. L., Numerical Methods in Engineering, Prentice Hall, Inc., Englewood Cliffs, N.J., 1961.

193. Vichnevetsky, R., "Treatment of Non-linear Terms in Hyperbolic Equations," TR 70-23, Sept. 1970, Electronic Associates, Inc., Princeton, N.J.

194. Kuo, K. K., Vichnevetsky, R., and Summerfield, M., "Generation of an Accelerated Flame Front in a Porous Propellant," AIAA Paper No. 71-210, Jan. 1971.

195. Isaacson, E. and Keller, H. B., Analysis of Numerical Methods, Wiley, New York, 1966, pp. 58-61.

196. Johnson, R. C., "Real-Gas Effects in Critical Flow through Nozzles and Tabulated Thermodynamic Properties," TN D-2565, Jan. 1965, NASA.

197. Din F., ed., Thermodynamic Functions of Gases, Vol. 3: Methane, Nitrogen, Ethane, Butterworths, London, 1961, pp. 22-71.

198. Steffensen, R. J., Agnew, J. T., and Olsen, R. A., "Combustion of Hydrocarbons - Property Tables," Engineering Extension Series No. 122, May 1966, Purdue University, Lafayette, Ind.

199. Jones, H. B., "Transient Pressure Transducer Design and Evaluation," Aeronautical Engineering Report No. 595b, Feb. 1962, Princeton University, Princeton, N.J.

200. Layton, J. P., Knauer, R. C., and Thomas, J. P., "Summary Technical Report on Transient Pressure Measuring Methods Research," Aeronautical Engineering Report No. 595i, Dec. 1963, Princeton University, Princeton, N.J.

201. Thomas, J. P. and Layton, J. P., "Summary Technical Report on Transient Pressure Measuring Methods Research," Aeronautical Engineering Report No. 595p, Nov. 1965, Princeton University, Princeton, N.J.

202. Thomas, J. P. and Layton, J. P., "Final Summary Technical Report on Transient Pressure Measuring Methods Research," AMS Report No. 595t, March 1967, Princeton University, Princeton, N.J.

203. Durbin, E. J., Princeton University, private communication.

204. Iberall, A. S., "Attenuation of Oscillatory Pressures in Instrument Lines," Journal of Research of the NBS, Vol. 45, July 1950, pp. 85-108.

205. Beckwith, T. C. and Buck, N. L., "Mechanical Measurements," 1st ed., Addison-Wesley, Reading, Mass., 1961.

206. Morris, S. O., Peretz, A., and Poli, T. J., "Instrumentation Manual, Solid-Propellant Test Cell, S.P. Laboratories," 1972. AMS Department, Princeton University, Princeton, New Jersey.

207. Strand, L. D. and Gerber, W. O., "A Study of Solid-Propellant-Rocket-Motor Command Termination by Water Injection," AIAA Paper No. 70-640, June 1970.

208. Beyer, R. B. and Fishman, N., "Solid Propellant Ignition Studies with High Flux Radiant Energy as a Thermal Source," ARS Progress in Astronautics and Rocketry; Vol. 1: Solid Propellant Rocket Research, edited by Summerfield, M., Academic Press Inc., New York, 1960, pp. 673-692.

209. Baer, A. D. and Ryan, N. W., "Ignition and Combustion of Solid Propellants," AFOSR 68-1858 (Final Report), 1968, Dept. of Chemical Engineering, University of Utah, Salt Lake City, Utah.

210. Price, E. W., "One-Dimensional, Steady Flow With Mass Addition and the Effect of Combustion Chamber Flow on Rocket Thrust," Jet Propulsion, Vol. 25, No. 2, February 1955, pp. 61-66, 78.

211. Vidal, R. J., "Model Instrumentation Techniques for Heat Transfer and Force Measurements in a Hypersonic Wind Tunnel," Rept. AD-917-A-1, February 1956, Cornell Aeronautical Lab., Inc., Cornell University, Buffalo, N.Y.

212. Knauss, D. T., "Techniques for Fabricating Fast Response Heat Transfer Gages," BRL TN 1629, September 1966, Ballistic Research Laboratories, Aberdeen, Md.

213. Cook, W. J., "Determination of Heat-Transfer Rates from Transient Surface Temperature Measurements," AIAA Journal, Vol. 8, No. 7, July 1970, pp. 1366-1368.

214. Shelton, S. V., "A Technique for Measurement of Solid Propellant Burning Rates During Rapid Pressure Transients," 4th ICRPG Combustion Conference (CPIA Publication No. 162), Vol. 1, December 1967, pp. 361-373.

215. Strand, L. D., Schultz, A. L. and Reedy, G. K., "Determination of Solid Propellant Transient Regression Rates Using a Microwave Doppler Shift Technique," AIAA Paper No. 72-1118, November-December 1972.

216. Caveny, L. H. and Summerfield, M., "Solid Propellant Micromotors and Impulsive Thrusters," SAE Paper No. 71-766, September 1971.

Table 1

Baseline Values

<u>Propellant properties:</u>

    Composition: 20% PBAA-EPON 828
                       80% AP (30% 15 micron & 70% 180 micron)

$r_{0@p=68\ atm}$ = 0.804 cm/sec = 0.32 in/sec

$n = 0.4$

$\lambda_{pr} = 0.9 \times 10^{-3}$ cal/cm-sec-°K

$\rho_{pr} = 1.6$ g/cm^3

$\alpha_{pr} = 0.1875 \times 10^{-2}$ cm^2/sec

$W = 22.01$ g/g-mole

$\gamma = 1.24$

$c_p = 0.4665$ cal/g-°K

$R = 3852$ gf-cm/g-°K

$T_{pi} = 298$°K

$T_{ps,ig} = 700$°K

$T_f = 2225$°K

$k = 5.72$ cm^3-°K/cal

$\beta = 105$

$\varepsilon_s = 0.001$ cm

<u>Motor parameters:</u>

$x_p = 6.2$ cm $x_E = 62.7$ cm

$b = 5.08$ cm $d_{h,i} = 1.02$ cm

$A_{p,i} = 1.61$ cm^2 $P_{w,i} = 6.35$ cm

$L^* = 62.7\ (A_p/A_t)$ cm

Table 2

Summary of the Experimental Study

A_p/A_t	m_{ig} g/sec	t_{ig} msec	t_{dp} msec	t_{fs} msec	t_{prm} msec	t_{pm} msec	$p_{1,fs}$ kgf/cm²	$p_{1,max}$ kgf/cm²	$p_{3,max}$ kgf/cm²	$p_{5,max}$ kgf/cm²	$\dfrac{p_{3,max}}{p_{1,max}}$	$\dfrac{p_{5,max}}{p_{1,max}}$	$(\partial p/\partial t)_{1,max}$ kgf/cm²-sec	$(\partial p/\partial t)_{3,max}$ kgf/cm²-sec	$(\partial p/\partial t)_{5,max}$ kgf/cm²-sec	r_{pi} cm/sec
1.06	15.1	–	67.0	–	74.5	87.0	–	37.2	35.8	24.0	0.963	0.645	3,010	3,160	1,960	–
"	17.2	–	55.0	–	64.5	78.5	–	37.0	35.8	24.1	0.968	0.652	2,960	2,980	1,860	–
"	17.9	–	49.5	–	59.0	71.5	–	39.8	38.4	25.7	0.965	0.645	3,160	3,330	2,140	–
"	19.5	–	44.0	–	53.5	67.5	–	37.3	36.2	23.8	0.970	0.638	3,130	3,200	1,950	–
"	21.5	–	33.0	–	40.0	54.0	–	40.6	39.1	26.1	0.963	0.643	3,380	3,780	2,450	–
1.20	8.5	–	104.5	–	113.0	124.0	–	40.2	–	30.0	–	0.753	4,160	–	2,520	–
"	11.5	54.5	64.0	87.3	88.0	99.5	19.2	38.6	36.9	28.8	0.956	0.746	3,590	3,720	2,330	450
"	12.9	44.0	57.0	–	65.0	76.0	–	41.6	40.5	30.6	0.973	0.736	3,900	3,950	2,700	–
"	15.0	36.0	52.0	59.5	60.0	72.0	19.0	43.2	42.2	31.3	0.978	0.724	4,030	4,350	2,750	750
" *	15.0	–	61.0	–	69.0	79.0	–	42.5	41.6	31.3	0.977	0.736	3,960	4,230	2,900	–
" **	15.0	35.5	48.0	–	56.5	71.0	–	25.7	23.4	17.8	0.911	0.693	2,500	2,300	1,550	–
"	19.5	23.8	42.5	–	49.5	61.5	–	44.2	43.0	32.0	0.972	0.723	4,230	4,300	2,980	–
"	21.5	21.3	38.0	–	44.5	57.0	–	45.8	44.8	33.7	0.978	0.736	4,440	4,480	3,020	–

*The adiabatic flame temperature of the igniter gas was 3360°K
**The length of the propellant slabs was 33.0 cm

Table 2 (Continued)

A_p/A_{tg}	m_{ig} tg/sec	t_{ig} msec	t_{dp} msec	t_{fs} msec	t_{prm} msec	t_{pm} msec	$p_{1,fs}$ kgf/cm²	$p_{1,max}$ kgf/cm²	$p_{3,max}$ kgf/cm²	$p_{5,max}$ kgf/cm²	$\dfrac{p_{3,max}}{p_{1,max}}$	$\dfrac{p_{5,max}}{p_{1,max}}$	$(\partial p/\partial t)_{1,max}$ kgf/cm²-sec	$(\partial p/\partial t)_{3,max}$ kgf/cm²-sec	$(\partial p/\partial t)_{5,max}$ kgf/cm²-sec	r_{pi} cm/sec
1.5	11.5	–	52.0	–	69.5	90.5	–	52.3	–	44.2	–	0.845	4,210	–	3,330	–
"	12.8	–	46.0	–	61.5	84.0	–	51.7	–	44.2	–	0.855	4,280	–	3,230	–
"	13.5	–	44.5	–	52.5	77.5	–	53.1	52.2	44.5	0.983	0.838	4,680	4,830	3,950	–
"	17.9	28.0	39.5	46.5	45.5	66.0	24.0	53.8	52.7	44.4	0.980	0.826	5,010	5,150	4,380	830
"	21.5	22.0	30.5	–	39.5	57.5	–	55.8	54.8	46.6	0.982	0.835	5,190	5,240	4,350	–
2.0	10.2	–	70.0	–	79.5	104.5	–	71.7	–	65.7	–	0.916	5,400	–	4,020	–
"	11.5	53.5	68.0	–	75.0	95.0	–	70.5	–	63.3	–	0.898	5,600	–	4,580	–
"	13.4	43.5	50.0	–	57.0	82.0	–	74.1	73.5	66.5	0.992	0.897	6,400	6,500	5,200	–
"	15.8	–	38.0	–	47.0	74.0	–	74.7	73.7	66.9	0.987	0.895	6,570	6,750	5,480	–
"	19.5	25.5	35.5	42.0	42.5	66.0	25.0	75.6	74.3	67.3	0.984	0.892	6,830	6,980	5,710	920

Table 3

Summary of the Theoretical parametric study about the Datum Case

A_p/A_{tg}	$\dot{m}_{ig}$ tg/sec	T_{ig} K	$a_h \times 10^3$	t_{ig} msec	t_{dp} msec	t_{fs} msec	t_{prm} msec	t_{pm} msec	$p_{1,fs}$ kgf/cm²	$p_{1,max}$ kgf/cm²	$p_{3,max}$ kgf/cm²	$p_{5,max}$ kgf/cm²	$p_{E,max}$ kgf/cm²	$p_{as,max}$ kgf/cm²	$\dfrac{p_{3,max}}{p_{1,max}}$	$\dfrac{p_{5,max}}{p_{1,max}}$	$\dfrac{p_{E,max}}{p_{1,max}}$	$\dfrac{p_{as,max}}{p_{1,max}}$	$(\partial p/\partial t)_{1,max}$ kgf/cm²-sec	$(\partial p/\partial t)_{3,max}$ kgf/cm²-sec	$(\partial p/\partial t)_{5,max}$ kgf/cm²-sec	$r_{p,i}$ cm/sec	$\dfrac{m_{u,max}}{m_{ig}}$
1.06	11.5	2430	1.56	57.5	82.0	92.0	92.0	104.0	18.2	34.8	32.9	21.9	19.9	28.1	0.945	0.629	0.573	0.807	7,200	6,900	4,560	240	0.038
"	12.9	:	:	49.5	69.0	79.5	79.5	91.0	18.3	35.3	33.3	22.2	20.2	28.5	0.943	0.628	0.572	0.807	7,350	7,200	4,700	300	0.042
"	17.2	:	:	34.5	46.5	55.5	55.5	67.0	19.0	36.7	34.6	23.1	20.9	29.6	0.943	0.629	0.570	0.807	7,760	7,300	4,900	460	0.054
"	19.5	:	:	30.0	39.0	49.0	49.0	60.0	19.3	37.3	35.3	23.6	21.4	30.3	0.942	0.629	0.571	0.808	8,020	7,600	5,100	640	0.059
1.20	11.5	2410	1.56	53.5	77.5	85.5	86.0	99.0	18.1	40.2	38.3	28.7	27.4	33.9	0.953	0.714	0.681	0.843	7,520	7,500	4,920	250	0.036
*	15.0	:	:	37.5	52.5	59.5	59.5	73.5	17.5	41.9	40.1	30.1	28.8	35.4	0.956	0.718	0.687	0.844	7,970	8,100	4,820	420	0.045
"	"	2650	:	28.5	40.5	47.5	47.5	61.5	17.3	41.9	40.0	30.0	28.7	35.1	0.954	0.715	0.685	0.838	7,870	8,080	4,880	510	0.045
"	"	2410	1.52	39.0	54.5	62.0	62.0	75.5	17.5	41.5	39.7	29.8	28.5	35.0	0.956	0.718	0.687	0.843	7,840	7,900	5,040	390	0.045
"	"	"	1.60	36.5	51.0	58.0	58.0	72.0	18.0	42.1	40.2	30.2	28.9	35.4	0.956	0.717	0.687	0.841	8,070	8,080	5,100	420	0.045
**	"	"	1.705	36.5	51.0	58.0	58.0	72.0	17.0	40.4	38.5	28.8	27.6	34.1	0.954	0.713	0.683	0.844	7,600	7,820	4,760	420	0.046
"	"	"	1.56	32.5	46.0	52.5	52.5	66.5	18.0	42.7	40.7	30.5	29.1	36.1	0.954	0.714	0.682	0.845	8,250	8,250	5,310	460	0.043
+	"	"	"	35.5	53.5	57.0	57.0	71.5	18.3	42.4	40.4	30.4	28.4	35.3	0.952	0.717	0.670	0.833	7,740	7,920	4,830	420	0.045
++	"	"	"	30.5	43.0	49.0	49.0	62.5	18.9	41.7	39.7	29.7	28.4	35.3	0.951	0.712	0.681	0.846	8,740	8,760	5,140	510	0.044
"	19.5	"	"	26.0	37.0	43.5	44.0	57.0	17.4	42.9	40.9	30.5	29.2	36.1	0.954	0.712	0.681	0.842	8,550	8,620	4,940	560	0.056
1.5	11.5	2340	1.56	48.5	72.0	77.5	77.5	94.5	23.6	53.1	51.5	43.3	42.5	47.7	0.970	0.815	0.801	0.899	8,150	8,160	6,340	250	0.032
§	"	"	"	51.5	77.5	82.0	82.0	100.5	25.2	52.5	50.8	42.8	42.4	47.6	0.968	0.815	0.807	0.906	8,180	8,360	6,100	250	0.032
"	17.9	"	"	27.0	39.0	45.0	45.0	60.5	22.7	55.4	53.6	45.0	44.1	49.6	0.967	0.813	0.797	0.896	9,500	9,640	7,220	560	0.047
"	19.5	"	"	24.5	34.0	38.5	38.5	55.5	20.2	56.7	54.8	46.3	45.3	50.9	0.966	0.812	0.798	0.897	9,840	9,900	7,520	610	0.050
"	15.0	2410	1.43	36.0	51.0	57.0	57.0	73.5	21.8	53.6	51.9	43.7	42.9	48.2	0.968	0.816	0.800	0.899	9,350	9,150	7,080	420	0.041
2.0	11.5	2150	1.56	49.5	72.5	76.0	76.0	93.0	22.7	74.8	73.4	66.6	66.0	70.2	0.981	0.892	0.883	0.938	9,810	9,910	8,800	250	0.030
"	15.8	"	"	32.5	48.0	51.0	51.0	72.0	21.2	78.2	76.7	69.8	69.0	73.3	0.981	0.892	0.862	0.937	10,900	11,300	9,260	390	0.037
"	19.5	"	"	24.0	35.5	38.5	39.0	60.5	22.8	81.3	80.0	73.1	72.3	76.7	0.982	0.897	0.887	0.941	11,800	11,600	9,780	640	0.044

*Datum Case
**In this calculation $\beta = 115$
†In this calculation $\epsilon_s/d_h = 10^{-2}$
‡In this calculation $\lambda_{pr} = 0.72 \times 10^{-3}$ cal/cm-sec-°l.
§The friction coefficient used in this calculation was 1/10 of that calculated from Eq. (III-33)

Table 4

Typical Mach and Reynolds Numbers (based on diameter) during the different stages of the transient for the four port-to-throat area ratios tested and m_{ig} = 11.5 g/sec

$A_p A_t$	Period	Fore-end Mach No.	Aft-end Mach No.	Fore-end Reynolds No.	Aft-end Reynolds No.
1.06	induction	0.58	0.42	11,500	17,000
"	flame-spreading	0.080	0.76	10,000	100,000
"	chamber filling	0.016	0.76	10,000	320,000
"	peak pressure	0.017	0.76	10,900	350,000
1.2	induction	0.55	0.39	11,500	17,500
"	flame spreading	0.090	0.60	10,000	100,000
"	chamber filling	0.015	0.60	10,000	330,000
"	peak pressure	0.016	0.60	11,000	360,000
1.5	induction	0.52	0.35	11,700	19,000
"	flame spreading	0.090	0.44	10,000	80,000
"	chamber filling	0.010	0.44	10,000	360,000
"	peak pressure	0.011	0.44	11,100	400,000
2.0	induction	0.45	0.28	12,000	21,000
"	flame spreading	0.060	0.31	10,000	50,000
"	chamber filling	0.009	0.31	12,000	400,000
"	peak pressure	0.009	0.31	16,000	450,000
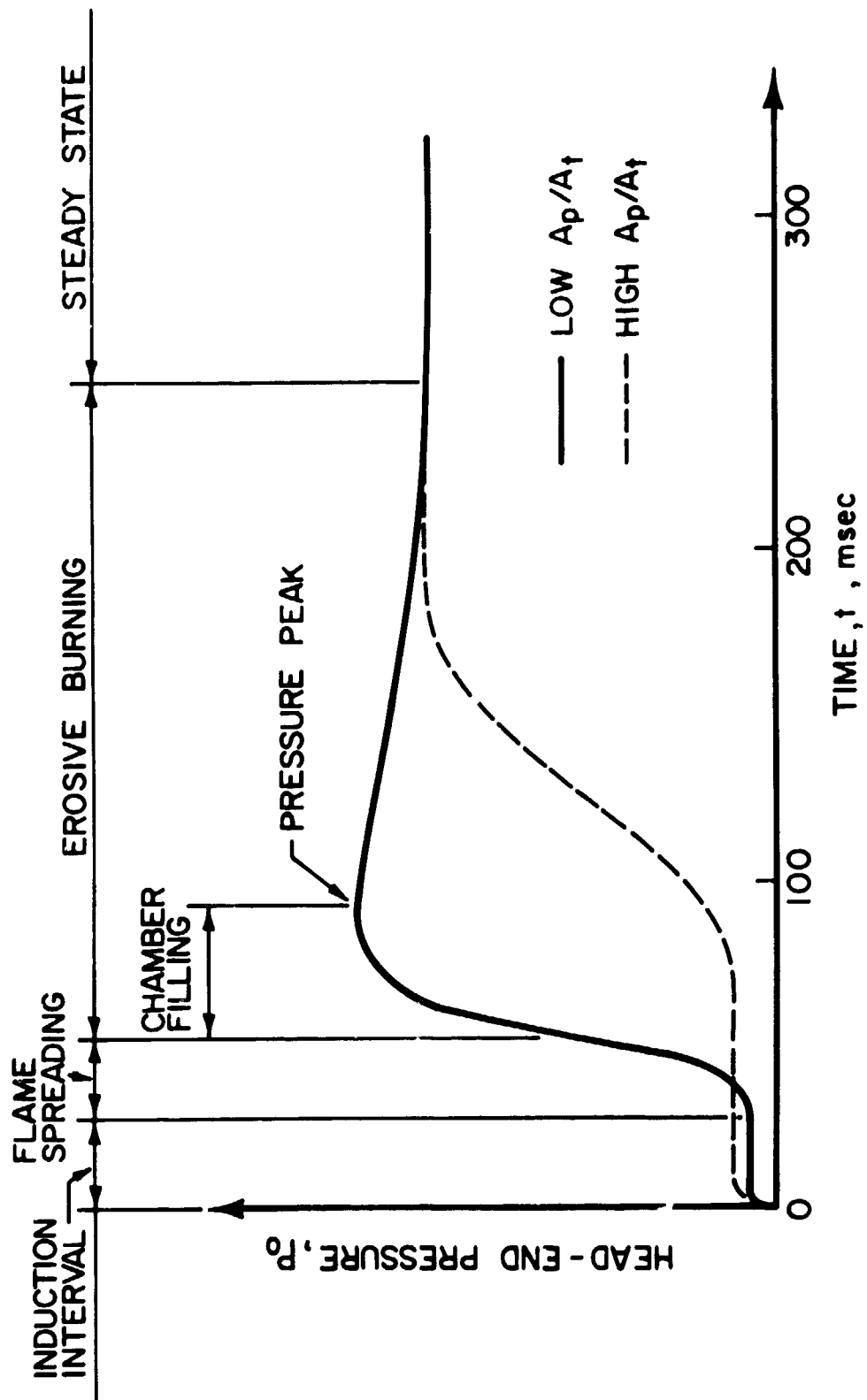
Fig. 1 Typical starting transient of HVT motors (low A_p/A_t) compared with that of motors having high A_p/A_t.
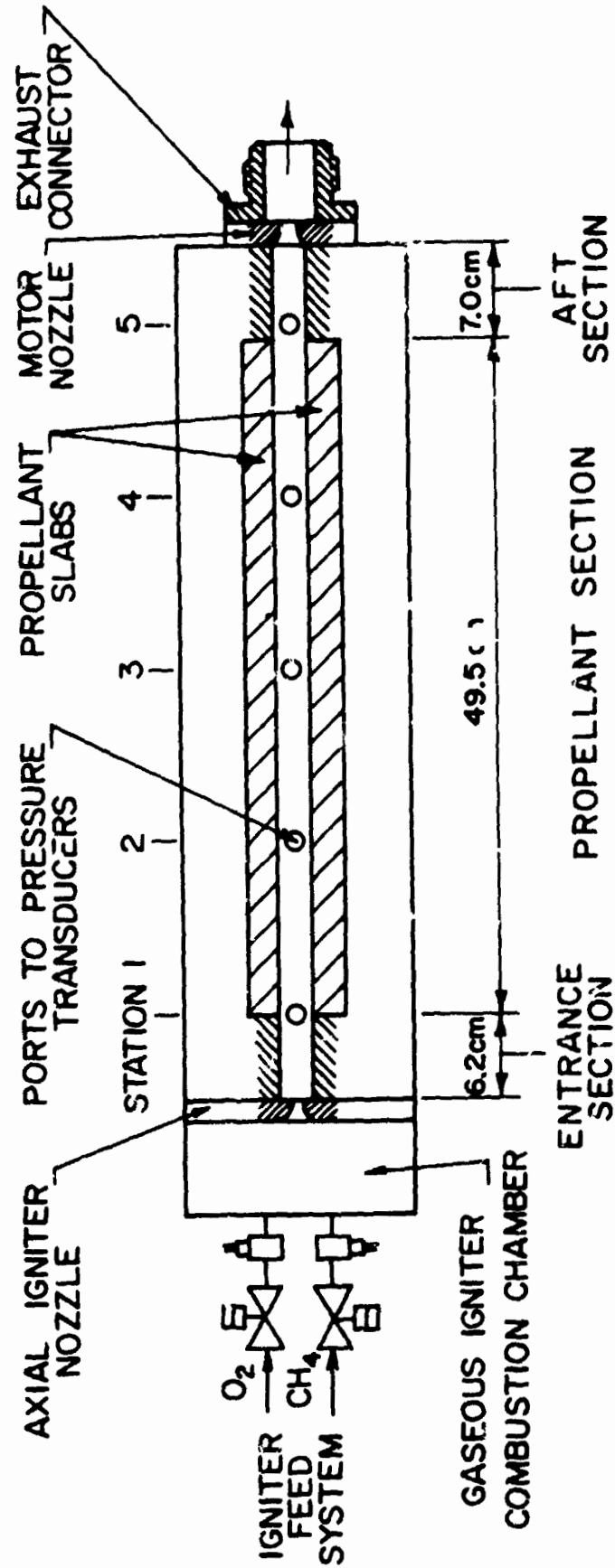
Fig. 2 Schematic view of the experimental rocket motor for starting transient studies.
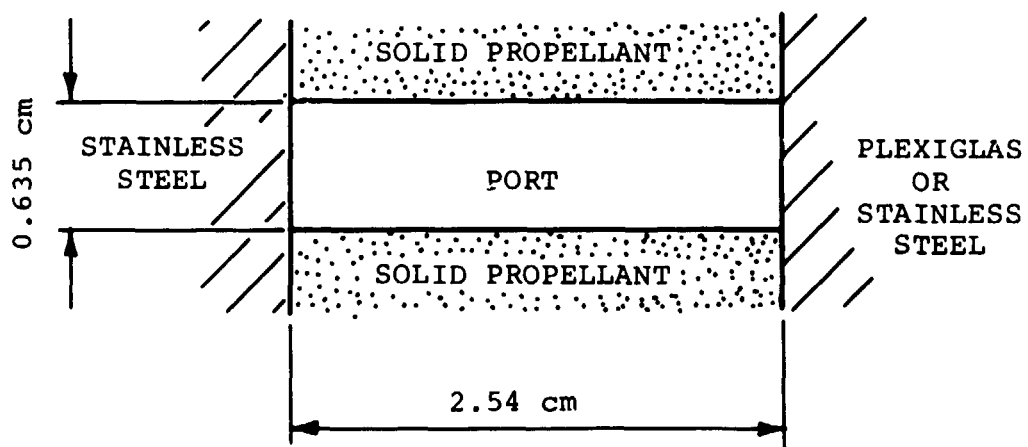
Fig. 3   Cross-section of experimental motor
showing port configuration.
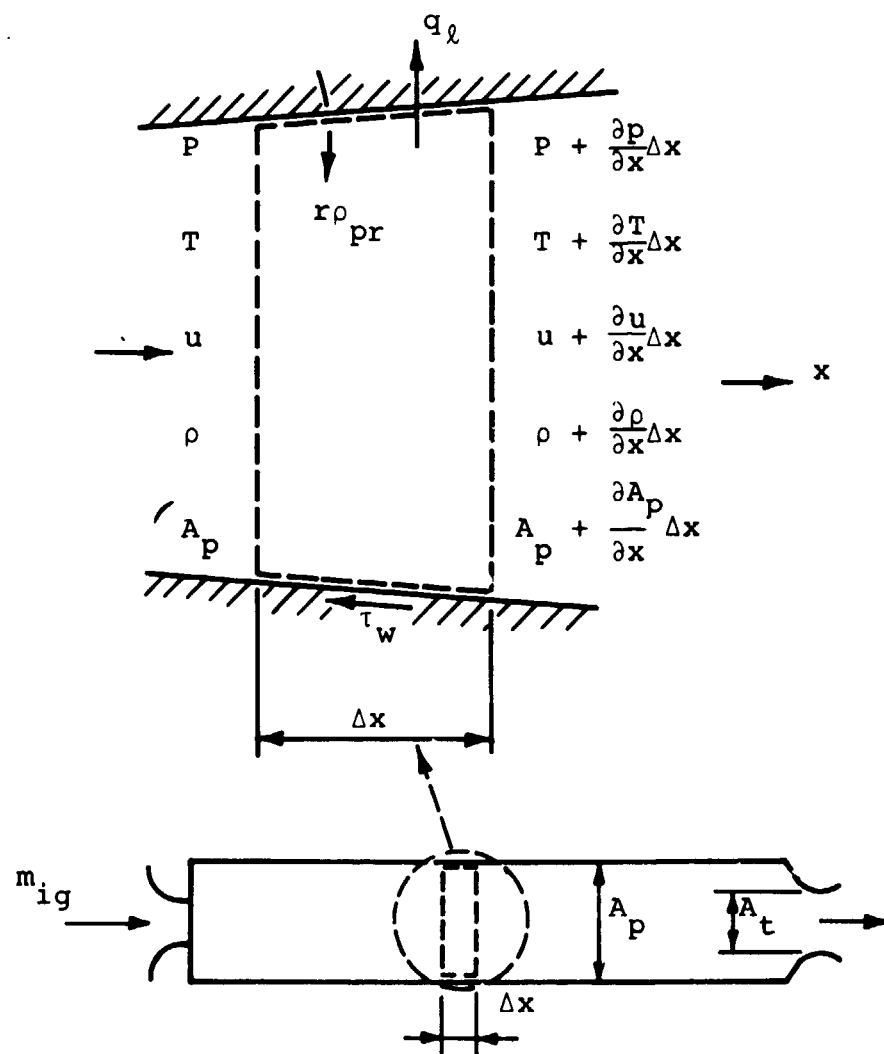
Fig. 4   Analytical control volume.

LOCATION OF MAXIMUM
HEAT TRANSFER

JET BOUNDARY

WALL IMPINGEMENT AND
REATTACHMENT OF JET

SONIC
NOZZLE

FLOW

OBLIQUE SHOCK

FLOW
SEPARATION
REGION

BOUNDARY LAYER
DEVELOPMENT
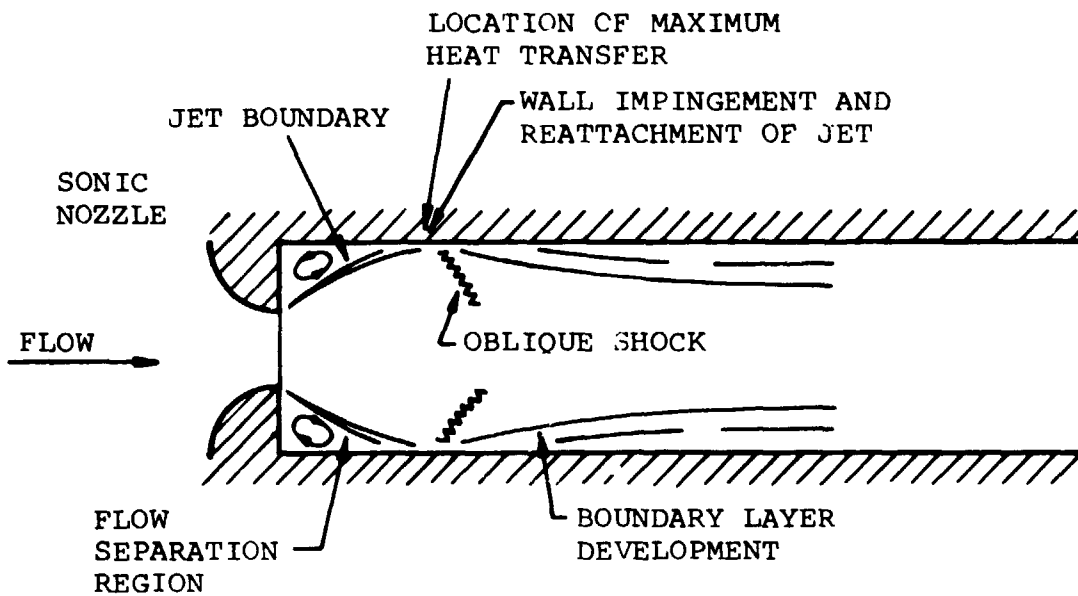
(a) duct of relatively small diameter

RECIRCULATION REGION

BARREL SHOCK

MACH DISK

SONIC
NOZZLE

SUPERSONIC
CORE

FLOW

JET DISINTEGRATION

JET BOUNDARY

TURBULENT SUBSONIC FLOW
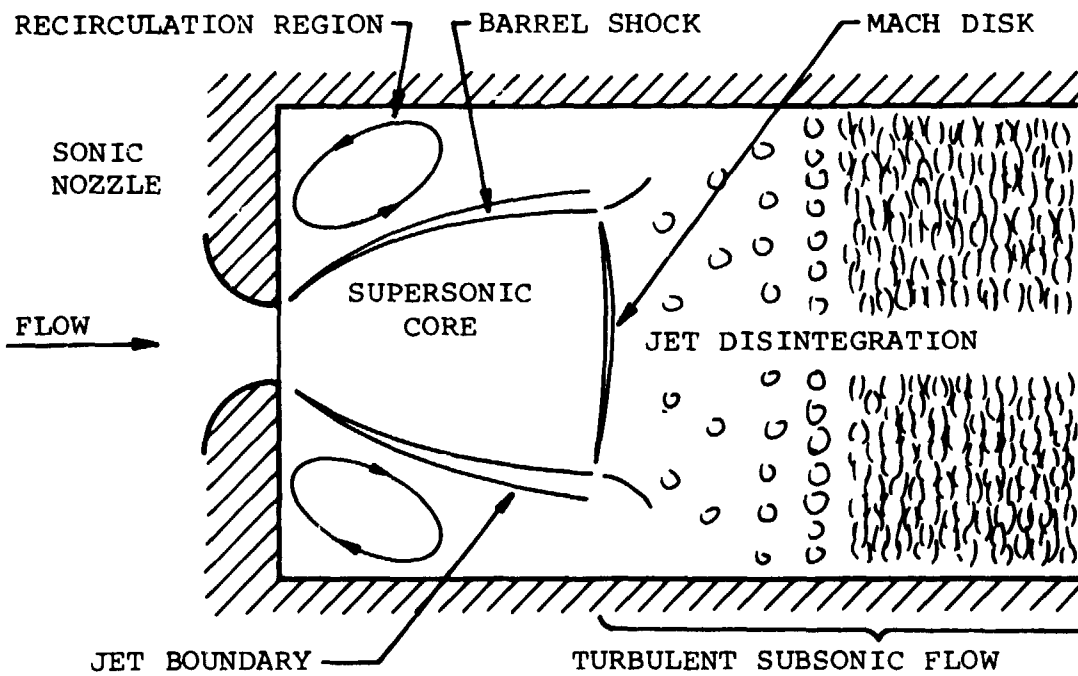
(b) duct of relatively large diameter

Fig. 5   Jet expansion from a sonic convergent nozzle into
         a duct (from Ref. 53).
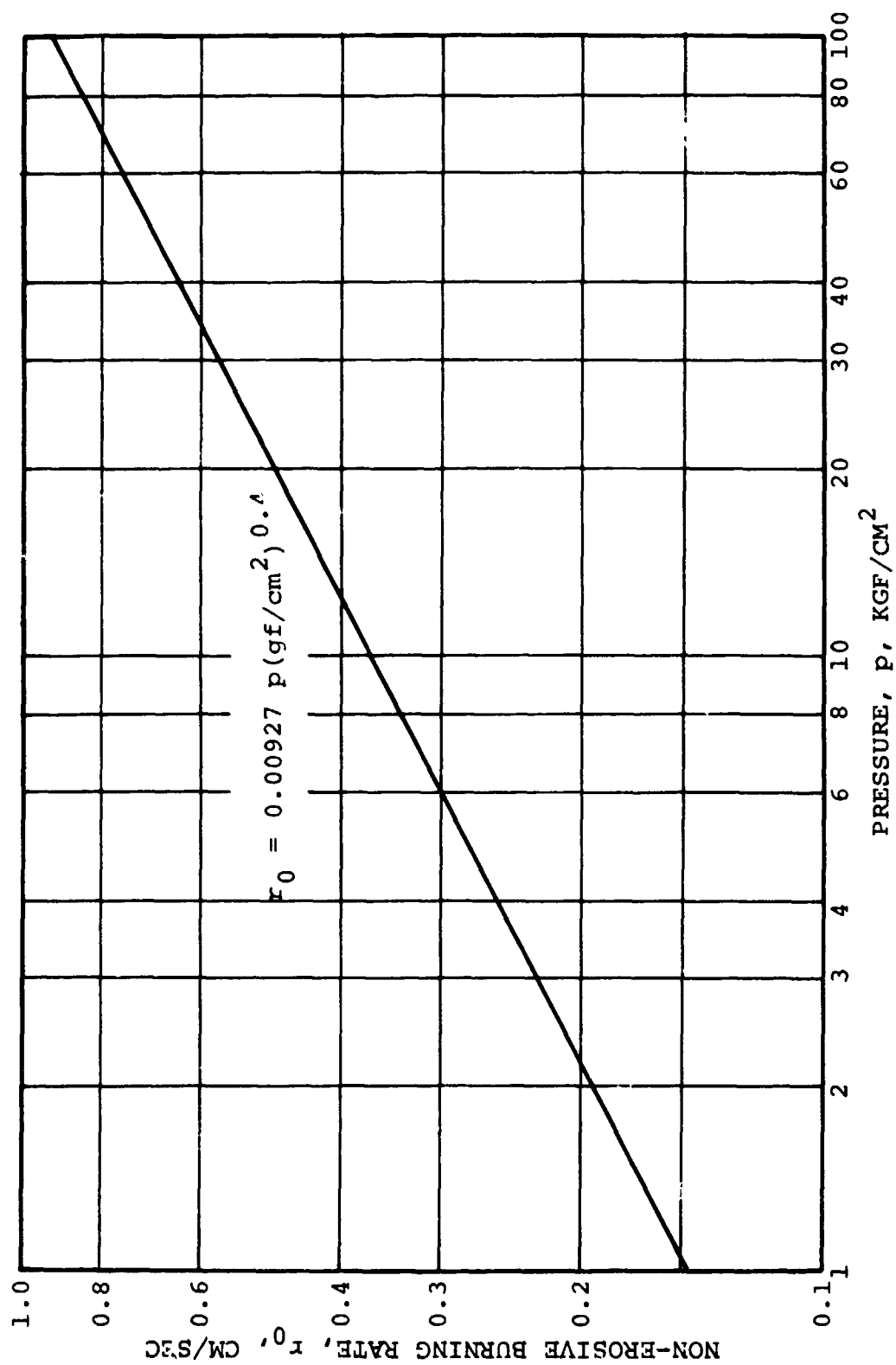
Fig. 6   Non-erosive burning rate law of propellant PBAA 80BM at initial
temperature of 298°K.

$$T_{pr} = T_{pi} + (T_{ps} - T_{pi})\left(\frac{\delta - y}{\delta}\right)^3$$
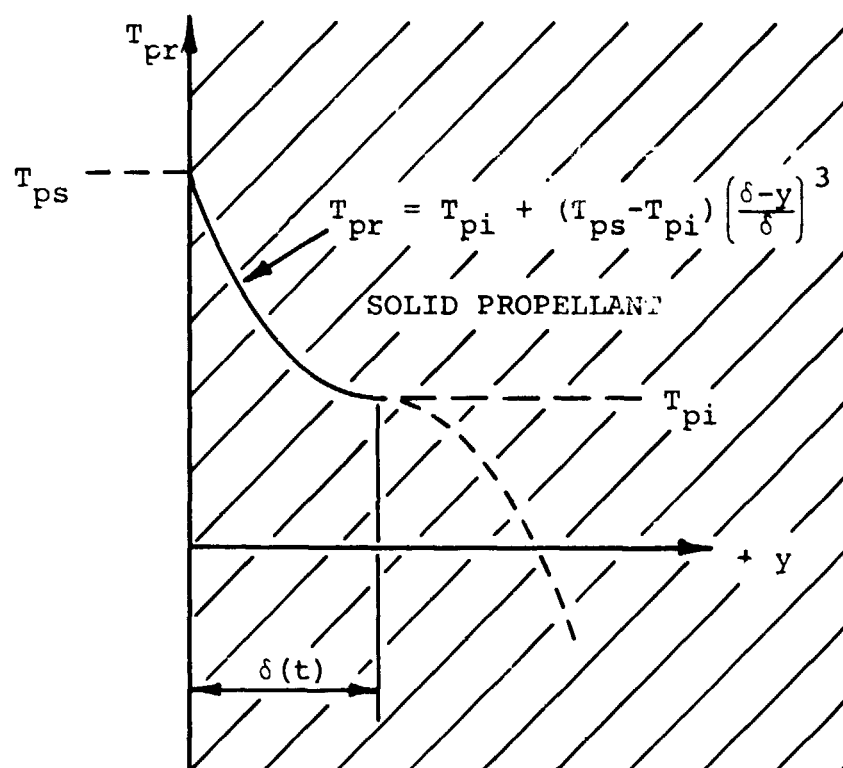
SOLID PROPELLANT

Fig. 7   Assumed temperature profile in the solid
         propellant and nomenclature for the use
         of integral method to calculate the
         propellant surface temperature.
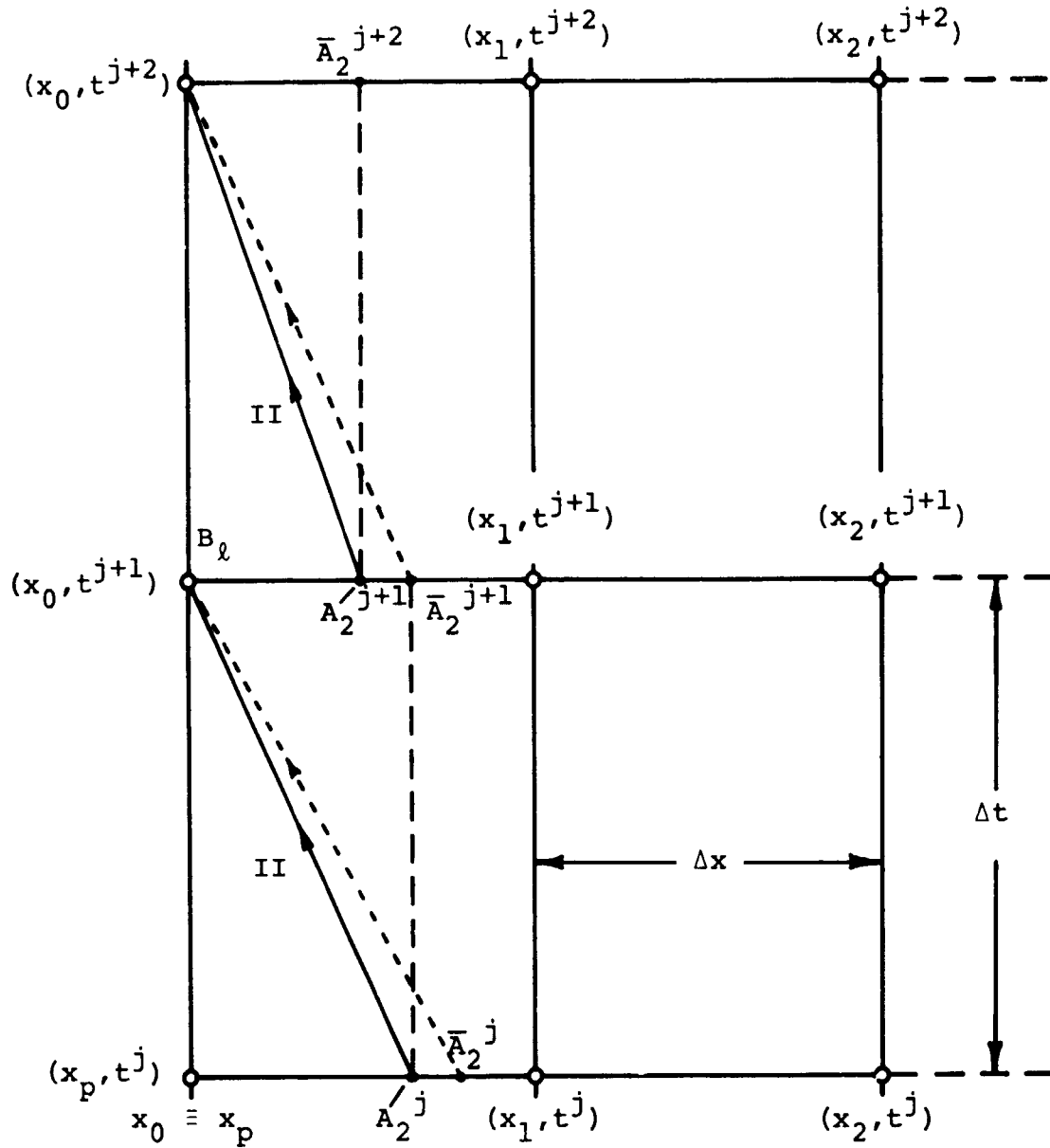
Fig. 8   Numerical calculation grid and characteristic
directions at the left boundary of the
calculated domain.
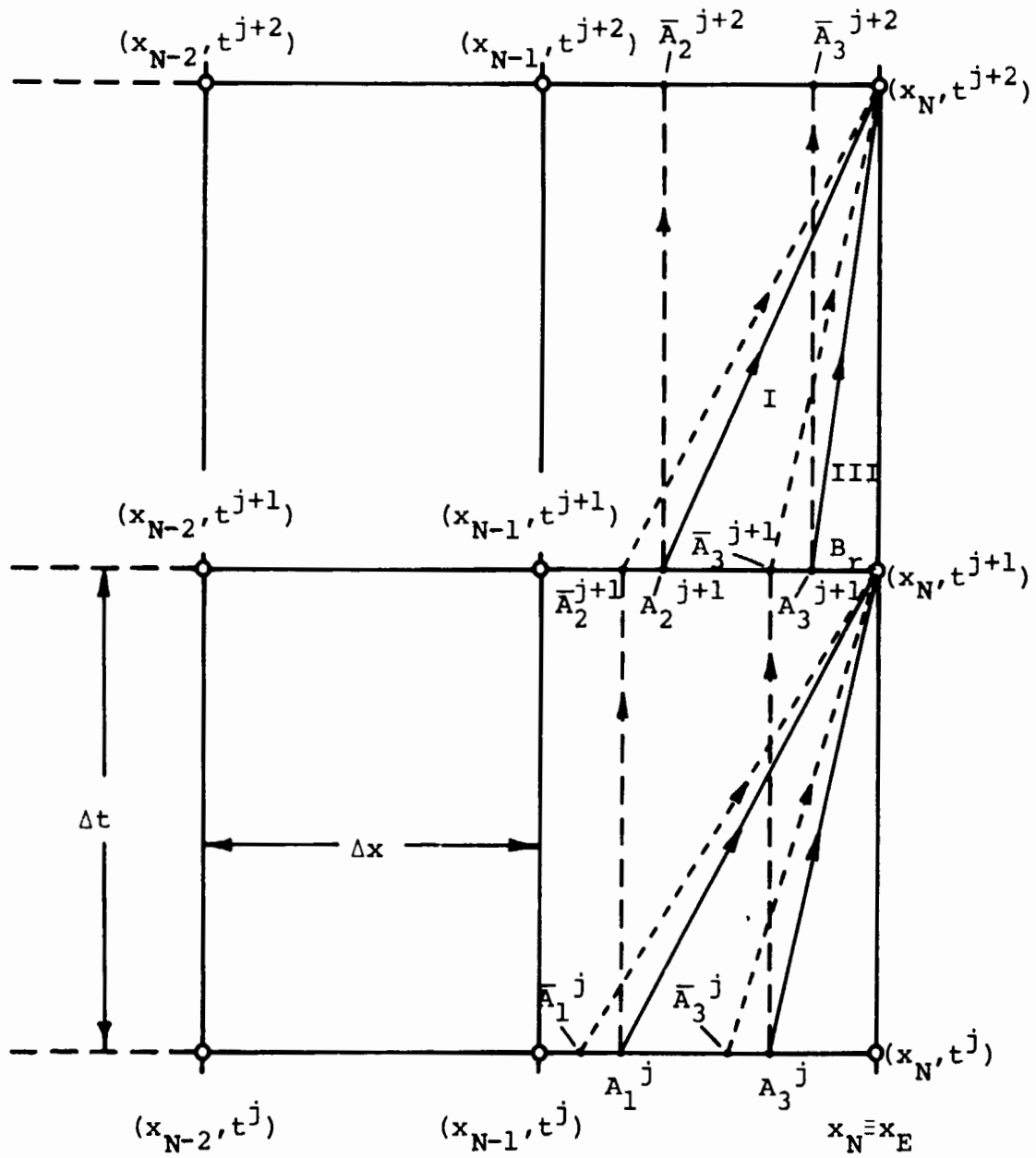
Fig. 9 Numerical calculation grid and characteristic directions at the right boundary of the calculated domain.

SECTION "A-A"

SECTION "B-B"
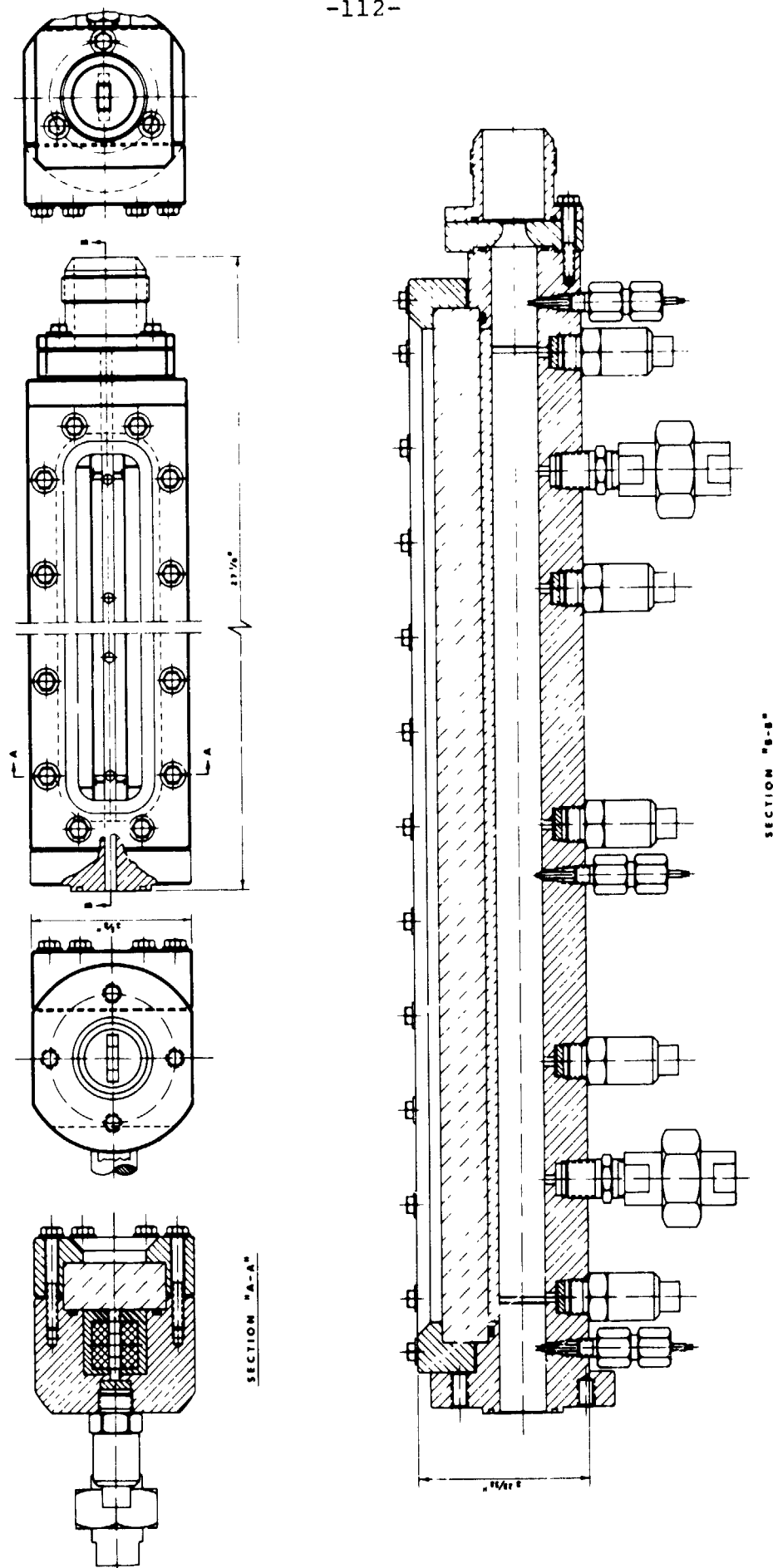
Fig. 10   Assembly drawing of the experimental window motor.
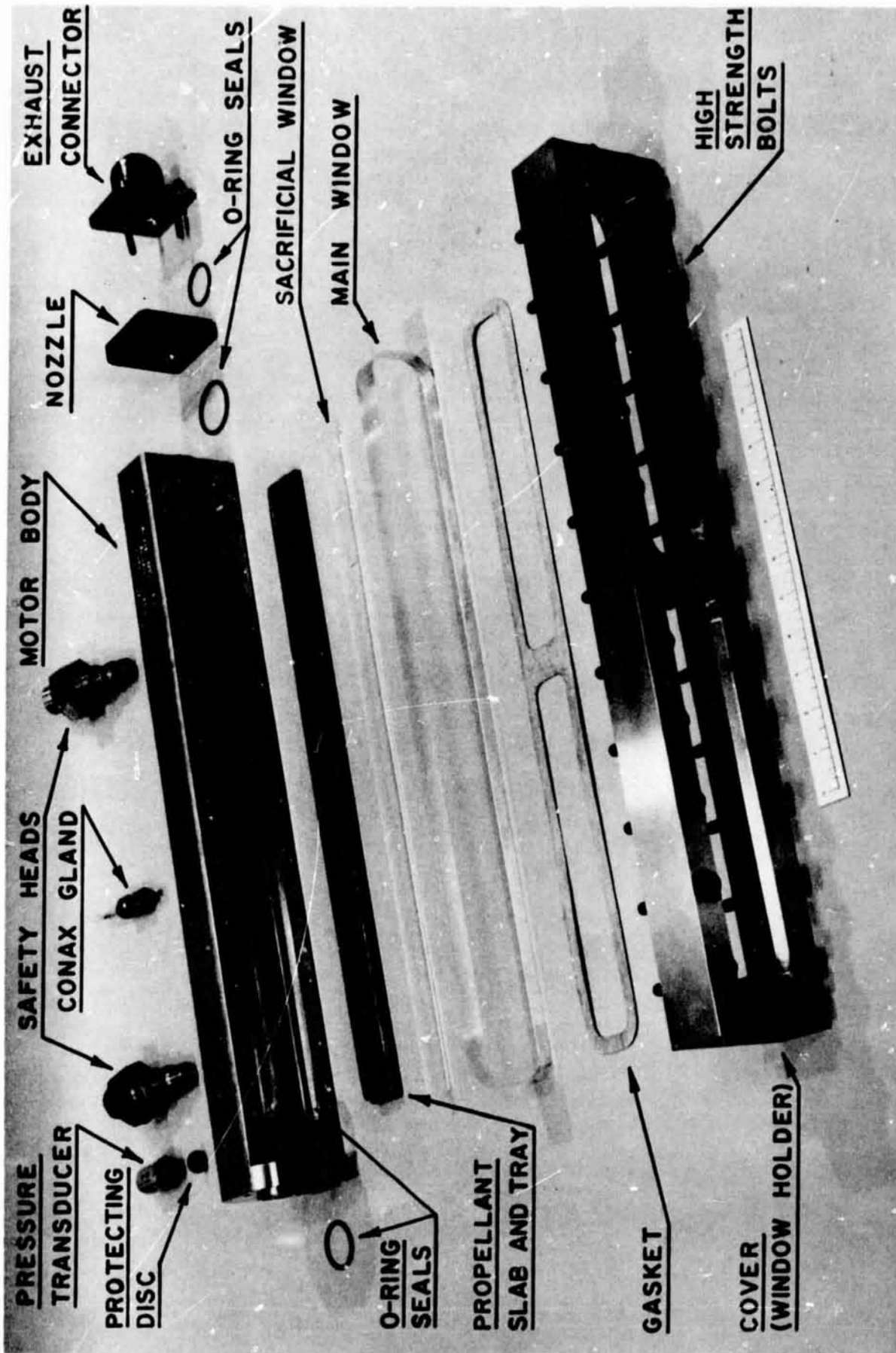
Fig. 11 Exploded view of the experimental window motor.
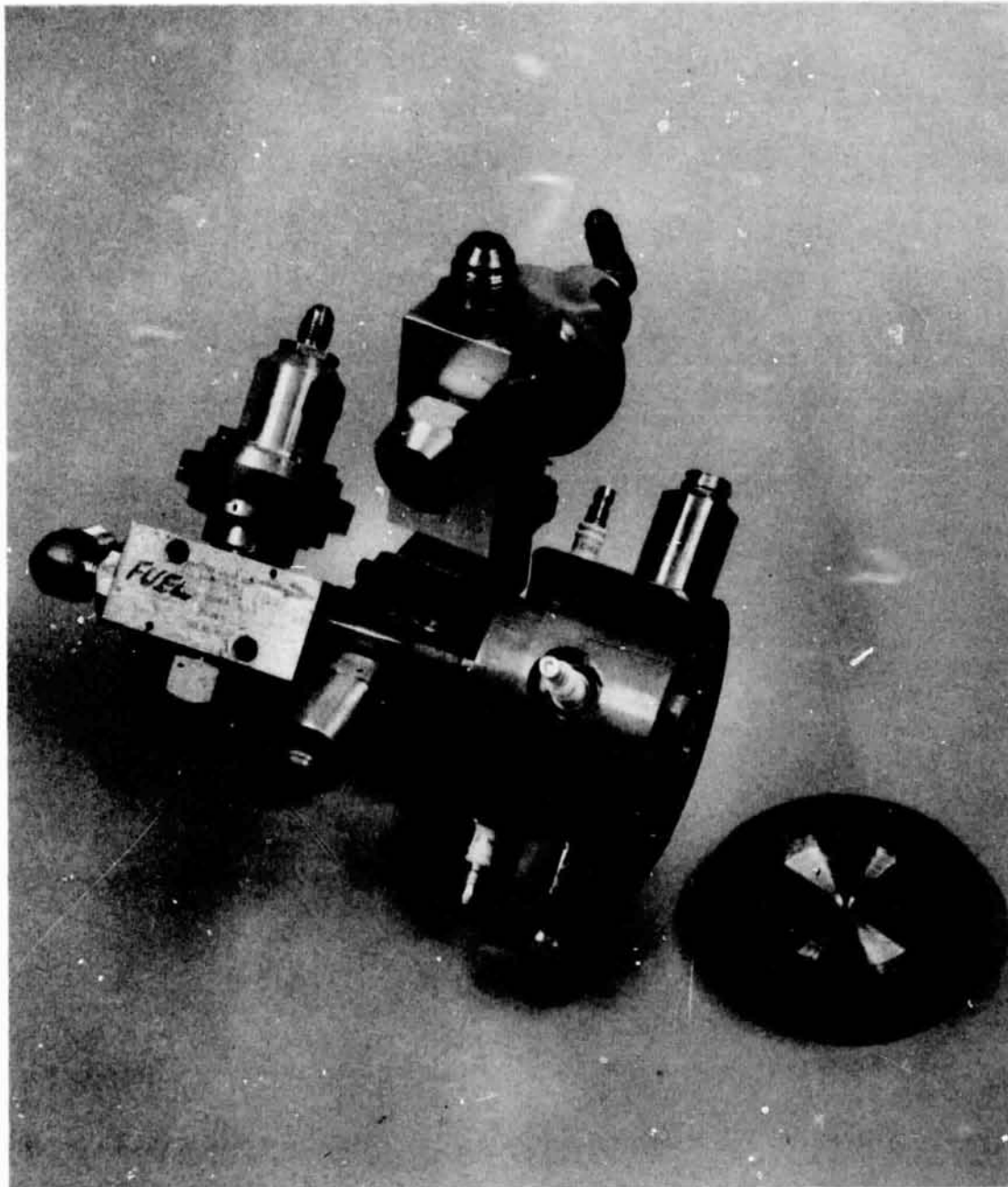
Fig. 12   Assembled gaseous igniter combustion
chamber and accessories.
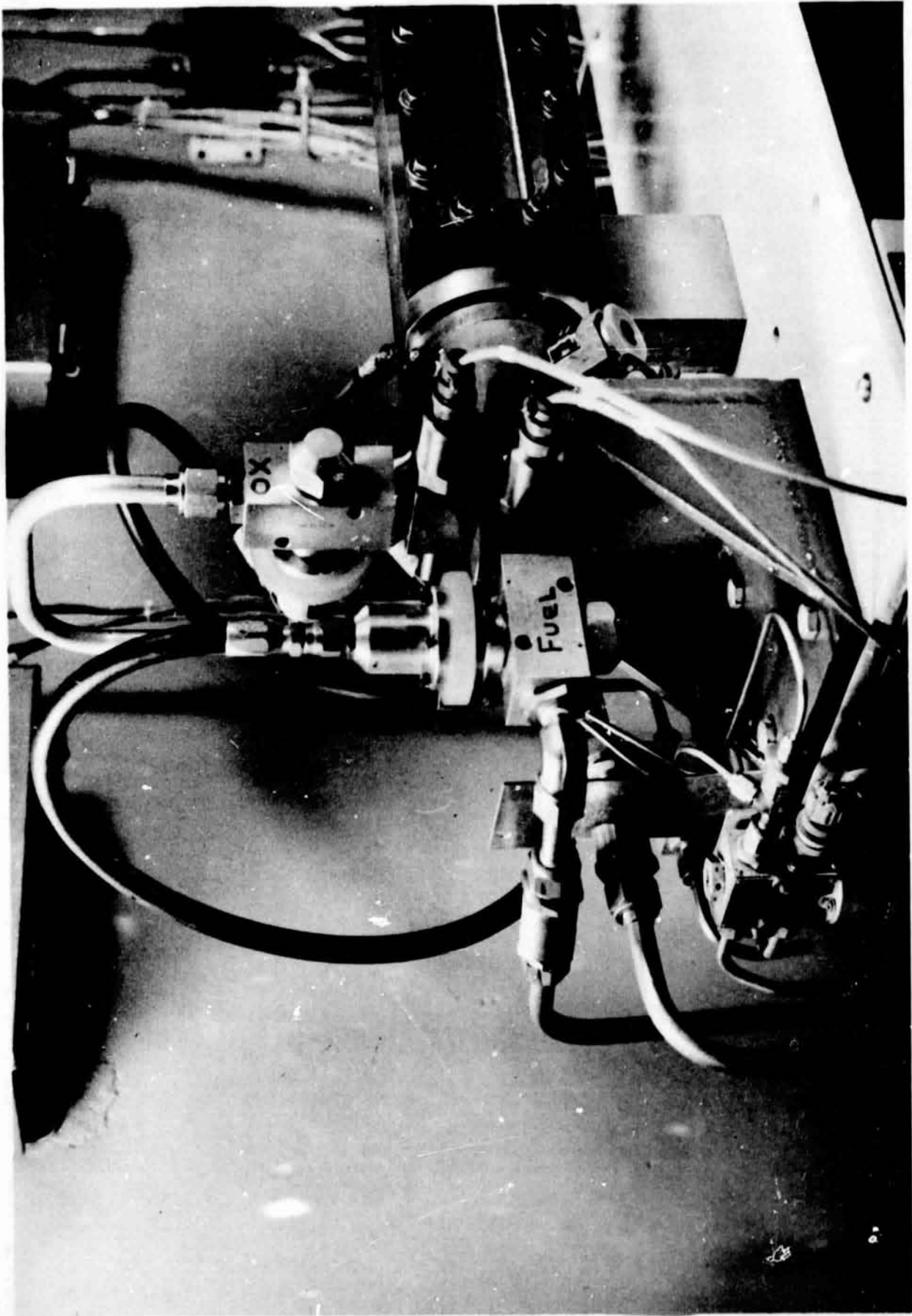
Fig. 13 Overall view of the assembled gaseous ignition system mounted on a test stand.
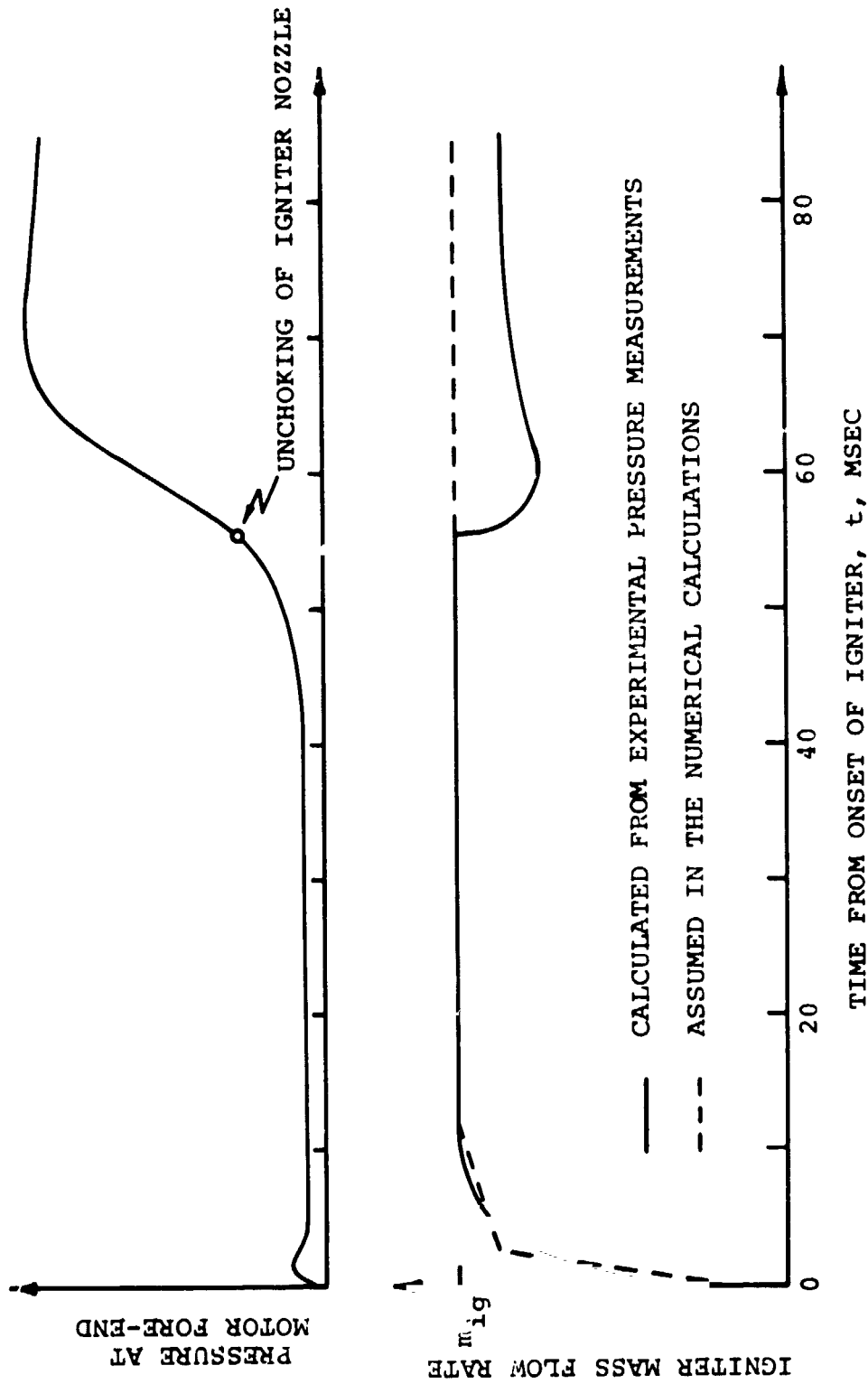
Fig. 14 Typical variation with time of the pressure at motor fore-end and igniter mass flow rate, showing the instant of igniter nozzle unchoking.
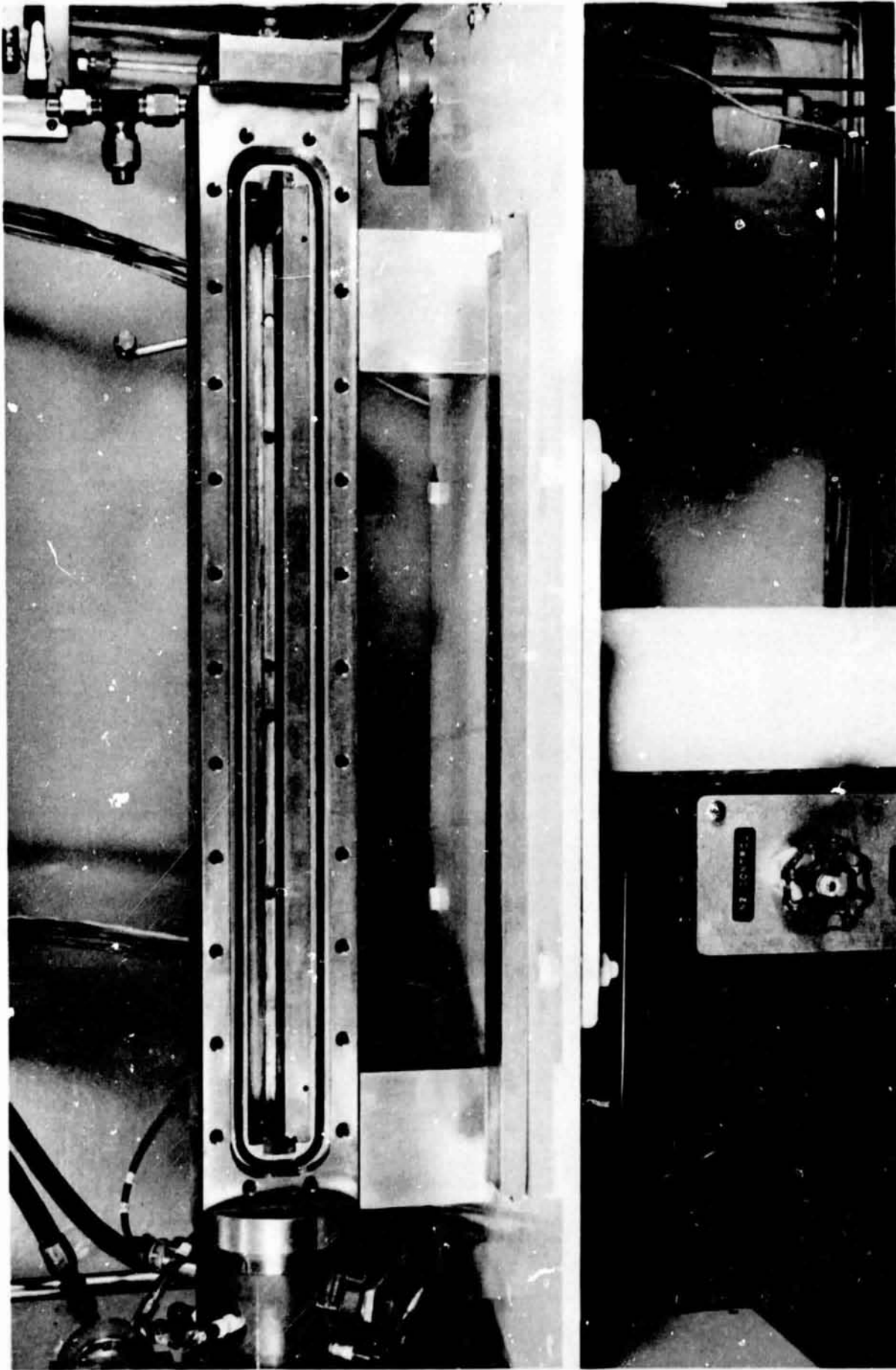
Fig. 15 View of the inside of the experimental motor mounted on the test stand, showing one tray in position and the other tray under the motor.
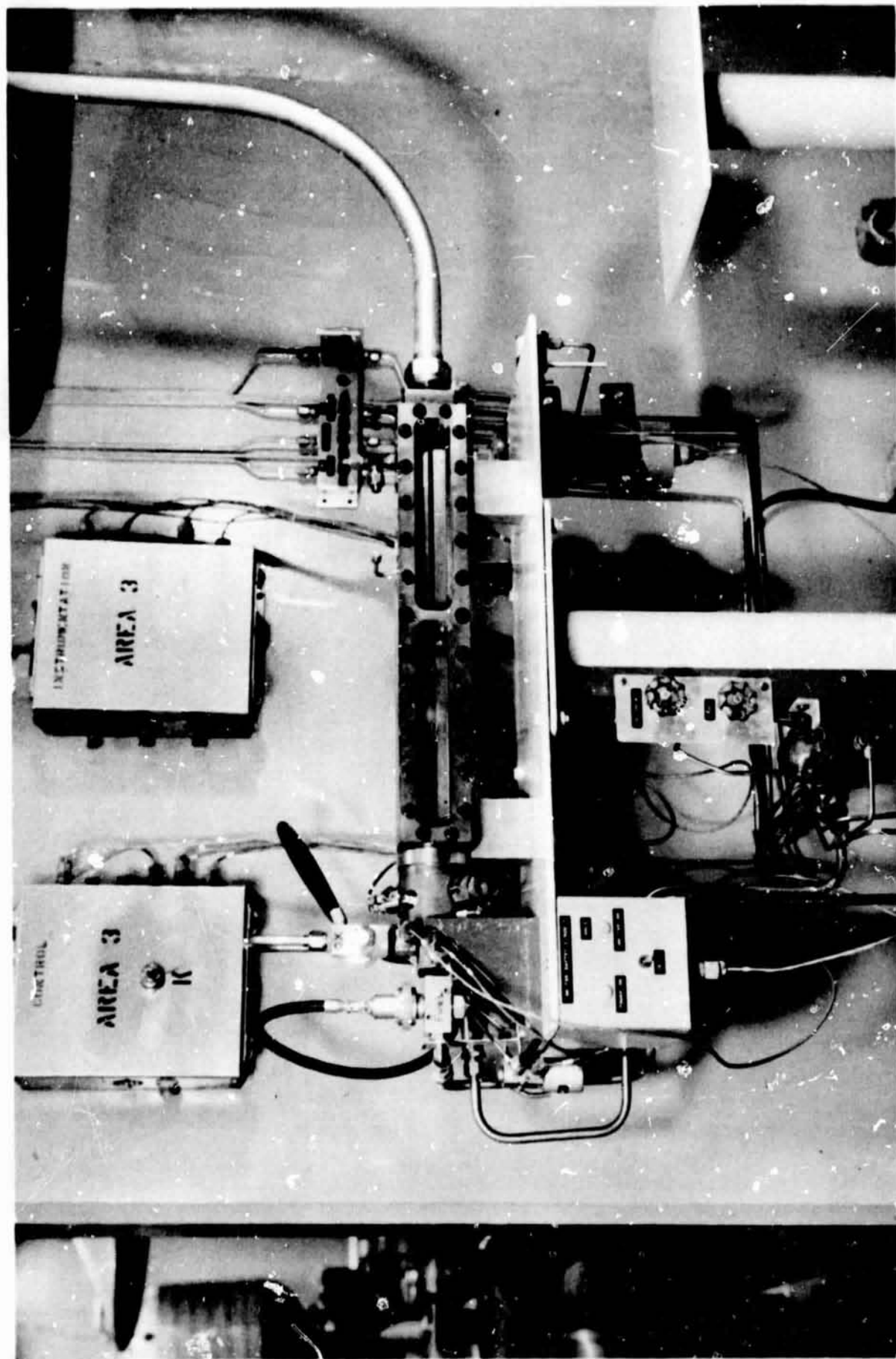
Fig. 16   Overall view of the assembled experimental set-up mounted on the test stand.
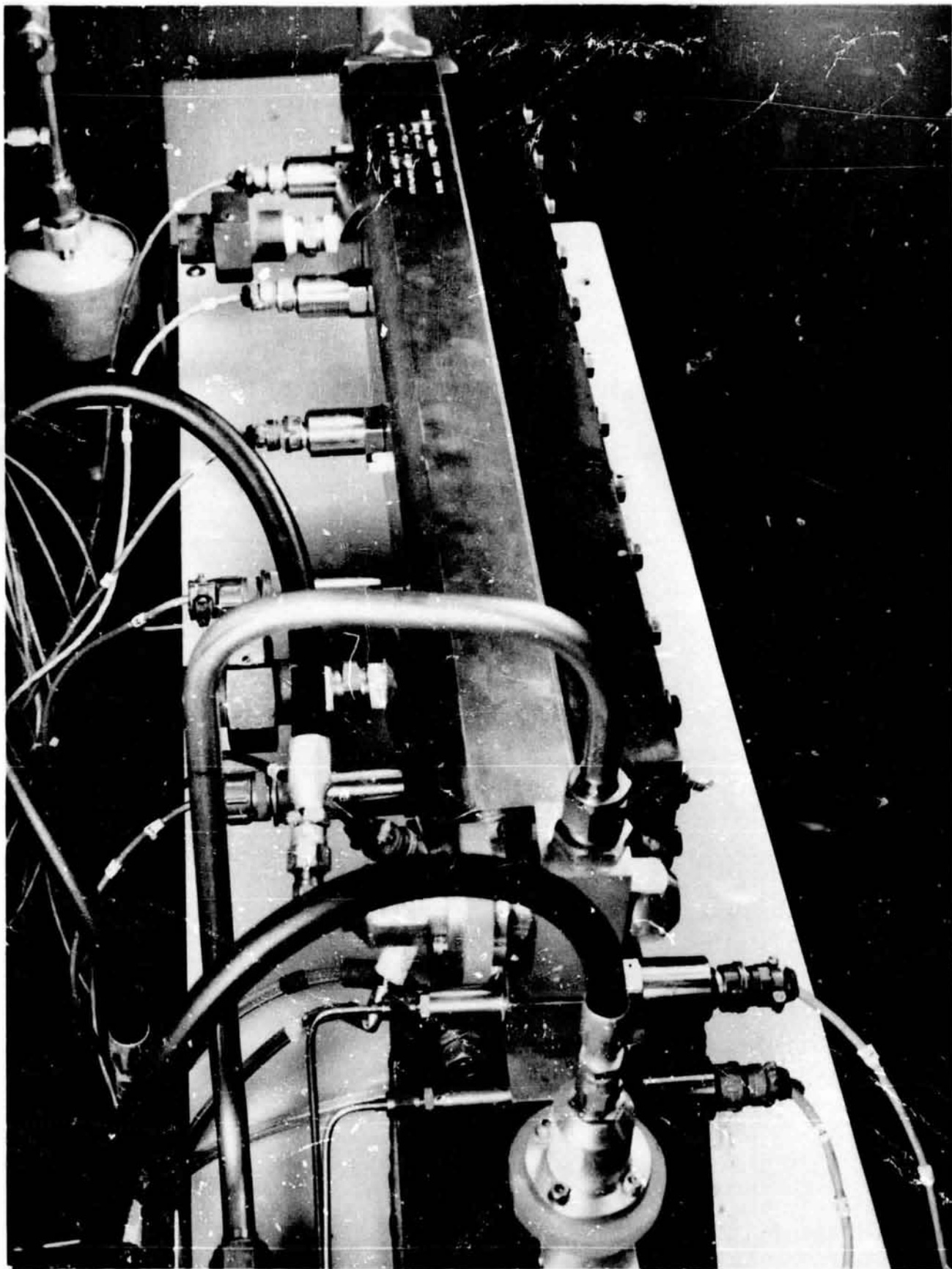
Fig. 17   View of the back side of the assembled experimental set-up
showing the pressure transducers installed along the motor.
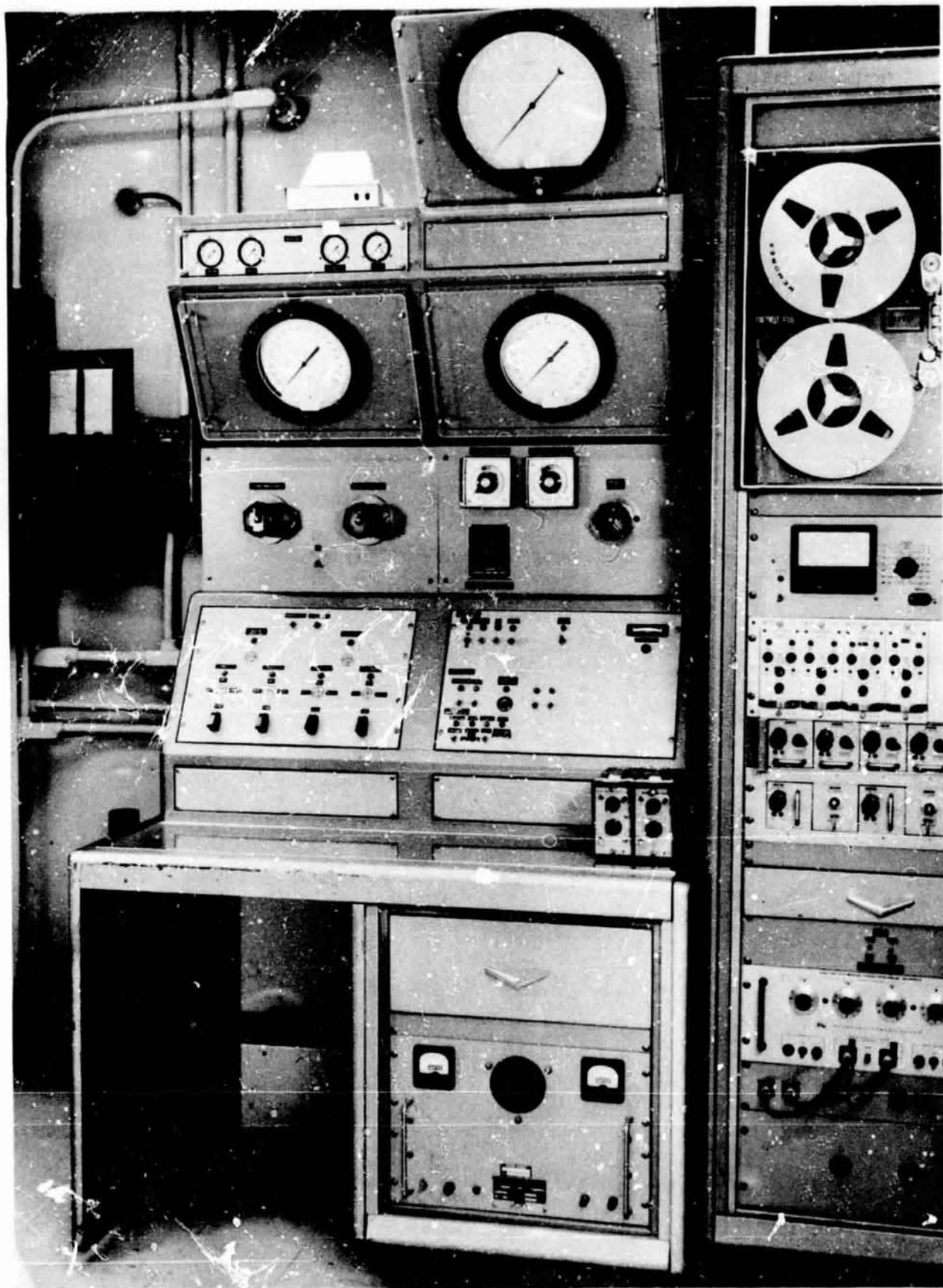
Fig. 18   The calibration and firing console of the
            solid-propellant test cell.
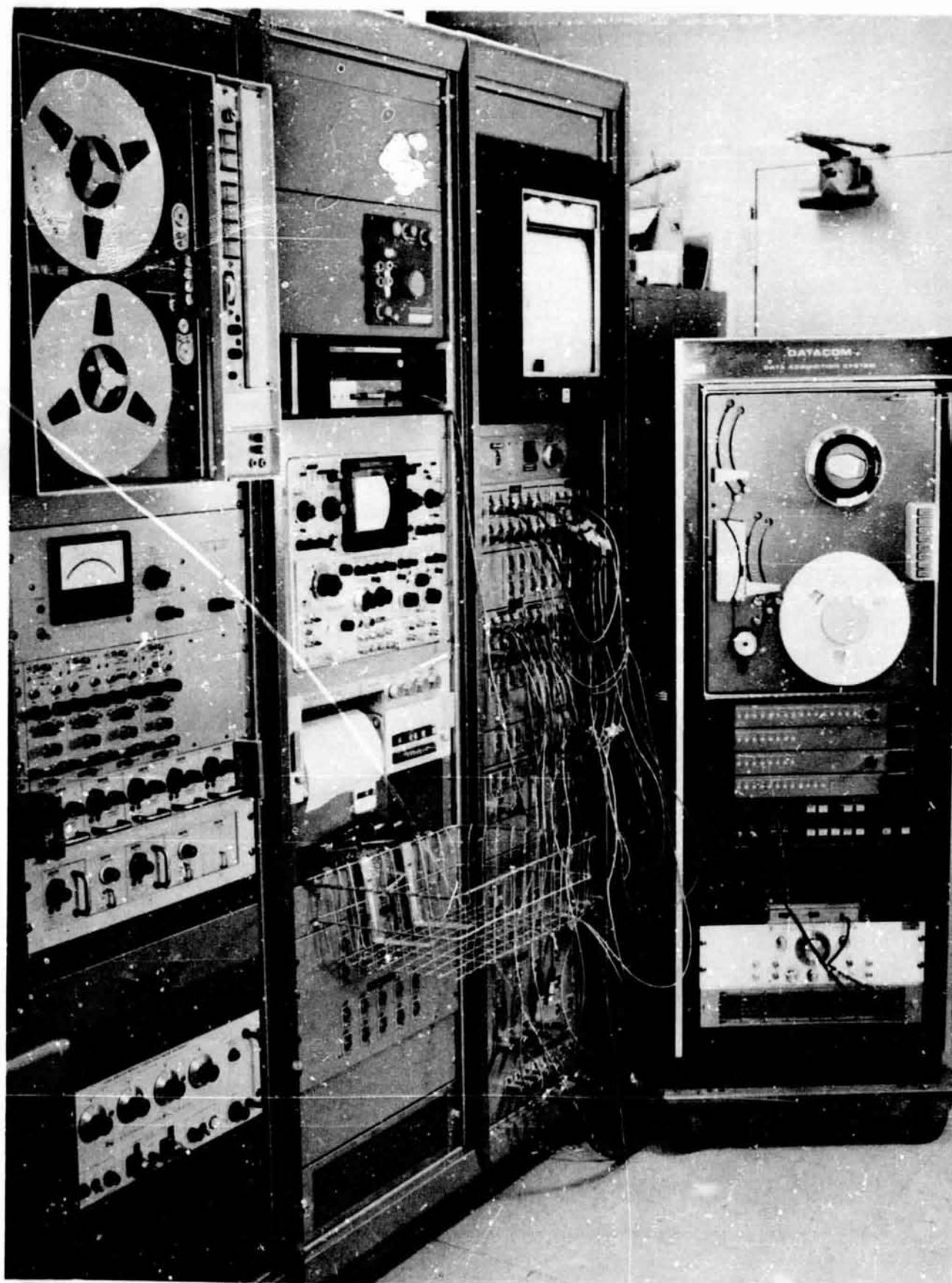
Fig. 19   View of the solid-propellant test cell instrumentation console (on the left) and the Datacom Data Acquisition System (on the right) with related wiring.
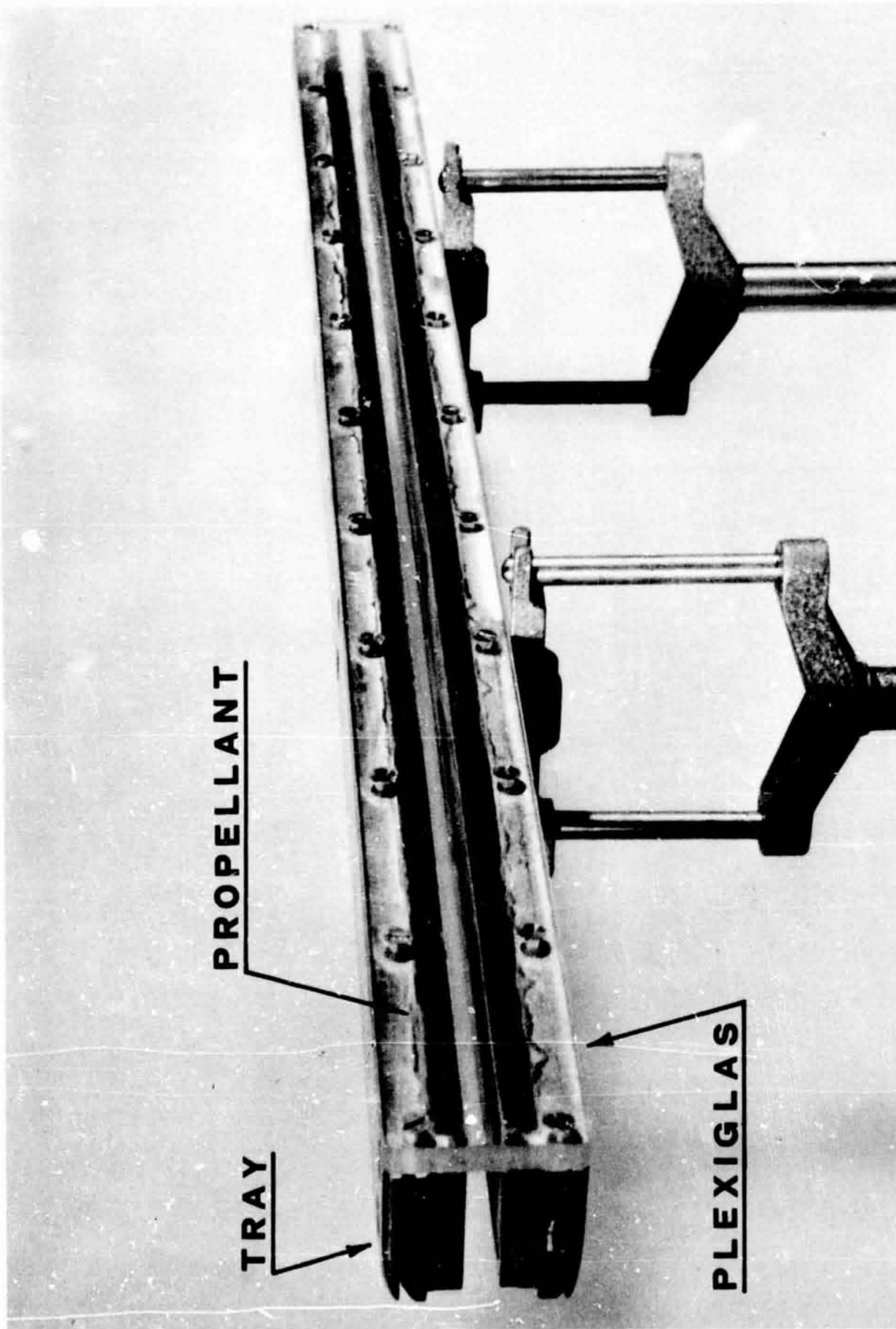
Fig. 20   Propellant cast in trays and on Plexiglas window for photographic observation of ignition and receding propellant surface during burning.
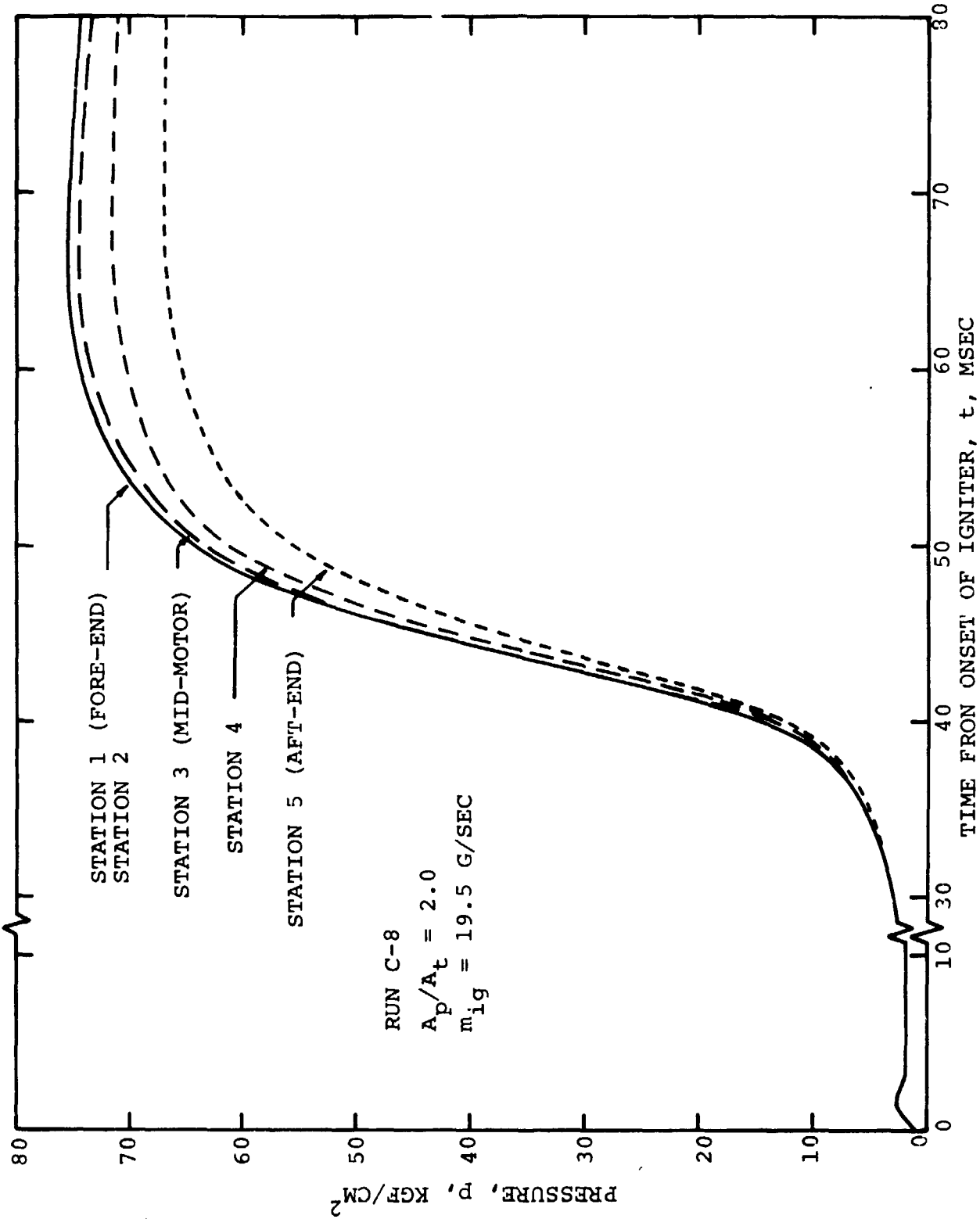
Fig. 21 Experimental starting pressure transients recorded during a test
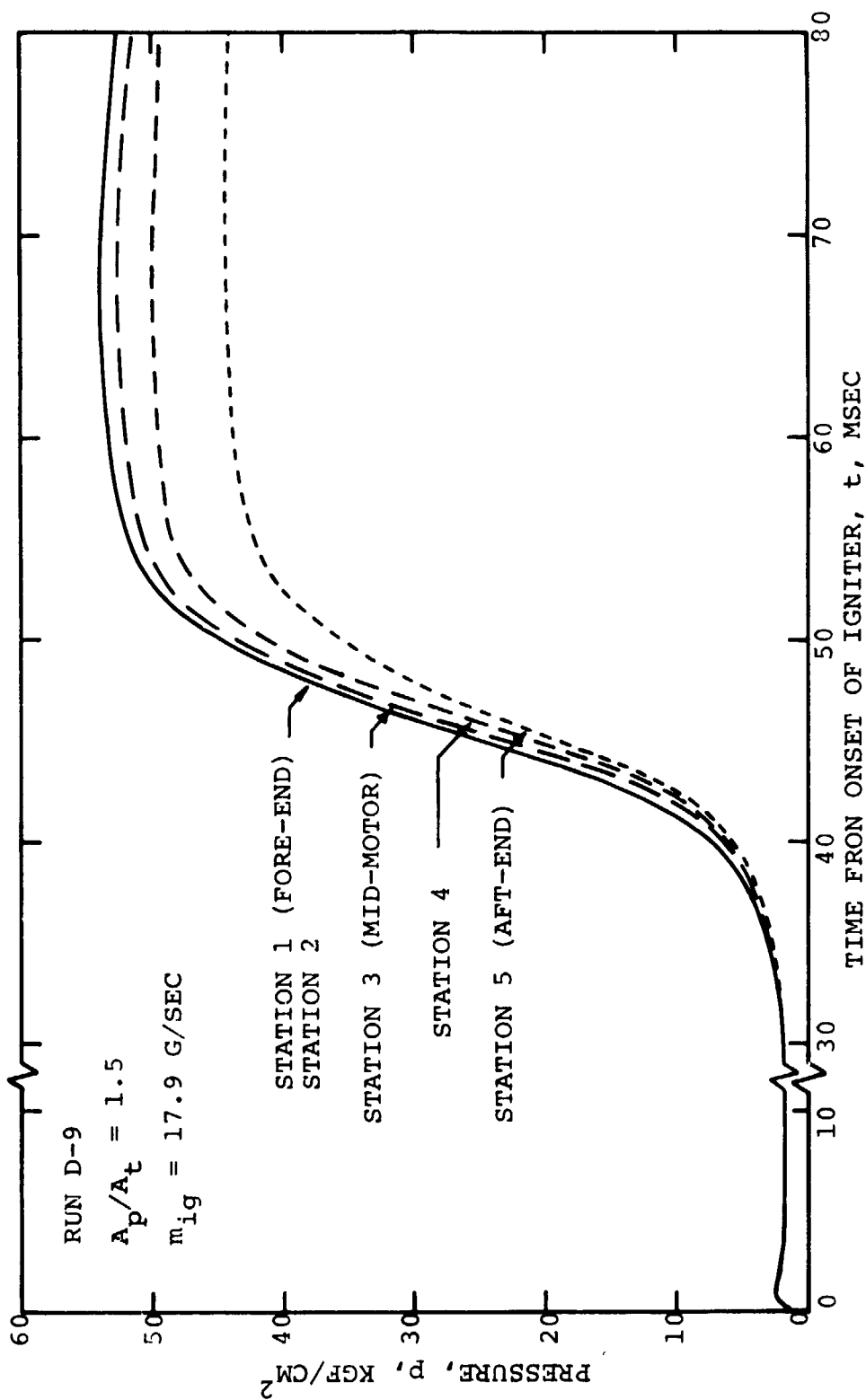with $A_p/A_t = 2.0$.

Fig. 22   Experimental starting pressure transients recorded during a test
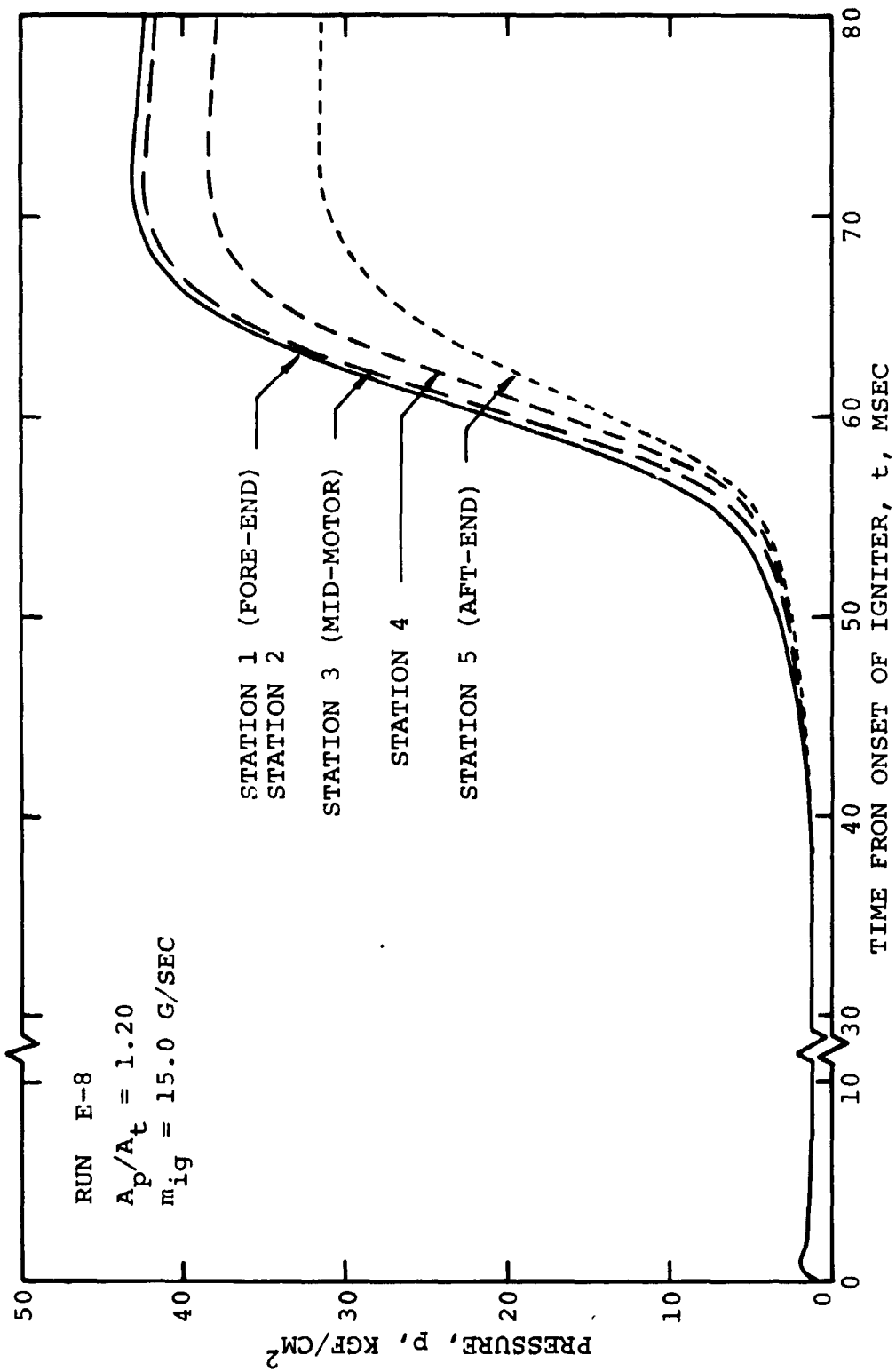with $A_p/A_t = 1.5$.

Fig. 23 Experimental starting pressure transients recorded during a test
with $A_p/A_t = 1.2$.

RUN F-2

$A_p/A_t = 1.06$

$m_{ig} = 19.5$ G/SEC

STATION 1 (FORE-END)
STATION 2

STATION 3 (MID-MOTOR)

STATION 4

STATION 5 (AFT-END)

PRESSURE, p, KGF/CM²

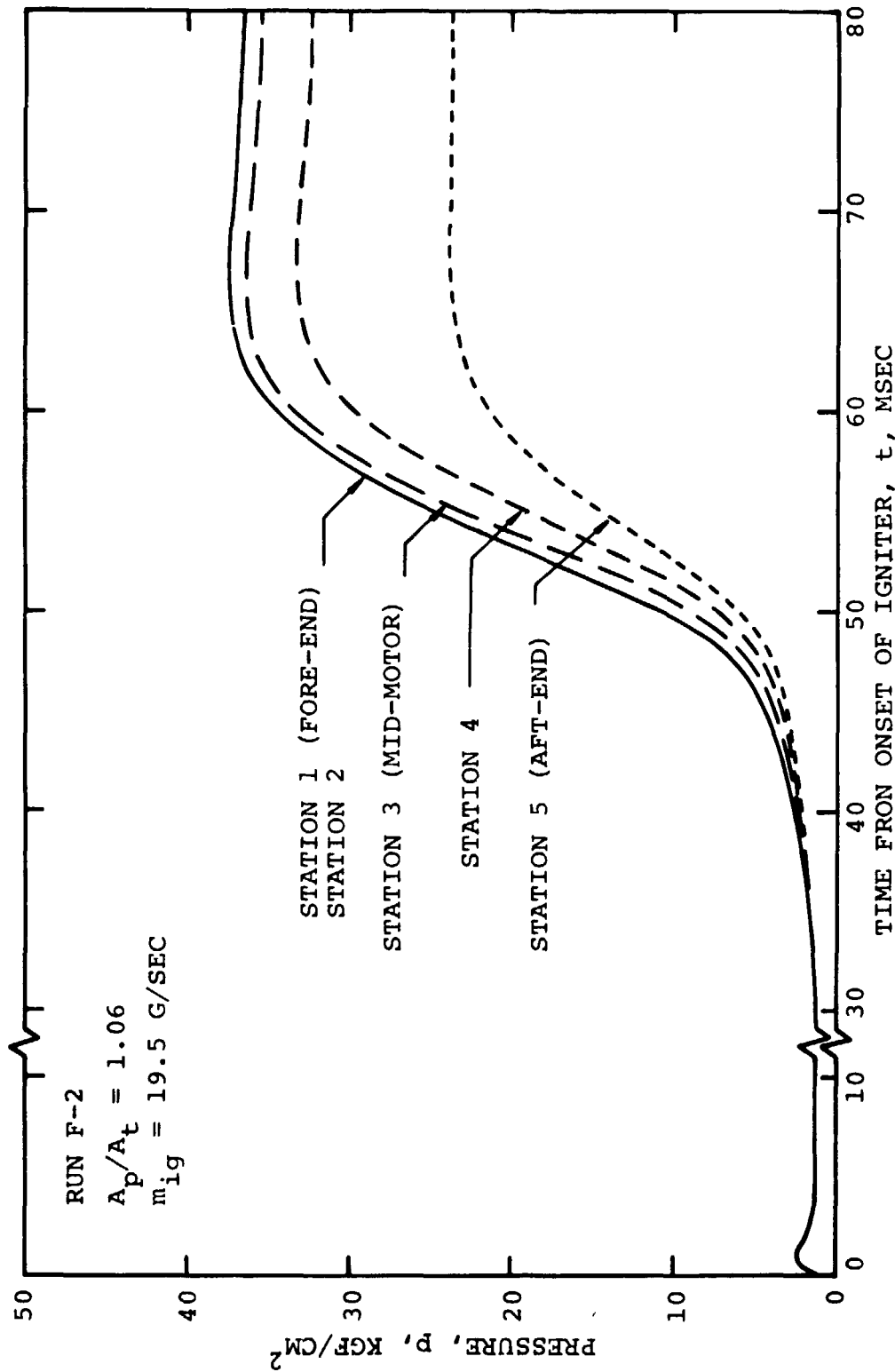TIME FRON ONSET OF IGNITER, t, MSEC

Fig. 24   Experimental starting pressure transients recorded during a test
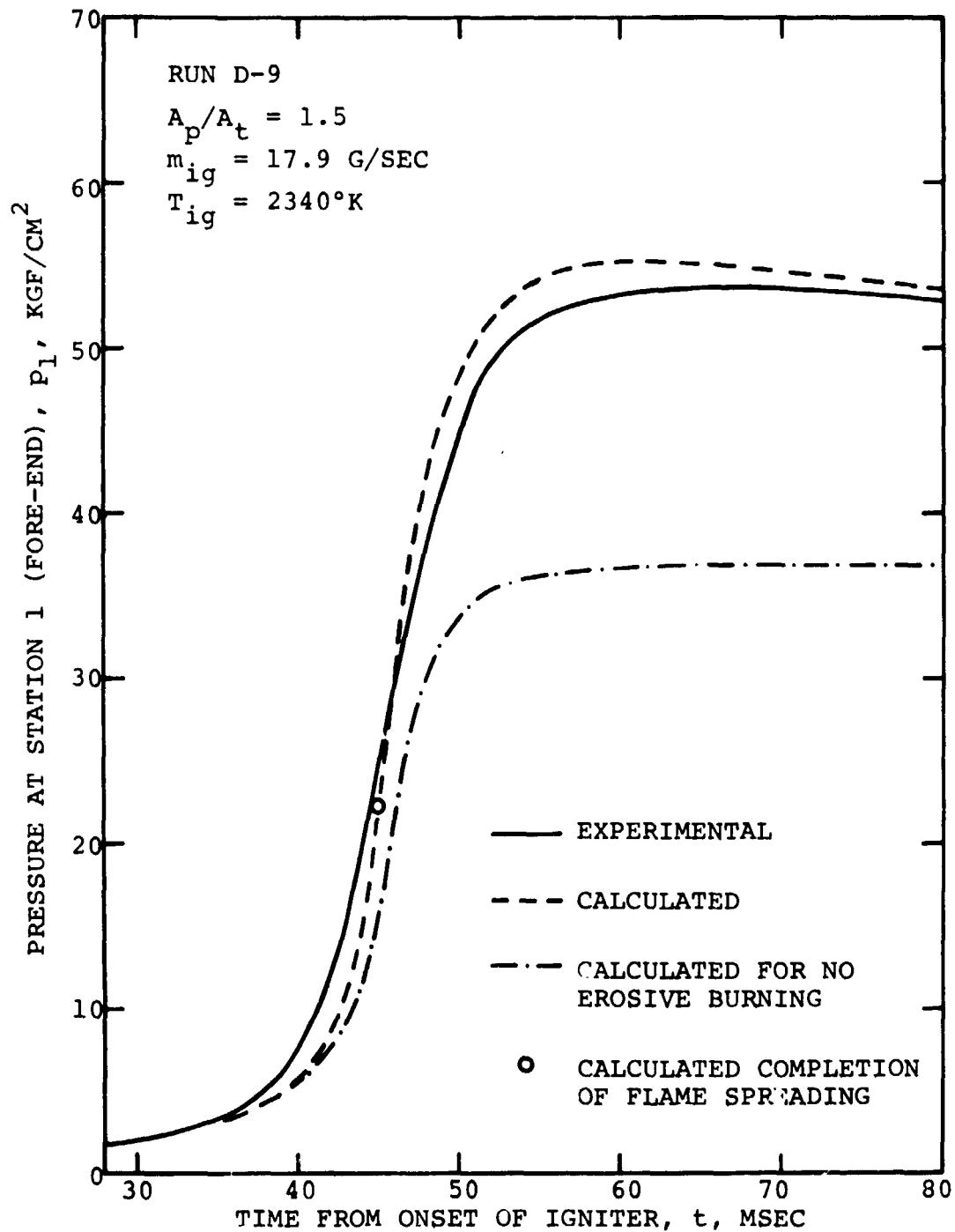with $A_p/A_t = 1.06$.

Fig. 25a   Comparison of measured and calculated pressure
vs time traces at station 1 (fore-end) for
$A_p/A_t = 1.5$.
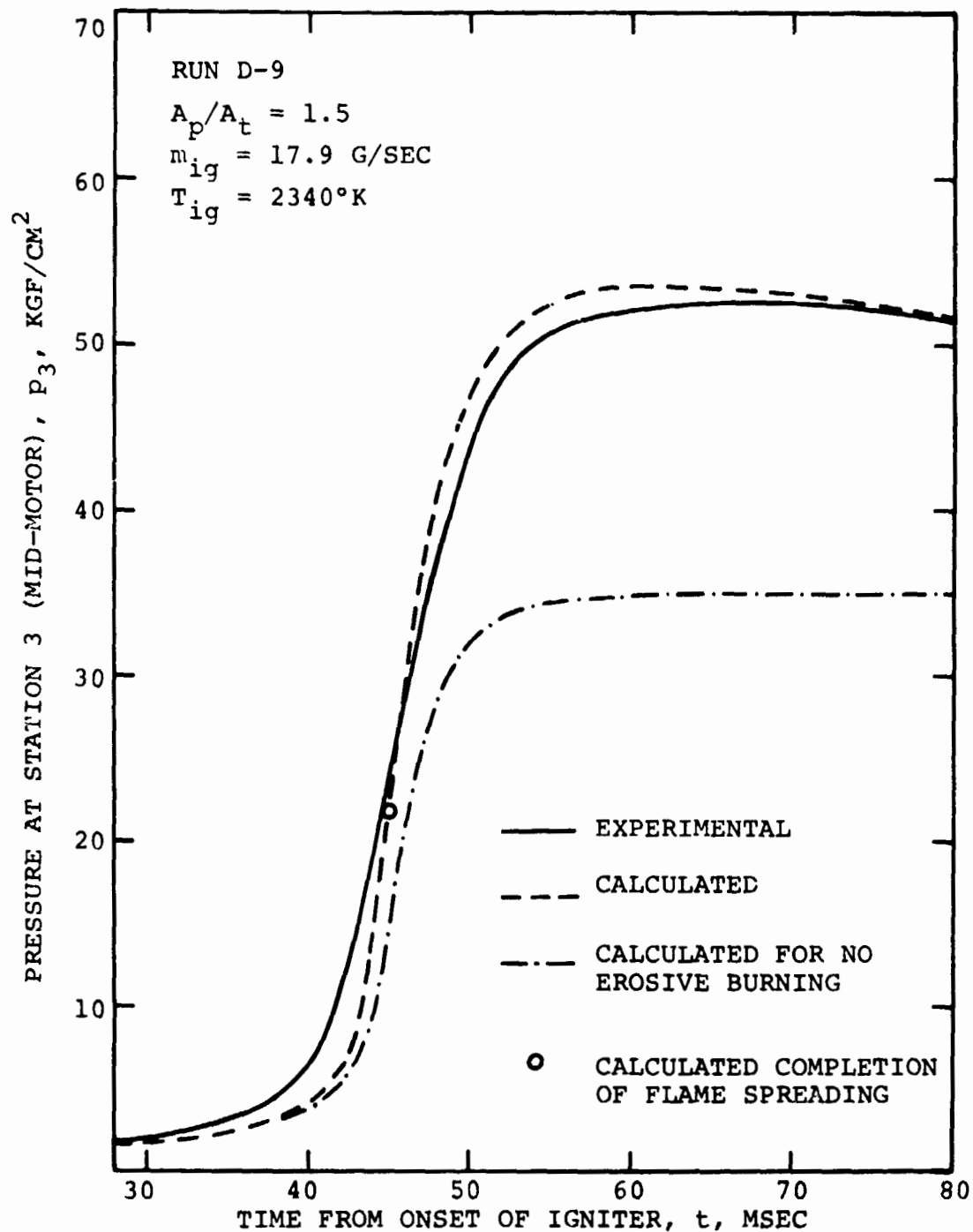
Fig. 25b   Comparison of measured and calculated pressure
            vs time traces at station 3 (mid-motor) for
            $A_p/A_t = 1.5$.

Fig. 25c   Comparison of measured and calculated pressure
vs time traces at station 5 (aft-end) for
$A_p/A_t = 1.5$.

Fig. 26a   Comparison of measured and calculated pressure
vs time traces at station 1 (fore-end) for
$A_p/A_t = 1.2$.

Fig. 26b Comparison of measured and calculated pressure vs time traces at station 3 (mid-motor) for $A_p/A_t = 1.2$.
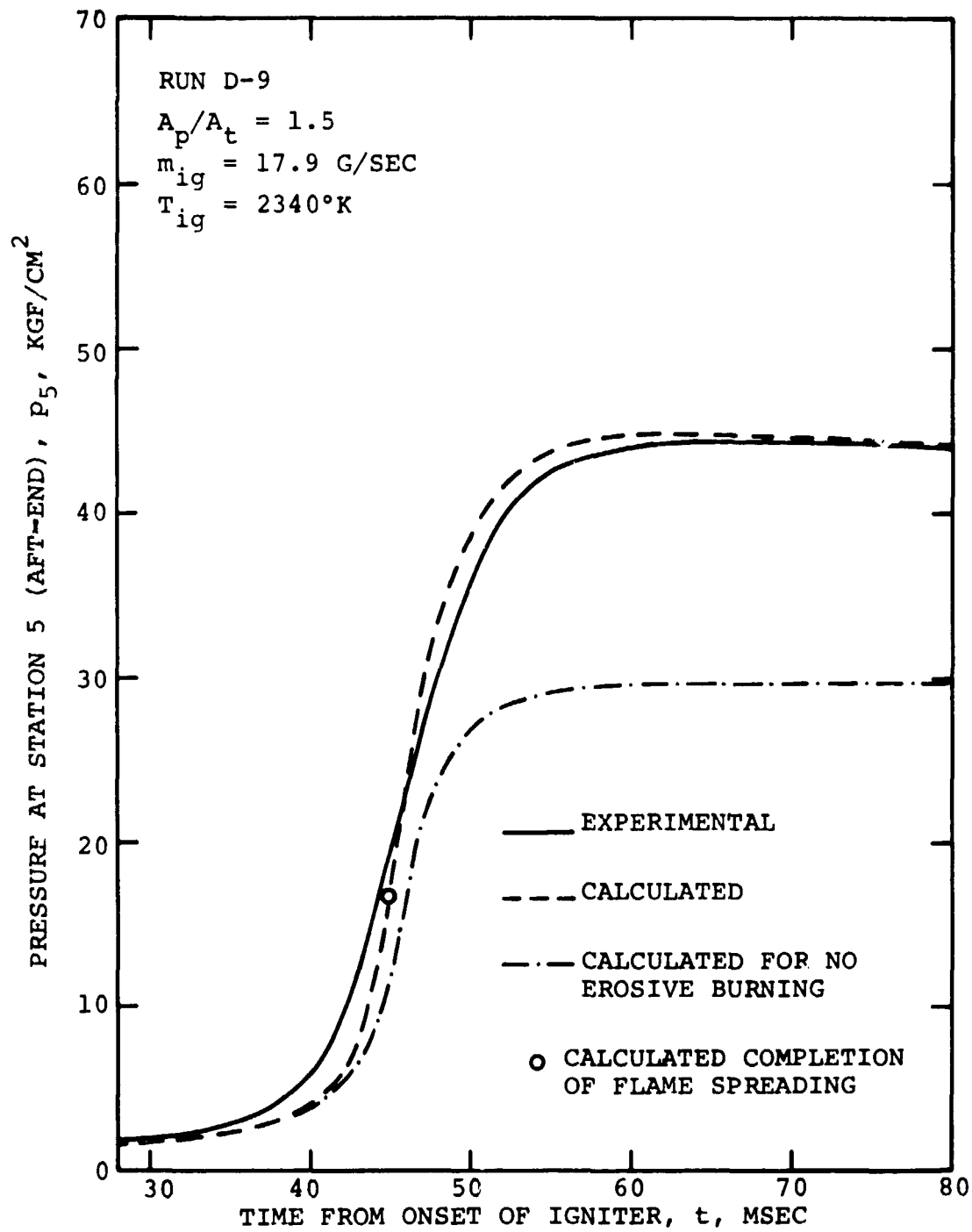
Fig. 26c Comparison of measured and calculated pressure vs time traces at station 5 (aft-end) for $A_p/A_t = 1.2$.
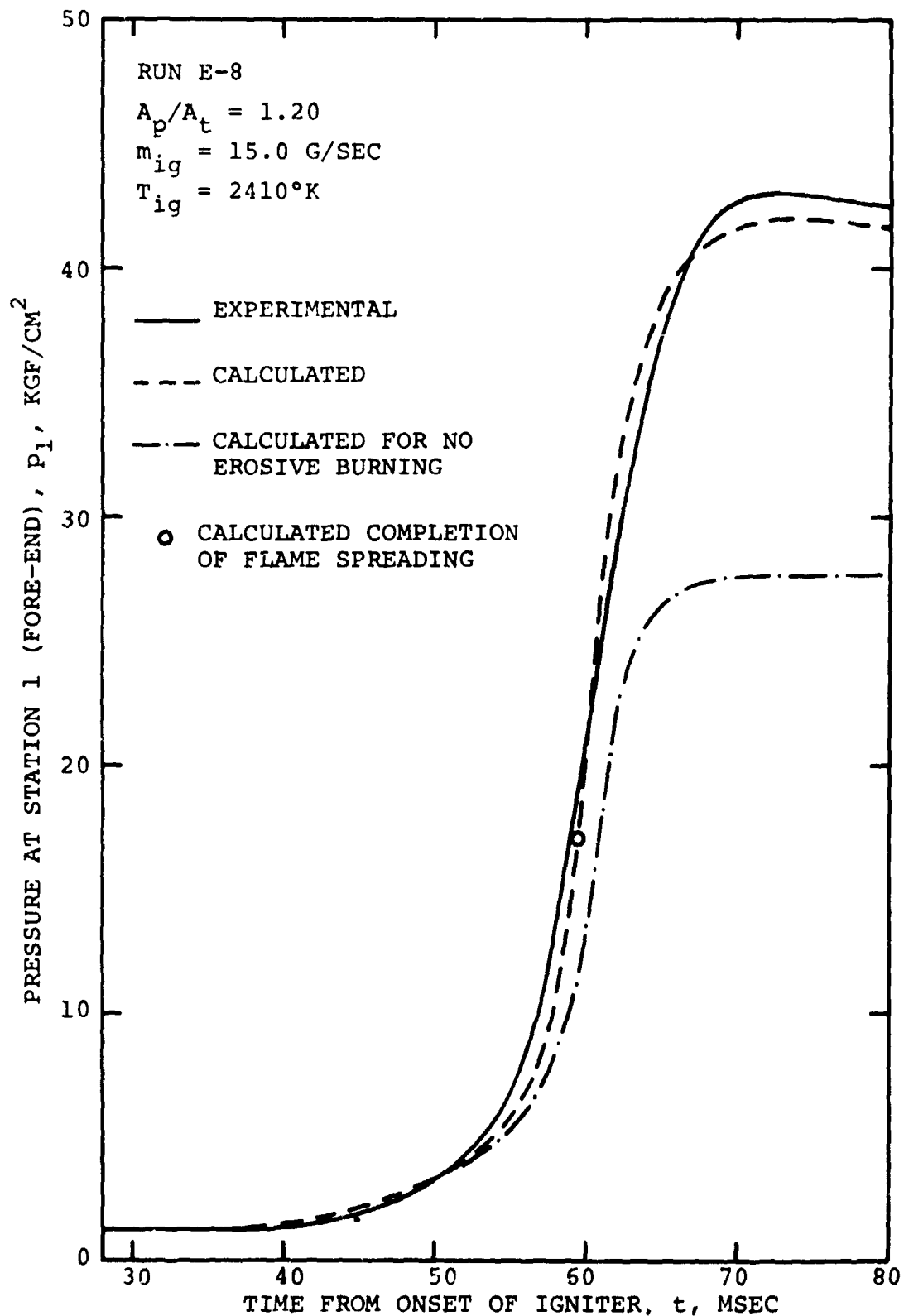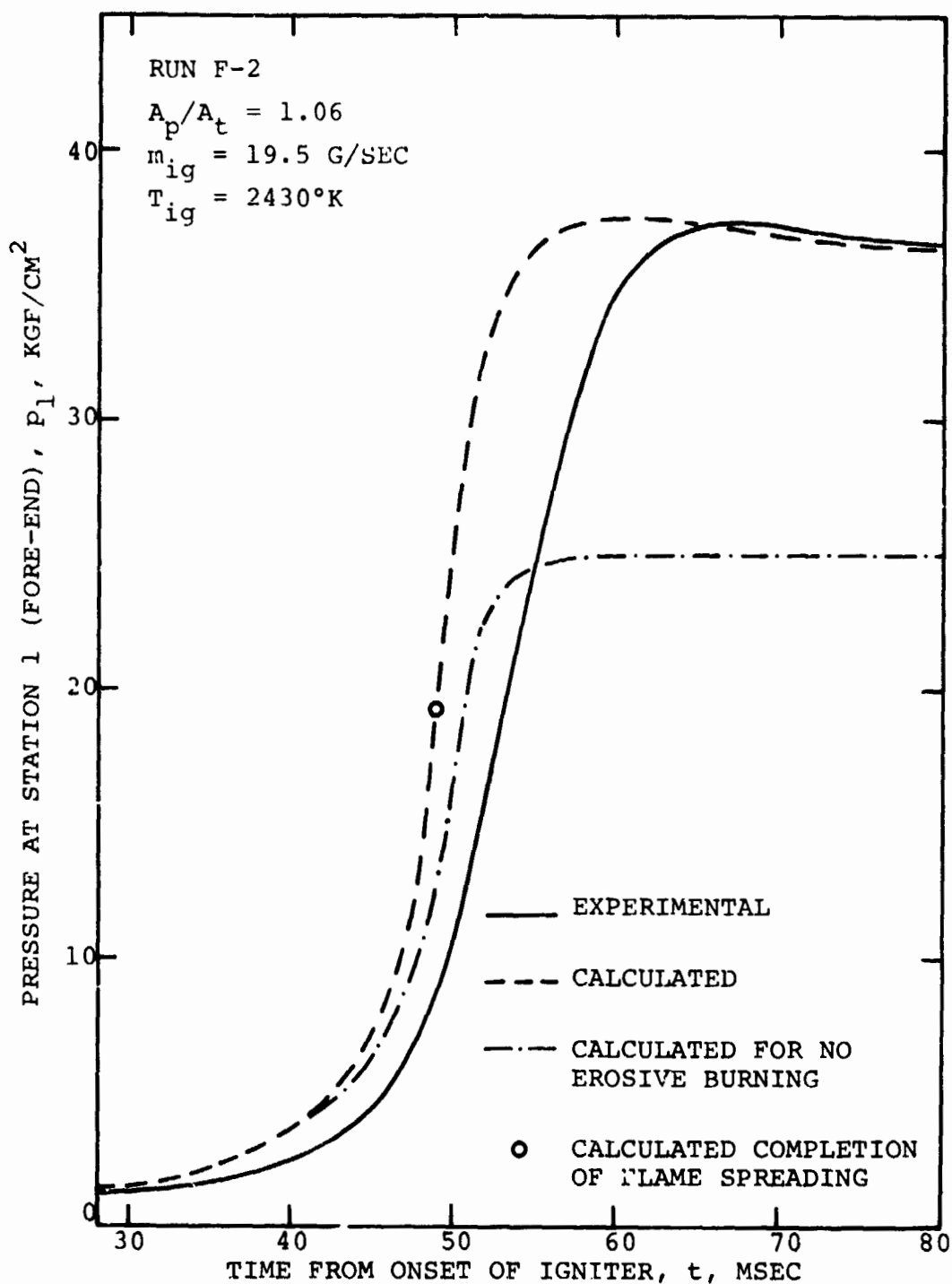
Fig. 27a   Comparison of measured and calculated
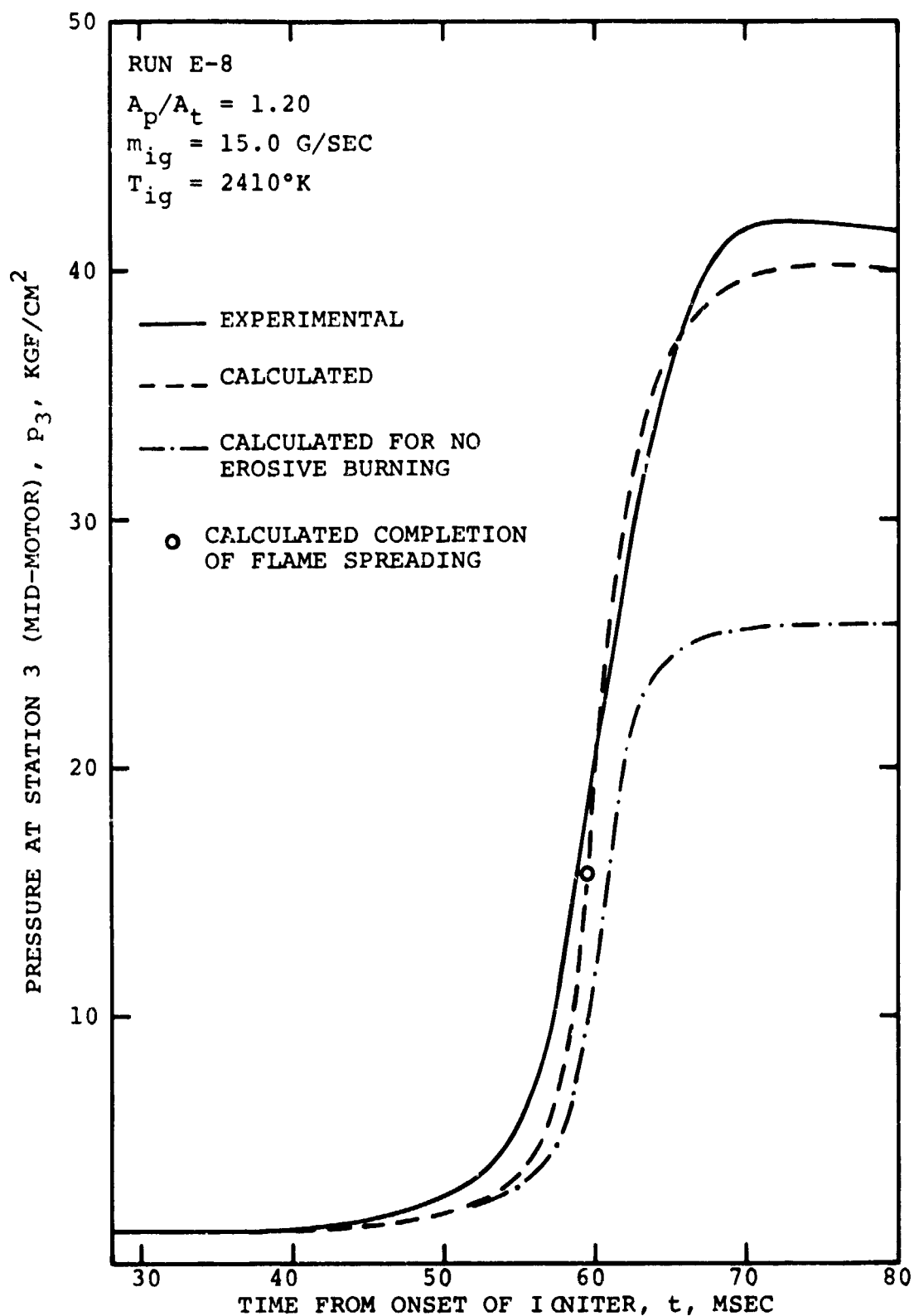pressure vs time traces at station 1
(fore-end) for A_p/A_t = 1.06.
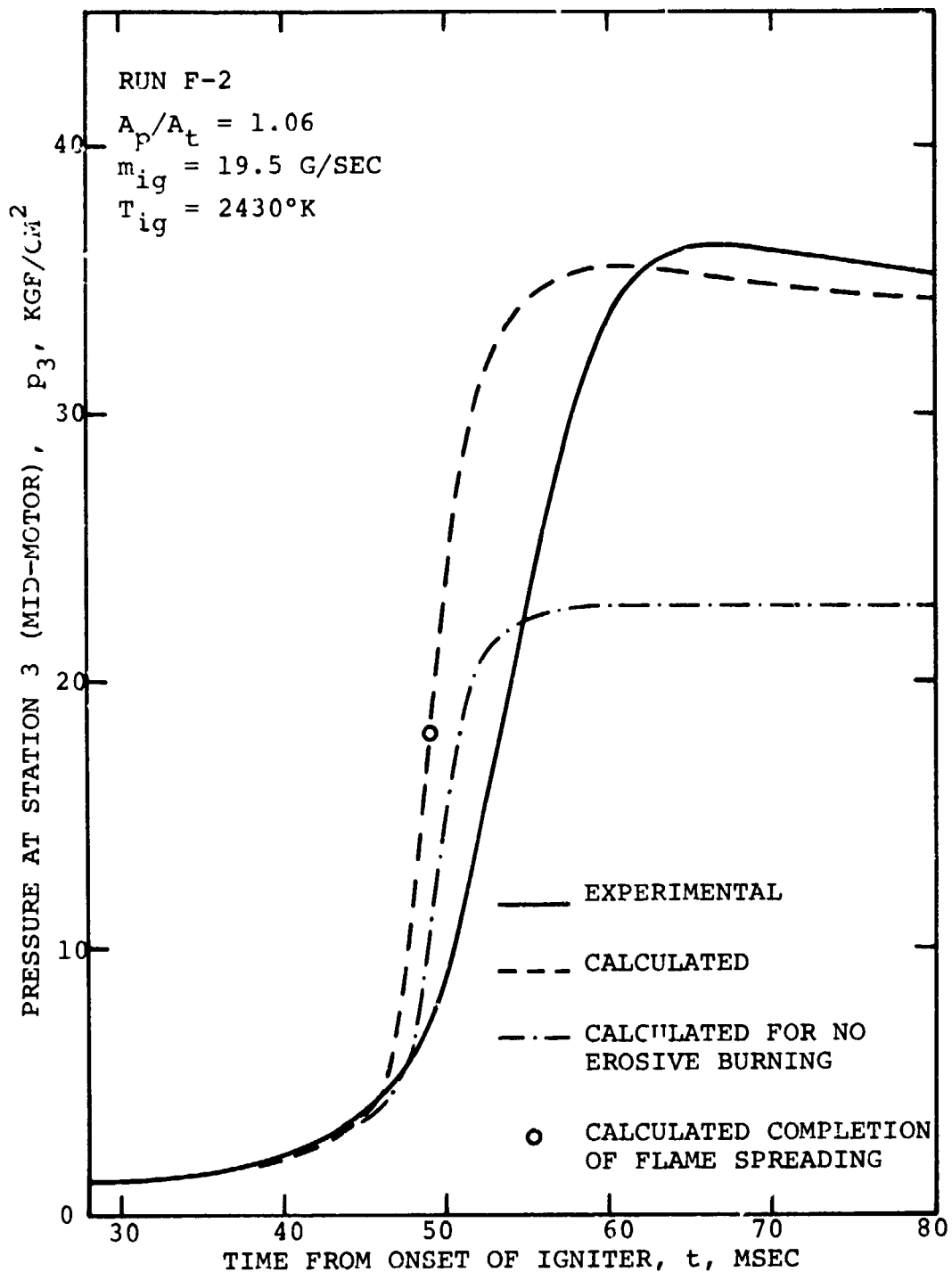
Fig. 27b   Comparison of measured and calculated pressure
vs time traces at station 3 (mid-motor) for
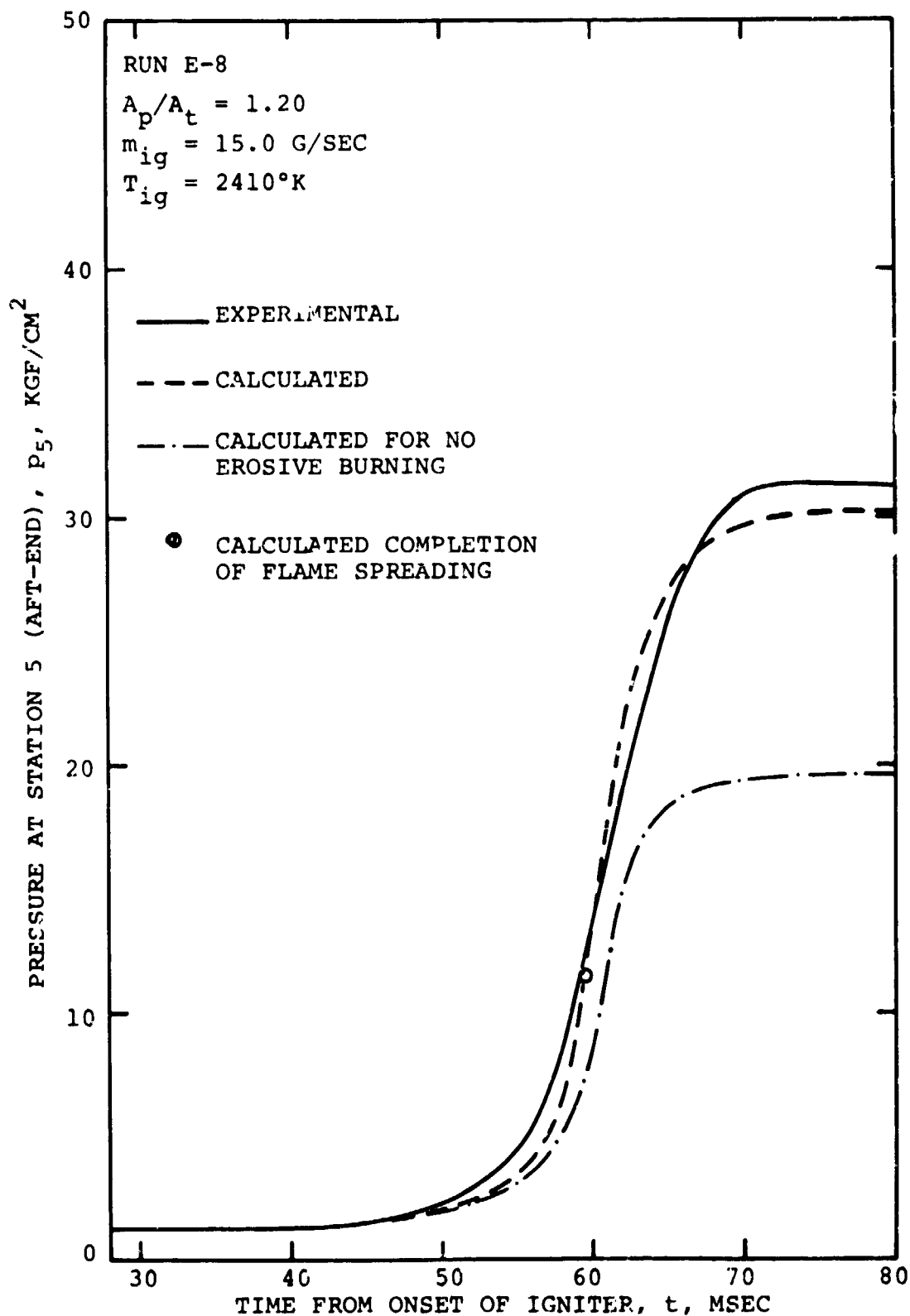A_p/A_t = 1.06.
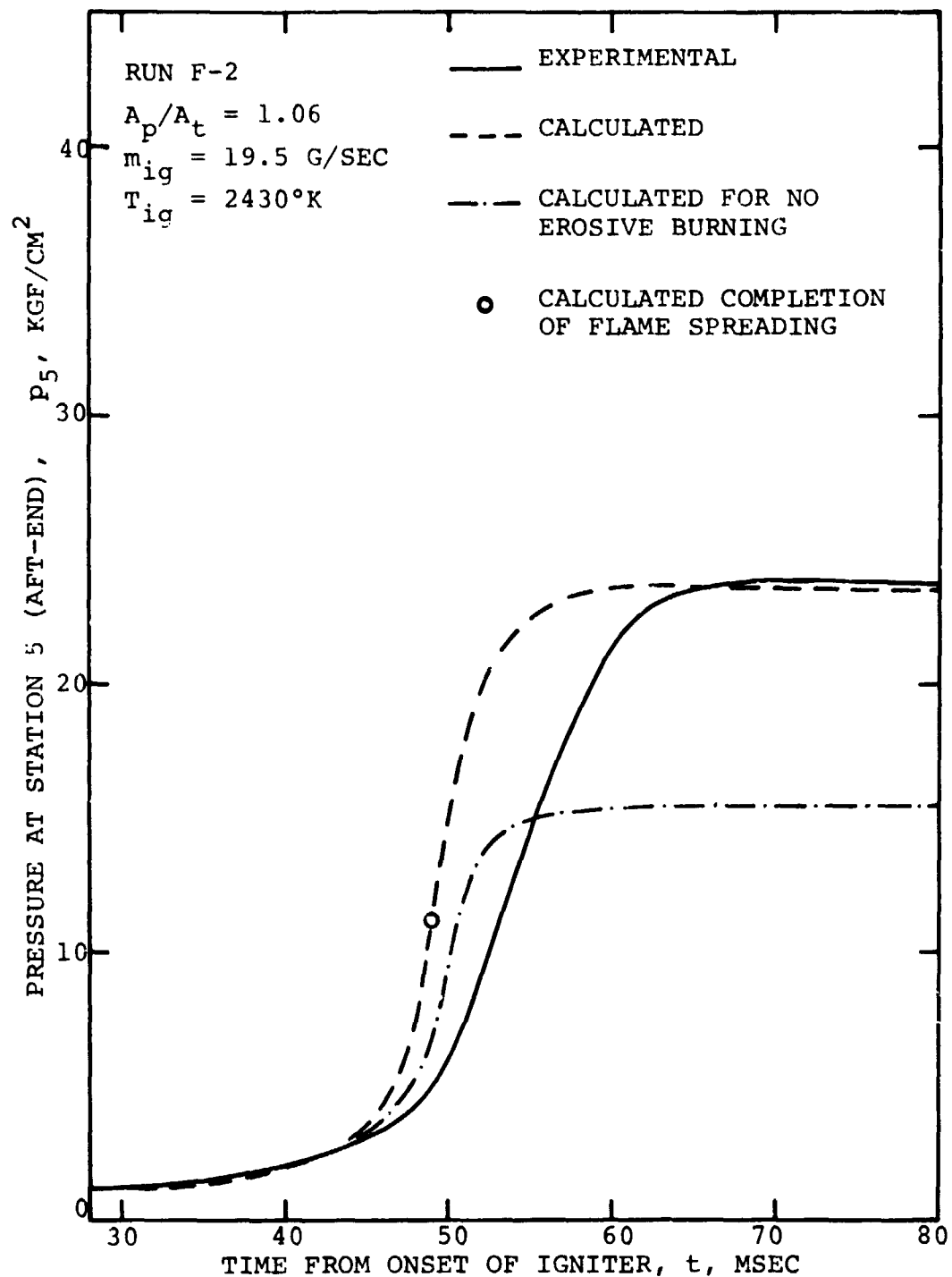
Fig. 27c   Comparison of measured and calculated pressure
vs time traces at station 5 (aft-end) for
A_p/A_t = 1.06.
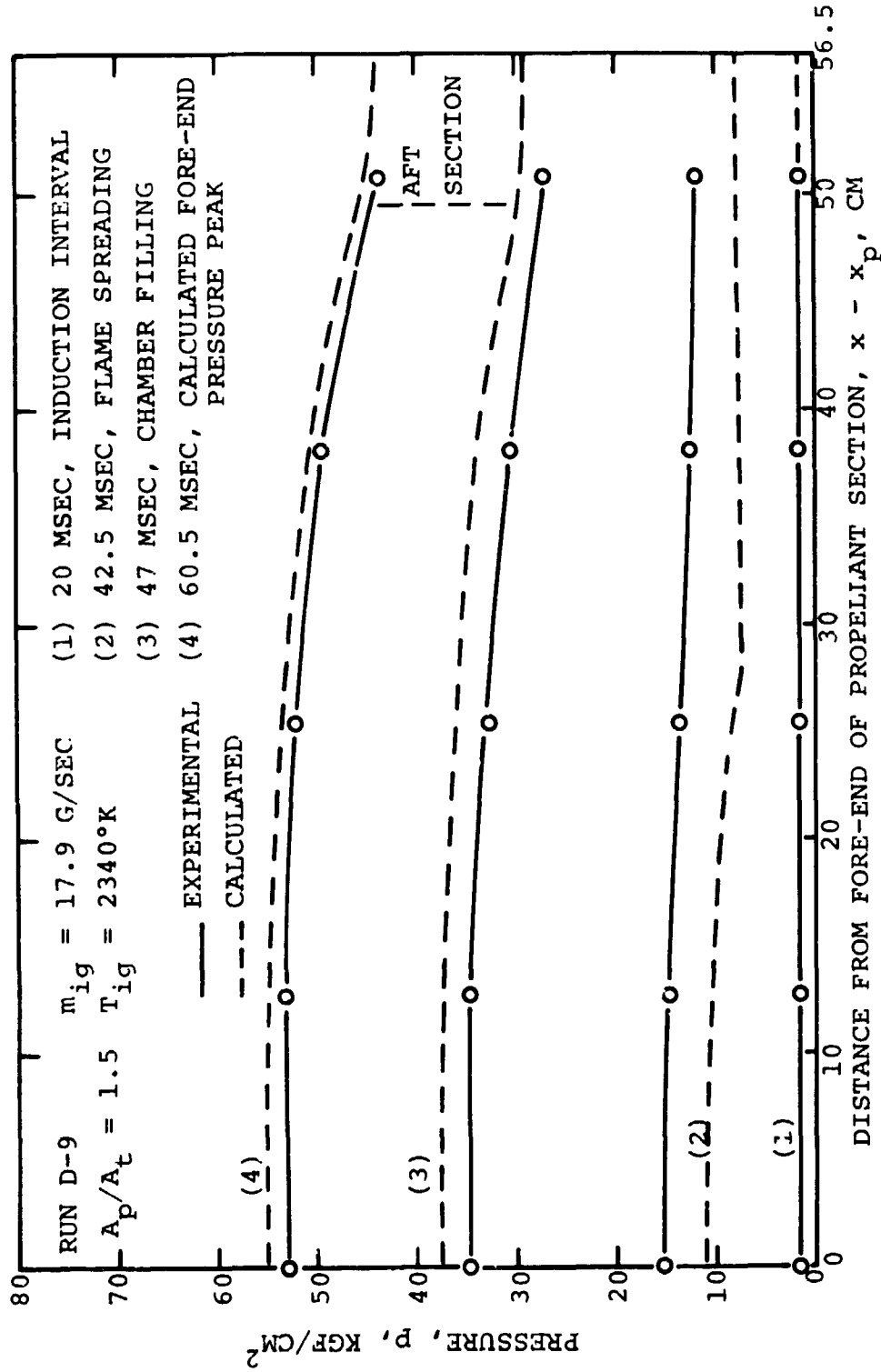
Fig. 28 Comparison of measured and calculated axial pressure distributions at four times during the starting transient of Test D-9 ($A_p/A_t = 1.5$).
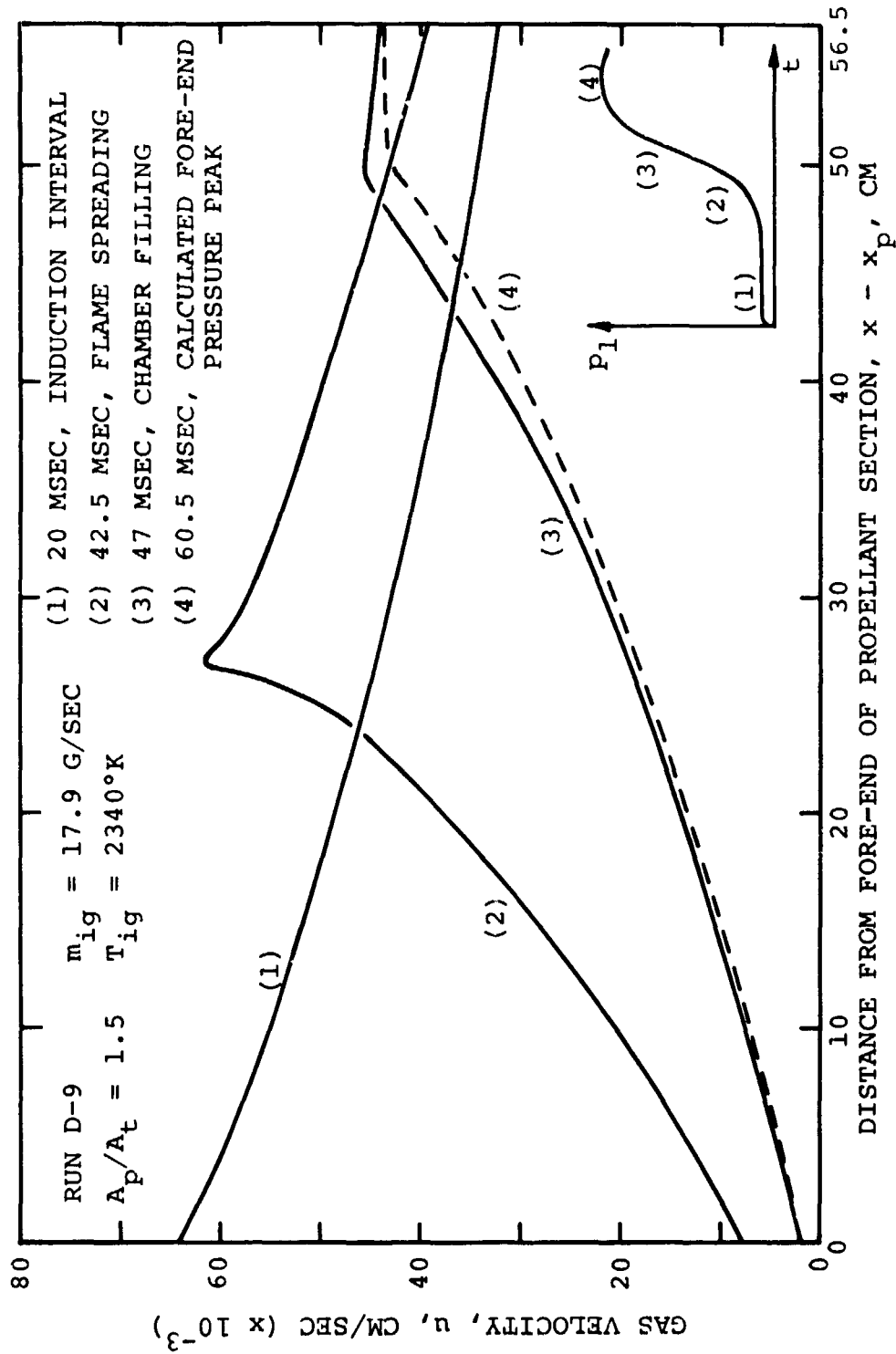
Fig. 29   Calculated axial gas velocity distributions at the same four times as in Fig. 28.

DISTANCE FROM FORE-END OF PROPELLANT SECTION, $x - x_p$, CM
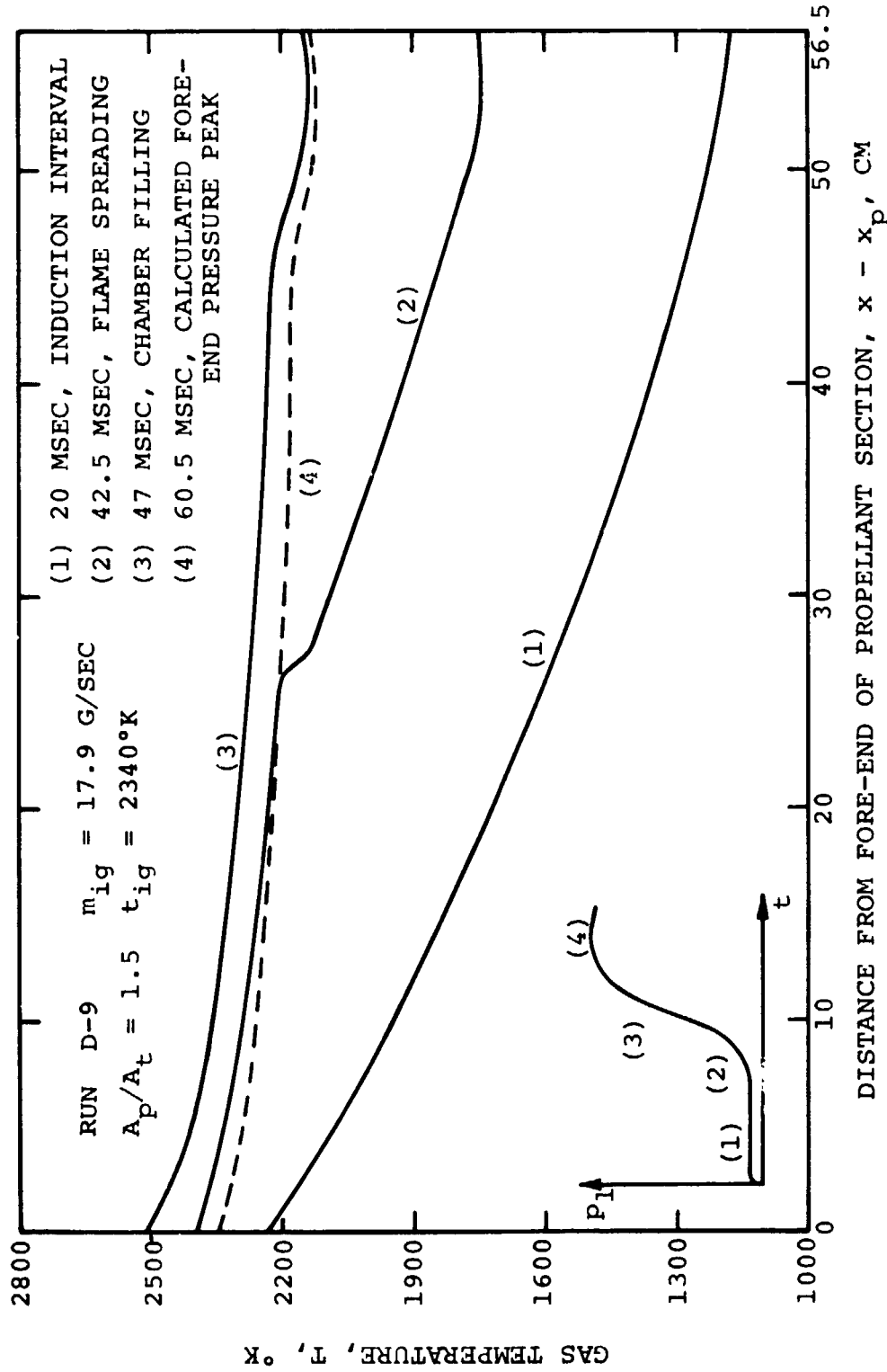
Fig. 30   Calculated axial gas temperature distributions at the same four
times as in Fig. 28.

Fig. 31   Comparison of measured and calculated axial pressure distributions at four times during the starting transient of Test F-2 $(A_p/A_t=1.06)$.
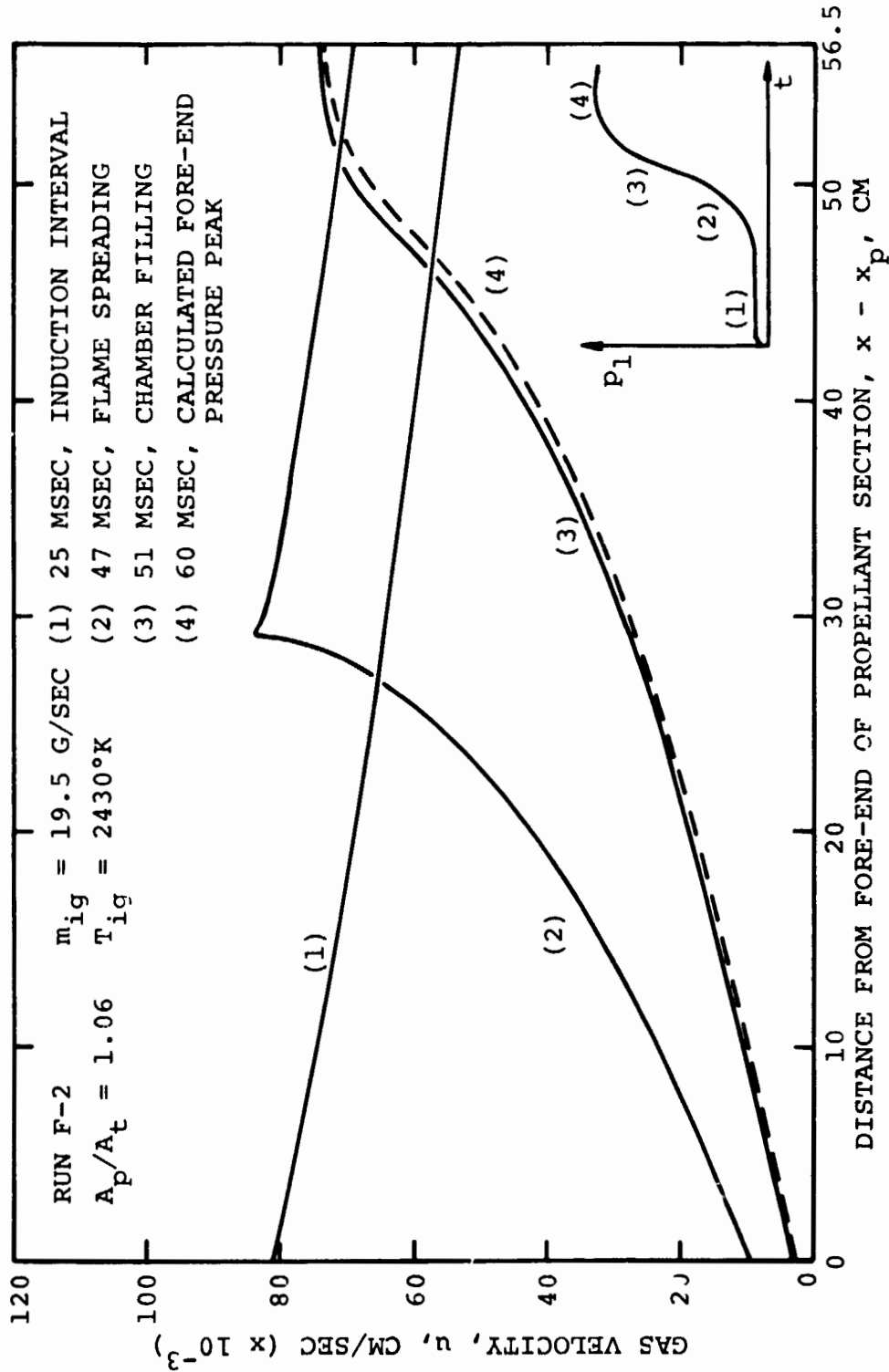
Fig. 32 Calculated axial gas velocity distributions at the same four times as in Fig. 31.

Fig. 33   Calculated axial gas temperature distributions at the same four
times as in Fig. 31.
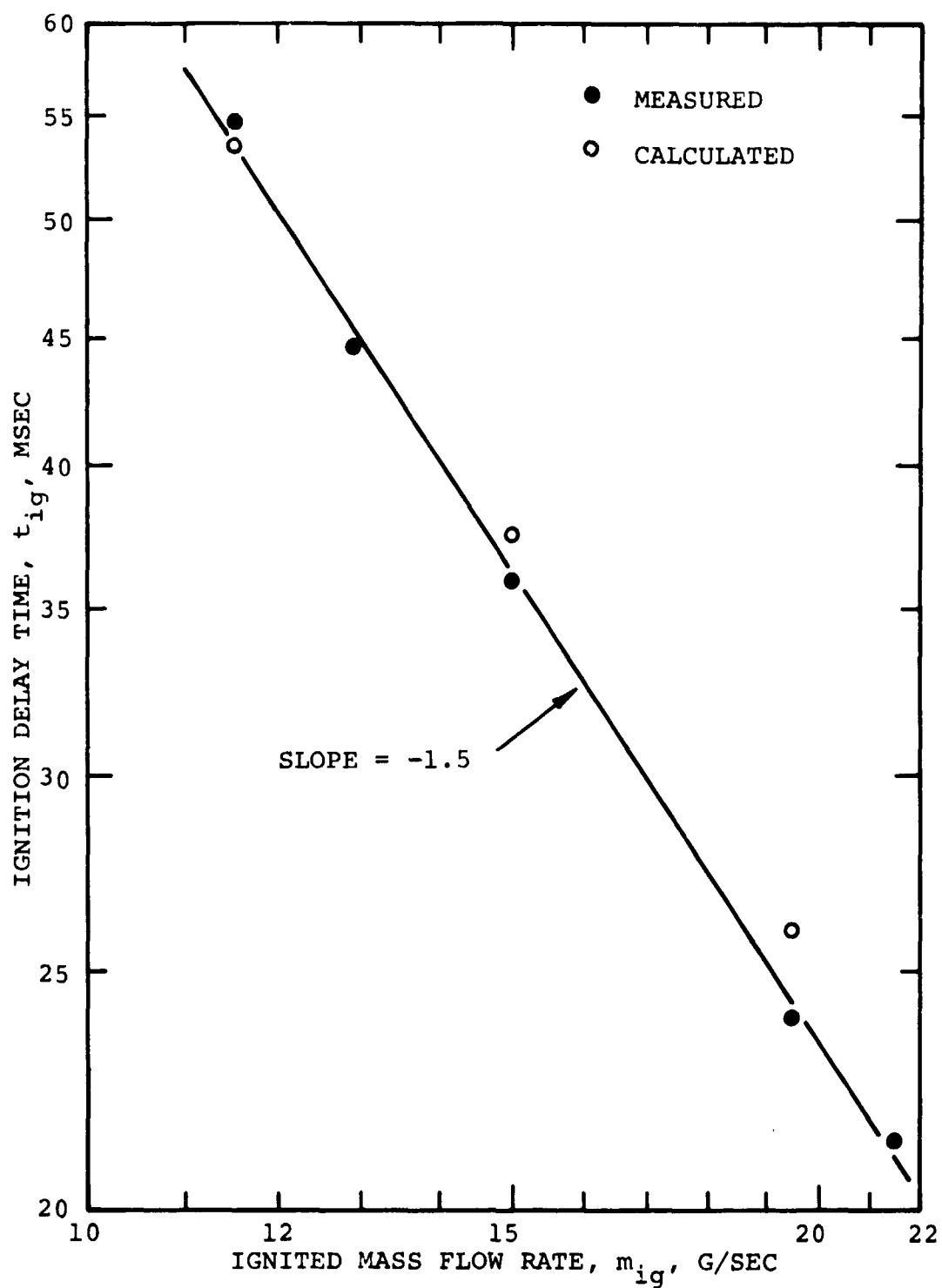
Fig. 34   Measured and calculated times of ignition delay
          for $A_p/A_t = 1.2$.
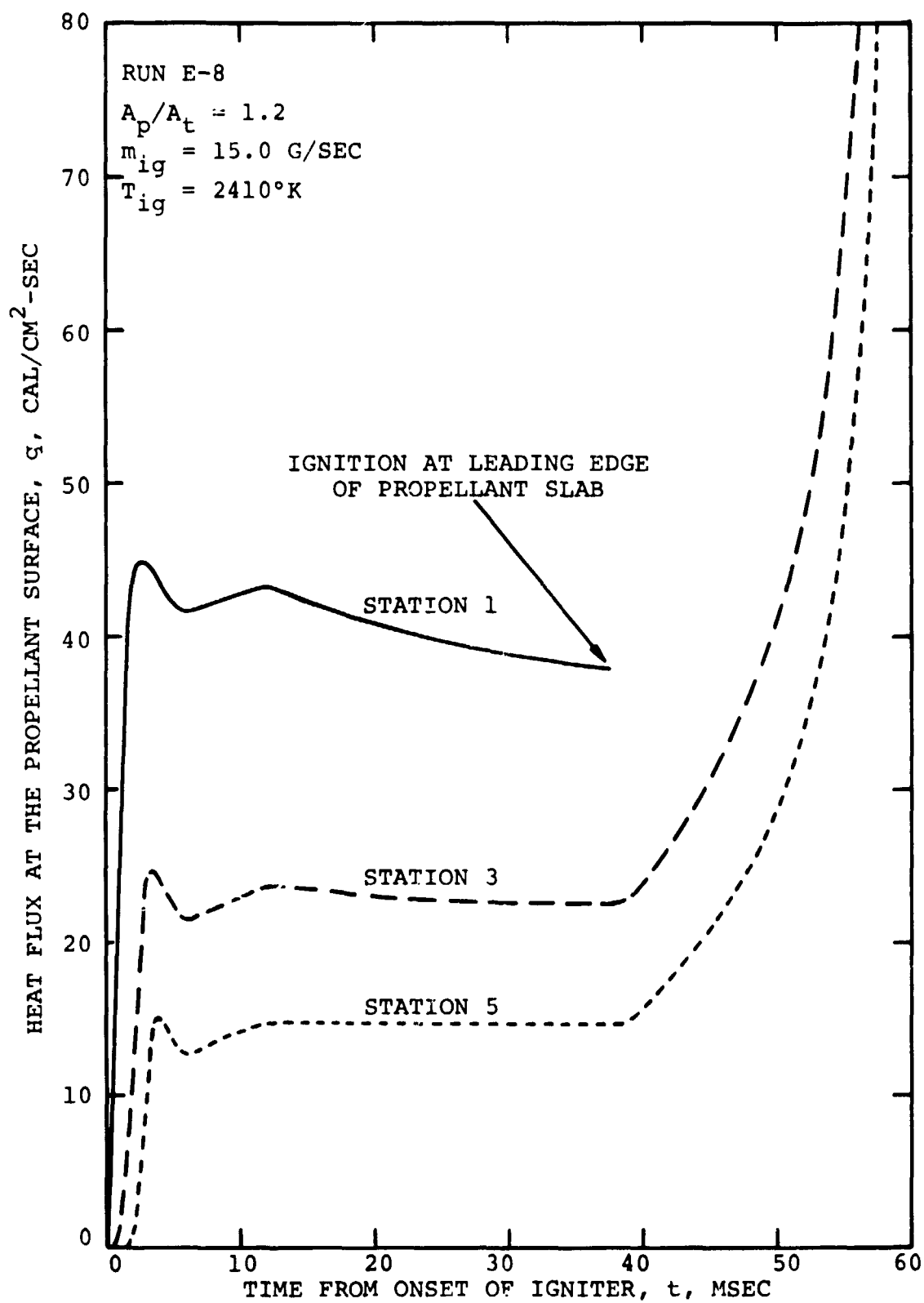
Fig. 35   Calculated heat flux at the propellant surface
vs time at three different positions along the
motor.
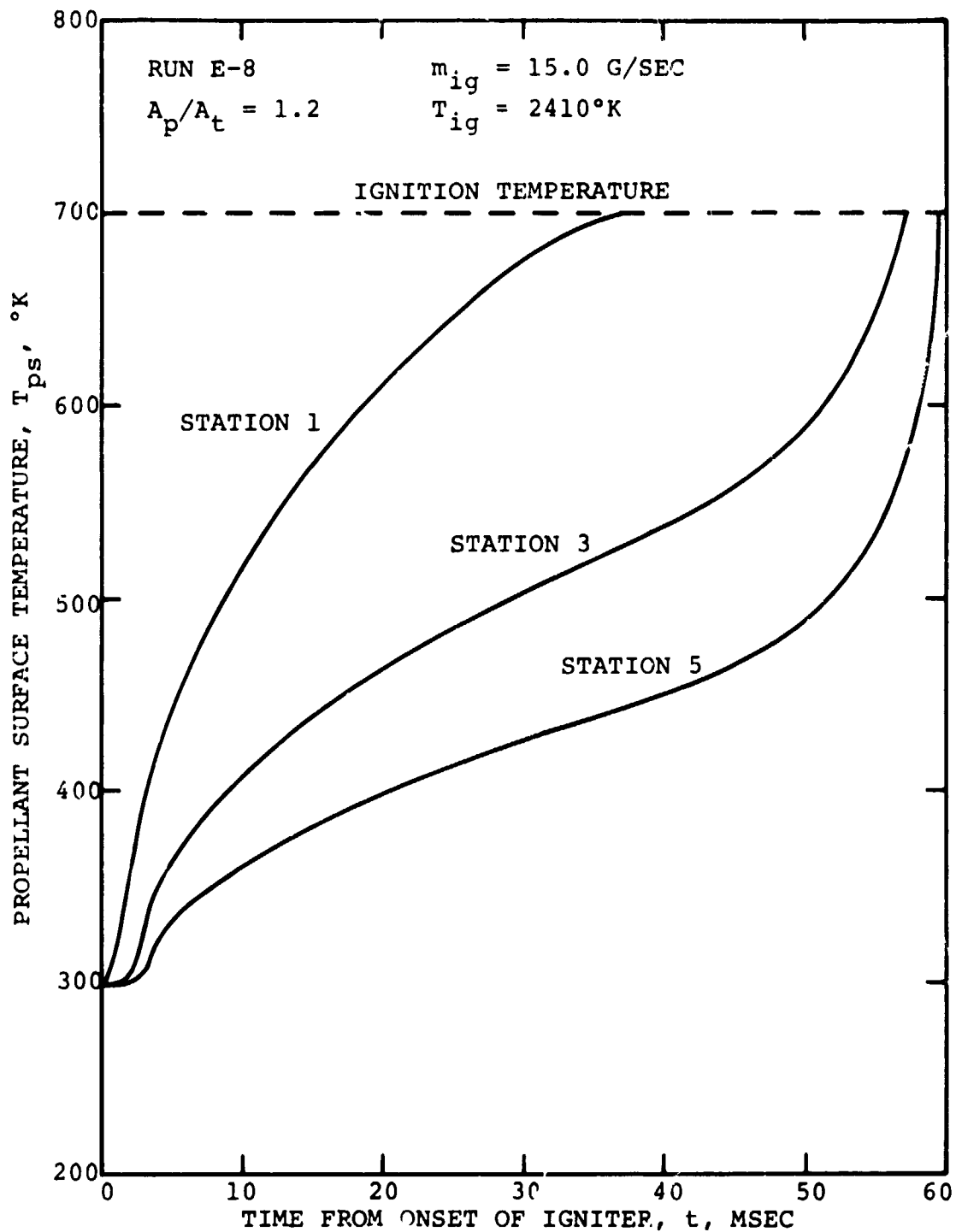
Fig. 36   Calculated propellant surface temperature vs
time at three different positions along the
port. The calculated surface heat flux is
shown in Fig. 35.
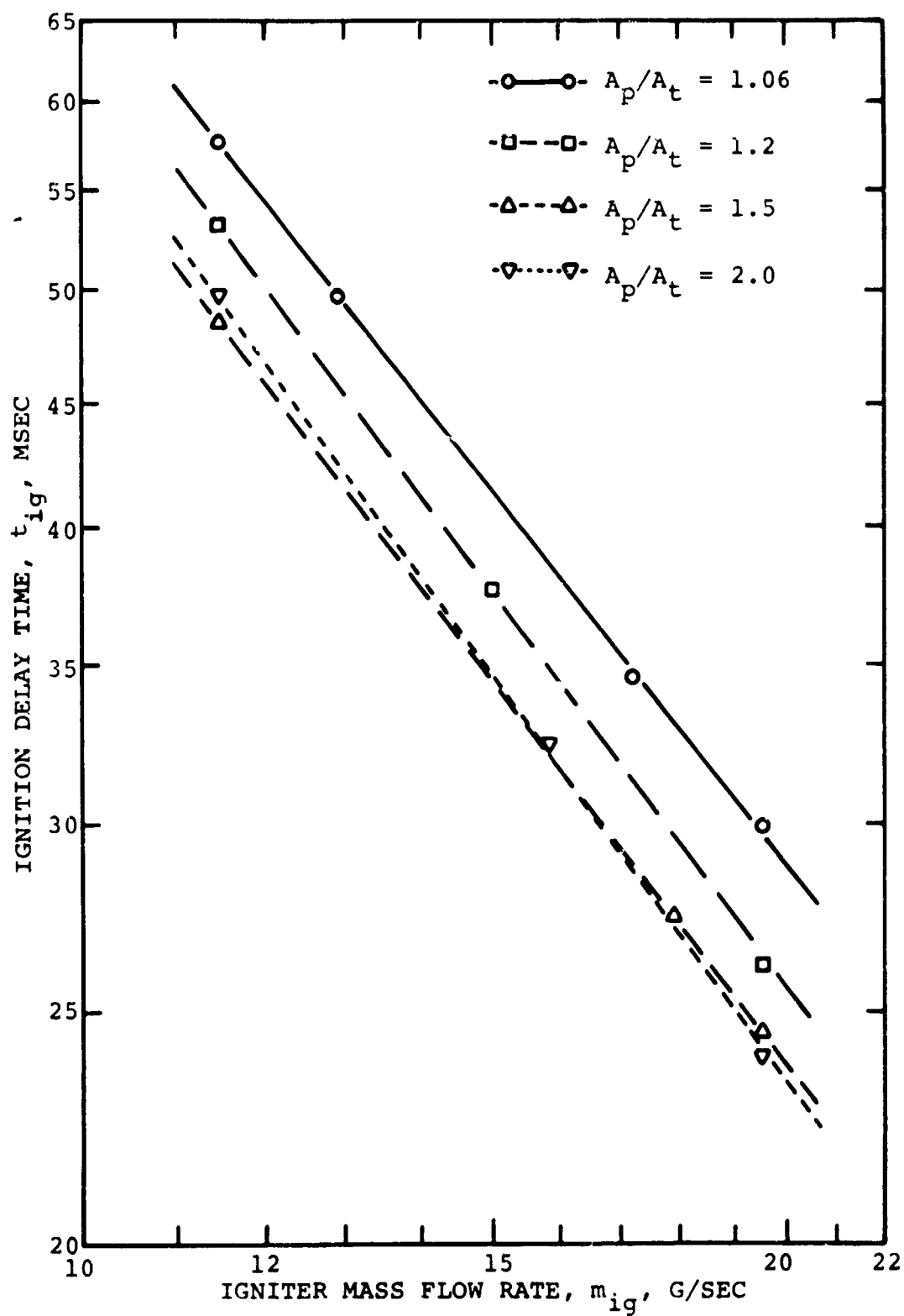
Fig. 37   Calculated ignition delay time vs igniter mass
flow rate for different A_p/A_t.
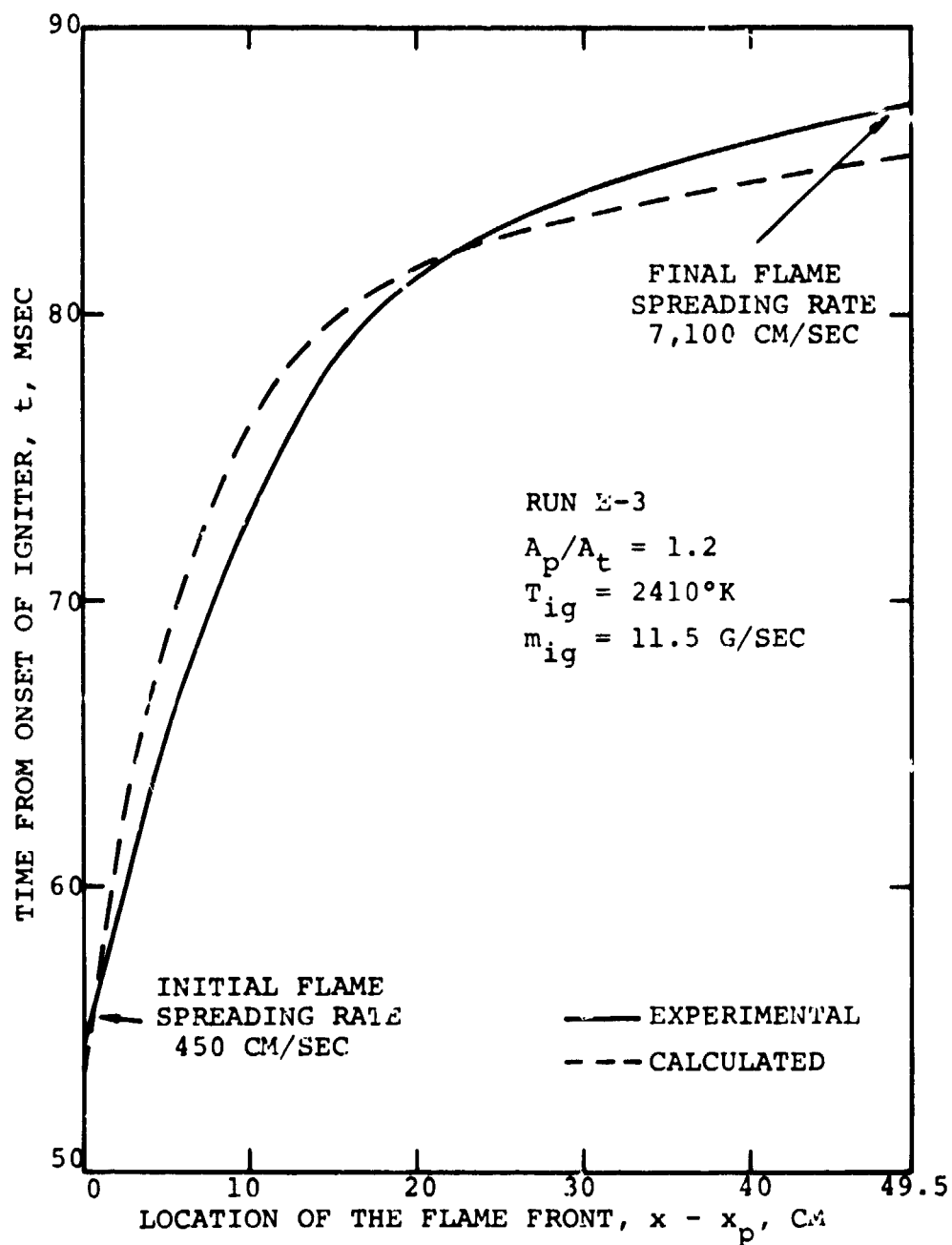
Fig. 38   Measured and calculated ignition flame
           front locations vs time, with flame
           spreading velocities noted.
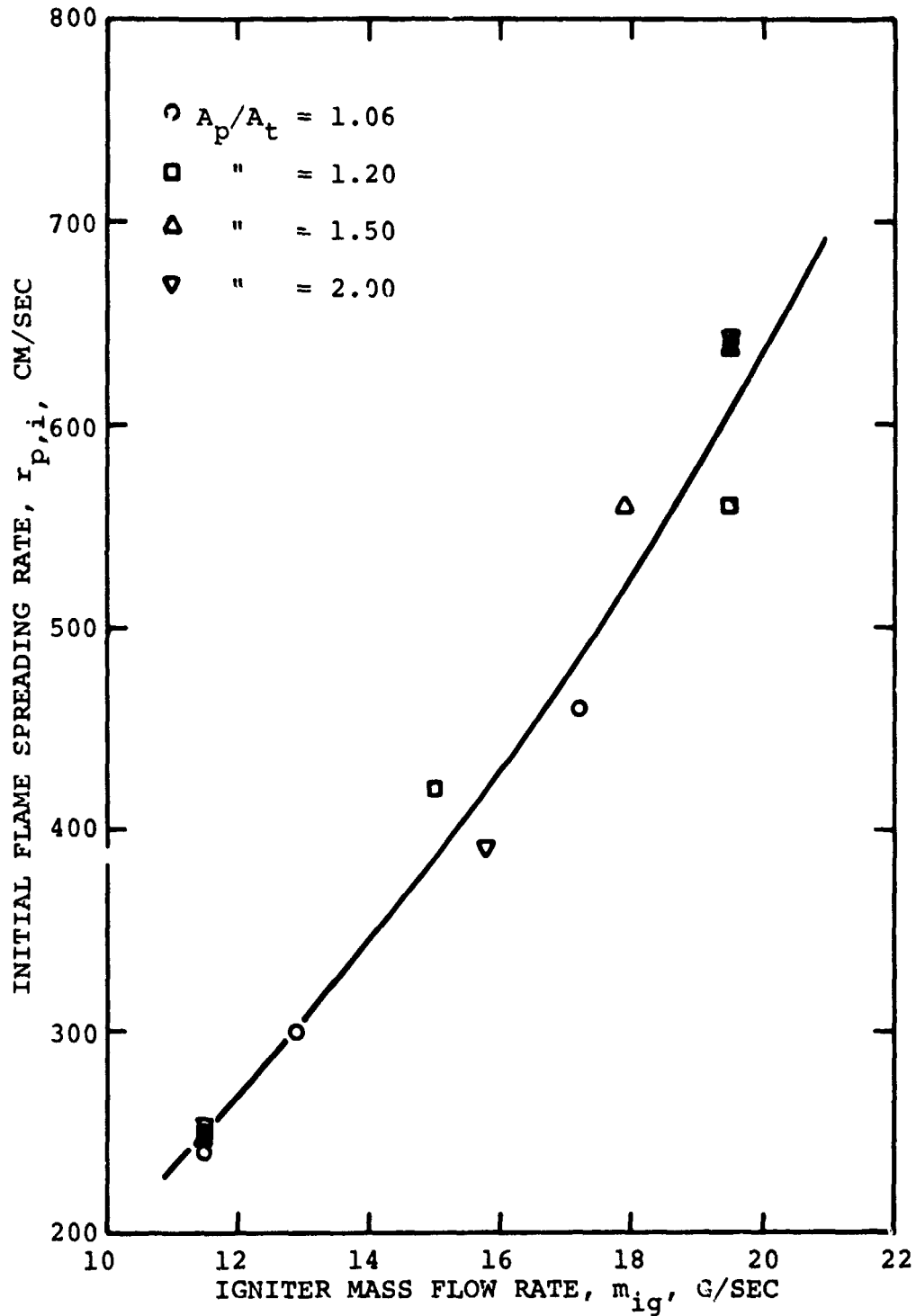
Fig. 39   Calculated initial flame spreading rate vs
          igniter mass flow rate.
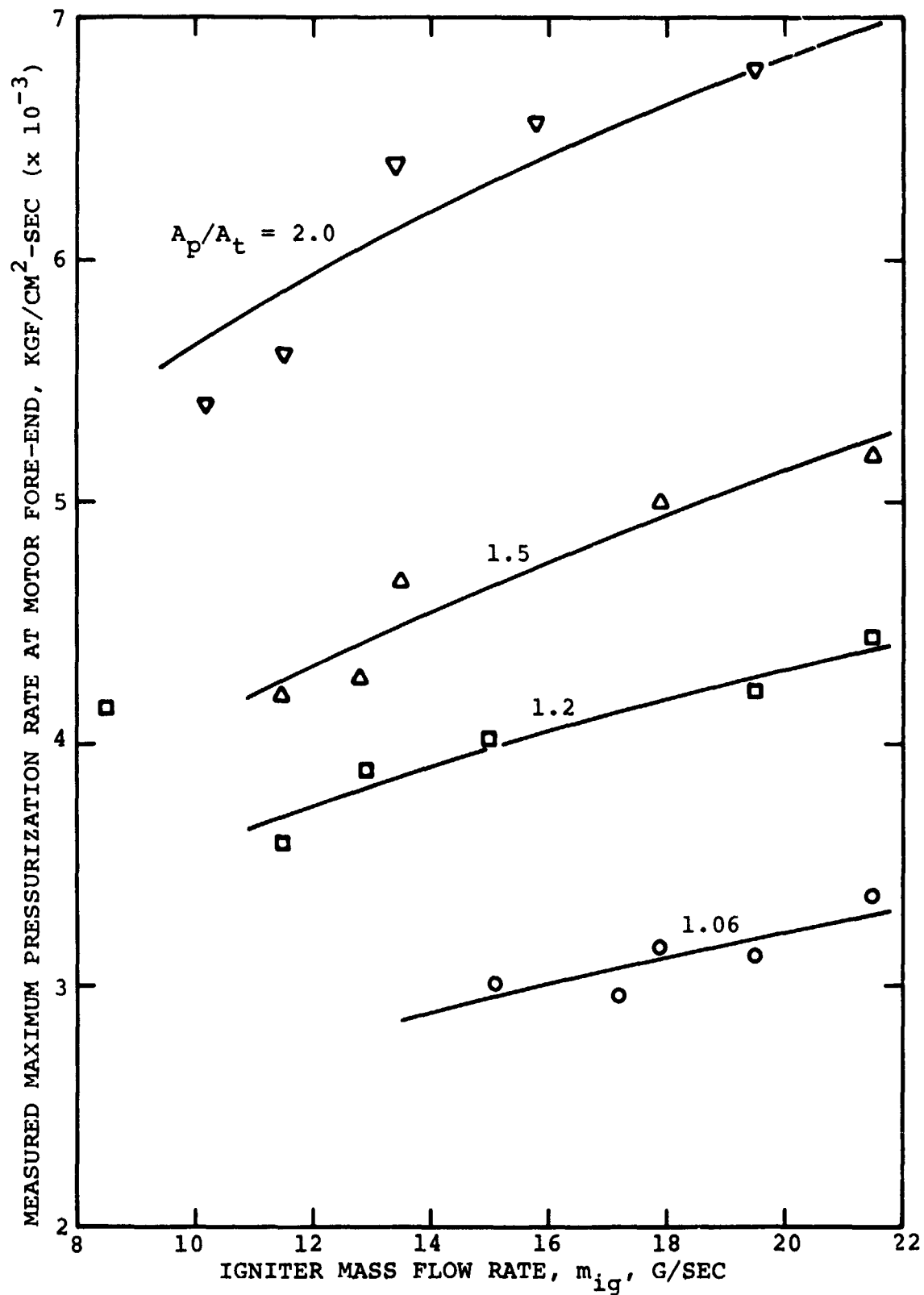
Fig. 40   Measured maximum pressurization rates at motor
fore-end (station 1) vs igniter mass flow rate
for different A_p/A_t.
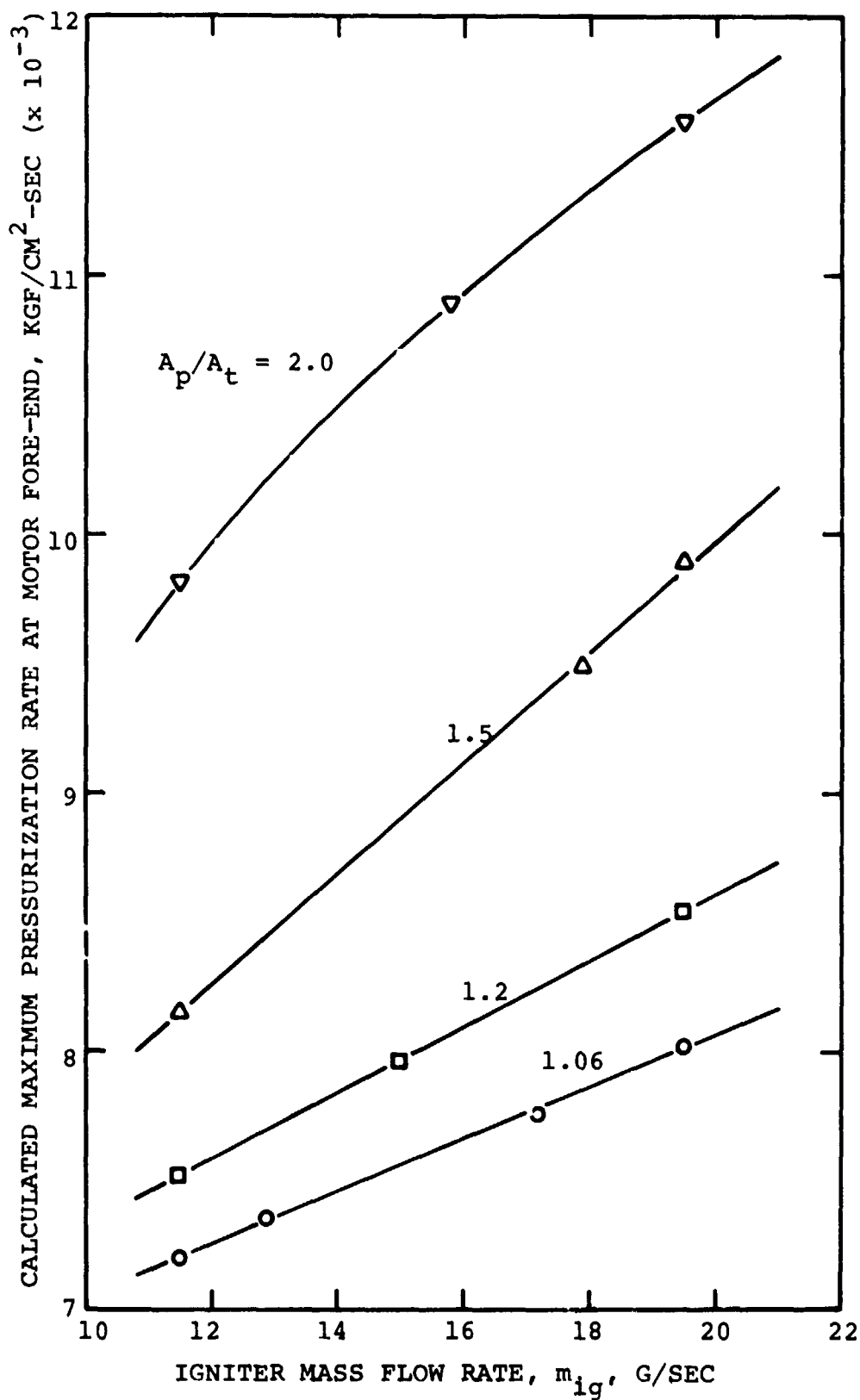
Fig. 41   Calculated maximum pressurization rates at
motor fore-end vs igniter mass flow rate for
different A_p/A_t.
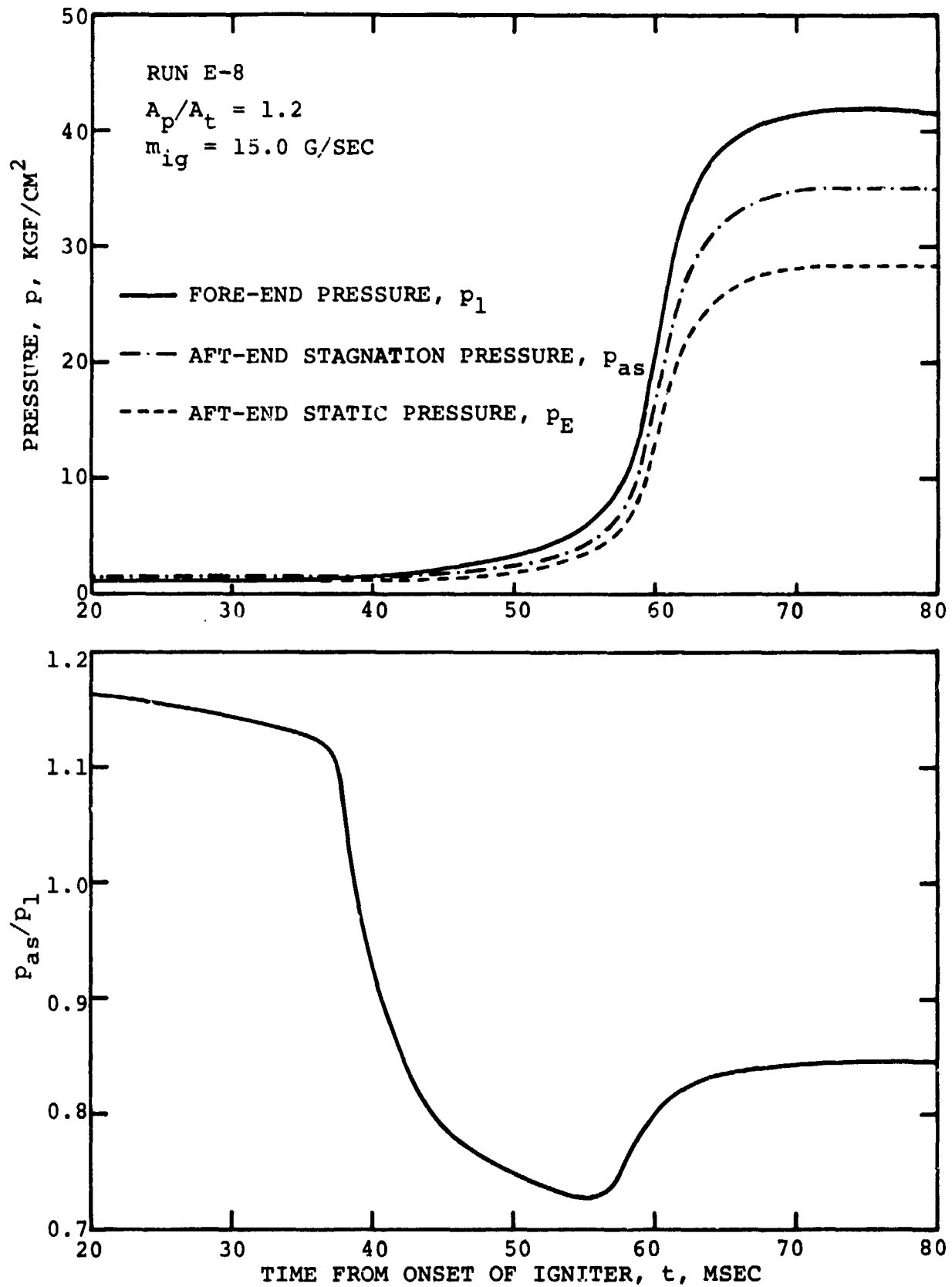
Fig. 42   Calculated transient variation of the fore-end and
aft-end static pressures, aft-end stagnation pressure
and ratio of aft-end stagnation to fore-end static
pressure.
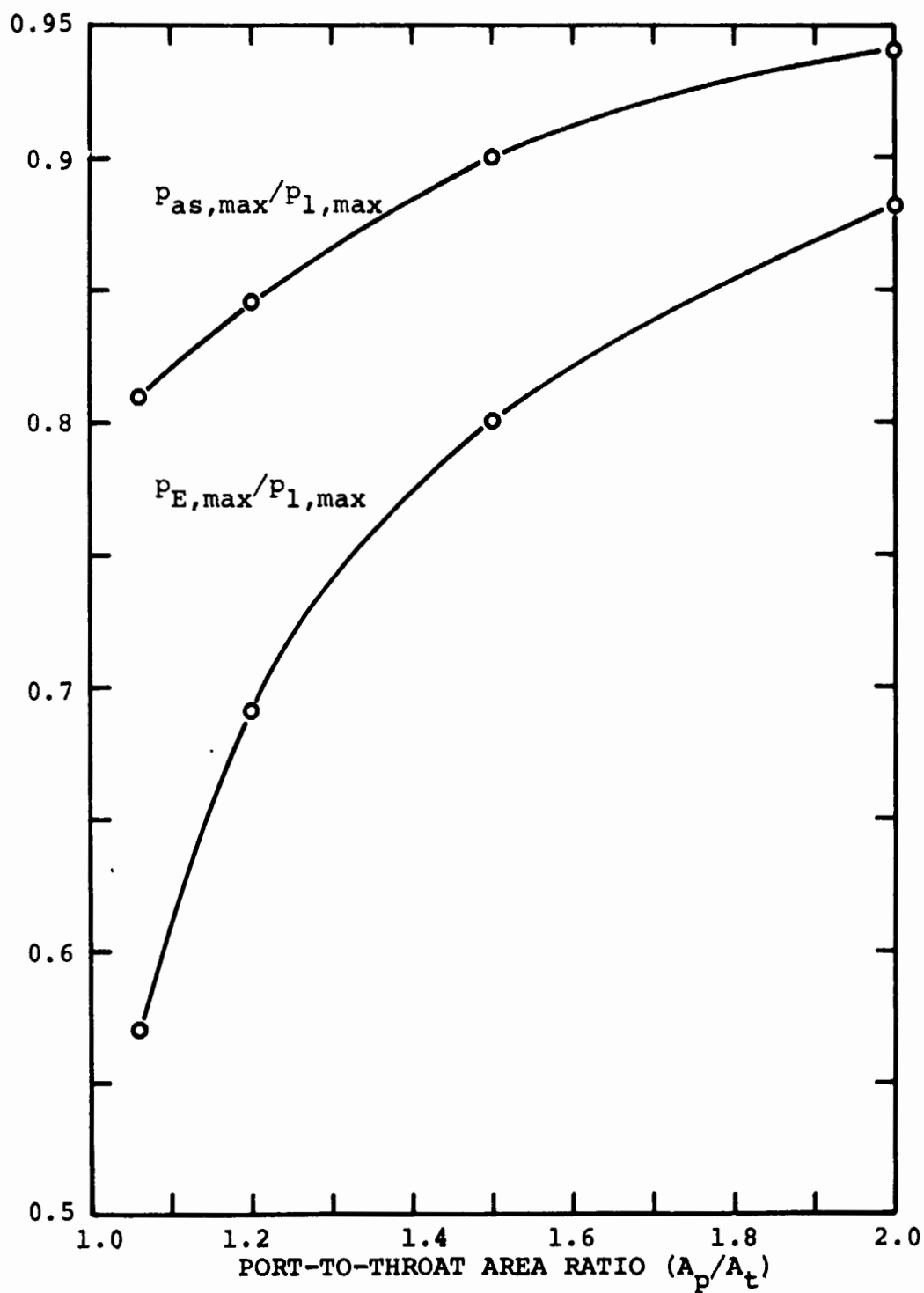
Fig. 43 Calculated ratios of maximum static and stagna-
tion pressures at motor aft-end to maximum
motor fore-end pressure vs port-to-throat area
ratio.
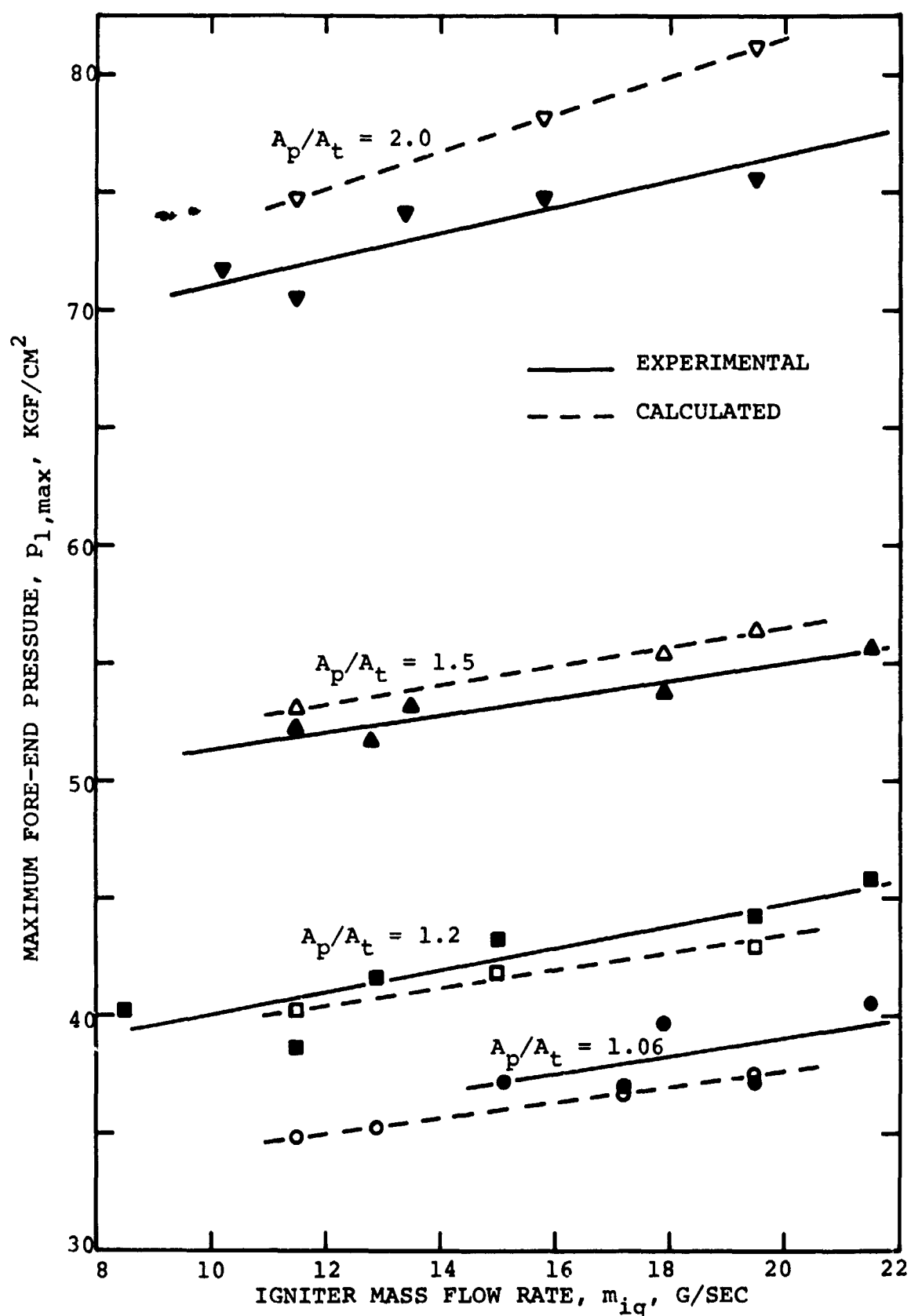
Fig. 44   Measured and calculated maximum fore-end pressure
vs igniter mass flow rate for different A_p/A_t.
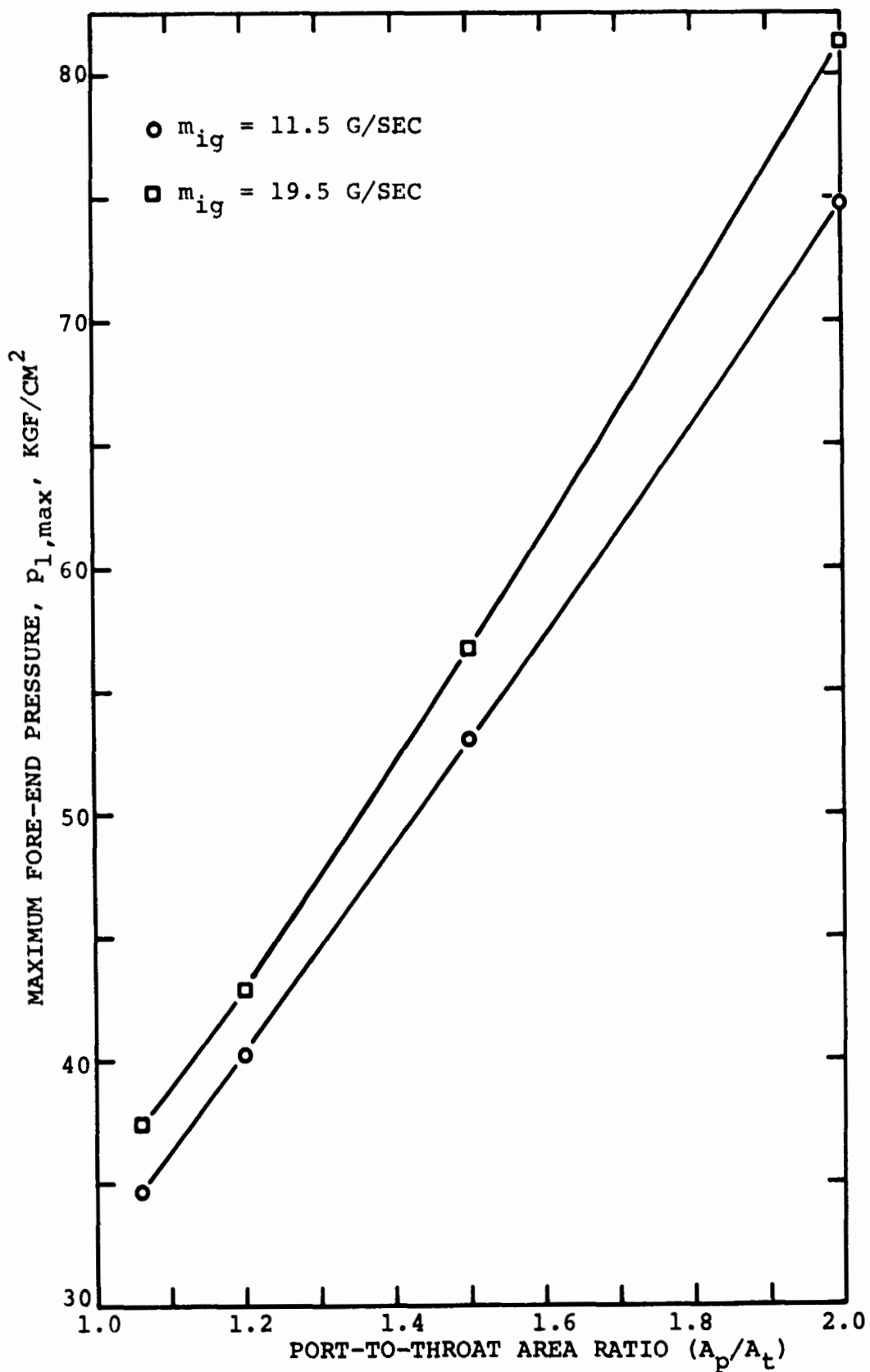
Fig. 45   Calculated maximum fore-end pressure vs
A_p/A_t for two different igniter mass flow
rates.
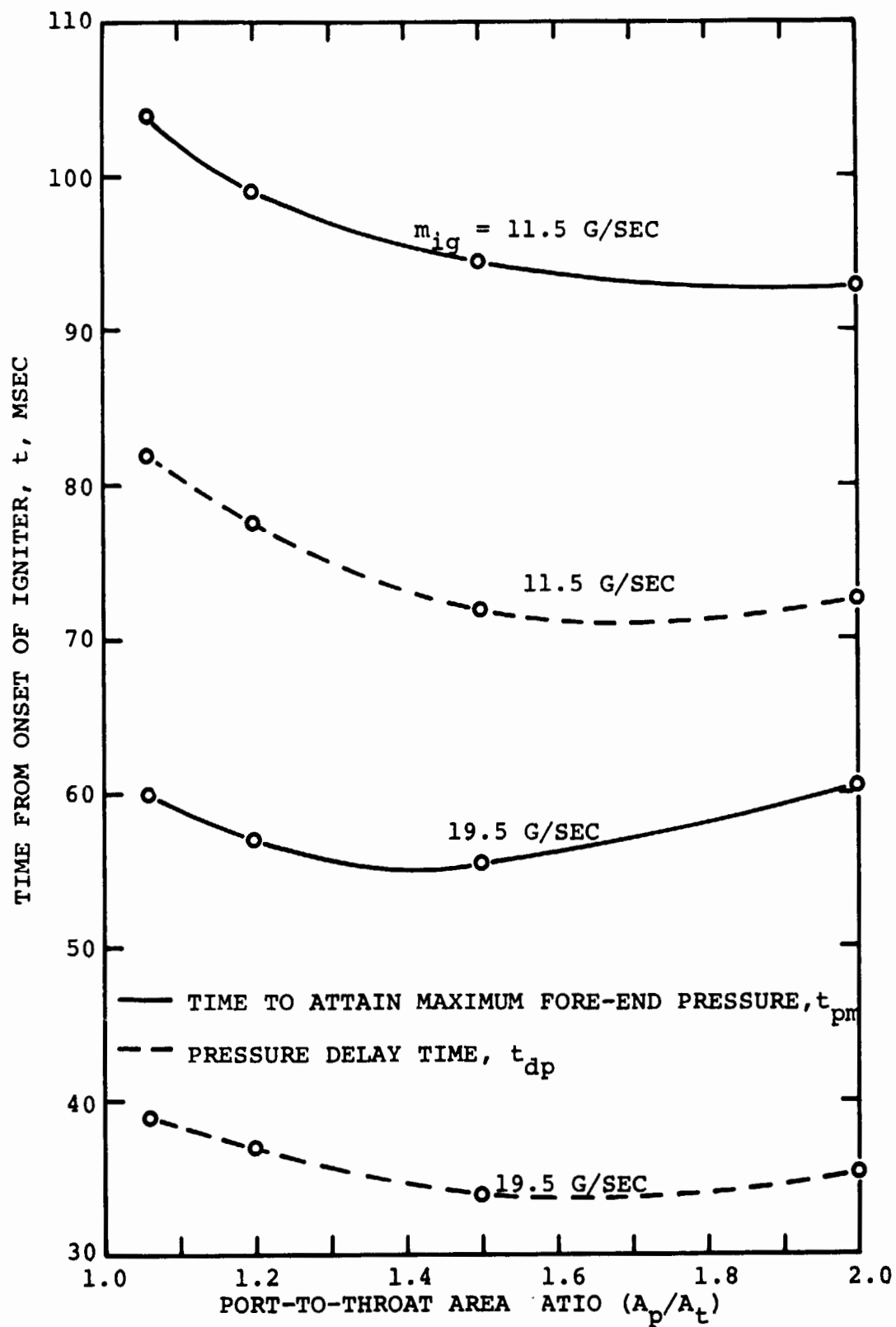
Fig. 46   Calculated time to attain maximum fore-end
pressure and pressure delay time vs A_p/A_t
for two igniter mass flow rates.
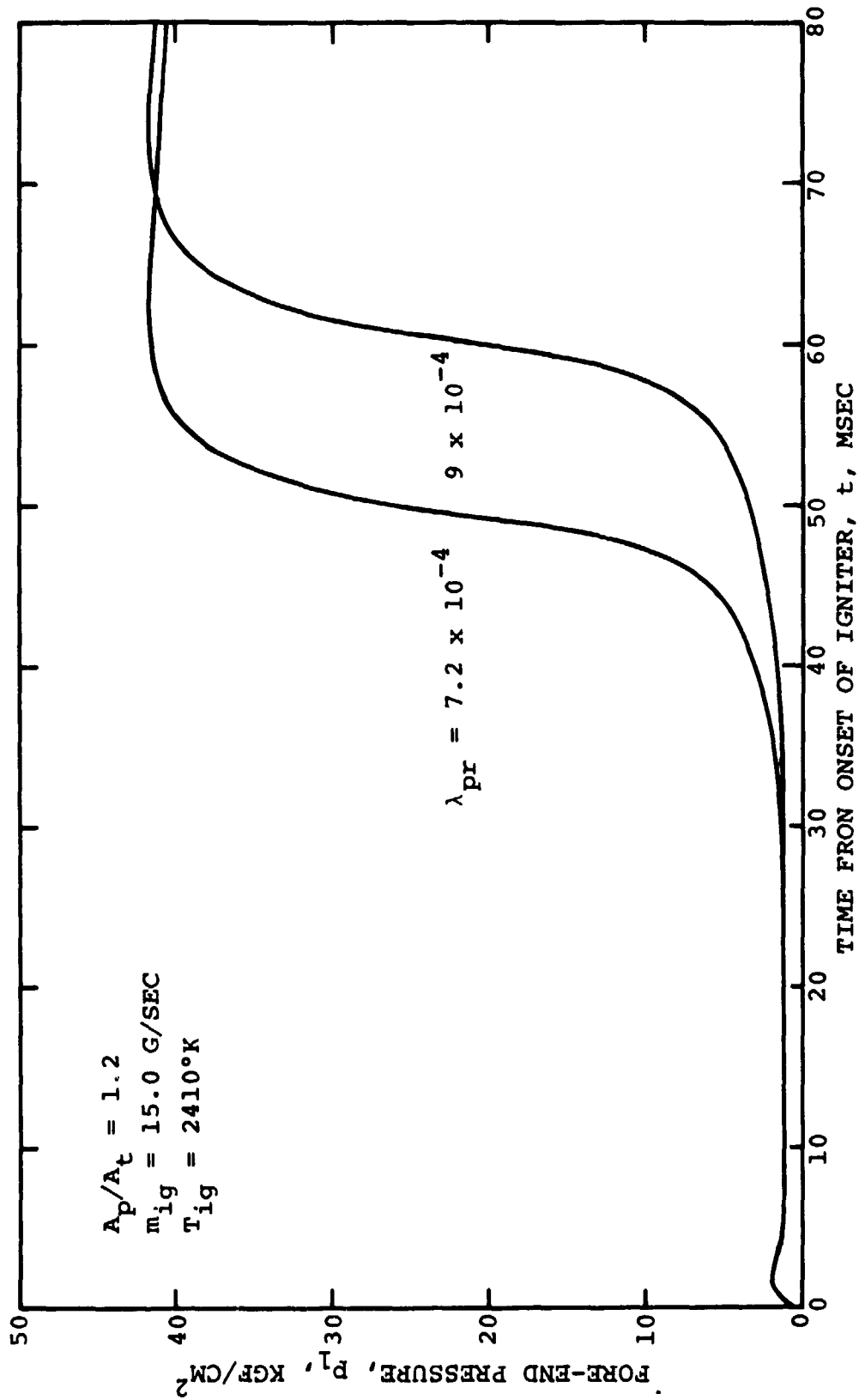
Fig. 47 Effect of uncertainty in propellant thermal conductivity on the fore-end pressure transient.
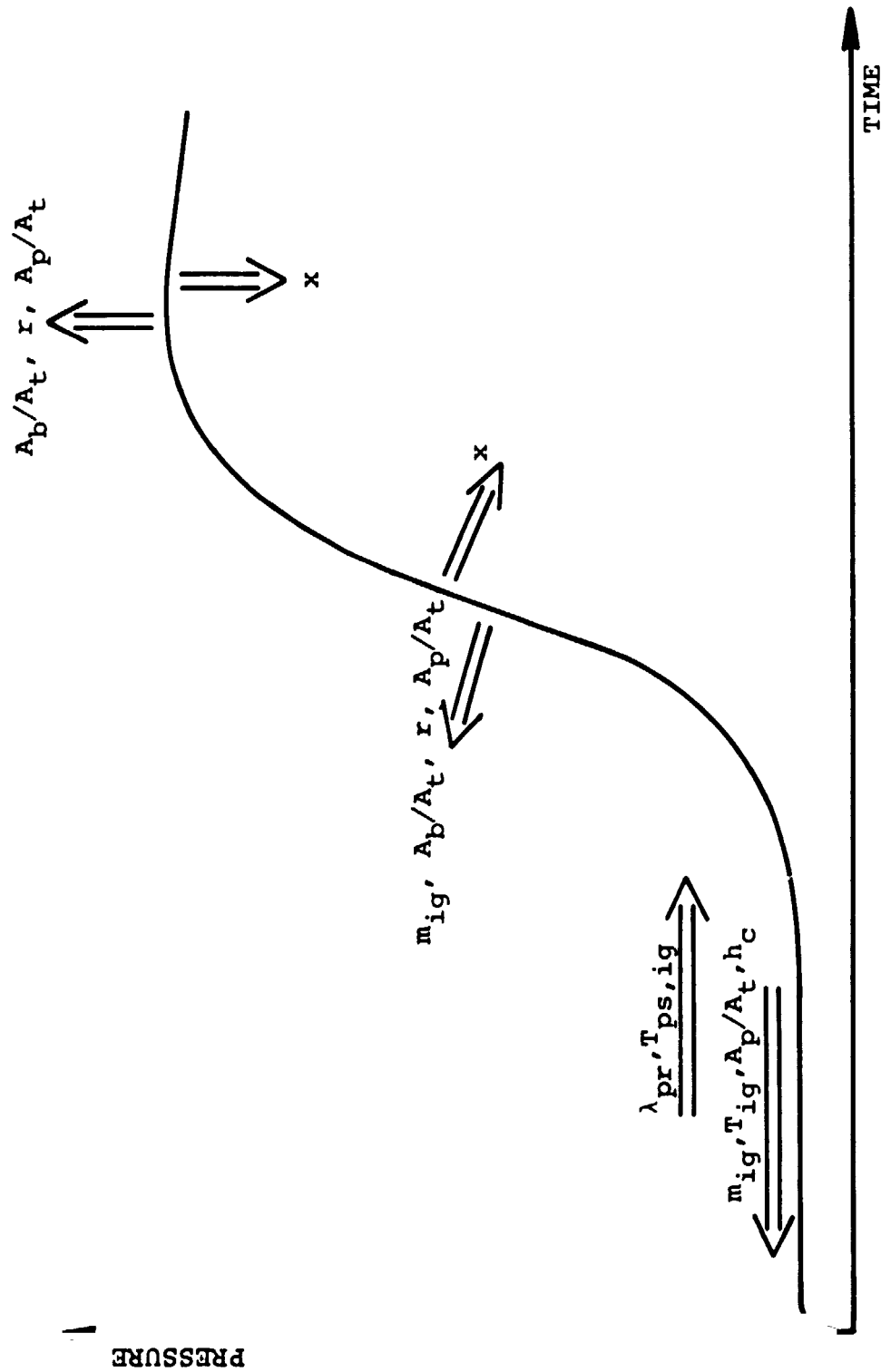
Fig. 48   Schematic representation of the effect of various parameters
          on the shape of the starting pressure transient of HVT motors.

APPENDIX A

NONDIMENSIONALIZATION AND ORDER OF MAGNITUDE

ANALYSIS OF THE CONSERVATION EQUATIONS

1. Main Reference Quantities

Nondimensionalization of the conservation equations is performed by normalizing all variable parameters with respect to well-defined reference quantities. The main reference quantities used for the nondimensionalization of the conservation equations [Eqs. (III-1) to (III-3)] are the following:

(1) Reference time, t^*, defined as the average residence time of the gas in the motor chamber;

$$t^* = \frac{\text{instantaneous mass of gas in the chamber}}{\text{mass rate of gas ejected out of the chamber}}$$

Assuming that the representative static pressure and temperature in the motor can be approximated by the stagnation pressure and temperature at the nozzle entrance, (p_{as} and T_{as}, respectively), the following expression for t^* may be obtained:

$$t^* = \frac{L}{\Gamma^2 c^*} \frac{A_p}{A_t} \tag{A-1}$$

where: L is the effective length of the chamber (the distance between the fore-end of the propellant section and the nozzle entrance)

c* is the characteristic velocity

and Γ is a function of γ, defined in the Nomenclature.

(2) Reference length, x^*, defined as the effective length of the motor chamber ($x^* = L$);

(3) Reference gas velocity, u^*, defined as the average gas velocity in the chamber port

$$u^* \equiv \frac{x^*}{t^*} = \Gamma^2 c^* \frac{A_t}{A_p} \tag{A-2}$$

(4) Reference pressure, p^*, defined as the maximum pressure obtained during the transient period at the motor fore-end ($p^* = p_{1,max}$);

(5) Reference gas temperature, T^*, defined as the adiabatic flame temperature of the solid propellant ($T^* = T_f$);

(6) Reference density, ρ^*, determined by the reference pressure and temperature, and

(7) Reference burning rate, r^*, defined as the non-erosive steady-state burning rate at the reference pressure ($r^* = ap^{*n}$).

All configuration (i.e., geometrical) parameters are nondimensionalized with respect to their initial values.

All reference quantities are denoted by the superscript "*" and all nondimensionalized variables are denoted by the sign "^". According to this convention

$$\hat{p} = \frac{p}{p^*} \; ; \quad \hat{u} = \frac{u}{u^*} \; ; \quad \hat{T} = \frac{T}{T^*} \; ; \quad \hat{\rho} = \frac{\rho}{\rho^*}$$

$$\hat{t} = \frac{t}{t^*} \; ; \quad \hat{x} = \frac{x}{L^*} \; ; \quad \text{etc.} \tag{A-3}$$

Derivatives with respect to time become

$$\frac{\partial p}{\partial t} = \frac{p^*}{t^*} \frac{\partial \hat{p}}{\partial \hat{t}} \; ; \quad \frac{\partial u}{\partial t} = \frac{u^*}{t^*} \frac{\partial \hat{u}}{\partial \hat{t}} \; ; \quad \text{etc.} \tag{A-4}$$

Derivatives with respect to distance become

$$\frac{\partial p}{\partial x} = \frac{p^*}{x^*} \frac{\partial \hat{p}}{\partial \hat{x}} \; ; \quad \frac{\partial u}{\partial x} = \frac{u^*}{x^*} \frac{\partial \hat{u}}{\partial \hat{x}} \; ; \quad \text{etc.} \tag{A-5}$$

Second derivatives with respect to distance become

$$\frac{\partial^2 T}{\partial x^2} = \frac{T^*}{x^{*2}} \frac{\partial^2 \hat{T}}{\partial \hat{x}^2} \; ; \quad \frac{\partial^2 u}{\partial x^2} = \frac{u^*}{x^{*2}} \frac{\partial^2 \hat{u}}{\partial \hat{x}^2} \tag{A-6}$$

2. Nondimensionalization of the Continuity Equation

The continuity equation, Eq. (III-1), is nondimensionalized according to Eqs. (A-2) to (A-5) to become

$$\frac{\rho^* u^*}{x^*}\left[\frac{\partial \hat{\rho}}{\partial \hat{t}} + \frac{\partial(\hat{\rho}\hat{u})}{\partial \hat{x}} + \frac{\hat{\rho}\hat{u}}{\hat{A}_p} \frac{\partial \hat{A}_p}{\partial \hat{x}}\right] = \frac{\rho^*_{pr} r^* b^*}{A^*_p} \frac{\hat{p}B}{\hat{A}_p}\left(\hat{\rho}_{pr} - \frac{\rho^*}{\rho^*_{pr}}\hat{\rho}\right)$$

$$\tag{A-7}$$

Dividing Eq. (A-6) by $\rho^* u^*/x^*$ the nondimensionalized continuity equation is obtained:

$$\frac{\partial \hat{\rho}}{\partial \hat{t}} + \frac{\partial (\hat{\rho}\hat{u})}{\partial \hat{x}} + \frac{\hat{\rho}\hat{u}}{\hat{A}_p}\frac{\partial \hat{A}_p}{\partial \hat{x}} = \frac{\rho^*_{pr}}{\rho^*} \quad \frac{r^*}{u^*} \quad \frac{b^* x^*}{A^*_p}\frac{\hat{r}\hat{b}}{\hat{A}_p}\left(\delta_{pr} - \frac{\rho^*}{\rho^*_{pr}}\hat{\rho}\right)$$

$$1 \qquad 1 \qquad 1 \qquad 10^2 \quad 10^{-4} \quad 10^2 \qquad 1 \qquad 10^{-2}$$

$$(A-8)$$

where an order of magnitude characteristic of the physical model is denoted under the terms.

The last term on the right-hand side of Eq. (A-8) is 10^2 times smaller than the other terms for the usual operating pressures, flame temperatures, gas molecular weights, and propellant densities encountered in solid-propellant rocket motors (20 to 80 atm; 2000 to 3000°K; 20 to 30 g/g-mole, and 1.5 to 2.0 g/cm³, respectively). It is therefore neglected in the analysis. The neglected term expresses the rate of mass accumulation in the free volume created by the propellant surface regression. After this simplification, the resulting dimensional continuity equation is presented by Eq. (III-4).

3. Nondimensionalization of the Momentum Equation

Substituting Eq. (III-1) into the momentum equation, Eq. (III-2), the latter becomes (using the expression for normal stress)

$$\rho\frac{\partial u}{\partial t} + \rho u\frac{\partial u}{\partial x} + g\frac{\partial p}{\partial x} = -\frac{\rho_{pr}rb}{A_p}u + \frac{4}{3}\mu\left(\frac{\partial^2 u}{\partial x^2} + \frac{1}{A_p}\frac{\partial A_p}{\partial x}\frac{\partial u}{\partial x}\right) - \frac{fP_w}{2A_p}\rho u^2$$

$$(A-9)$$

where μ may be considered to include the eddy viscosity.

Nondimensionalization of Eq. (A-9) yields

$$\frac{\rho^*(u^*)^2}{x^*}\left(\hat{\rho}\frac{\partial \hat{u}}{\partial \hat{t}}\right) + \frac{\rho^*(u^*)^2}{x^*}\left(\hat{\rho}\hat{u}\frac{\partial \hat{u}}{\partial \hat{x}}\right) + \frac{\gamma g R^* T^*}{\gamma x^*}\rho^*\frac{\partial \hat{p}}{\partial \hat{x}} = -\frac{\rho^*_{pr}r^*b^*}{A^*_p}u^*\frac{\hat{\rho}_{pr}\hat{r}\hat{b}}{\hat{A}_p}\hat{u}$$

$$+ \frac{4}{3}\mu^*\hat{\mu}\frac{u^*}{x^{*2}}\left(\frac{\partial^2 \hat{u}}{\partial \hat{x}^2} + \frac{1}{\hat{A}_p}\frac{\partial \hat{A}_p}{\partial \hat{x}}\frac{\partial \hat{u}}{\partial \hat{x}}\right) - \frac{f^* P^*_w}{2A^*_p}\rho^*(u^*)^2\frac{\hat{f}\hat{P}_w}{\hat{A}_p}\hat{\rho}\hat{u}^2 \quad (A-10)$$

Dividing throughout by $\rho^*(u^*)^2/x^*$ and denoting

$$Re^*_d = \frac{\rho^* u^* d^*_h}{\mu^*} \qquad \text{and} \qquad (M^*)^2 = (u^*)^2/\gamma g R^* T^*$$

the nondimensionalized momentum equation becomes

$$\hat{\rho}\frac{\partial\hat{u}}{\partial\hat{t}} + \hat{\rho}\hat{u}\frac{\partial\hat{u}}{\partial\hat{x}} + \frac{1}{\gamma(M^*)^2}\frac{\partial\hat{p}}{\partial\hat{x}} = -\frac{\rho_{pr}^*}{\rho^*}\quad\frac{r^*}{u^*}\quad\frac{b^*x^*}{A_p^*}\quad\frac{\hat{\rho}_{pr}}{\hat{A}_p}\hat{u}$$

$$\quad 1 \qquad\quad 1 \qquad\qquad 1 \qquad 1 \qquad 10^2 \quad 10^{-4} \quad 10^2 \qquad 1$$

$$+ \frac{4}{3}\frac{1}{Re_d^*}\quad\frac{d_h^*}{x^*}\quad\hat{u}\left\{\overset{0}{\cancel{\frac{\partial^2\hat{u}}{\partial\hat{x}^2}}} + \frac{1}{\hat{A}_p}\frac{\partial\hat{A}_p}{\partial\hat{x}}\frac{\partial\hat{u}}{\partial\hat{x}}\right\} - 2f^*\quad\frac{x^*}{d_h^*}\quad\frac{fP_w}{\hat{A}_p}\hat{\rho}\hat{u}^2$$

$$\quad 10^{-4}\quad 10^{-2}\quad 1 \quad 1 \qquad\qquad 1 \qquad\qquad 10^{-2}\quad 10\quad 1$$

$$\tag{A-11}$$

where an order of magnitude characteristic of the physical

model is denoted under the terms.

The second term on the right-hand side of Eq. (A-11), expressing the viscous forces between gas molecules is several orders of magnitude smaller than other terms. Therefore it is neglected in the analysis. The term describing the wall friction forces acting on the fluid is one order of magnitude smaller than the other terms and is, therefore, kept in the analysis. Other reasons for keeping the wall-friction term are described in Chapter III, Section C. After the aforementioned simplification, the resulting dimensional momentum equation is presented by Eq. (III-5).

4. Nondimensionalization of the Energy Equation

Substituting the original continuity and momentum equations [Eqs. (III-1) and (III-2)] into the energy equation, Eq. (III-3), the latter becomes (in terms of the static gas temperature)

$$\rho c_p\left(\frac{\partial T}{\partial t} + u\frac{\partial T}{\partial x}\right) - \left(\frac{\partial p}{\partial t} + u\frac{\partial p}{\partial x}\right) - \lambda\frac{\partial^2 T}{\partial x^2}$$

$$= \frac{\rho_{pr}rbc_p}{A_p}\left\{T_f - T + \frac{u^2}{2gJ_c c_p}\right\} - \frac{P_w\sigma\ell}{A_p} + \frac{\lambda}{A_p}\frac{\partial T}{\partial x}\frac{\partial A_p}{\partial x}$$

$$+ \frac{4}{3}\mu\left(\frac{\partial u}{\partial x}\right)^2 + \frac{fP_w}{2A_p}\rho u^3$$

Nondimensionalization of Eq. (A-12) yields

$$\frac{\rho^* c_p^* T^* u^*}{x^*}\hat{\rho}\hat{c}_p\left(\frac{\partial \hat{T}}{\partial \hat{t}} + \hat{u}\frac{\partial \hat{T}}{\partial \hat{x}}\right) - \frac{\gamma-1}{\gamma}\frac{\rho^* c_p^* T^* u^*}{x^*}\left(\frac{\partial \hat{p}}{\partial \hat{t}} + \hat{u}\frac{\partial \hat{p}}{\partial \hat{x}}\right)$$

$$- \lambda^*\frac{T^*}{(x^*)^2}\hat{\lambda}\frac{\partial^2 \hat{T}}{\partial \hat{x}^2} = \frac{\rho_{pr}^* r^* b^* c_p^* T^*}{A_p^*}\frac{\hat{\rho}_{pr}\hat{r}\hat{b}\hat{c}_p}{A_p}\left[\hat{T}_f - \hat{T} + \frac{\gamma-1}{2}(M^*)^2\frac{\hat{u}^2}{\hat{c}_p}\right]$$

$$- \frac{4q_\ell}{d_h^* d_h} + \frac{\lambda^* T^*}{(x^*)^2}\frac{\hat{\lambda}}{A_p}\frac{\partial \hat{T}}{\partial \hat{x}}\frac{\partial \hat{A}_p}{\partial \hat{x}} + \frac{4}{3}\frac{M^*(u^*)^2}{(x^*)^2}\hat{u}\left(\frac{\partial \hat{u}}{\partial \hat{x}}\right)^2$$

$$+ \frac{2f^*\rho^*(u^*)^3}{d_h^*}\frac{\hat{f}\hat{\rho}_w}{A_p}\hat{\rho}\hat{u}^3 \tag{A-13}$$

Assuming the heat transfer to the port walls to be convective and using the Dittus-Boelter correlation for the heat-transfer coefficient ($Nu_d = a_1 Re_d^{0.8}Pr^{0.4}$), the former may be expressed by the following equation

$$q_\ell = Nu_d\frac{\lambda}{d_h}(T - T_{ps})$$

$$= Nu_d^*\frac{\lambda^*}{d_h^*}T^*\hat{Nu}_d\frac{\hat{\lambda}}{d_h}(\hat{T} - \hat{T}_{ps}) \tag{A-14}$$

Substituting Eq. (A-14) into Eq. (A-13) and dividing through by $\rho^* c_p^* T^* u^*/x^*$ yields the following form of the nondimensional energy equation and the corresponding order of magnitude of the different terms:

$$\hat{\rho}\hat{c}_p\left(\frac{\partial \hat{T}}{\partial \hat{t}} + \hat{u}\frac{\partial \hat{T}}{\partial \hat{x}}\right) - \frac{\gamma-1}{\gamma}\left(\frac{\partial \hat{p}}{\partial \hat{t}} + \hat{u}\frac{\partial \hat{p}}{\partial \hat{x}}\right)$$

$$\quad 1 \quad\quad 1 \quad\quad 1 \quad\quad 2\times10^{-1} \quad 1 \quad\quad 1$$

$$- \frac{1}{Re_d^* Pr^*}\frac{d_h^*}{x^*}\overset{0}{\nearrow}\hat{\lambda}\frac{\partial^2 \hat{T}}{\partial \hat{x}^2} = \frac{\rho_{p\perp}^*}{\rho^*}\frac{r^*}{u^*}\frac{b^* x^*}{A_p^*}\frac{\hat{\rho}_{pr}\hat{r}\hat{b}\hat{c}_p}{A_p}\left[\hat{m}_f - \hat{T} + \frac{\gamma-1}{2}(M^*)^2\frac{\hat{u}^2}{\hat{c}_p}\right]$$

$$10^{-4} \quad 10^{-2} \quad 1 \quad\quad 10^2 \; 10^{-1} \; 10^2 \quad\quad 1 \quad 1 \quad 1 \quad 1$$

$$- 4St^* \frac{x^*}{d_h^*} \hat{N}u_d \frac{\lambda}{d_h^2} (\hat{T}-\hat{T}_{ps}) + \frac{1}{Re_d^*Pr^*} \frac{d_h^*}{x^*} \overset{\nearrow 0}{\frac{\lambda}{A_p}} \frac{\partial \hat{T}}{\partial \hat{x}} \frac{\partial A_p}{\partial x}$$

$$\quad 10^{-2} \quad 10^{2} \quad 1 \quad 1 \quad 1 \qquad 10^{-4} \quad 10^{-2} \quad 1 \quad 1 \quad 1$$

$$\neg \frac{4}{3}(\gamma-1)\frac{(M^*)^2}{Re_d^*} \overset{\nearrow 0}{\frac{d_h^*}{x^*}} \hat{\mu}\left(\frac{\partial \hat{u}}{\partial \hat{x}}\right)^2 + 2(\gamma-1)f^*(M^*)^2 \frac{x^*}{d_h^*} \frac{\hat{f}\hat{P}_w\hat{\rho}\hat{u}^3}{A_p}$$

$$\quad 10^{-1} \quad 10^{-5} \quad 10^{-2} \quad 1 \qquad 10^{-2} \quad 10^{-1} \quad 10^{2} \quad 1$$

$$(A-15)$$

where St^* is the reference Stanton Number ($St^* = Nu^*/Re^*Pr^*$).

The following terms in Eq. (A-15) are several orders of magnitude smaller than the other terms: (1) the third term on the left-hand side and the third term on the right-hand side, which describe the axial heat conduction between gas molecules; (2) the fourth term on the right-hand side, which describes the viscous dissipation. Therefore, these terms are neglected in the analysis. The term describing the rate of work performed on the fluid by the wall friction forces is one order of magnitude smaller than the other terms and is kept in the analysis. After this simplification the resulting dimensional energy equation is presented by Eq. (III-6).

APPENDIX B

THE AXIAL VARIATION OF PRESSURE, VELOCITY AND

TEMPERATURE IN THE MOTOR PORT

The effects of the various processes taking place during the pressure transient on the axial variation of pressure, velocity and temperature are shown in the following paragraphs.

Equations (III-7) and (III-9) can be solved for the partial space derivatives of pressure and gas velocity to yield the following expressions:

$$\frac{\partial p}{\partial x} = \frac{M^2}{1-M^2} \left\{ \frac{1}{u} \frac{\partial p}{\partial t} - \frac{\gamma p}{u^2} \frac{\partial u}{\partial t} \right.$$

<div align="center">

VARIATIONS W.R.T. TIME

(UNSTEADINESS EFFECTS)

</div>

$$+ \frac{\gamma p}{A_p} \frac{\partial A_p}{\partial x} \qquad\qquad - \gamma R \frac{\rho_{pr} r b}{A_p} \frac{T}{u}\left(1 + \frac{T_f}{T} + \frac{\gamma-1}{2}M^2\right)$$

<div align="center">

EFFECT OF AXIAL EFFECT OF PROPELLANT GASES
PORT AREA VARIATION ENTERING THE STREAM

</div>

$$+\frac{(\gamma-1)J_c P_w}{A_p u} q_\ell \qquad - \frac{\gamma}{2} \frac{fP_w}{A_p} p\left[(\gamma-1)M^2 + 1\right]\left.\right\} \qquad (B-1)$$

<div align="center">

EFFECT OF HEAT EFFECT OF FRICTION
TRANSFER TO PORT WALLS LOSSES

</div>

and

$$\frac{\partial u}{\partial \cdot} = \frac{1}{1-M^2}\left[\frac{M^2}{u} \frac{\partial u}{\partial t} - \frac{1}{\gamma p} \frac{\partial p}{\partial t}\right.$$

$$- \frac{u}{A_p} \frac{\partial A_p}{\partial x} + \frac{R\rho_{pr} r b}{A_p} \frac{T}{p}\left(\frac{\gamma+1}{2}M^2 + \frac{T_f}{T}\right)$$

$$+ \frac{(\gamma-1)J_c}{\gamma} \frac{P_w}{A_p} \frac{q_\ell}{p} - \frac{\gamma P_w}{2A_p} fM^2 u\left.\right] \qquad (B-2)$$

From Eq. (III-8) an expression for the partial space derivative of gas temperature is obtained:

$$\frac{\partial T}{\partial x} = -\frac{1}{u}\frac{\partial T}{\partial t} - (\gamma-1)\frac{T}{u}\frac{\partial u}{\partial x} - \frac{(\gamma-1)T}{A_p}\frac{\partial A_p}{\partial x}$$

$$+ \gamma R \frac{\rho_{pr} r^{b}}{A_p} \frac{T^2}{\rho u}\left[\frac{T_f}{T} - \frac{1}{\gamma} + \frac{\gamma-1}{2} M^2\right]$$

$$- (\gamma-1)J_c \frac{P_w}{A_p}\frac{T}{\rho u}q_\ell + \frac{\gamma(\gamma-1)}{2}\frac{P_w fu}{A_p} M^2 \qquad (B-3)$$

The effects of the various parameters on the axial variation of pressure, temperature and velocity are clearly expressed in Eqs. (B-1) through (B-3). The pressure variation along the port [Eq. (B-1)] is of particular interest. For the subsonic flow existing in the motor, increases of cross-sectional port area and heat loss to the port walls tend to increase the pressure with distance from the fore-end, whereas increases of added mass and friction cause axial decrease of pressure. During the induction period the unsteadiness effects are negligible as compared with the effects of other terms, except for a very short time (1 to 4 msec) at the igniter onset. The pressure distribution (and the distribution of temperature and velocity as well) is determined by the heat flux to the port walls, the wall friction, and the initial port area distribution. During the flame spreading period and the early part of chamber filling interval, however, the flow is largely unsteady and the effects of the terms containing time derivatives [first two terms on the right-hand side of Eq. (B-1)] become significant. The dominant term is that expressing the effect of added mass [third term on the right-hand side of Eq. (B-1)]. Typically, for $A_p/A_t = 1.2$ the combined magnitude of unsteadiness terms for flow over the unignited part of the port during flame spreading is between 10 and 20% of that of the heat-transfer term. Immediately following the completion of flame spreading the magnitude of unsteadiness terms at the fore-end of the propellant section is about 10% of that of the mass-addition term. Thereafter the effect of unsteadiness decreases and that of mass addition increases.

APPENDIX C

COMPARISON OF SOLID PHASE RELAXATION TIMES WITH

THE CHARACTERISTIC TIME OF MOTOR PRESSURIZATION

The phenomenon of dynamic burning following ignition of the solid propellant due to preheating is discussed in Section F, Chapter III. An estimate of its importance in view of the characteristic time of pressure change during the transient (τ_p) is given in the following paragraphs.

The characteristic thickness of preheated layer at the time of ignition (δ_{ph}), assuming constant heat flux to an inert propellant surface can be estimated from the expression

$$\delta_{ph} = \frac{T_{ps,ig} - T_{pi}}{|(\partial T_{pr}/\partial y)_{y=0}|} = \frac{\lambda_{pr}(T_{ps,ig} - T_{pi})}{q_\ell} \qquad (C-1)$$

The time to burn through the preheated layer (τ_{ph}) is given by

$$\tau_{ph} = \delta_{ph}/\bar{r} \qquad (C-2)$$

where $\bar{r}$ is an average burning rate evaluated at average pressure between the induction-period pressure and the maximum pressure.

Consider the following two definitions of characteristic time for motor pressurization: (1) the total time of pressurization, $\tau_{p,t}$, from the instant of pressure rise following the induction-interval level to the attainment of maximum pressure; and (2) the pressurization time interval corresponding to maximum pressure rise, $\tau_{p,m}$. The latter is given by the relation

$$\tau_{p,m} = \frac{p_{max} - p_{ind}}{(\partial p/\partial t)_{max}} \qquad (C-3)$$

where p_{ind} is the pressure level during the induction interval.

For a typical test with the experimental motor at $A_g/A_t = 1.2$, $\tau_{p,t} = 40$ msec and $\tau_{p,m} = 10$ msec (at the fore end of the propellant section).

For the baseline values listed in Table 1 and an average constant value of 40 cal/cm^2-sec for q_ℓ (see Fig. 35) expression (C-1) yields a value of 0.009 cm for δ_{ph}. If the burning rate in Eq. (C-2) is evaluated as the non-erosive

burning rate at an average pressure of 20 kgf/cm^2 (see Fig. 6), then the time to burn through the preheated layer, τ_{ph}, is 18 msec. An estimation of the relaxation time for the solid phase steady-state burning ($\tau_c = \alpha_{pr}/\bar{r}^2$) for the same burning rate yields a value of 7.8 msec.

Comparing these values of τ_{ph} and τ_c with the afore-mentioned typical values for $\tau_{p,m}$ and $\tau_{p,t}$, it may be con-cluded that, as far as the entire pressurization time is con-cerned, the effect of dynamic burning due to preheating is small. For the limited time of fast pressure change the effect is significant. However, for properly designed motors the period of large dynamic burning effects is over before the pressure overshoot occurs.[96,216] Thus the dyn-amic burning is not expected to significantly increase p_{max}. As mentioned in Chapter VII, combined consideration of ero-sive and dynamic burning may improve the analysis and extend its application.

APPENDIX D

GENERAL FLOW CHART FOR THE SOLUTION OF THE GOVERNING EQUATIONS

Initial conditions, igniter mass flow rate, and properties of igniter gas are given

Solve the system of one right-boundary condition and compatibility relations along the right running characteristic and particle-path line

$u(t,x_E)$
$T(t,x_E)$
$p(t,x_E)$

Solve the system of two left-boundary conditions and compatibility relation along the left-running characteristic line

$u(t,x_p)$
$T(t,x_p)$
$p(t,x_p)$

Solve Governing Equations (P.D.E.) for velocity, temperature, pressure and port configuration distributions for all required time steps

APPENDIX E

OVERALL COMPUTER PROGRAM FLOW CHART

```
                          ┌───────┐
                          │ Start │
                          └───┬───┘
                              ↓
                  ┌───────────────────────┐
                  │ Read Initial Conditions│
                  │    and Input Data      │
                  └───────────┬───────────┘
                              ↓
   ┌─────┐          ┌─────────────────┐
   │ End │          │ Set  t = t + Δt │
   └──↑──┘          └────────┬────────┘
      │                      ↓
   ┌─────┐          ┌─────────────────┐
   │ Stop│          │ Calculate m_ig  │
   └──↑──┘          └────────┬────────┘
      │                      ↓
  No  │      Yes   ┌─────────────────────────┐
      │            │ Calculate Boundary Values│
      │            └────────┬────────┘
      │                      ↓
      │        ┌──────────────────────────────┐
      │        │ Perform Predictor Calculations│
      │        │ to Obtain  u(x), T(x), p(x)   │
      │        └──────────────┬───────────────┘
      │                       ↓
      │        ┌──────────────────────────────┐
  Is  │        │ Perform Corrector Calculations│
 t < t_max?    │ to Obtain  u(x), T(x), p(x)   │
      │        └──────────────┬───────────────┘
      │                       ↓
      │        ┌──────────────────────────────┐
      │        │ Calculate  T_ps, T_ws and r   │
      │        └──────────────┬───────────────┘
      │                       ↓
      │              ┌─────────────────┐
      │              │ Calculate  A_p  │
      │              └────────┬────────┘
      └────────────────────────
```

Start

Read Initial Conditions and Input Data

Set $t = t + \Delta t$

Calculate m_{ig}

Calculate Boundary Values

Perform Predictor Calculations to Obtain $u(x)$, $T(x)$, $p(x)$

Perform Corrector Calculations to Obtain $u(x)$, $T(x)$, $p(x)$

Calculate T_{ps}, T_{ws} and r

Calculate A_p

Is $t < t_{max}$?

No — End — Stop

Yes

APPENDIX F

LISTS OF COMPUTER PROGRAM SUBROUTINES

AND INPUT DATA CARDS

1. Description of Subroutines

The computer program consists of a main program and thirteen subroutines.

Subroutines LBCUOP and RBC calculate the left-boundary and right-boundary values of the flow parameters, respectively.

Subroutine TSCAL calculates the propellant surface temperature by integrating Eq. (III-50).

Subroutine TPSABL calculates the propellant surface temperature during a decomposition-gasification period (when assumed) by integrating an equation similar to Eq. (III-50) obtained by the integral method.

Subroutines TRID, DECOMP, SOLV, GSOLV, ASOLV, VSOLV, REPL2, REPL1, and SING solve the block-tridiagonal matrix of the finite-difference equations by decomposing it into two bidiagonal matrices.

2. Input Data Cards

There are nine input data cards, placed at the end of the computer program deck. Each card contains up to seven input parameters, placed in consecutive groups of ten columns. The format of each parameter is F10. Therefore the number may be specified either as X.XXXXE±0X or XXXX.XXXX, as required. The designation in the following list is the notation used in the computer program.

The First Card contains the following input information:

      1)   XP = position at the entrance to the propellant section, cm (x_p in the text);

      2)   XG = position at the aft-end of the propellant slab, cm;

      3)   XE = position at the entrance to the motor nozzle, cm (x_E in the text);

      4)   API = initial port area, cm^2;

      5)   APIAT = initial port-to-throat area ratio (A_p/A_t in the text);

6) BP = burning perimeter, cm (b in the text);

7) WPI = initial wetted perimeter, cm ($P_{w,i}$ in the text).

The Second Card contains the following input information:

1) W = molecular weight of the combustion gases, g/g-mole (W in the text);

2) GAMA = ratio of specific heats (γ in the text);

3) ROPR = density of the solid propellant, g/cm^3 (ρ_{pr} in the text);

4) FKPR = thermal conductivity of the solid propellant, cal/cm-sec-°K (λ_{pr} in the text);

5) ALPHAP = thermal diffusivity of the solid propellant, cm^2/sec (α_{pr} in the text) (c_{pr} is calculated in the program from inputs 3, 4, and 5)

6) Leave blank;

7) ROUGH = equivalent relative roughness of the port walls (ε_s/d_h in the text).

The Third Card contains the following input information:

1) TF = adiabatic flame temperature of the solid propellant, °K (T_f in the text);

2) TPSCRI = critical propellant surface temperature for start of decomposition-gasification, °K;

3) TPSBRN = propellant surface temperature, at which propellant ignition occurs, ($T_{ps,ig}$ in the text);

4) A = pre-exponential factor in the non-erosive burning rate law, ap^n (a in the text);

5) BREXP = pressure exponent in the non-erosive burning rate law (n in the text);

6) EBC = erosive burning constant, cm^3-°K/cal
   (k   in the text);

7) EBEX = erosive burning exponent (β in the
   text).

The Fourth Card contains the following input information:

1) TCOR = time of the first corner in the multi-
   linearized m_{ig} vs t plot (see Fig. 14),
   sec;

2) TSS = time, at which steady-state igniter
   operation is reached (second corner in
   Fig. 14), sec;

3) TCUT = time, at which linear igniter cut-off
   starts (third corner in Fig. 14), sec;

4) TOFF = time, at which igniter is completely
   turned off, sec;

5) MIGN(O) = initial igniter mass flow rate
   (at t = 0) to facilitate the
   numerical calculation, g/sec,
   ($m_{ig,i}$ in the text);

6) MIGNC = igniter mass flow rate at time TCOR,
   g/sec;

7) MIGNSS = steady-state igniter mass flow rate,
   g/sec.
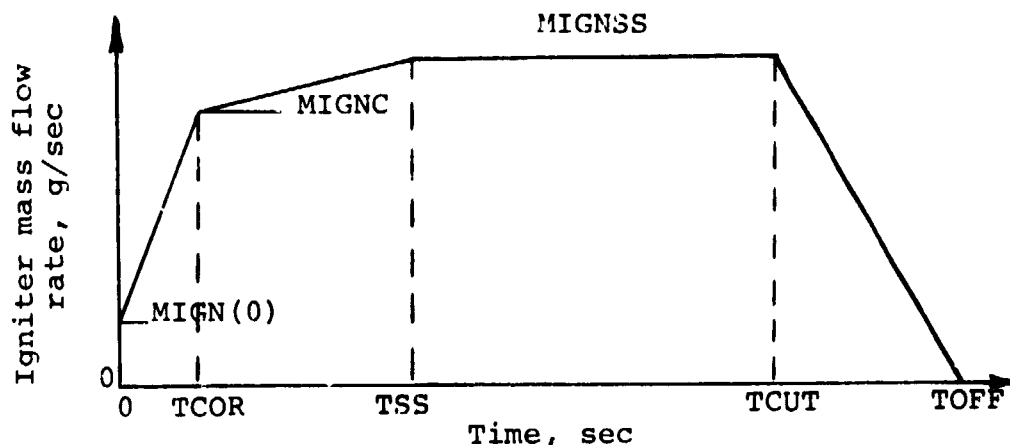
The Fifth Card contains the following input information:

    1) TGI = initial gas temperature in the motor, °K (T_i in the text);

    2) PCI = initial pressure in the motor, gf/cm^2 (p_i in the text);

    3) PAM = ambient pressure, gf/cm^2 (p_a in the text);

    4) TPI = initial propellant temperature, °K (T_{pi} in the text);

    5) TIGN = effective mean temperature of the igniter gas, °K (T_{ig} in the text);

    6) UCI = initial gas velocity in the motor, cm/sec (u_i in the text).

The Sixth Card contains the following input information:

    1) NITER = number of iterative predictor calculations;

    2) NPRINT = number of time-step calculations, after each of which an output is printed out;

    3) NPUN = number of time-step calculations, after each of which an output is punched out for plotting and restart;

    4) NSPAVE = number of time step calculations, after each of which space averaging takes place;

    5) NBL = number of time-step calculations, after each of which balance of the conservation and governing equations is performed and printed out

The Seventh Card contains the following input information:

    1) DELTAX = spacewise step for the numerical calculation (must result in a whole number of increments), cm (Δx in the text);

    2) DELTAT = time step in the numerical calculation, sec (Δt in the text);

3) TI = initial time of a computer run, or a restart run, sec;

4) TMAX = maximum time of a computer run, or a restart run, sec;

5) EPSLON = a small number in Eq. (III-51), °K (ε in the text);

6) DDRG = a factor, by which the expression for the friction coefficient [Eq. (III-33)] is multiplied (for parametric studies);

7) DDHC = a factor, by which the expression for the heat-transfer coefficient [Eq. (III-31)] is multiplied (for parametric studies).

The Eighth Card contains the following input information:

1) TSAV1 = time, before which the space-averaging weight SAVMIN (see below) is used, sec;

2) TSAV2 = time, after which the space-averaging weight SAVMAX (see below) is used, sec;

3) SAVMIN = space-average percentage weight of the values at the neighboring mesh points specified for the time before TSAV1;

4) SAVMAX = space-average percentage weight of the values at the neighboring mesh points specified for the time after TSAV2. Between the times TSAV1 and TSAV2 linear increase n the space-average weight is specified.

The Ninth Card contains the following input information:

1) TTT1 = time, before which the Crank-Nicolson parameter has the value THETAN (see below), sec;

2) TTT2 = time, after which the Crank-Nicolson parameter has the value THETAX (see below), sec;

3) THETAN = value of Crank-Nicolson parameter, specified for the time before TTT1;

4) THETAX = value of Crank-Nicolson parameter, specified for the time after TTT2. Between the times TTT1 and TTT2 linear increase in the parameter is specified

Table F1

List of Input Values for Datum Case

XP	=	6.16	TGI	=	298.0
XG	=	54.42	PCI	=	1.0331×10^3
XE	=	62.04	PAM	=	1.033×10^3
API	=	1.613	TPI	=	298.0
APIAT	=	1.20	**TIGN**	=	2410.0
BP	=	5.08	UCI	=	727.0
WPI	=	6.35	NITER	=	1.0
W	=	22.01	NPRINT	=	20.0
GAMA	=	1.24	NPUN	=	400.0
ROPR	=	1.60	NSPAVE	=	1.0
FKPR	=	0.0009	NBL	=	200.0
ALPHA.	=	0.001875	DELTAX	=	2.54
ROUGH	=	0.001	DELTAT	=	0.000025
TF	=	2225.0	TI	=	0.0
TPSCRI	=	690.0	TMAX	=	0.080
TPSBRN	=	700.0	EPSLON	=	0.10
A	=	0.00927	DDRG	=	1.0
BREXP	=	0.40	DDHC	=	1.0
EBC	=	5.72	TSAV1	=	0.01
EBEX	=	105.0	TSAV2	=	0.02
TCOR	=	0.002	SAVMIN	=	0.06
TSS	=	0.012	SAVMAX	=	0.06
TCUT	=	0.150	TTT1	=	0.01
TOFF	=	0.220	TTT2	=	0.02
MIGN(O)	=	1.055	THETAN	=	0.60
MIGNC	=	12.0	THETAX	=	0.60
MIGNSS	=	15.0			